

On the structural maturation, plasticity, function
and computation of adult-born hippocampal granule
cells

*Über die strukturelle Maturation, Plastizität,
Funktion und Modellierung adult-geborener
Körnerzellen im Hippokampus*

PhD dissertation submitted to the faculty of biological sciences

*Dissertation zur Erlangung des Doktorgrades der Naturwissenschaften
vorgelegt beim Fachbereich Biowissenschaften*

Johann Wolfgang Goethe-Universität, Frankfurt am Main

by / von

Marcel Beining

from / aus

Speyer

Frankfurt am Main, 2017

Vom Fachbereich Biowissenschaften der

Johann Wolfgang Goethe-Universität als Dissertation angenommen.

Dekanin: Prof. Dr. Meike Piepenbring

Betreuer im Fachbereich: Prof. Dr. Amparo Acker-Palmer

Externer Betreuer: Dr. med. habil. Stephan Wolfgang Schwarzacher

Gutachter:

Prof. Dr. Amparo Acker-Palmer

Dr. Stephan Schwarzacher

Datum der Disputation: 03.05.2017

1. Table of Contents

1. Table of Contents	1
2. Zusammenfassung / Summary (German)	2
3. List of abbreviations	8
4. Introduction	10
4.1. The hippocampus.....	11
4.1.1 Anatomy.....	11
4.1.1 Role of the dentate gyrus	14
4.1.2 Learning at the structural and molecular level	15
4.2 Adult neurogenesis	20
4.1.2 History of adult neurogenesis research in rodents, primates, and humans 20	
4.2.2 Adult hippocampal neurogenesis	23
4.2.2.1 Role	23
4.2.2.2 Structural development and integration of adult-born GCs.....	24
4.2.2.3 Functional integration of adult-born GCs and the critical phase	27
4.3. Compartmental modeling	28
4.3.1 Modeling passive properties: passive cable theory.....	28
4.3.2 Modeling active properties: Hodgkin-Huxley and Markov chain.....	32
4.3.3 Compartmental models of dentate granule cells.....	38
5. Scope of this thesis	40
6. Discussion	42
7. References	53
8. Publications	80
8.1. Publication 1	81
8.2. Publication 2	133
8.3. Publication 3	177
9. Danksagung / Acknowledgements (German)	270
10. Curriculum vitae	273

2. Zusammenfassung / Summary (German)

Der Hippocampus ist eine Hirnregion im Endhirn, die auf die Verarbeitung und Speicherung von räumlichen und zeitlichen Informationen, die ein Individuum erfährt, spezialisiert ist. Den Großteil dieser Informationen erhält der Hippocampus vom entorhinalen Cortex über den *Tractus perforans*, dessen Fasern zuerst den *Gyrus dentatus*, die erste Region des sogenannten trisynaptischen hippocampalen Schaltkreises, erreichen. Während in fast allen anderen Hirnarealen von Säugetieren keine neuen Nervenzellen nach der Geburt gebildet werden, besitzt der *Gyrus dentatus* die einzigartige Fähigkeit zeitlebens bis ins hohe Alter neue primäre Nervenzellen (im GD als Körnerzellen bezeichnet), zu generieren und in das Netzwerk perinatal geborener Körnerzellen zu integrieren. Diese adult-geborenen Körnerzellen durchlaufen in ihrer Entwicklung von der neuralen Stammzelle zur maturaen Körnerzelle eine sogenannte „kritische Phase“ in der sie besonders leicht erregbar sind, wenig inhibiert werden und eine erhöhte Plastizität ihrer synaptischen Kontakte aufweisen. Es wird vermutet, dass die Zellen auf diese Weise trotz der generell starken Inhibition im *Gyrus dentatus* auf neue Muster reagieren und diese im Weiteren kodieren können. Dies könnte besonders die Separierung ähnlicher und neuer Gedächtnismuster unterstützen, die Hauptfunktion des *Gyrus dentatus*, wie vermutet wird. Daher ist es nicht verwunderlich, dass Störungen der adulten Neurogenese und der funktionellen Integration junger Körnerzellen, eine Rolle in diversen neurologischen Krankheiten spielen. Unklarheit besteht jedoch darin, wann genau sich adult-geborene Zellen funktionell integrieren und was mit ihnen anschließend passiert. Die meisten Studien grenzen die kritische Phase auf einen Zeitraum von 4 – 8 Wochen nach der Zellmitose ein und gehen davon aus, dass adult-geborene Zellen anschließend die gleichen Eigenschaften und Funktionen wie alte, perinatal (i.e. um den Zeitpunkt der Geburt) geborene Körnerzellen, besitzen. Während die kritische Phase gut mit elektrophysiologischen und verhaltensbiologischen Studien belegt ist, weist das Bild über die strukturelle Maturation dieser Zellen viele Lücken auf. Zudem existieren bisher keine Studien oder Modelle, mit denen die Auswirkung der besonderen Eigenschaften

junger, adult-geborener Körnerzellen auf deren Verarbeitung synaptischer Informationen untersucht werden konnte.

Im Rahmen der vorliegenden Dissertation wurde die strukturelle Entwicklung und Plastizität adult-geborener Körnerzellen in der Ratte anhand detaillierter morphologischer Rekonstruktionen und Computermodellen untersucht. Hierfür wurden adult-geborene Körnerzellen verschiedenen Alters (21 – 77 Tage nach Mitose) sowie mature perinatal-geborene Körnerzellen rekonstruiert, verglichen und deren strukturelle Veränderungen nach einer Hochfrequenzstimulation der Afferenzen des *Tractus perforans* untersucht. Die detaillierte Analyse umfasste die dendritische Morphologie sowie die Struktur dendritischer Dornfortsätze (engl. spines), welche Rückschlüsse auf Anzahl und Stärke erregender Synapsen zulassen. Des Weiteren wurde ein biologisch fundiertes Computermodell der Elektrophysiologie junger (adult-geborener) und adulter Körnerzellen entwickelt, um eine Grundlage zu schaffen, Unterschiede in der Informationsverarbeitung dieser Zellen zu untersuchen.

Auf der makrostrukturellen, dendritischen Ebene veränderten sich adult-geborene Körnerzellen im Alter zwischen 3 und 11 Wochen nur geringfügig, hauptsächlich durch eine Verringerung kurzer dendritischer Endsegmente zwischen Woche 4 und 5. Neben diesem aus der Entwicklungsbiologie bekannten Trimmen (engl. pruning) des jungen Dendritenbaumes fanden sich keine weiteren morphologischen Änderungen. Dies lässt darauf schließen, dass die strukturelle Maturation der funktionellen Maturation, im Sinne der vollständigen Integration adult-geborener Zelle in das hippocampale Netzwerk, vorausgeht.

Überraschenderweise waren alte, adult-geborene Körnerzellen morphologisch immer noch von alten, perinatal geborenen Körnerzellen unterscheidbar. Die Dendriten alter, perinatal geborener Körnerzellen reichten stets bis zur Fissur, wiesen kaum kurze dendritische Endsegmente auf, waren weniger kurvig und zeigten ein anderes schichtenspezifisches Verzweigungsmuster auf. Wir entwickelten daraufhin ein morphologisches Computermodell, welches zeigte, dass die Zunahme von Volumen und afferenten Fasern des *Gyrus dentatus* im

heranwachsenden Tier ausreichen kann, um die gefundenen morphologischen Unterschiede perinatal und adult-geborener Körnerzellen zu erklären.

Auf der mikrostrukturellen Ebene untersuchten wir Anzahl und Morphologie dendritischer Dornfortsätze, um einen strukturellen Hinweis auf die Anzahl und Stärke der Synapsen von adult-geborenen Körnerzellen zu verschiedenen Zellaltern zu bekommen. Deren Dornfortsatzdichte und -größe nahm von Woche 4 zu Woche 11 stetig zu, besonders zwischen Woche 5 und 6. Der Anteil an großen Dornfortsätzen ($> 0.2 \mu\text{m}^2$) belief sich hierbei stets auf ca. 15 %, was auf eine, in der Literatur schon oft diskutierte, homöostatische Regelung der Synapsenstärke in Körnerzellen hinweisen kann. In alten, adult-geborenen Körnerzellen (Woche 11) war die Anzahl und Größenverteilung mit denen alter, früh-geborener Zellen vergleichbar, was auf einen ähnlichen Einfluss der Afferenzen auf beide Zellpopulationen schließen lässt. In einer der beiden Hirn-Hemisphären führten wir jedoch auch eine zweistündige *in vivo* Hochfrequenzstimulation (HFS) des medialen *Tractus perforans* durch, um die Körnerzellsynapsen in der mittleren Molekularschicht zu aktivieren und einer Langzeitpotenzierung (LTP) ihrer synaptischen Stärke zu unterziehen. Synaptische LTP und LTD (Langzeitdepression) bilden die Grundlage für die Gedächtnisbildung im Gehirn. Alte, perinatal geborene Körnerzellen, zeigten nach solch einer Stimulation, im Vergleich zu unstimulierten Zellen in der gegenüberliegenden Hemisphäre, deutlich vergrößerte Dornfortsätze in der mittleren, stimulierten Molekularschicht auf. Interessanterweise fanden wir gleichzeitig eine Verkleinerung der Dornfortsätze in den nicht stimulierten, inneren und äußeren Molekularschichten, sodass der Anteil an großen Fortsätzen insgesamt wieder konstant blieb. Damit fanden wir das erste Indiz für ein strukturelles Korrelat der in früheren Studien beschriebenen homo- und heterosynaptischen Plastizität bzw. gleichzeitigen LTP und LTD in Körnerzellen nach HFS. Auch auf individuellen rekonstruierten Dendriten der selben Körnerzelle wurde das Expandieren stimulierter Dornfortsätze durch das Schrumpfen unstimulierter Dornfortsätze kompensiert. Dies deutet auf eine, bereits früher diskutierte, homöostatische, strukturelle Plastizität hin, welche die Gewichtung aller Synapsen stets normalisiert.

Interessanterweise zeigten adult-geborene Körnerzellen ab einem Alter von 4 Wochen nicht nur solch eine synaptische, sondern zwischen 4 und 5 Wochen auch eine dendritische Plastizität in Form eines Entfernens kurzer Dendritenendsegmente in der äußeren, unstimulierten Molekularschicht. Diese dendritische Reorganisation war korreliert mit der zellulären Expression des Proteins Arc (activity-regulated cytoskeleton-associated protein), ein sogenanntes immediate-early-gene, welches in die Endozytose synaptischer Rezeptoren und dadurch in die Induktion bestimmter Formen von LTP und LTD involviert ist. Dies führte uns zu der Hypothese, dass eine HFS-induzierte heterosynaptische Abnahme großer, stabilisierender Dornfortsätze in der äußeren Molekularschicht zu einer Destabilisierung der dortigen Dendriten führen kann, wenn die lokale Anzahl an Dornfortsätzen, wie in jungen adult-geborenen Körnerzellen, generell schon niedrig ist. Von der Destabilisierung sind hauptsächlich kurze, dendritische Endsegmente betroffen, die daraufhin retrahieren. Ungeachtet der tatsächlichen Grundlage dieses Phänomens, zeigt dieser Befund, dass junge, adult-geborene Körnerzellen in der kritischen Phase auch strukturell plastischer sind als mature Körnerzellen.

Im letzten Teil meiner Dissertation befasste ich mich damit ein elektrophysiologisches Computermodell junger und alter Körnerzellen zu entwickeln. Im Vergleich zu vorherigen Modellen, sollte dieses viele elektrophysiologische Studien von Körnerzellen gleichzeitig reproduzieren können, dabei aber nur realistische Morphologien nutzen. Das Modell sollte zudem ausschließlich auf Ionenkanälen beruhen, deren Existenz und schichtenspezifische Verteilung in der Körnerzelle eindeutig gezeigt wurde. Die exakte Verteilung und Dichte einzelner Ionenkanäle und Parameter wurde schrittweise per Hand angepasst und die korrekte Funktion durch den Vergleich mit pharmakologischen Experimenten aus der Literatur überprüft.

Das Modell erwies sich als sehr robust und konnte eine Vielzahl experimenteller Studien reproduzieren. Zudem zeigte es sowohl für echte als auch für synthetische Morphologien ein realistisches passives und aktives Verhalten. Dies macht das Modell zur Erstellung und Simulation beliebig vieler synthetischer Körnerzellen, z.B. zur Verwendung in großen Netzwerkmodellen des *Gyrus dentatus*, geeignet.

Wir untersuchten das Computermodell der Körnerzelle zudem auf Kompatibilität mit Rattenmorphologien und –experimenten, welche Unterschiede zur Maus aufweisen. Um eine Vielzahl an Experimenten aus der Ratte zu reproduzieren war lediglich eine Erhöhung des passiven Kir Kanals nötig. Dies lässt einerseits auf eine erhöhte Expression dieses Kanals in der Ratte schließen, was zur bekannten niedrigeren Exzitabilität von Rattenkörnerzellen führt. Andererseits bedeutet es, dass sich Ergebnisse vieler Publikationen, die unterschiedliche Nagerspezies nutzten, im Modell miteinander vereinbaren lassen.

Da wir auch an einem aktiven Modell junger, adult-geborener Körnerzellen interessiert waren, reduzierten wir im Modell Ionenkanäle welche laut Literatur in sich entwickelnden Körnerzellen reduziert sind. Damit konnte das Modell das Verhalten junger, adult-geborener Körnerzellen in der kritischen Phase in vielen Eigenschaften reproduzieren, was für die generelle Konsistenz des Modells spricht.

Die entwickelten elektrophysikalischen Modelle junger und maturer Körnerzellen erlaubten uns nun Unterschiede in der Prozessierung synaptischer Signale zu untersuchen. Dabei beschränkten wir uns auf die Synapsen zwischen Körnerzellen und dem medialen und lateralen entorhinalen Cortex (d.h. mit den Synapsen der mittleren und äußeren Molekularschicht), da dies die beiden wichtigsten Afferenzen darstellen. Wir aktivierten Synapsen mit einer festgelegten Frequenz und untersuchten die Ausgangsfrequenz der Körnerzellen. Die höhere intrinsische Exzitabilität junger Körnerzellen sorgte dafür, dass die Zellen der synaptischen Eingangsfrequenz besser folgen konnten. Allerdings zeigen Studien aus der Literatur, dass junge Körnerzellen nur halb so viele Synapsen besitzen wie mature Körnerzellen. Eine entsprechende Korrektur resultierte in einem vergleichbaren Verhalten junger und alter Körnerzellen, was die in der Literatur diskutierte Kompensation niedriger synaptischer Aktivität durch erhöhte Exzitabilität unterstützt. Um die zeitliche Summation in beiden Zellmodellen zu messen, versetzten wir die Signale der medialen und lateralen Afferenzen um wenige Millisekunden. Dabei stellte sich heraus, dass junge Körnerzellen zeitlich versetzte Signale im Niedrigfrequenzbereich (< 40 Hz) besser integrieren konnten als mature Körnerzellen, aber bei höheren Frequenzen eine schlechtere Präzision

aufwiesen. Beide Befunde unterstützen die Hypothese einer größeren Bandbreite der Reaktivität junger Körnerzellen während der kritischen Phase und bieten interessante, neue, experimentell nachprüfbar Vorhersagen an.

Zusammengefasst wurden in der vorliegenden Dissertation die strukturellen Unterschiede zwischen adult- und perinatal geborenen Körnerzellen sowie deren Ursprung untersucht, die Fähigkeit dieser Zellen zur homo- und heterosynaptischen strukturellen Plastizität bewiesen und ein biologisch fundiertes morphologisches und elektrophysiologisches Computermodell erstellt, mit dem experimentell sonst schwer durchführbare Versuche zur Rolle adult-geborener Körnerzellen im hippocampalen Netzwerk voraussagekräftig simuliert werden können.

3. List of abbreviations

AAV	adeno-associated virus
abGC	adult newborn granule cell
AHP	afterhyperpolarization
AIS	axon initial segment
ANOVA	analysis of variance
AP	action potential or anterior-posterior (axis)
Arc	activity-related cytoskeleton-associated (protein)
ATP	adenosine triphosphate
bAP	backpropagating action potential
BK	big-conductance potassium channel
BP	branch point
BrdU	bromodeoxyuridine
BSA	bovine serum albumin
CA	cornu ammonis
$[Ca^{2+}]_{o/i}$	intra- (i) or extra- (o) cellular Ca^{2+} concentration
Ca_v	voltage-gated Ca^{2+} (channel)
C_m	specific membrane capacitance
CR	Cajal-Retzius (cells)
DAP	depolarizing afterpotential
DCX	doublecortin
DG	dentate gyrus
dpi	days post injection
EC	entorhinal cortex
E_K	equilibrium/reversal potential for potassium
E_M	electron microscopy
E_{Na}	equilibrium/reversal potential for sodium
fAHP	fast afterhyperpolarization
fEPSP	field excitatory postsynaptic potential
F-I	frequency-current (relationship)
GCL	granule cell layer
GC	granule cell
GFP	green fluorescent protein
g_{Kir}	Kir conductance
HCN	hyperpolarization-activated cyclic nucleotide-gated channel
HFS	high frequency stimulation
IEG	immediate early gene
ISI	interspike interval

List of abbreviations

$I_{\text{threshold}}$	current threshold for spiking
I-V	current-voltage (relationship)
IML	inner molecular layer
KATP	ATP-sensitive potassium channel
K2P	2-pore potassium channel
Kir	inward-rectifying potassium channel
K_v	voltage-gated potassium channel
LFP	local field potential
LPP	lateral perforant path
LTD	long term depression
LTP	long term potentiation
mGCs	mature (perinatal born) granule cells
mEPSC	miniature excitatory postsynaptic current
ML	molecular layer
MML	middle molecular layer
MPP	medial perforant path
mRNA	messenger ribonucleic acid
MST	minimum spanning tree
Na_v	voltage-gated sodium channel
OML	outer molecular layer
pA	picoampère
PBS	phosphate-buffered saline
pF	picofarad
PFA	paraformaldehyde solution
PP	perforant path
Prox1	Prospero homeobox protein 1
PSD	postsynaptic density
R_a	axial resistance
R_{in}	input resistance
RV	retrovirus
SGZ	subgranular zone
SK	small-conductance potassium channel
STS	short terminal segment
Syn1	synapsin 1 (promoter)
TBS	Tris-buffered saline
TDL	total dendritic length
TLE	temporal lobe epilepsy
TP	termination point
V_{Rest}	resting membrane potential
$V_{\text{threshold}}$	voltage threshold for spiking

4. Introduction

Adult neurogenesis in the hippocampus has received world-wide attention, as it revealed basic principles of brain function and opens doors to promising therapies for neurodegenerative diseases and injuries such as Alzheimer's disease and stroke. Hence, the field attracts researchers from multiple fields such as biology, medicine, and informatics, and there is a steadily increasing amount of scientific publications. Still, there is a plethora of unanswered questions concerning the process of functional integration of new adult-born neurons into the brain and their subsequent role in brain function. In my thesis, I provide novel insights into the structural maturation and plasticity of adult-born hippocampal granule cells during the critical phase of integration. Moreover, I developed new tools and models making it possible to test the impact of environmental and intrinsic changes on the morphology and electrophysiology of these cells *in silico*.

4.1. The hippocampus

The hippocampus is a brain region within the limbic system located ventrally to the cerebral cortex. The important role of the hippocampus in consolidation of episodic and spatial memory has been recognized due to the famous clinical case of Henry Molaison (better known as H.M.) in the 50s of the last century, who developed severe anterograde amnesia (interestingly, learning of motoric exercises was not affected) after parts of his brain, including his hippocampi, were surgically removed in order to cure him from severe epileptic seizures (Scoville and Milner, 1957). Since then, numerous studies allowed further development of theories on hippocampal involvement in memory consolidation (Alvarez and Squire, 1994; Burgess, 1996; Thompson and Kim, 1996; Eichenbaum et al., 1996; Kandel and Pittenger, 1999; Shors, 2004; Fanselow and Dong, 2010; McKenzie and Eichenbaum, 2011; Preston and Eichenbaum, 2013; Cheng, 2013; Mayford, 2013; Howard and Eichenbaum, 2015; Eichenbaum, 2016; Guan et al., 2016) and navigation (Moser et al., 2008; Derdikman and Moser, 2010; Buzsáki and Moser, 2013), including the role of adult hippocampal neurogenesis (for review, see Kitamura and Inokuchi, 2014).

4.1.1. Anatomy

The hippocampus can be divided into several subregions, namely the cornus ammonis (CA) 1 to 3 and the dentate gyrus (DG). The hippocampus is embedded within the hippocampal formation which further comprises the entorhinal cortex (EC), subiculum, presubiculum, and parasubiculum (Figure 1). These regions are interconnected but exhibit a mostly unidirectional information processing tract (Figure 1, lower right) which was first described by Ramon y Cajal in the beginning of the 20st century (Cajal, 1995, english edition): Fibers from layers II and III of the EC form the perforant path which runs through the parasubiculum to the DG. The dentate granule cells (GCs) in turn send their axons, the so called mossy fibers, to the CA3 pyramidal cells (Claiborne et al., 1986; Frotscher, 1991) which form the Schaffer collaterals terminating at CA1 cells. Finally, the information is projected back to the EC and to the subicular regions. Later on it was recognized that the “trisynaptic loop” has some exceptions, as parts of the perforant path also reach and activate CA1-3

neurons (Steward, 1976; Yeckel and Berger, 1990) and some CA3 interneurons can project back to the DG (reviewed in Myers and Scharfman, 2011).

When the hippocampus is cut into frontal or horizontal sections, two U-shapes opposing each other can be observed (Figure 1, lower right, blue and green shapes). These are the densely packed cell layers of the DG and CA1-3, containing the primary neurons, respectively. The granule cell layer (GCL) of the DG mostly contains GCs, which are the primary neurons of the DG. They extend their cone-shaped dendritic tree into the molecular layer (ML) up to the hippocampal fissure, delineating the DG from the CA regions (Claiborne et al., 1990). The ML is a highly laminated structure where most inputs run parallel to the GCL. Accordingly, the outer and middle ML (OML and MML) are occupied by perforant path fibers from the lateral and medial EC, respectively, and GC dendrites in the inner ML receive input from ipsi- and contralateral mossy cells which are located in the hilus (or polymorphic layer), the region between the upper (suprapyramidal) and lower (infrapyramidal) blade of the DG. The input of mossy cells is excitatory, but as they also project to GC-targeting inhibitory interneurons, their net effect on GCs is highly discussed (Santhakumar et al., 2005; Jinde et al., 2012, 2013; Scharfman and Myers, 2012). Most inhibitory interneurons that synapse onto GCs reside in the ML (e.g. axo-axonic chandelier cells) and in the hilus (e.g. basket cells, Freund and Buzsáki, 1998). Besides excitatory and inhibitory inputs, GCs also receive modulatory input from various brain regions such as serotonergic input from the raphe nuclei, cholinergic input from the septal nuclei, noradrenergic input from the locus coeruleus, and dopaminergic input from the ventral tegmental area (Amaral et al., 2007). GCs themselves send excitatory fibers, the mossy fibers, through the polymorphic layer to the stratum lucidum of the CA3 region (Claiborne et al., 1986; Frotscher, 1991). Their name originates from the mossy appearance as they have many varicosities along their way to CA3. These include smaller “en passant” synapses with mossy cells and basket cells as well as larger multisynaptic terminals with mossy and CA3 cells which can be easily identified through their large postsynaptic spine structure called “thorny excrescences” (Gonzales et al., 2001; Amaral et al., 2007). These represent very strong

synaptic connections such that very few GCs are sufficient to activate CA3 cells (Henze et al., 2000).

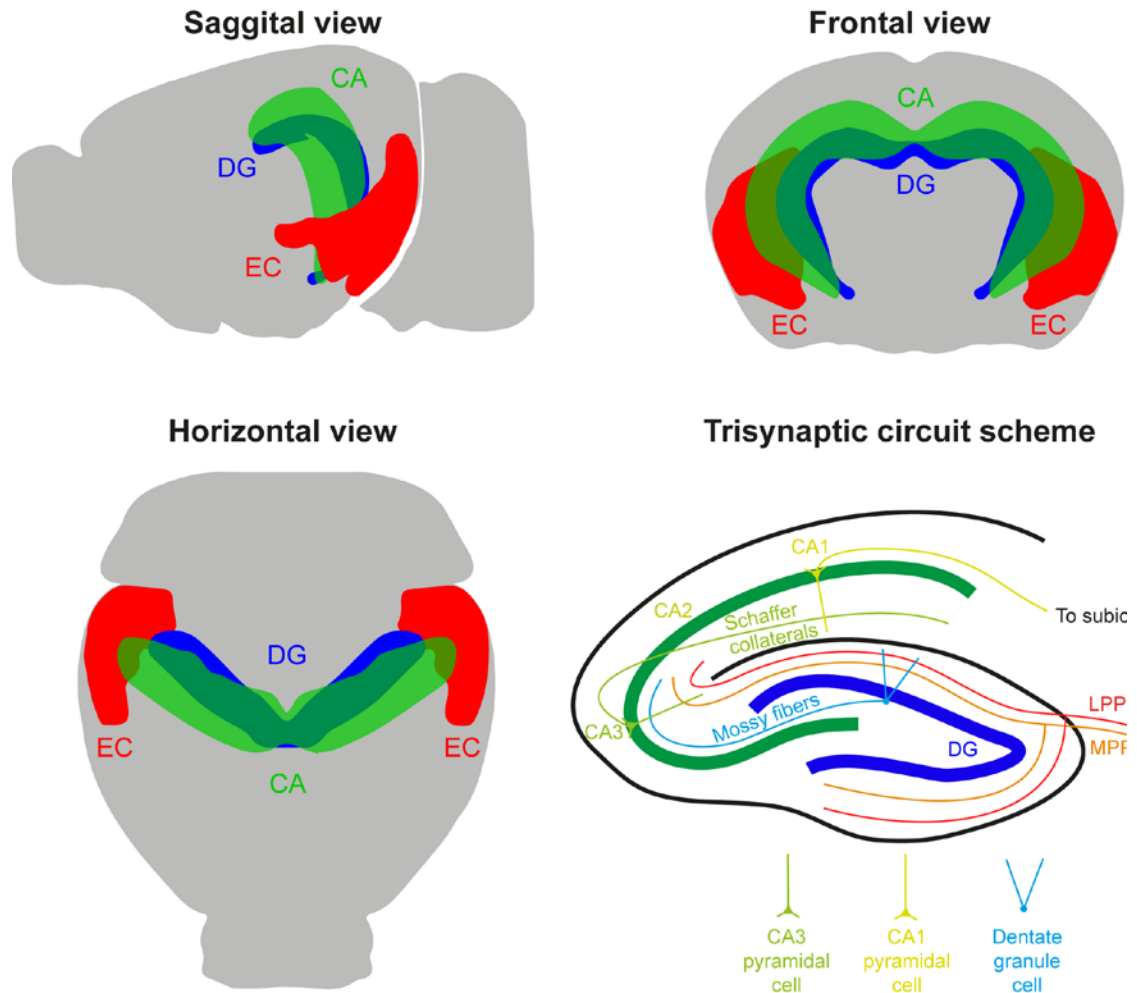


Figure 1: Anatomy and principal cells of the hippocampus. The dentate gyrus (DG, blue) and cornu ammonis (CA, green) region of the hippocampus are schematically illustrated within the mouse brain (gray) from three different anatomical views (upper row and lower left). Also shown is the entorhinal cortex (EC, red) from which the medial and the lateral perforant path (MPP and LPP) afferents originate. Lower right: Schematic illustration of the trisynaptic circuit. The LPP and MPP which come from layer 2 and 3 of the EC innervate the outer and medial molecular layer of the DG and parts of CA3. Dentate granule cells (GCs) which are the main target of the PP send axons, called mossy fibers, to the CA3 region where they target (amongst others) CA3 pyramidal cells. These cells in turn project to CA1 pyramidal cells via the Schaffer collaterals. Finally, from there, signals leave the hippocampus and are projected to the subiculum and back to the EC.

4.1.2. Role of the dentate gyrus

There is evidence that the DG receives spatial (Moser and Moser, 2008; Igarashi, 2016) information from the medial EC and contextual information from the lateral EC (Yoganarasimha et al., 2011; Chao et al., 2016) and that this information is processed in the hippocampus to generate episodic and spatial memory, helping the individual to successfully navigate through and interact with its environment. How this takes place exactly is still not clear, however, it is believed that specific locations and events activate subpopulations of neurons that will become synaptically associated with each other. Recent studies showed that if such a trace memory or engram is later artificially reactivated (Liu et al., 2012) or inhibited (Denny et al., 2014; Tanaka et al., 2014), the memory (e.g. freezing in a chamber where foot shocks had been applied) could be retrieved or suppressed, respectively, suggesting that the animal “remembered” or “forgot” the memory. Interestingly, due to the engram’s synaptic association, an individual is also able to remember a certain situation if only a part of the context is presented, a process called “pattern completion”. Moreover, the hippocampus is also able to perform “pattern separation”, which is the discrimination between two similar situations, such as the location of a car in the same parking deck but on another specific day (Leutgeb et al., 2007). It is highly debated which cells in the hippocampus perform which of these two computations. One idea is that GCs perform pattern separation, especially because the number of GCs is much higher than the number of their pre- and postsynaptic partners, e.g. the GC versus CA3 number in the dorsal DG is 12:1 (Amaral et al., 1990; Schmidt et al., 2012). This divergence should in principle facilitate pattern separation by decorrelation of EC inputs. Furthermore, unlike CA pyramidal cells, GCs do not show recurrent (or auto-associative) connections which would rather favor pattern completion. Indeed, most studies, with one exception (Nakashiba et al., 2012), show solely pattern separation performance of the dentate GCs (Jung and McNaughton, 1993; Deng et al., 2013) and involvement of CA3 cells in pattern completion (Neunuebel and Knierim, 2014). However, others also suggest pattern separation for proximal (close to DG) CA3 cells (Lee et al., 2015). One computational study even suggested that both DG and CA3 perform pattern separation (Myers and Scharfman, 2011). On the cellular level, mature dentate GCs show properties

that are well suited for pattern separation: Due to their hyperpolarized resting membrane potential, the absence of dendritic spikes, linear signal integration, and strong feedforward and feedback inhibition (Spruston and Johnston, 1992; Staley et al., 1992; Schmidt-Hieber et al., 2007; Krueppel et al., 2011; Temprana et al., 2015), these cells exhibit sparse firing, and require simultaneous excitatory input from many presynaptic partners in order to fire action potentials, making them excellent coincidence detectors of distinct patterns including their discrimination and separation, respectively.

To be able to perform pattern separation and completion, patterns have to be learned by the hippocampal network. Learning occurs mostly at the level of synaptic connections, thus synapses have to be very plastic. As the concept of synaptic plasticity is important in regard to my thesis, I will introduce the different aspects of synaptic plasticity.

4.1.3. Learning at the structural and molecular level

A well-known hypothesis on how learning occurs at the level of neuronal networks has already been developed more than 60 years ago by Donald Hebb: “When an axon of cell A is near enough to excite a cell B and repeatedly or persistently takes part in firing it, some growth process or metabolic change takes place in one or both cells such that A's efficiency, as one of the cells firing B, is increased” (Hebb, 1949) or (oversimplified) “Cells that fire together, wire together”. Since then, neuronal networks are believed to store information by an orchestrated and continuous adjustment of their synaptic weights according to the preceding pre- and postsynaptic activity, a mechanism called synaptic plasticity. Such plasticity can occur on the short-term or long-term and can potentiate or depress synaptic strength. Long-term potentiation and depression (LTP and LTD, respectively) are regarded as the underlying mechanisms for learning and memory (Escobar and Derrick, 2007). Synaptic plasticity can further be categorized depending on where it occurs: Homosynaptic plasticity can be induced at synapses that are directly activated, whereas heterosynaptic plasticity occurs at inactive synapses located next to active synapses (Abraham et al., 1985; Oh et al., 2015). In the ML of the DG, such input-specific forms of

plasticity can in principle be easily distinguished due to the mentioned laminated inputs of the lateral and medial perforant path as well as the associational/commissural pathway (Amaral et al., 2007). This allows selective stimulation of one input even in a slice preparation, e.g. by using a bipolar electrode in the corresponding layer. In addition, due to its densely packed parallel neurons, and synchronously firing of GCs and CA pyramidal cells, the hippocampus is highly suited to measure extracellular field potentials which can be used to reveal changes in synaptic strengths: Synaptic activation of GCs evokes depolarizing postsynaptic membrane potentials (EPSPs) which can also be measured in the extracellular space (field EPSPs or fEPSPs), if many neurons become synaptically activated at the same time in this region. The rising slope of the fEPSP recorded in the GCL is positively correlated to the strength of the activated synapses. Furthermore, the population spike indicated by a negative deflection in the fEPSP is correlated with the number of simultaneously spiking neurons. These simple relations allow the investigation of many different aspects of the hippocampal EC-GC synapse. Indeed, the phenomenon of LTP was first described with fEPSP recordings at this synapse (Bliss and Lomo, 1973). By now, several stimulation protocols were established which can induce robust LTP and LTD at this synapse (reviewed in Albensi et al., 2007), one of which is the high-frequency stimulation (HFS) consisting of 8 pulses (500 μ A, 0.1 ms pulse duration) at 400 Hz every 10 s (Sutula and Steward, 1987). Importantly, former studies showed that selective HFS of either the medial or lateral perforant path induced homosynaptic LTP in the activated, and heterosynaptic LTD in the non-activated ML layer (Bliss and Lomo, 1973; Abraham et al., 1985, 1994, 2007; Christie and Abraham, 1992; Doyère et al., 1997), suggesting that these two afferents compete with each other for synapses on GCs, a process that has later been intensively studied in computational models (Hayashi and Nonaka, 2011; Jedlicka et al., 2015). Interestingly, it has recently been suggested that heterosynaptic LTD may act as a homeostatic mechanism by normalizing the overall synaptic weights in order to avoid runaway LTP of single synapses and thereby neuronal hyperexcitability (Chistiakova et al., 2015).

What are the molecular mechanisms in the GC synapse during LTP and LTD induction? Two glutamatergic receptors determine most of the strength and plasticity of a glutamatergic excitatory synapse: AMPA and NMDA receptors (AMPA and NMDARs). Both are depolarizing ionotropic receptors that are permeable to cations. AMPARs constitute four subunits which can be a homomeric or heteromeric assembly of subunits GluR1-4 (Dingledine et al., 1999). Upon binding of glutamate, AMPA receptors elicit fast and large excitatory postsynaptic potentials (EPSPs) and provide the majority of excitatory synaptic currents. In contrast, NMDARs are normally non-conducting at resting membrane potentials due to pore blockade by Mg^{2+} . When the synapse is depolarized due to a backpropagating action potential or the opening of sufficient numbers of AMPA receptors, the Mg^{2+} block is relieved and NMDARs add their conductance to the EPSP. After binding of glutamate and Mg^{2+} unblock, NMDARs can remain open for hundreds of milliseconds, compared to only a few milliseconds for AMPARs. This is of special importance, as NMDARs are also permeable to Ca^{2+} , which can trigger various intracellular signaling cascades, thereby inducing changes in synaptic strength. Depending on the frequency of synaptic activity, it was shown that new AMPARs are either inserted/activated (HFS protocols), or existing AMPARs are removed/inactivated (low-frequency stimulation – LFS – protocols) from the postsynaptic membrane, resulting in LTP or LTD, respectively (O'Dell and Kandel, 1994; Beattie et al., 2000; Lu et al., 2001; Malinow, 2003). The amount of LTP or LTD also depends on the NMDAR subunit composition (NR1, NR2A-D, NR3A). For instance, NR2B, which is often expressed in developing neurons, allows very long influx of ions (Vicini et al., 1998; Rumbaugh et al., 2000), thereby facilitating LTP (Tang et al., 1999; Massey et al., 2004).

Importantly, it was found that general blockade of mRNA translation into proteins also abolished the induction of LTP in hippocampal slices, meaning that *de novo* synthesis of synaptic proteins is required in the signaling cascade leading to LTP (Nguyen et al., 1994). The same correlation was later reported for LFS-induced LTD in young-adult rats (Manahan-Vaughan et al., 2000; but see Abbas, 2016). Furthermore, it was shown that a certain group of genes such as Arc (activity-regulated cytoskeleton-associated protein) and c-fos, later

named immediate-early genes (IEGs), was regularly and quickly transcribed when LTP had been induced artificially (Dragunow and Robertson, 1987; Lyford et al., 1995) or during learning tasks (Soulé et al., 2008). Arc interacts with the endocytic proteins endophilin and dynamin in the postsynaptic density to remove AMPA receptors from the postsynaptic membrane (Chowdhury et al., 2006). Furthermore, the *de novo* transcription of c-fos and Arc was found to be required for synaptic plasticity (Fleischmann et al., 2003; Bramham et al., 2008), making both valuable markers for synaptic activation and plasticity. Interestingly, expression of Arc was shown to be necessary for cell survival and proliferation of adult-born GCs (Kuipers et al., 2009). Moreover, Arc was shown to be implicated in several forms of synaptic LTD, but not in NMDAR-dependent LTD (Park et al., 2008; Waung et al., 2008; Smith-Hicks et al., 2010), indicating that complex and parallel signaling cascades exist which regulate synaptic plasticity.

As synaptic plasticity occurs at the synapse in dendritic spines whereas the mRNA of plasticity-related genes is typically transcribed at the nucleus, one question comes up: How does the neuron know which synapses became activated and need to be supplied with new proteins? Interestingly, Steward and coworkers showed that HFS of the perforant path led to the transport of Arc mRNA into activated dendrites (Steward et al., 1998), suggesting that there has to be some kind of synaptic tag leading to the correct transport of crucial molecules to activated synapses (Frey and Morris, 1998). However, this finding also caused confusion, as Arc should rather tag inactive synapses due to its role in AMPAR endocytosis and LTD. Indeed, a decade later Okuno et al. (2012) found an intriguingly inverse tagging of non-activated synapses by the binding of the Arc protein to CaMKII β , a synaptic protein that is normally bound to the calcium-sensor Calmodulin in active synapses (Okuno et al., 2012). However, the transport and local translation and regulation of Arc mRNA is still unclear and debated (Nonaka et al., 2013; Farris et al., 2014; Steward et al., 2015).

It is further possible to assess the strength of a neuron's excitatory synapses without measuring each individual EPSP and without ultrastructural analysis in electron microscopy images but by analyzing the number and morphology of dendritic spines. Most excitatory glutamatergic synaptic inputs in the brain are located on postsynaptic spines (Harris, 2001), thus the number of spines on a neuron's dendritic tree is a good measure for the amount of excitatory presynaptic partners. The shape of spines is typically categorized into three different types: thin, stubby, and mushroom spines. When a new spine is developing, it often has the thin morphology with a long neck and a small head and is very unstable yet. Stubby spines have a big head but lack a neck. Their usually high number in light and confocal microscopy has recently been shown to be overestimated, as high-resolution STED microscopy reveals that most spines have a neck (Tønnesen et al., 2014). Mushroom spines commonly represent mature spines, as they have a large head, a moderate neck, and are relatively stable over time (Bosch and Hayashi, 2012; Rochefort and Konnerth, 2012). It has been shown several times that the size of spines (mainly referred to the spine head) provides an estimate for its current synaptic strength (for reviews, see Yuste and Bonhoeffer, 2001; Alvarez and Sabatini, 2007): Stimulation protocols known to induce changes in synaptic strength were found to simultaneously influence spine morphologies (Huber et al., 2004; Zhou et al., 2004) and spine sizes were shown to correlate with the size of the postsynaptic density and the amount of AMPA receptors (Reymann and Frey, 2007). Hence, these relations open the possibility to analyze learning (in the form of LTP, LTD as well as homo- and heterosynaptic plasticity) on the single-cell level, especially in such a highly laminated brain region such as the DG.

Intriguingly, besides synaptic plasticity, the DG and possibly very few other brain regions have an additional mechanism that facilitates the storage and retrieval of memory, on which I will elaborate in the next chapter: the addition of new neurons to the existing neuronal network.

4.2. Adult neurogenesis

4.2.1. History of adult neurogenesis research in rodents, primates, and humans

Adult neurogenesis is the capability of stem cells and neuroblasts to give rise to new neurons in the adult brain. In the late 1960s, adult neurogenesis was discovered in the hippocampus (Altman and Das, 1965) and olfactory bulb (Altman, 1969) of rats. This was rather surprising, as the common paradigm had been that the brain is not able to produce new neurons in adulthood. More than a decade later, neurogenesis and functional integration of the newborn neurons was discovered in the tectum of adult singing birds (Goldman and Nottebohm, 1983; Paton and Nottebohm, 1984). However, the question whether adult neurogenesis is also relevant for humans could not be answered until the end of the last century when labeling of newly synthesized DNA with the nucleotide analogue Bromodeoxyuridine (BrdU) made it possible to find evidence for hippocampal adult neurogenesis in primates (Gould et al., 1998, 1999b; Kornack and Rakic, 1999) and humans (Eriksson et al., 1998). The brain samples from the latter were obtained from cancer patients that had received BrdU to observe cell proliferation in the cancer tissues. Later, neural stem and precursor cells could successfully be isolated and cultivated from human surgical tissue (Johansson et al., 1999; Arsenijevic et al., 2001) originating from the hippocampus or from the subventricular zone (SVZ) which surrounds the lateral ventricle. Both brain regions still represent the location with the most prominent rate of adult neurogenesis. Noticeably, a study from 2010 showed adult neurogenesis in the hypothalamus of mice, which might act as a compensatory mechanism to regulate energy balance (Pierce and Xu, 2010), however, this phenomenon requires further analysis, yet (see review Yuan and Arias-Carrión, 2011). It was also suggested that adult neurogenesis occurs in the neocortex of rodents and primates (Bernier et al., 2002; Dayer et al., 2005). However, these findings were controversial as others only found neural progenitor cells and no differentiation of these cells into new neurons (Kornack, 2001; Koketsu et al., 2003), suggesting that only gliogenesis occurred there. Another explanation for this discrepancy was that adult-born neurons in the neocortex have only a transient existence (Gould et al., 2001). Eventually, a

new technique, the C^{14} birth-dating, could show that at least for humans, neocortical neurogenesis is restricted solely to development (Spalding et al., 2005; Bhardwaj et al., 2006). This technique utilized the fact that the formerly constant atmospheric concentration of the radioactive isotope C^{14} peaked considerably during the Cold War (1955-1963) when nuclear bombs were tested frequently. As the C^{14} concentration was exponentially decaying since then and C^{14} atoms had been integrated into newborn cells of human beings, measuring the amount of C^{14} atoms in the genomic DNA of human neurons allowed the determination of the cell's age and therefore the region-specific exclusion or evidence of adult neurogenesis.

Interestingly, neurons born in the adult SVZ, a region which shows similar rates and an age-related decline of neurogenesis as the hippocampus, were found to migrate to different brain regions in primates, including humans, compared to rodents: In rodents, the immature cells born in the SVZ migrate through the rostral migratory stream (RMS) to the olfactory bulb (OB) (Lois et al., 1996; Ming and Song, 2011). These immature cells were found to be involved in the fine modulation of olfaction (Lepousez et al., 2013; Gheusi and Lledo, 2014), neuronal repair, and immune response against pathological or toxic particles (Loseva et al., 2009). In contrary, the human RMS only showed migration of newborn neurons from the SVZ to the OB during the postnatal period (< 6 months) (Sanai et al., 2011), followed by the closure of the olfactory ventricle (Sanai et al., 2007). This was also validated by the mentioned C^{14} technique (considering the limitations of this technique, the amount of OB neurons being exchanged over 100 years might be 1 % at maximum) (Bergmann et al., 2012). Earlier findings of immature neurons in the adult human OB (Bédard and Parent, 2004; Curtis et al., 2007) might be explained by local cell proliferation (Liu and Martin, 2003). Strikingly, the SVZ-neurons in humans were found to migrate to the striatum instead (Ernst et al., 2014) which is involved in emotions, movement coordination, and cognitive flexibility, meaning the ability to adapt behavioral goals in response to changing contextual demands (Cools et al., 2004, 2006). Indeed, striatal adult neurogenesis was reported in adult nonhuman primates but it was unclear if these cells proliferated locally or migrated through the RMS (Bédard et al., 2002, 2006). Similarly, some studies

suggested marginal postnatal generation of striatal interneurons in mice, rats, and rabbits (Dayer et al., 2005; Luzzati et al., 2006; Inta et al., 2008), but the rate of integration of new neurons was not comparable to that found in the human striatum (Ernst et al., 2014). A recent review (Kempermann, 2014) suggested that the SVZ-striatum migration of adult-born neurons is the common route in humans, but can also be induced in other mammals in the case of striatum-located injuries as it was shown for ischemia and tumors (Arvidsson et al., 2002; Tonchev et al., 2003, 2005; Glass et al., 2005; Hou et al., 2008; Wei et al., 2011). Noticeably, a large number of disorders interfere with striatal neuronal function, including stroke, Huntington's disease, Parkinson's disease, schizophrenia, and addiction. A recent study showed depletion of striatal neurogenesis in Huntington's disease (Ernst et al., 2014), a hereditary neurodegenerative disease resulting in striatal atrophy and movement disorders. This indicates that newborn neurons in the striatum might be used to replenish lost cells. However, striatal neurogenesis research is still at the beginning (Inta et al., 2015), and a functional role of these neurons beyond repair remains to be established. A recent study showed that striatal astrocytes in mice can be forced to enter the neurogenic cycle by blocking the Notch signaling pathway (Magnusson et al., 2014), representing an adequate model to analyze this process in a standard experimental species, as research in primates, including humans, is difficult. Together, the findings of inducible adult neurogenesis in the striatum or potentially other extra-hippocampal regions raises hope for future therapeutic strategies in brain repair.

4.2.2. Adult hippocampal neurogenesis

4.2.2.1. Role

In the last two decades, adult hippocampal neurogenesis has received world-wide interest in the neuroscience field (for recent reviews, see (Bergmann et al., 2015; Kempermann, 2015)) due to several reasons. First, adult-born dentate GCs do not simply fulfill a repair function: Loss-of-function studies using irradiation or antimetabolic drugs to kill neural stem cells showed learning and memory deficits in the treated animals (Shors et al., 2001; Madsen et al., 2003). Similarly, the decrease of hippocampal neurogenesis in aged macaques was correlated to a reduced learning performance (Aizawa et al., 2009). Intriguingly, more recent studies provided evidence for a role of young adult-born GCs in the aforementioned (see 4.1.2) pattern separation function of the DG (Clelland et al., 2009; Nakashiba et al., 2012; Neunuebel and Knierim, 2014; Johnston et al., 2016), especially when context differences that had to be distinguished were minimal (Leutgeb et al., 2007).

Second, adult hippocampal neurogenesis in rodents and primates was found to be regulated by various factors (reviewed in Lucassen et al., 2010 and Chambers, 2013), a few of which are stress (Gould et al., 1998; Coe et al., 2003), aging (Gould et al., 1999b; Leuner et al., 2007; Aizawa et al., 2009), learning (Gould et al., 1999a), exercise (van Praag et al., 1999), enriched environments (Kempermann et al., 1997), body metabolism (Perera et al., 2011b), global and focal brain ischemia (Tonchev et al., 2003; Koketsu et al., 2006; Tonchev and Yamashima, 2006), addiction (Taffe et al., 2010), and, interestingly, antidepressant treatment (Malberg et al., 2000; Perera et al., 2007, 2011a). Hence, understanding these interactions might help to develop improved therapeutics or even prevent the development of some psychological disorders such as depression.

Third, as mentioned above (4.2.1), it was found that adult hippocampal neurogenesis plays a much more prominent role in humans than previously thought. The C^{14} method revealed a quite extensive average neuronal turnover of about 1.75 % per year (Spalding et al., 2013). This was comparable to middle-aged mice, however, there were some differences in the spatial

distribution of neurogenesis: In humans, the rate of hippocampal neurogenesis showed a less pronounced decline during aging compared to mice (Spalding et al., 2013). This means that the majority of GCs in the human DG are presumably exchanged during life, compared to about 10 % in mice.

Lastly, the situation for a neuron to integrate into an already existing neural network is probably different to the embryonic situation when all neurons develop together and the general expression of growth factors facilitates development. Much work has been done in rodents to decipher the mechanisms and factors regulating adult neurogenesis and growth (reviewed in Aimone et al., 2014). These studies open doors to promising therapies for neurodegenerative diseases/injuries such as Alzheimer's disease and stroke by artificial incorporation of new neurons into damaged brain areas. In summary, the research on adult hippocampal neurogenesis covers multiple interesting aspects and attracts researchers from multiple fields such as biology, medicine, and informatics.

4.2.2.2. Structural development and integration of adult-born GCs

Dendrites generate the basic frame, defining amount and specificity of inputs (recently reviewed in Lefebvre et al., 2015), shaping input–output behavior (Mainen and Sejnowski, 1996), and performing local computations (reviewed in Sidiropoulou et al., 2006; Branco and Häusser, 2010), thus defining most functions of a neuron (Beining et al., 2016). For adult-born GCs the growth of their dendritic arbor is quite challenging, as the dendrites have to find their way through a dense matrix of already established dendrites, axons, blood vessels, and glia cells. At the beginning of adult hippocampal neurogenesis research, analysis of dendritic morphology had not been possible, as BrdU only labeled the nucleus. In a key study, van Praag et al. (2002) genetically modified a replication-incompetent murine leukemia retrovirus (RV) so that it expressed GFP under the strong unspecific CAG promoter in infected cells (van Praag et al., 2002). As RVs are only able to infect dividing cells, the intrahippocampal injection of this vector allowed birthdating of adult-born GCs as well as the first images of their morphology at different cell ages. Since then this viral vector has

been widely used to label adult-born GCs in order to analyze their development and structural maturation.

During embryogenesis, the radial glia cells (RGCs) are the first to form the pool of stem cells in the hippocampus (Seri et al., 2001). They and their descendants, the neural precursor cells (NPCs) reside in neurogenic niches in the subgranular zone (SGZ) of the DG which are specialized microenvironments that allow NPC proliferation (Moore and Lemischka, 2006; Nicola et al., 2015). When a proliferating NPC exits the cell cycle, it adopts one of the three neural phenotypes: astrocyte, oligodendrocyte, or GC (Gage, 2000). It only differentiates into a GC if it receives neurogenic cues from its environment such as Neurogenesis-1 (Ueki et al., 2003). During the first few days after proliferation, the very immature GC is still located in the SGZ, extends mainly a few short processes within or parallel to the GCL and shows no signs of synaptic input (van Praag et al., 2002; Espósito et al., 2005; Zhao et al., 2006; Ribak and Shapiro, 2007). At this stage it already expresses doublecortin (DCX), a microtubule-associated protein involved in cell migration (Gleeson et al., 1999) that is a commonly used marker for immature neurons. Strong axon growth to CA3 starts at the end of the first week (Hastings and Gould, 1999), preceding dendritic growth by approximately 3 days (Sun et al., 2013). In the period from the first to the second week, dendrites are extended through the GCL and into the inner ML (IML). Interestingly, it was found that newborn GCs are tightly associated with their RGCs and the dendrites extend along RGC processes, suggesting that these cells represent guiding paths for the dendrites (Shapiro et al., 2005). In addition, adult-born GCs at that stage showed remarkable migration from the SGZ towards the lower GCL, coinciding with the highest expression of DCX (Espósito 2005). Dendritic spines are still missing, but GCs were found to already receive functional (at this stage depolarizing) GABAergic input from local interneurons such as hilar basket cells (Espósito et al., 2005; Vivar et al., 2012; Deshpande et al., 2013). This input is important because adult-born GC activity increases the likelihood of survival (Jagasia et al., 2009; Lin et al., 2010; Pallotto and Deprez, 2014), as up to 75 % of newborn cells die during the first 4 weeks (Dayer et al., 2003; Snyder et al., 2009). During the third week, adult-born GCs extend more dendrites into the

ML, including the middle and outer ML (MML and OML). Furthermore, they start to express dendritic spines and receive first glutamatergic inputs from hilar mossy cells (Chancey et al., 2014) followed by perforant path synapses from the medial and lateral entorhinal cortex at the end of week 3 (Toni et al., 2007; Toni and Sultan, 2011; Vivar et al., 2012; Deshpande et al., 2013). Interestingly, in rats, the end of the 3rd week shows the sharpest increase in spine numbers (Ohkawa et al., 2012), whereas this peak is delayed by one week in mice (Zhao et al., 2006; Toni et al., 2007), supporting the general idea that adult-born GCs mature faster in rats than in mice (Snyder et al., 2009). Furthermore, new spines on abGCs were reported to preferentially contact preexisting axonal boutons forming multi-synapse boutons, before single synaptic boutons develop (Toni et al., 2007), indicating an ongoing competition for synaptic contacts between mature and adult-born GCs (McAvoy et al., 2016). Axonal maturation has been reported to be already completed and mossy fiber boutons density reached its plateau by the end of the 3rd week (Zhao et al., 2006; Sun et al., 2013). Nevertheless, the electrophysiological behavior of 3-week-old adult-born GCs is mostly immature at this point (Schmidt-Hieber et al., 2004; Mongiat et al., 2009; Yang et al., 2015). Furthermore, many of them still express DCX (Radic et al., 2015) even though some already express NeuN (Espósito et al., 2005), a neuronal nuclear protein which is often used as a neuronal marker (Mullen et al., 1992) and Calbindin, a calcium-binding protein which replaces the earlier expressed DCX and is often used to label mature GCs (Brandt et al., 2003). During the fourth week, spine density in adult-born GCs increases massively. Eventually, by the end of the fourth week, adult-born GCs are established in their final position (Espósito et al., 2005) and their dendritic morphology appears to be mature (Seri et al., 2001; Espósito et al., 2005; Sun et al., 2013). However, spine density continues to increase moderately until it reaches a plateau at about ten weeks of cell age. Furthermore, the amount, timing and maturation of dendritic spines in adult-born GCs can be altered by reducing (e.g. by genetic insertion of hyperpolarizing ion channels) or increasing (e.g. by running or enriched environments) network activity (Zhao et al., 2006, 2014; Piatti et al., 2011; Bergami et al., 2015), indicating that adult-born GCs are very plastic at early cell ages. In the next chapter, I will elucidate further special properties in young adult-born GCs.

4.2.2.3. Functional integration of adult-born GCs and the critical phase

Only a decade ago, researchers started to discover that young adult-born GCs have a transient phase during their maturation when they exhibit several features that make them unique and therefore distinct from old mature GCs: They had a higher intrinsic excitability (Mongiat et al., 2009), a higher synaptic plasticity (Schmidt-Hieber et al., 2004; Ge et al., 2007), received less inhibition (and exerted less inhibition on other GCs) (Marín-Burgin et al., 2012; Temprana et al., 2015) and, if strongly activated by exposure of the animal to enriched environments, they were able to remodel their pre- and postsynaptic connectivity even to brain regions otherwise not found in normal GC connectivity (Bergami et al., 2015; Restivo et al., 2015). The mentioned studies indicate that there is a critical time window of enhanced function at around 3-8 weeks after cell birth. After that phase, adult-born GCs are thought to functionally converge to the pool of old GCs (Laplagne et al., 2006; Stone et al., 2011). However, increased synaptic plasticity and excitability was also shown for very young, PSA-NCAM-expressing GCs (i.e. at postmitotic week 1-3) and was attributed to increased T-type calcium channel expression and different calcium buffering (Schmidt-Hieber et al., 2004; Stocca et al., 2008). Furthermore, some studies argue that even several-months-old adult-born GCs are still necessary for specific tasks (Lemaire et al., 2012; Tronel et al., 2015). Even though there is this controversy on the exact time window, the generally accepted view is that this transient phase of enhanced sensitivity, enables young GCs to receive and learn spatial and episodic information that cannot be learned by mature GCs. In line with that, young adult-born GCs in the critical phase were found to be more frequently incorporated in circuits that were active during spatial learning than matured GCs (Kee et al., 2007). How does the critical phase relate to primates, including humans? There is little data available, yet. In monkeys, it was found that maturation of adult-born GCs exceeds six months (Kohler et al., 2011). In humans, the time course of maturation or functional integration is not known. However, it has been suggested that it should be even longer than in primates, under the assumption that adult neurogenesis recapitulates embryonic neurogenesis which is longer in humans (Ho et al., 2013)

4.3. Compartmental modeling

As the vast amount and complexity of biophysical and chemical processes makes it hard to understand the behavior of single neurons, many biophysical models of neurons have been created to approximate various biophysical (e.g. opening of ion channels or Ca^{2+} binding of an enzyme) and electrochemical (e.g. influx of ions) processes that occur in cells and during neural signal transduction. Compartmental models form a subgroup of biophysical models that allow for the consideration and interplay of different neuronal electrotonic compartments. These compartments mainly comprise soma, dendrites, and axons but compartmental modeling may also be used to model spines or intracellular organelles. As the development of a consistent compartmental model of mature GCs and young adult-born GCs has been one main aspect of my thesis, I will introduce two basic aspects of compartmental single cell models in this chapter: the passive and the active model.

4.3.1. Modeling passive properties: passive cable theory

The passive model of a neuron comprises all basic electric properties that emerge from its morphology (dendrite, soma, axon, or even spines) and from its leaky membrane (Ermentrout and David, 2010). In many simple network models, neurons are treated as dimensionless points; however, real neurons possess very long processes, some of which can even span dozens of centimeters (e.g. motor neurons along the spinal column). Such spatial separation allows neurons to gather or spread information from/to different regions and even perform local computation (Mattson and Bruce-Keller, 1999; Polsky et al., 2004; Chen and Nedivi, 2010). However, for computational analysis, it is necessary to transform this large 3D structure into simple electric circuits and equations. Hence, the basis of the passive neuron model is the assumption that neuronal processes behave similarly to electrical cables. These have already been described mathematically over 150 years ago in the form of long electric cables such as the transatlantic telegraph cables (Thomson, 1854). The assumptions and equations established there were later directly adopted (assuming that no current flows out of dendritic ends) for neurons (Rall, 1962). The first assumption was that neuronal processes can be approximated by a cylinder that is only filled with cytoplasm (Figure 2A, left), which is a strong

simplification of the complex intracellular machineries, but reflects basic electrotonic properties of dendrites and axons surprisingly well (Rall, 1959, 1962).

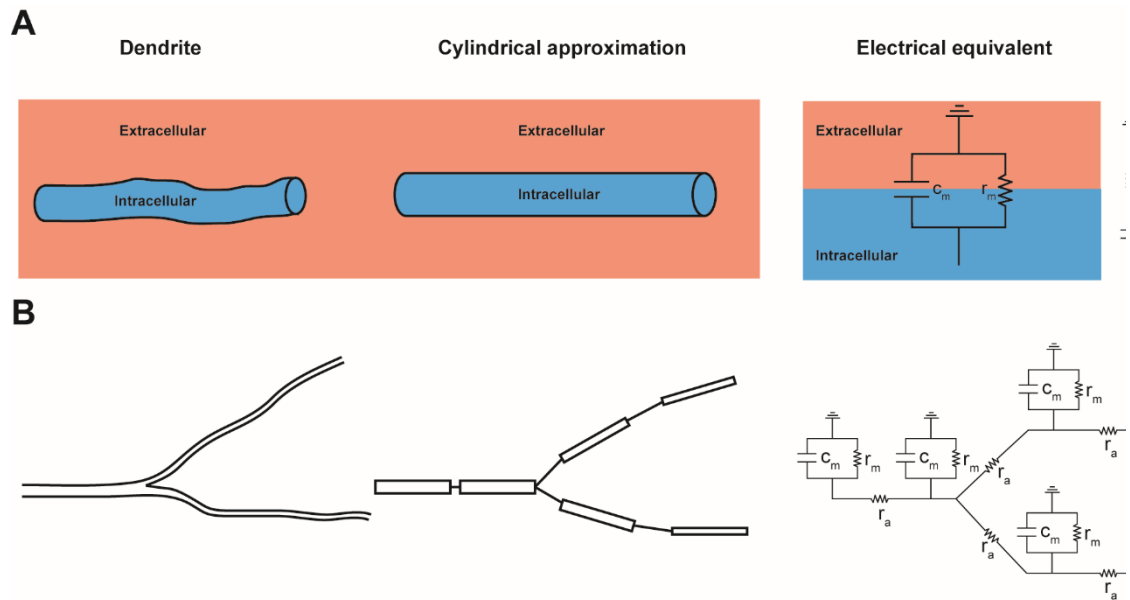


Figure 2: The equivalent circuit of a neuron. (A) Left: In compartmental modeling, a piece of dendrite is approximated by a cylinder filled with cytoplasm. Right: The current that flows across the membrane of such a cylinder can be described by a capacitor (with the membrane-specific capacitance C_m) and a resistor (with the specific membrane resistance r_m) connected in parallel. (B) Similarly, a dendritic (or axonal) branch (left) can be approximated by several cylindrical pieces connected in parallel (middle), for which an equivalent circuit can be described (right). This circuit consists of single circuit units each connected in series with each other and an axial resistor (with the specific axial resistivity r_a) representing the electrical resistance of the cytoplasm.

Furthermore, neuronal processes were considered as being one-dimensional. The reasoning behind that is that, the dendritic/axonic extent and arborization of a neuron is very extensive, thus the voltage variation along dendrites and axons is much higher than the intracellular voltage variation at one specific cross section (Rall, 1959, 1962). This drastic reduction of dimensions allowed to analyze dendrites in a mathematically easier way and to describe an equivalent electric circuit for a piece of dendrite (Figure 2A, right): As the insulating neuronal membrane separates intracellular from extracellular charges, and

charges can accumulate at both sides of the membrane, the electric equivalent of this configuration is a capacitor with the specific capacitance c_m (units pF/cm²). However, as the membrane is no perfect insulator, some charges (in the form of ions) cross the leaky membrane through unspecific ion channels. Hence, Rall (1959) approximated a small piece of dendrite (or axon, soma) – like an electric cable – as an electric circuit with a capacitor and a resistor connected in parallel (Figure 2A).

This leaky membrane follows Ohm's law with

$$\Delta I = \frac{V - V_E}{R_{in}} \quad (1)$$

where V_E is the reversal potential of the leak ion (which is mainly governed by K^+) and R_{in} is the input resistance of the membrane which (assuming a cylindrical piece of dendrite of length l and radius a) is defined by

$$R_{in} = \frac{r_m}{2\pi a l} \quad (2)$$

In compartmental modeling, instead of the specific membrane resistance r_m (units $\Omega \cdot \text{cm}^2$), its reciprocal counterpart, the membrane leak conductance g_{leak} is mostly used which has the units $\text{S} \cdot \text{cm}^{-2}$. This means that the conductance increases with larger dendritic surfaces. Hence the leak current can also be described by

$$\Delta I = g_{leak} \cdot 2\pi a l \cdot (V - V_E) \quad (3)$$

Importantly, the length of this compartment has to be so small that it has roughly the same potential in each location of this piece. In order to create a complete neuron (or electric cable) many of such pieces (electrical circuits) are concatenated (Figure 2B) thereby considering that ions flowing from one to another compartment of the cell experience the attenuating resistance of the cytoplasm, which acts like a resistor connected in series between each compartment.

$$R_a = \frac{r_a l}{\pi a^2} \quad (4)$$

with r_a being the cytoplasm's specific axial resistivity (units Ω cm), which, for simplicity, is often assumed to be constant along the different compartments.

All these equations can be combined to the passive cable equation (Thomson, 1854), to describe the spatiotemporal voltage spread and attenuation along a passive cable or neuronal compartment with radius r :

$$\lambda^2 \frac{\partial^2 V}{\partial x^2} = \tau \frac{\partial V}{\partial t} + V \quad (5)$$

with the electrotonic length constant

$$\lambda = \sqrt{\frac{a \cdot r_m}{2 \cdot r_a}} \quad (6)$$

being the distance from a point of current injection where the voltage has dropped to $1/e$, and the membrane time constant

$$\tau = r_m c_m \quad (7)$$

being the time after current injection when the voltage at the source has dropped to $1/e$. These relations have several implications for a neuron: First, dendrites or axons with a large diameter have less axial resistance and thus a faster voltage spread and higher λ . Second, due to the capacitive properties of neuronal membranes, synaptic inputs are low-pass filtered when arriving at the soma, meaning that slow and steady currents have a higher influence on the soma than fast and transient activity, and reasonably synchronous synaptic currents can add up. Third, holding a neuron at a specific voltage by injecting a current to the soma (called voltage clamp) only works for electrotonically compact neurons, as currents are attenuating over distance, which means that dendritic parts far away from the soma do not follow the defined voltage (Rall and Segev, 1985).

These and more relations can be easily observed once the complete passive model has been established. Freely available software such as GENESIS (Bower and Beeman, 1998) or NEURON (Carnevale and Hines, 2006) provide a convenient environment to establish the morphology and the passive model.

The advantage of passive models is their simplicity as there are only 4 parameters defining the morphology (number, length, and width of cylinders and their connectivity) and 4 parameters defining the passive properties (r_m or g_{leak} , r_a , c_m , e_{pas}). As dendrites of dentate GCs were found to have very moderate active conductances, passive compartmental models have been used to analyze dendritic signal propagation and integration in GCs and found strong attenuation and linear integration of synaptic inputs (Jaffe and Carnevale, 1999; Schmidt-Hieber et al., 2007; Krueppel et al., 2011). However, the main function of a neuron requires active conductances that allow signal transmission, thus there are also active models that implement such active properties.

4.3.2. Modeling active properties: Hodgkin-Huxley and Markov chain

The active model of a neuron comprises at least the important voltage-dependent currents that contribute to the depolarization and repolarization of the membrane during an action potential (Ermentrout and David, 2010), but can be arbitrarily extended, e.g. to include Ca^{2+} and Ca^{2+} -dependent currents or synapses. The different depolarizing and hyperpolarizing currents found in neurons originate from different voltage-dependent ion channels within the membrane. Thereby the direction of the current flux across the channel is dependent on the distribution of ions (Johnston and Wu, 1995). Most ions, especially the important Na^+ and K^+ ions, are differently distributed across the membrane with Na^+ being more highly concentrated (typically 145 mM extracellular : 12 mM intracellular) on the extracellular and K^+ being more highly concentrated (typically 144 mM intracellular: 5 mM extracellular) on the intracellular side (Figure 3A). Ions follow their concentration gradient towards the lower concentration but are also affected by the electrical field repelling equally charged ions (Johnston and Wu, 1995). Hence, for an ion X there is a potential V_{Ex} , called reversal, equilibrium, or Nernst potential, where both forces cancel out and there is no net flux across the membrane. This reversal potential can be calculated by the Nernst equation:

$$V_{Ex} = \frac{RT}{z_x F} \ln\left(\frac{[X]_o}{[X]_i}\right) \quad (8)$$

where R is the gas constant, T the absolute temperature, z_x the valence of the ion X , F is the Faraday constant and $[X]_o / [X]_i$ is the extra- and intracellular concentration of the ion (Ermentrout and David, 2010). The key point is that ion channels are more or less selective for a specific ion. In the case of Na^+ this means that upon opening of a solely Na^+ -selective channel, Na^+ will flow into the cell, thereby depolarizing it, until the channel closes, or the reversal potential of about +64 mV (at 25 °C, assuming aforementioned Na^+ concentrations) is reached. In contrast, the opening of a solely K^+ -selective channel, results in K^+ leaving the cell, thereby hyperpolarizing it, until the channel closes, or the reversal potential of about -85.5 mV (at 25 °C, assuming aforementioned K^+ concentrations) is reached. Different Na^+ - or K^+ - selective ion channels activate or de-/inactivate at different voltages with different kinetics, hence the neuron is capable, for instance, to elicit an action potential with their typical shape, once sufficient synaptic current depolarized it above the threshold for Na^+ channel opening.

For computational studies, it is necessary to model this complex orchestration of ion channels in a more simple way. The opening of channels and subsequent flow of ions corresponds to adding additional current onto the intracellular side of the electrical circuit. Again, this current can be calculated by Ohm's law (equation (1)) with V_E being the reversal potential of the ion the channel is selective for. However, in the case of an ion channel, the term conductance is mostly used instead of resistance which is its reciprocal. Hence, the current per unit cylindrical surface can be calculated as:

$$\Delta I_x = g_x \cdot (V - V_{Ex}) \quad (9)$$

Figure 3B illustrates the electrical circuit being extended by a Na^+ - and a K^+ -selective ion channel and could, of course, be arbitrarily extended by more channels such as Ca^{2+} and Cl^- channels as well as channels being selective for more than one ion (there, the reversal potential can be calculated with the Goldman-Hodgkin-Katz equation, see Goldman, 1943; Hille, 2001).

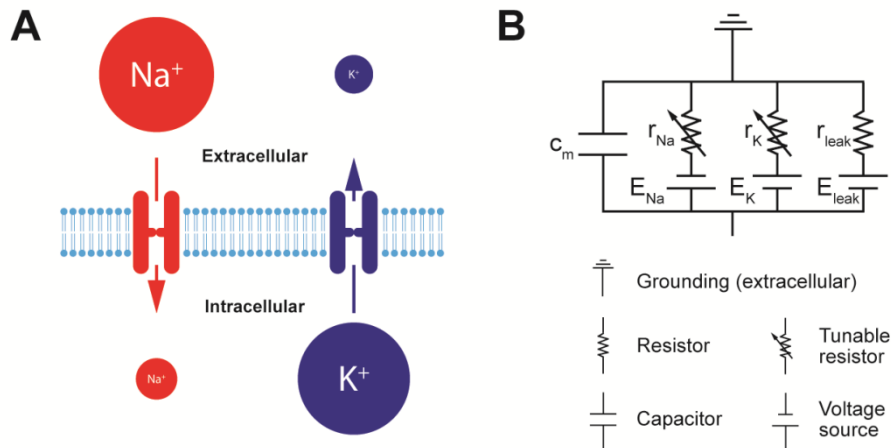


Figure 3: Equivalent circuit of ion-selective channels. (A) Schematic illustration of Na^+ (red) and K^+ (blue) selective ion channels in the membrane. The physiological distribution of Na^+ is high extracellular and low intracellular and of K^+ high intracellular and low extracellular. Ions follow their concentration (and electric field) gradient. Hence, upon opening of Na^+ -selective ion channels, Na^+ flows into the cell and depolarizes it, whereas upon opening of K^+ -selective ion channels, K^+ flows out of the cell, thereby hyperpolarizing it. **(B)** The circuit for a passive piece of membrane has been extended with ion-selective, tunable (i.e. active) resistors representing active ion channels, whereby chloride (Cl^-) selective channels have been ignored here. The potential of the ion-specific voltage sources is equivalent to the Nernst potential, which is generated by the electrochemical gradient of each ion. The equilibrium potential of the passive channel E_{leak} is mainly governed by E_{K} with small contributions of E_{Cl} and E_{Na} .

As mentioned before, the conductances of most ion channels are voltage- and time-dependent with some being even dependent on further parameters such as $[\text{Ca}^{2+}]$. Thus, finding a model that describes the dynamics of a specific ion channel has been and is still very challenging.

The first and still most widely-used phenomenological model schema of ion channel dynamics is the Hodgkin-Huxley model which was developed for Na^+ and K^+ -channels on giant squid axons that have been penetrated longitudinally with a wire electrode in order to clamp the whole axon to the same potential (Hodgkin and Huxley, 1952). Their experiments led them to hypothesize that there are charged particles on the membrane (today it is known that these reside in the pore of an ion channel) which have to be redistributed in such a way that an ion is able to move through the membrane. As all of these activation particles (or gates) have to be in the “open” state to allow ion flux, the

channel is either in an activated or deactivated state. Further, they hypothesized that, in contrast to “persistent channels” such as the K^+ channel which only has these two states, the Na^+ channel that underlies action potential generation is of transient nature, meaning it can go further into an inactivated state which is due to the movement of a blocking particle (or inactivation gate) which terminates Na^+ flow. Based on this hypothesis, they developed a mathematical model assuming that the activation and inactivation gates 1) can only be in an open or closed state, 2) open and close independently, 3) open and close in a probabilistic fashion, and 4) follow a simple first-order kinetic. Hence, when C and O are the probabilities that the channel is closed or opened, then $C + O = 1$ and $C = 1 - O$. Further, the probabilities change depending on time and voltage according to a first-order kinetic process



where α denotes the transition rate from closed to the open state and β vice versa, both being dependent on voltage but not on time. For such a kinetic process the rate of change in O can be calculated with:

$$\frac{dO}{dt} = \alpha \cdot (1 - O) - \beta \cdot O \quad (11)$$

As Hodgkin and Huxley held the membrane potential artificially constant with an electrode (voltage clamp), α and β became constants and the differential equation (11) could be solved into:

$$O(t) = O(0) \cdot e^{-(\alpha+\beta)t} + \frac{\alpha}{\alpha+\beta} (1 - e^{-(\alpha+\beta)t}) \quad (12)$$

where $O(0)$ denotes the open probability at the start of the clamp. From this equation it can be seen that O converges exponentially to a value of

$$O_{inf} = \frac{\alpha}{\alpha+\beta} \quad (13)$$

with a time constant

$$\tau = \frac{1}{\alpha+\beta} \quad (14)$$

Hodgkin and Huxley named the open probability of the activation gate for the K⁺-channel n , for the Na⁺-channel m and the open probability of the Na⁺ inactivation gate h with $1-h$ being the probability that the inactivation gate blocks the channel (Figure 4A, left). By clamping the axon to different voltages they could develop voltage-dependent functions for the rates α_n , β_n , α_m , β_m , α_h , and β_h . When they fitted their model to the measured conductances of each channel, they found that they had to assume 4 activation gates for the K⁺-channel as well as 3 activation and 1 inactivation gates for the Na⁺-channel in order to conveniently fit the experimental data resulting in:

$$I_K = g_K \cdot (V - V_{EK}) \cdot n^4 \quad (15)$$

and

$$I_{Na} = g_{Na} \cdot (V - V_{ENa}) \cdot m^3 h \quad (16)$$

with g_K and g_{Na} being the maximal conductances for the K⁺- and Na⁺-channel, respectively (Hodgkin and Huxley, 1952). Interestingly, ultrastructural x-ray analysis of the K⁺ and Na⁺ channel pores revealed four voltage sensor domains (Jiang et al., 2003; Long et al., 2005; Payandeh et al., 2011), of which only three (S4 segments I-III) were necessary for Na⁺ channel opening (Chanda and Bezanilla, 2002), thus revealing an intriguing analogy between Hodgkin and Huxley's phenomenological model and the channels' real nature. Hence, their model was found to be a convenient scheme underlying many different channels (including Ca²⁺-channels).

4.3.3. Compartmental models of dentate granule cells

The first compartmental model of mature dentate GCs had been established relatively early because GCs were known to show no prominent Ca^{2+} -related events, to have large linear current-voltage relations around resting membrane potential, as well as well-established anatomical and electrotonic properties (Yuen and Durand, 1991). Later, Aradi and Holmes extended this model with a detailed morphology and with several Ca^{2+} -related channels to reproduce depolarizing after-potentials (Aradi and Holmes, 1999). Since then, many computational studies came out that were based on this model and which provided insights into the action of feedforward inhibition (Ferrante et al., 2009) and GABA (Chiang et al., 2012) in GCs, the impact of the $\beta 4$ -subunit to repolarizing properties of the BK channel (Jaffe et al., 2011), synaptic integration along GC dendrites (Krueppel et al., 2011), the compensatory morphological alterations in newly born GCs after status epilepticus (Tejada et al., 2012), the complementary functions of SK and Kv7 channels (Mateos-Aparicio et al., 2014), the possible role of spike-timing-dependent plasticity and metaplasticity to establish LTP and LTD in GCs *in vivo* (Jedlicka et al., 2015), and a homeostatic principle following lesion-induced dendritic GC remodeling (Platschek et al., 2016). The model has even been incorporated into large-scale network modeling of the DG, e.g. to analyze origins of DG hyperexcitability in temporal lobe epilepsy (Santhakumar et al., 2005; Dyhrfjeld-Johnsen et al., 2007; Tejada and Roque, 2014; Hendrickson et al., 2015).

However, the very first GC models on which these models are based on used simplified morphologies and lacked detailed knowledge on the ion channel distribution and kinetics. Hence, many parameters were guessed or adopted from other cell types or species. Probably due to these factors, more recent GC models often had to be modified *ad hoc* to reproduce single experiments (Jaffe et al., 2011; Chiang et al., 2012; Mateos-Aparicio et al., 2014; Platschek et al., 2016), which renders this model family inconsistent with the behavior of real GCs and thus of low predictive value. Also, a common practice is to fit such models on single morphologies, thereby increasing the risk of an over-fitted biophysical model that is not compatible with any other GC morphology.

Concerning realistic modeling of adult-born GCs in the critical phase of integration, former studies are even more disillusioning, as modeling was restricted to rather abstract network models that did not implement any elements concerning morphology, ion channels, or even real-time (Becker, 2005; Wiskott et al., 2006; Chambers and Conroy, 2007; Aimone et al., 2009; Appleby and Wiskott, 2009; Weisz and Argibay, 2009; Chow et al., 2012).

As new insights from more recent studies on mature and adult-born GC electrophysiology and protein expression are accumulating, and more complete GC morphologies become available, the urgent need emerges to update/develop the compartmental model standard of mature and adult-born GCs to become more biologically sound, more consistent with experiments, and thus more predictive for further investigations.

5. Scope of this thesis

As outlined in the Introduction, basic morphological and most electrophysiological features of adult-born GC have been described earlier, and some biophysical models of adult-born GCs exist. However, there are still many unanswered questions which require a deeper understanding of the structural and functional integration of adult-born GCs and what impact occurring changes have on the cells' input processing (see reviews Ming and Song, 2011; Piatti et al., 2013; Aimone et al., 2014)

First, the morphological picture during the critical phase of adult-born GC integration and thereafter is very sparse. This is partly due to missing time points, partly because only 2D or massively incomplete morphological reconstructions of adult-born GCs exist so far, and moreover, the morphological analysis, if any, was solely restricted to the number of branch points and the total dendritic length (for a more thorough overview, see Beining et al. Publ. 1). Second, even though it is known that dendrites and spines can be highly plastic especially during development (Yuste and Bonhoeffer, 2001; Tavosanis, 2012), and even though the reported high synaptic plasticity of adult-born GCs indirectly implies that afferent activity should at least induce structural changes in spines, activity-induced structural plasticity of adult-born GCs has never been investigated before. Recently, the importance of such a detailed knowledge about adult-born GC morphologies for the understanding, prevention, and treatment of neuropathological alterations that emerge in conjunction with impaired adult hippocampal neurogenesis has been underlined (Llorens-Martín et al., 2016). Third, the contribution of each unique property during the critical phase to the adult-born GC's computation has not been investigated, yet. Experimental approaches to investigate this would be very challenging as many factors such as the activity of afferents and of feedback neurons would be needed to be observed or controlled to exclude multisynaptic side effects. On the computational side, a data-driven single-cell compartmental model with realistic morphology and ion channel composition would provide an excellent tool to analyze the effect of changes in intrinsic and synaptic properties during GC maturation and integration. However, existing active compartmental models

of GCs have limited predictive capability since they, similar to most other biophysical models, were constructed *ad hoc* usually in order to replicate one single experiment. A recent review revealed the poor functionality of published compartmental models once they are stretched beyond the specific problem for which they had been designed (Almog and Korngreen, 2016). Hence, a compartmental model of mature and young GCs, which is biologically and physiologically consistent enough to be able to make reasonable predictions, is missing so far.

Accordingly, I designed my studies...

- 1) ...to provide a detailed and complete picture of the morphological maturation of adult-born GCs, including full 3D reconstructions of dendrites as well as qualitative and quantitative analysis of spines using the RV labeling method.
- 2) ...to test the capability of adult-born GCs for activity-induced structural changes at the dendritic and spine level using an *in vivo* HFS protocol to stimulate the medial perforant path together with subsequent reconstruction, staining for the IEG Arc, and quantitative analysis of dendrites and spines.
- 3) ...to establish a compartmental model of mature and young GCs that is consistent with the known ion channel composition of GCs and that is able to replicate experimental data from various studies and remains stable over a wide range of different reconstructed morphologies. Such a model could then be used as the basic, extendible framework to analyze the computational impact of the different properties that make young adult-born GCs so unique.

6. Discussion

Our studies provide several new findings. First, in order to achieve a detailed morphological analysis and a realistic modeling of adult-born GCs, we developed and adapted several new techniques, such as an improved workflow of dendritic reconstruction, including semi-automated mapping of anatomical layers to the reconstructed trees (Publ. 1), and a user-friendly Matlab-NEURON interface featuring the TREES toolbox to allow easy use of morphologies in NEURON, easy setup of arbitrarily complex compartmental models as well as handling of parallel simulation runs with subsequent organized transfer of the output to Matlab. (Publ. 3). Second, we obtained new insights into the process of structural and functional maturation of adult-born GCs as well as their capabilities of synaptic integration and activity-induced reorganization on which I will elaborate in this section in more detail.

We were able to obtain the first complete 3D-reconstructed dendritic trees of adult-born GCs at several (21, 28, 35, 77 dpi) time points in the rat (Publ. 1). As we further analyzed the cell-specific number and size distribution of dendritic spines in a laminar-specific way (Publ. 2), we obtained a complete picture of the amount, strength, and location of the neuron's synaptic input. We found that the mature dendritic arborization was already established at 21 dpi followed by only minor changes, suggesting that macroscopic structural maturation precedes functional integration (Publ. 1). In contrast, spine numbers were continuously increasing until 11 weeks post injection (Publ. 2). These observations were complementary to those reported by previous studies in the rat (Teixeira et al., 2012) and mice (Zhao et al., 2006; Toni et al., 2007, 2008; Ohkawa et al., 2012; Sun et al., 2013).

Interestingly, though spine density continuously increased, we found a relatively constant percentage of big mushroom spines throughout all ages, suggesting that the amount of strong input is constantly normalized (Publ. 2). Such a homeostatic scaling of synaptic strength has been suggested to keep the afferent drive of a neuron within a physiological range (Turrigiano, 2008; Pozo and Goda, 2010).

Whereas at 11 weeks of age, density and morphology of adult-born GCs spines was comparable to perinatally born mature GCs (Publ. 2), we surprisingly found that the dendritic tree was still distinguishable from the latter, as the branching, curvature, segment length, and termination of their dendrites were considerably different (Publ. 1). By developing a morphological model of adult- and perinatally born GCs, we could infer that these differences might arise from different growth environments in the young and old DG. A part of this model is based on the assumption that in the adult DG, reelin-expressing cells in the OML, which might represent target points for the growing dendrites, are drastically reduced (Alcántara et al., 1998; Pesold et al., 1998), whereas commissural axons have populated the IML (Alcántara et al., 1998; Förster et al., 2006; Yu et al., 2014). Of note, adult-born GCs might also direct their dendrites to different signaling cues, such as the radial glia cells (RGCs, Shapiro et al., 2005). However, the establishment of the radial glia scaffold is notch and reelin dependent, too (Sibbe et al., 2009), and reelin was reported to highly regulate migration and dendritic growth of adult-born GCs during their maturation (Teixeira et al., 2012). In contrast, the postnatal ingrowth of the commissural/associational pathway in the IML is reelin-independent and axons are oriented towards GC dendrites (Zhao et al., 2003), which we also considered in the model. Hence, we think that our morphological model provides a biologically sound explanation for the structural differences between adult- and perinatally born GCs in the rat.

Moreover, together with the later developed morphological model of mouse GCs (Publ. 3), it is now possible to create an arbitrary number of synthetic but realistic mouse and rat GCs. These might be used in network models that include full morphologies, or to test compartmental models for their robustness concerning morphological variations, which we performed for our developed compartmental GC model (Publ. 3). Our model proved to be working on a wide range of different reconstructed and synthetic morphologies. From our own observations, we did not find such robustness in other GC models from literature (see Publ. 3 for references). Most of them had been established on single (realistic or abstract) morphologies which involves the danger of overfitting. Furthermore, most models were created *ad hoc* to reproduce very

few electrophysiological aspects/experiments and performed poorly when used for different situations. The issue of a poor stability of compartmental models in general has been critically discussed in a recent review on “realistic” models of L5 pyramidal cells (Almog and Korngreen, 2016). In contrast to most compartmental models from literature, we could show that a biologically sound distribution of ion channel models, whose biological analogues are known to be expressed in mature GCs, is sufficient to reproduce the vast amount of electrophysiological properties of these cells.

By comparison and fitting of the I-V relationship in mouse and rat GCs we could further predict that rat GCs have a much higher expression of the inward-rectifying Kir channel (Publ. 3). However, the exact composition of Kir channels in mouse and rat GCs is unknown. In the literature we only found a study suggesting that mice lack the G-protein-coupled Kir3.3 channel (or GIRK3, Kobayashi et al., 1995; but see Karschin and Dißmann, 1996)). This difference would be important for rodent models of diseases and addiction because GIRKs have been shown to be activated by ethanol and morphine (Nassirpour et al., 2010; Bodhinathan and Slesinger, 2013), inhibited by the anti-depressant fluoxetine (Kobayashi et al., 2003), and be less expressed following expression of the Alzheimer’s disease-related Amyloid- β protein (Mayordomo-Cava et al., 2015). Hence, it might be the case that mouse and rat models of depression, addiction, and neurodegenerative diseases provide different results under the same experimental conditions.

Intriguingly, by reducing the expression of seven ion channels that are known to be reduced during development, we transformed our compartmental model of mature GCs into a model for young (~28 dpi) adult-born GCs and replicated important electrophysiological properties of these cells during the critical time window (Publ. 3). As we did not investigate the whole parameter space, e.g. by genetic algorithms, this model represents one of probably several possible configurations that produce reasonable results. For all ion channels except Kir2 (Mongiati et al., 2009) the reported reduced channel expressions were based on postnatally born GCs. As there is a general consensus that adult neurogenesis recapitulates embryonic and postnatal neurogenesis and maturation (Espósito et al., 2005; Laplagne et al., 2006), we used this information for our adult-born

GC model. However, it is difficult to compare the exact time windows of expression because maturation of adult-born GCs might be slower compared to postnatal maturation (Zhao et al., 2006; Snyder et al., 2012). Moreover, we did not consider the possibility that some channels might also be more strongly expressed, as it was shown to be the case for T-type Ca^{2+} -channels in very immature adult-born GCs (Schmidt-Hieber et al., 2004). However, until now, modeling adult neurogenesis and young adult-born GCs was only performed in simple network models without implementing morphology, ion channels, or even real-time (Becker, 2005; Wiskott et al., 2006; Chambers and Conroy, 2007; Aimone et al., 2009; Appleby and Wiskott, 2009; Weisz and Argibay, 2009; Chow et al., 2012; or review by Aimone and Gage, 2011). In contrast, our model is the very first compartmental model of young adult-born GCs and reproduces all important electrophysiological properties. It can thus be used as the basic frame to investigate mechanisms and functions involved in the process of integration of young GCs in the mature network in great detail.

However, we were not only interested in the static properties of young adult-born GCs during the critical phase but also in their capability to exert structural plasticity upon stimulation (Publ. 1&2). HFS-induced homo- and heterosynaptic plasticity have been well-studied in the DG (Abraham et al., 1985; Benuskova and Abraham, 2007; Jedlicka et al., 2015), and heterosynaptic plasticity has been suggested to normalize synaptic weights and ensure ongoing synaptic competition (Chistiakova et al., 2015). However, the onset of homo- and heterosynaptic plasticity during the maturation of adult-born GCs has not been investigated before. In order to elicit significant activity and synaptic plasticity under *in vivo* conditions, we used a HFS protocol with which we stimulated the medial perforant path of one hemisphere, thus obtaining material of activated (ipsilateral hemisphere) and non-activated (contralateral hemisphere) adult-born GCs in the same animal. In this context, we used Arc staining as a marker for functional integration of adult-born GCs, as our lab recently reported a cell-age-dependent increase in Arc expressing adult-born GCs cells after HFS, arguing for a step-wise integration of adult-born GCs (Jungenitz et al., 2014). Importantly, a HFS of 2 h was necessary, as shorter intervals do not result in complete Arc expression (Kuipers et al., 2009). The correct targeting of our HFS

to synapses located in the MML was validated by the layer-specific accumulation of F-actin and synaptopodin, which is in agreement with the earlier observations correlating this reorganization of F-actin with NMDA-dependent LTP (Fukazawa et al., 2003). We further found a hitherto unreported significant decrease of F-actin and synaptopodin in the adjacent unstimulated IML and OML after stimulation of the MML (Publ. 2). Synaptopodin is a protein associated with the actin network and involved in the formation of the spine apparatus, an important Ca^{2+} store located only in big mushroom spines and important for LTP (Deller et al., 2003, 2006; Jedlicka et al., 2009; Vlachos et al., 2009). F-actin, the filamentous form of actin, is an important cytoskeletal component of the postsynaptic density, regulating the anchoring of synaptic receptors and defining the size and morphology of dendritic spines (Bosch and Hayashi, 2012). Moreover, polymerization and depolymerization of actin filaments were shown to be involved in LTP and LTD, respectively (Kim and Lisman, 1999; Huber et al., 2004; Okamoto et al., 2004). Thus, our reported layer-specific shift of F-actin and synaptopodin suggests that both are involved not only in the regulation of homosynaptic LTP, but also in heterosynaptic LTD.

Intriguingly, when we compared stimulated and non-stimulated mature GCs at the level of dendritic spines, we found a structural correlate of these two plasticity forms (Publ. 2). These manifested as an increase in the number of big mushroom spines in the stimulated MML, and a decrease in the unstimulated OML. In addition, more than 60 % of the mature GCs also showed such heterosynaptic plasticity at commissural / associational IML synapses, which has not been reported before, but has been suggested by computational modeling (Beňušková and Jedlička, 2012). Moreover, our data revealed that the overall spine density and percentage of large spines was not altered by HFS in adult-born and mature GCs, thus challenging previously discussed LTP-related *de novo* spine formation (Wosiski-Kuhn and Stranahan, 2012) and supporting the idea that heterosynaptic plasticity is a homeostatic mechanism normalizing all synapses of a neuron (Chistiakova et al., 2015).

When we analyzed developing adult-born GCs, we found plasticity-related spine changes, too (Publ. 2): From 28 dpi on, adult-born GCs exhibited an increase in the number of big spines that was confined to the stimulated MML. However,

significant spine shrinkage in non-stimulated layers (IML and OML) was not observed until 35 dpi. Hence, to our knowledge, this is the first study providing evidence that young adult-born GCs exhibit heterosynaptic plasticity during the critical phase of integration. Together with homosynaptic plasticity, this supports the general idea that adult-born GCs contribute to hippocampus-dependent learning and memory (Cameron and Glover, 2015). The delayed onset of heterosynaptic plasticity might be explained by the fact that spine density is low in the first weeks but shows a tremendous increase around the fourth week, as we and others reported (Publ. 2; Zhao et al., 2006; Toni et al., 2007; Ohkawa et al., 2012). This might make it necessary to introduce heterosynaptic plasticity to avoid excitation runaway (Chistiakova et al., 2015).

However, not only spines were found to show structural plasticity: When we compared dendritic trees from stimulated and unstimulated hemispheres, we found an Arc-correlated reduction of small terminal segments (Publ. 1). Intriguingly, this phenomenon was only observed in 28-35 dpi adult-born GCs and restricted to the unstimulated OML. Interestingly, a recent *in vivo* time lapse study of adult-born GCs showed that during the first 3 weeks, many dendritic segments, especially short ones, become pruned (Gonçalves et al., 2016). These authors further found that this pruning process is increased in animals with increased branching (e.g. by exposure to enriched environments), thus homeostatically counteracting excessive branching. Why are these previously unknown high dendritic dynamics restricted to young GCs? The key point here might be the stabilization of the dendritic tree by the increase in spine density from week 4 to 11. Spines could stabilize dendrites (Koleske, 2013), thus dendrites with few spines might be rather instable and undergo pruning. This might be the explanation for our observed phenomenon in young adult-born GCs at 28-35 dpi: Synapses in the unstimulated OML became depressed. The subsequent spine shrinkage or loss destabilizes the dendrite, leading to retraction of segments with no or only few weak synapses, which mainly applied to short terminal segments. There might be two (not mutually exclusive) explanations for the role of Arc in this context: One is that not all young adult-born GCs received sufficient stimulation to undergo LTP and LTD because their spine density was low. In this case, the phenomenon is correlated with Arc

because only Arc-positive young GCs reacted to the electrical stimulation. The fact that adult-born GCs did not show any Arc at 21 dpi, whereas 100 % of mature GCs expressed Arc following HFS, supports this possibility. The other explanation is that Arc-expressing young GCs are those that underwent LTD. In this case, Arc might be directly involved in the pruning process, as it is known to induce removal of AMPA receptors from the postsynaptic membrane (Chowdhury et al., 2006), and to transform stable spines into instable thin spines (Peebles et al., 2010).

Regardless of the role of Arc, the three structural phenomena (homo- and heterosynaptic spine changes and activity-induced dendritic reorganization) found by our studies (Publ. 1&2) draw a picture of medial and lateral perforant path (MPP and LPP) competing with each other to increase their impact on each GC while reducing the impact of the other. Competition and cooperation between these spatial and non-spatial information pathways has also been suggested by computational modeling (Hayashi and Nonaka, 2011). Furthermore, presynaptic strength was shown to be decreasing proportionally with the distance to the soma in GCs, suggesting that the MPP has a larger impact as the LPP (de Jong et al., 2012).

However, recent retroviral tracing studies found a considerably enhanced connectivity of young adult-born GCs to the lateral entorhinal cortex (via the LPP), especially when the animals experienced exercise or enriched environments during the critical phase (Vivar et al., 2012; Bergami et al., 2015). Why is that? One explanation might be that the easy excitable young adult-born GCs can better receive and thus potentiate LPP synapses than mature GCs; however the same is true for MPP synapses. To bring clarity to this question, we used our compartmental models to investigate if young adult-born GCs show differences in the cooperation of both pathways (Publ. 3). For this, we developed an *in silico* stimulation protocol with which we activated MPP and LPP synapses with the same frequency but with a shifted onset. Excitingly, by testing different shifts and frequencies we found that young adult-born GCs, compared to mature GCs, could sum up postsynaptic signals from a broader time window if the frequency was low (<20 Hz). This difference disappeared at high frequencies. Notably, the most important hippocampal frequency (theta) is

in the range of 4–10 Hz. Hence, our computational study suggests that young adult-born GCs are able to become activated by medial combined with lateral inputs which are temporally too far separated or too weak to activate mature GCs. As it has been postulated that DG activity forces new pattern-separated representations onto CA3 neurons in order to reduce memory interference (Rolls, 2007), an idea would be that this newly emerging adult-born GC activity further improve hippocampal pattern separation by refining the memory traces stored in CA3.

Summarized, our studies contribute to the following picture of the structural and functional integration of adult-born GCs in the rat: Young adult-born GCs have their dendritic structure already established at 21 dpi when spine density is low, i.e. before they receive considerable synaptic input (Publ. 1&2). This widespread arborization allows them to establish synapses with preexisting boutons through all layers, including the OML. At these multisynapses, they compete with mature GCs for their input (Toni et al., 2007). As young adult-born GCs exhibit an enhanced capability for LTP (Schmidt-Hieber et al., 2004; Ge et al., 2007), a delayed capability for LTD (Publ. 2), as well as a better temporal summation of temporally separated MPP and LPP inputs (Publ. 3), they are able to take over a part of these synapses, especially at the LPP. Furthermore, their dendrites are still dynamic enough to retract from locations where they could not make synapses or did not receive considerable input to undergo LTP and spine stabilization (Publ. 1; Gonçalves et al., 2016). Finally, after the critical period, they are tuned for a specific input pattern (Temprana et al., 2015) and their high spine density prevents further dendritic dynamics, except under a pathological condition, such as an entorhinal denervation which leads to spine loss and dendritic reorganization (Vuksic et al., 2011). However, if there was not enough hippocampal activity in the form of novel environmental stimuli (e.g. exercise and enriched environment), the young adult-born GCs are not functionally integrated during the critical phase, thus lose the competition with mature GCs for input, and undergo apoptosis. In order to reduce energy costs, the hippocampus is able to homeostatically adjust the rate of neurogenesis depending on the intensity of hippocampal activity. (Gould et al., 1999a; van Praag et al., 1999; Lin et al., 2010; Kempermann, 2015)

What could be done next? It would be very interesting to have a complete picture of our reported dendritic and spine dynamics (and their interrelation) during the functional integration of adult-born GCs. However, our developed approaches to investigate dendritic and spine morphology only provided snapshots due to the requirement of fixation and slicing of the brain for the imaging process. *In vivo* time-lapse approaches to continuously observe vital hippocampal neurons have been performed recently (Velasco and Levene, 2014; Gonçalves et al., 2016), however until now they entail massive surgical injuries of the cortex, as parts of the brain have to be removed. *In vitro* time-lapse approaches using organotypic slice cultures (OTCs) have similar caveats but provide the possibility to stimulate afferents specifically, to apply pharmacological blockers, and even to study de- and reinnervation by co-culturing the entorhinal cortex and hippocampus (Stoppini et al., 1991; Del Turco and Deller, 2007). Such an approach would offer the possibility to test our computational prediction about improved temporal integration in adult-born GCs by using patch-clamp and afferent-specific dual stimulation. Furthermore, it would allow investigating structural dynamics and homo-/heterosynaptic plasticity of adult-born GCs in the light of altered hippocampal activity (e.g. seizures) or changes in the environment (e.g. hypoxia or growth factors). However, until then, progress has to be made to prolong the survival of adult-born GCs in OTCs or OTC-like preparations as previous studies indeed showed neurogenesis there (Kamada et al., 2004; Raineteau et al., 2004) but were only able to investigate structural maturation within the first week (Kleine Borgmann et al., 2013).

Moreover, our suggestion on the role of competition between mature and adult-born GCs could be tested experimentally. Indeed, a very recent report, where transient genetic overexpression of a negative regulator of spines was utilized in mature GCs to provide them with a competitive handicap, showed that this manipulation led to enhanced integration of adult-born GCs combined with an improvement in memory precision (McAvoy et al., 2016). This approach could be adapted for more precise manipulations, e.g. to analyze the impact on contextual vs spatial learning when only the MML or OML spines are handicapped. Similarly, when the manipulation is tested in the dorsal versus

ventral DG the highly discussed different role of neurogenesis (spatial/contextual vs. emotional) in these areas can be analyzed in more detail (Sahay and Hen, 2007; Kheirbek and Hen, 2011).

On the computational side, there are many open questions and ways for improvements as well. For instance, our compartmental model was established on the hitherto best knowledge about the GCs ion channel composition, biophysics and distribution. However, even with this exact information, the function of ion channels can be transiently modified by a vast amount of different factors: Heteromeric assembly, addition of beta or ancillary subunits, binding to scaffold proteins such as PSD-95, temperature, concentration of ions such as Mg^{2+} , phosphorylation, as well as secondary messenger molecules such as cAMP and PIP_2 , are able to strongly influence an ion channel's activation and inactivation properties (Rettig et al., 1994; Cohen et al., 1996; Kramer et al., 1998; Soom et al., 2001; Chen et al., 2001; McCrossan et al., 2003; Jow et al., 2004; Brenner et al., 2005; Gordon et al., 2006; Panama et al., 2010; Andrade et al., 2012; Wang et al., 2014) and some of them may even influence its subcellular localization (Arnold and Clapham, 1999; Piwonska et al., 2008; Wynne et al., 2009; Kanda et al., 2011; Shruti et al., 2012; Cox et al., 2014). Such dependencies can be further included in our model to study their impact on electrophysiology or to move the model even closer to reality. For instance, the electrophysiological properties of GCs were recently assessed *in vivo* (Kowalski et al., 2016). Accordingly, by providing each channel with correct temperature dependence one could test the model on these properties to validate its prediction accuracy for *in vivo* conditions.

Moreover, it would be of high value to endow our model with models of AMPARs and NMDARs and add mechanisms of synaptic plasticity (e.g. spike-timing, voltage, or Ca^{2+} dependent plasticity models (Castellani et al., 2001; Yeung et al., 2004; Graupner and Brunel, 2007; Gidon and Segev, 2009; Clopath and Gerstner, 2010; Jedlicka et al., 2015). With these properties, one might investigate how increased excitability (Mongiat et al., 2009) and preferential expression of the subunit NMDAR-2b cooperate to enhance synaptic plasticity in young adult-born GCs during their critical phase of integration (Ge et al., 2007; Evans et al., 2012). Furthermore, the influence of

increased synaptic plasticity on single-cell computation such as temporal integration can be assessed. In this context, the here reported change of dendritic and spine morphology during homo- and heterosynaptic plasticity should be considered as well. For instance, spine size and machinery (e.g. spine apparatus; (Deller et al., 2006) has a large influence on local voltage and thus Ca^{2+} transients due to voltage-dependent Ca^{2+} -channels and intracellular release. Ca^{2+} is the most important signal for plasticity-related mechanisms (Ataei et al., 2015), hence modeling explicit spines and their structural plasticity might strongly influence synaptic plasticity.

Single-cell modeling of mature and adult-born GCs may reveal many properties important for hippocampal function; however, many more functions arise from their interplay with thousands of other neurons. For instance, the impact of the reported reduced excitation/inhibition balance in young adult-born GCs (Marín-Burgin et al., 2012; Temprana et al., 2015) cannot be analyzed without modeling interneurons. Indeed, many DG network models already exist with (Becker, 2005; Wiskott et al., 2006; Chambers and Conroy, 2007; Aimone et al., 2009; Appleby and Wiskott, 2009; Weisz and Argibay, 2009; Chow et al., 2012) or without (Santhakumar et al., 2005; Dyhrfjeld-Johnsen et al., 2007; Myers and Scharfman, 2011) adult neurogenesis implemented, but most of them use no or only simplified morphologies and electrophysiological properties due to both, limitations of more detailed knowledge and computational power. Hence, with time, network models of the DG (possibly including CA) that use realistic morphologies, detailed electrophysiology, and young adult-born GCs, should be possible. In such a context, the DG could be analyzed and manipulated in ways that are inaccessible for experimental approaches, thus shedding new light on the role of mature and adult-born GCs in pattern processing and storage of hippocampal memory.

7. References

- Abbas A-K (2016) Protein Synthesis Inhibitors Did Not Interfere with Long-Term Depression Induced either Electrically in Juvenile Rats or Chemically in Middle-Aged Rats Kavushansky A, ed. PLoS One 11:e0161270.
- Abraham WC, Bliss TVP, Goddard G V (1985) Heterosynaptic changes accompany long-term but not short-term potentiation of the perforant path in the anaesthetized rat. *J Physiol* 363:335–349.
- Abraham WC, Christie BR, Logan B, Lawlor P, Dragunow M (1994) Immediate early gene expression associated with the persistence of heterosynaptic long-term depression in the hippocampus. *PNAS* 91:10049–10053.
- Abraham WC, Logan B, Wolff A, Benuskova L (2007) “Heterosynaptic” LTD in the dentate gyrus of anesthetized rat requires homosynaptic activity. *J Neurophysiol* 98:1048–1051.
- Aimone JB, Gage FH (2011) Modeling new neuron function: A history of using computational neuroscience to study adult neurogenesis. *Eur J Neurosci* 33:1160–1169.
- Aimone JB, Li Y, Lee SW, Clemenson GD, Deng W, Gage FH (2014) Regulation and function of adult neurogenesis: from genes to cognition. *Physiol Rev* 94:991–1026.
- Aimone JB, Wiles J, Gage FH (2009) Computational influence of adult neurogenesis on memory encoding. *Neuron* 61:187–202.
- Aizawa K, Ageyama N, Yokoyama C, Hisatsune T (2009) Age-dependent alteration in hippocampal neurogenesis correlates with learning performance of macaque monkeys. *Exp Anim* 58:403–407.
- Albensi BC, Oliver DR, Toupin J, Otero G (2007) Electrical stimulation protocols for hippocampal synaptic plasticity and neuronal hyper-excitability: are they effective or relevant? *Exp Neurol* 204:1–13.
- Alcántara S, Ruiz M, Arcangelo GD, Ezan F, Lecea L De, Curran T, Sotelo C, Soriano E (1998) Regional and cellular patterns of reelin mRNA expression in the forebrain of the developing and adult mouse. *J Neurosci* 18:7779–7799.
- Almog M, Korngreen A (2016) Is realistic neuronal modeling realistic? *J Neurophysiol* 2:jn.00360.2016.

References

- Altman J (1969) Autoradiographic and histological studies of postnatal neurogenesis. IV. Cell proliferation and migration in the anterior forebrain, with special reference to persisting neurogenesis in the olfactory bulb. *J Comp Neurol* 137:433–457.
- Altman J, Das GD (1965) Autoradiographic and histological evidence of postnatal hippocampal neurogenesis in rats. *J Comp Neurol* 124:319–335.
- Alvarez P, Squire LR (1994) Memory consolidation and the medial temporal lobe: a simple network model. *PNAS* 91:7041–7045.
- Alvarez V a, Sabatini BL (2007) Anatomical and Physiological Plasticity of Dendritic Spines. *Annu Rev Neruoscience* 30:79–97.
- Amaral DG, Ishizuka N, Claiborne B (1990) Neurons, numbers and the hippocampal network. *Prog Brain Res* 83:1–11.
- Amaral DG, Scharfman H, Lavenex P (2007) The dentate gyrus: fundamental neuroanatomical organization (dentate gyrus for dummies). *Prog Brain Res* 153:390–394.
- Andrade R, Foehring RC, Tzingounis A V. (2012) The calcium-activated slow AHP: cutting through the Gordian knot. *Front Cell Neurosci* 6:47.
- Appleby PA, Wiskott L (2009) Additive neurogenesis as a strategy for avoiding interference in a sparsely-coding dentate gyrus. *Network* 20:137–161.
- Aradi I, Holmes WR (1999) Role of multiple calcium and calcium-dependent conductances in regulation of hippocampal dentate granule cell excitability. *J Comput Neurosci* 6:215–235.
- Arnold DB, Clapham DE (1999) Molecular determinants for subcellular localization of PSD-95 with an interacting K⁺ channel. *Neuron* 23:149–157.
- Arsenijevic Y, Villemure JG, Brunet JF, Bloch JJ, Déglon N, Kostic C, Zurn A, Aebischer P (2001) Isolation of multipotent neural precursors residing in the cortex of the adult human brain. *Exp Neurol* 170:48–62.
- Arvidsson A, Collin T, Kirik D, Kokaia Z, Lindvall O (2002) Neuronal replacement from endogenous precursors in the adult brain after stroke. *Nat Med* 8:963–970.
- Ataei N, Sabzghabae AM, Movahedian A (2015) Calcium/Calmodulin-dependent Protein Kinase II is a Ubiquitous Molecule in Human Long-term Memory Synaptic Plasticity: A Systematic Review. *Int J Prev Med* 6:88.
- Baranauskas G, Martina M (2006) Sodium currents activate without a Hodgkin-and-Huxley-type delay in central mammalian neurons. *J Neurosci* 26:671–684.

References

- Beattie EC, Carroll RC, Yu X, Morishita W, Yasuda H, von Zastrow M, Malenka RC (2000) Regulation of AMPA receptor endocytosis by a signaling mechanism shared with LTD. *Nat Neurosci* 3:1291–1300.
- Becker S (2005) A computational principle for hippocampal learning and neurogenesis. *Hippocampus* 15:722–738.
- Bédard A, Cossette M, Lévesque M, Parent A (2002) Proliferating cells can differentiate into neurons in the striatum of normal adult monkey. *Neurosci Lett* 328:213–216.
- Bédard A, Gravel C, Parent A (2006) Chemical characterization of newly generated neurons in the striatum of adult primates. *Exp brain Res* 170:501–512.
- Bédard A, Parent A (2004) Evidence of newly generated neurons in the human olfactory bulb. *Brain Res Dev Brain Res* 151:159–168.
- Beining M, Jungenitz T, Radic T, Deller T, Cuntz H, Jedlicka P, Schwarzacher SW (2016) Adult-born dentate granule cells show a critical period of dendritic reorganization and are distinct from developmentally born cells. *Brain Struct Funct*.
- Beňušková L., Jedlička P. (2012) Computational modeling of long-term depression of synaptic weights: Insights from stdp, metaplasticity and spontaneous activity. *Neural Netw World* 22:161–180.
- Benuskova L, Abraham WC (2007) STDP rule endowed with the BCM sliding threshold accounts for hippocampal heterosynaptic plasticity. *J Comput Neurosci* 22:129–133.
- Bergami M, Masserdotti G, Temprana SGG, Motori E, Eriksson TMM, Göbel J, Yang SMM, Conzelmann K-KK, Schinder AFF, Götz M, Berninger B (2015) A critical period for experience-dependent remodeling of adult-born neuron connectivity. *Neuron* 85:710–717.
- Bergmann O, Liebl J, Bernard S, Alkass K, Yeung MSY, Steier P, Kutschera W, Johnson L, Landén M, Druid H, Spalding KL, Frisén J (2012) The age of olfactory bulb neurons in humans. *Neuron* 74:634–639.
- Bergmann O, Spalding KL, Frisén J (2015) Adult Neurogenesis in Humans. *Cold Spring Harb Perspect Biol* 7:1–12.
- Bernier PJ, Bedard A, Vinet J, Levesque M, Parent A (2002) Newly generated neurons in the amygdala and adjoining cortex of adult primates. *PNAS* 99:11464–11469.
- Bhardwaj RD, Curtis MA, Spalding KL, Buchholz BA, Fink D, Björk-Eriksson T, Nordborg C, Gage FH, Druid H, Eriksson PS, Frisén J (2006) Neocortical neurogenesis in humans is restricted to development. *PNAS* 103:12564–12568.

References

- Bliss T V, Lomo T (1973) Long-lasting potentiation of synaptic transmission in the dentate area of the anaesthetized rabbit following stimulation of the perforant path. *J Physiol* 232:331–356.
- Bodhinathan K, Slesinger PA (2013) Molecular mechanism underlying ethanol activation of G-protein-gated inwardly rectifying potassium channels. *PNAS* 110:18309–18314.
- Bosch M, Hayashi Y (2012) Structural plasticity of dendritic spines. *Curr Opin Neurobiol* 22:383–388.
- Bower JM, Beeman D (1998) *The book of GENESIS: exploring realistic neural models with the GGeneral NEural Simulation System*, 2nd Ed. New York: Springer-Verlag.
- Bramham CR, Worley PF, Moore MJ, Guzowski JF (2008) The immediate early gene *arc/arg3.1*: regulation, mechanisms, and function. *J Neurosci* 28:11760–11767.
- Branco T, Häusser M (2010) The single dendritic branch as a fundamental functional unit in the nervous system. *Curr Opin Neurobiol* 20:494–502.
- Brandt MD, Jessberger S, Steiner B, Kronenberg G, Reuter K, Bick-Sander A, von der Behrens W, Kempermann G (2003) Transient calretinin expression defines early postmitotic step of neuronal differentiation in adult hippocampal neurogenesis of mice. *Mol Cell Neurosci* 24:603–613.
- Brenner R, Chen QH, Vilaythong A, Toney GM, Noebels JL, Aldrich RW (2005) BK channel beta4 subunit reduces dentate gyrus excitability and protects against temporal lobe seizures. *Nat Neurosci* 8:1752–1759.
- Burgess N (1996) Cognitive graphs, resistive grids, and the hippocampal representation of space. *J Gen Physiol* 107:659–662.
- Buzsáki G, Moser EI (2013) Memory, navigation and theta rhythm in the hippocampal-entorhinal system. *Nat Neurosci* 16:130–138.
- Cajal SR y (1995) *Histology of the Nervous System of Man and Vertebrates*. Oxford University Press; 1. edition.
- Cameron HA, Glover LR (2015) Adult Neurogenesis: Beyond Learning and Memory. *Annu Rev Psychol* 66:53–81.
- Carnevale NT, Hines ML (2006) *The NEURON Book*. Cambridge, UK: Cambridge University Press.

References

- Castellani GC, Quinlan EM, Cooper LN, Shouval HZ (2001) A biophysical model of bidirectional synaptic plasticity: dependence on AMPA and NMDA receptors. *PNAS* 98:12772–12777.
- Chambers RA (2013) Adult hippocampal neurogenesis in the pathogenesis of addiction and dual diagnosis disorders. *Drug Alcohol Depend* 130:1–12.
- Chambers RA, Conroy SK (2007) Network Modeling of Adult Neurogenesis: Shifting Rates of Neuronal Turnover Optimally Gears Network Learning according to Novelty Gradient. *J Cogn Neurosci* 19:1–12.
- Chancey JH, Poulsen DJ, Wadiche JI, Overstreet-Wadiche L (2014) Hilar mossy cells provide the first glutamatergic synapses to adult-born dentate granule cells. *J Neurosci* 34:2349–2354.
- Chanda B, Bezanilla F (2002) Tracking voltage-dependent conformational changes in skeletal muscle sodium channel during activation. *J Gen Physiol* 120:629–645.
- Chao OY, Huston JP, Li J-S, Wang A-L, de Souza Silva MA (2016) The medial prefrontal cortex-lateral entorhinal cortex circuit is essential for episodic-like memory and associative object-recognition. *Hippocampus* 26:633–645.
- Chen JL, Nedivi E (2010) Neuronal structural remodeling: is it all about access? *Curr Opin Neurobiol* 20:557–562.
- Chen S, Wang J, Siegelbaum SA (2001) Properties of hyperpolarization-activated pacemaker current defined by coassembly of HCN1 and HCN2 subunits and basal modulation by cyclic nucleotide. *J Gen Physiol* 117:491–504.
- Cheng S (2013) The CRISP theory of hippocampal function in episodic memory. *Front Neural Circuits* 7:88.
- Chiang P-H, Wu P-Y, Kuo T-W, Liu Y-C, Chan C-F, Chien T-C, Cheng J-K, Huang Y-Y, Chiu C-D, Lien C-C (2012) GABA is depolarizing in hippocampal dentate granule cells of the adolescent and adult rats. *J Neurosci* 32:62–67.
- Chistiakova M, Bannon NM, Chen J-Y, Bazhenov M, Volgushev M (2015) Homeostatic role of heterosynaptic plasticity: models and experiments. *Front Comput Neurosci* 9:89.
- Chow S-F, Wick SD, Riecke H (2012) Neurogenesis drives stimulus decorrelation in a model of the olfactory bulb. *PLoS Comput Biol* 8:e1002398.
- Chowdhury S, Shepherd JD, Okuno H, Lyford G, Petralia RS, Plath N, Kuhl D, Huganir RL, Worley PF (2006) Arc/Arg3.1 interacts with the endocytic machinery to regulate AMPA receptor trafficking. *Neuron* 52:445–459.

References

- Christie BR, Abraham WC (1992) NMDA-Dependent Heterosynaptic Long-Term Depression in the Dentate Gyms of Anaesthetized Rats. *Synapse* 10:1–6.
- Claiborne BJ, Amaral DG, Cowan WM (1986) A light and electron microscopic analysis of the mossy fibers of the rat dentate gyrus. *J Comp Neurol* 246:435–458.
- Claiborne BJ, Amaral DG, Cowan WM (1990) Quantitative, three-dimensional analysis of granule cell dendrites in the rat dentate gyrus. *J Comp Neurol* 302:206–219.
- Clelland CD, Choi M, Romberg C, Clemenson GD, Fagniere A, Tyers P, Jessberger S, Saksida LM, Barker R a, Gage FH, Bussey TJ (2009) A functional role for adult hippocampal neurogenesis in spatial pattern separation. *Science* (80-) 325:210–213.
- Clopath C, Gerstner W (2010) Voltage and Spike Timing Interact in STDP - A Unified Model. *Front Synaptic Neurosci* 2:25.
- Coe CL, Kramer M, Czéh B, Gould E, Reeves AJ, Kirschbaum C, Fuchs E (2003) Prenatal stress diminishes neurogenesis in the dentate gyrus of juvenile rhesus monkeys. *Biol Psychiatry* 54:1025–1034.
- Cohen NA, Brenman JE, Snyder SH, Brecht DS (1996) Binding of the inward rectifier K⁺ channel Kir 2.3 to PSD-95 is regulated by protein kinase A phosphorylation. *Neuron* 17:759–767.
- Cools R, Clark L, Robbins TW (2004) Differential responses in human striatum and prefrontal cortex to changes in object and rule relevance. *J Neurosci* 24:1129–1135.
- Cools R, Ivry RB, D'Esposito M (2006) The Human Striatum is Necessary for Responding to Changes in Stimulus Relevance. *J Cogn Neurosci* 18:1973–1983.
- Cox N, Toro B, Pacheco-Otalora LF, Garrido-Sanabria ER, Zarei MM (2014) An endoplasmic reticulum trafficking signal regulates surface expression of β 4 subunit of a voltage- and Ca²⁺-activated K⁺ channel. *Brain Res* 1553:12–23.
- Curtis MA, Kam M, Nannmark U, Anderson MF, Axell MZ, Wikkelso C, Holtås S, van Roon-Mom WMC, Björk-Eriksson T, Nordborg C, Frisén J, Dragunow M, Faull RLM, Eriksson PS (2007) Human neuroblasts migrate to the olfactory bulb via a lateral ventricular extension. *Science* (80-) 315:1243–1249.
- Dayer AG, Cleaver KM, Abouantoun T, Cameron HA (2005) New GABAergic interneurons in the adult neocortex and striatum are generated from different precursors. *J Cell Biol* 168:415–427.
- Dayer AG, Ford AA, Cleaver KM, Yassaee M, Cameron HA (2003) Short-term and long-term survival of new neurons in the rat dentate gyrus. *J Comp Neurol* 460:563–572.

References

- de Jong APH, Schmitz SK, Toonen RFG, Verhage M (2012) Dendritic position is a major determinant of presynaptic strength. *J Cell Biol* 197:327–337.
- Del Turco D, Deller T (2007) Organotypic entorhino-hippocampal slice cultures—a tool to study the molecular and cellular regulation of axonal regeneration and collateral sprouting in vitro. *Methods Mol Biol* 399:55–66.
- Deller T, Basorth C, Del Turco D, Vlachos A, Burbach G, Drakew A, Chabanis S, Korte M, Schwegler H, Haas C, Delturco D (2006) A role for synaptopodin and the spine apparatus in hippocampal synaptic plasticity. *Ann Anat* 189.
- Deller T, Korte M, Chabanis S, Drakew A, Schwegler H, Stefani GG, Zuniga A, Schwarz K, Bonhoeffer T, Zeller R, Frotscher M, Mundel P (2003) Synaptopodin-deficient mice lack a spine apparatus and show deficits in synaptic plasticity. *PNAS* 100:10494–10499.
- Deng W, Mayford M, Gage FH (2013) Selection of distinct populations of dentate granule cells in response to inputs as a mechanism for pattern separation in mice. *Elife* 2:e00312.
- Denny CA, Kheirbek MA, Alba EL, Tanaka KF, Brachman RA, Laughman KB, Tomm NK, Turi GF, Losonczy A, Hen R (2014) Hippocampal Memory Traces Are Differentially Modulated by Experience, Time, and Adult Neurogenesis. *Neuron* 83:189–201.
- Derdikman D, Moser EI (2010) A manifold of spatial maps in the brain. *Trends Cogn Sci* 14:561–569.
- Deshpande A, Bergami M, Ghanem A, Conzelmann K-K, Lepier A, Götz M, Berninger B (2013) Retrograde monosynaptic tracing reveals the temporal evolution of inputs onto new neurons in the adult dentate gyrus and olfactory bulb. *PNAS* 110:E1152-61.
- Destexhe A, Mainen ZF, Sejnowski TJ (1994) Synthesis of models for excitable membranes, synaptic transmission and neuromodulation using a common kinetic formalism. *J Comput Neurosci* 1:195–230.
- Dingledine R, Traynelis SFF, Borges K, Bowie D, Traynelis SFF (1999) The glutamate receptor ion channels. *Pharmacol Rev* 51:7–61.
- Doyère V, Srebro B, Laroche S (1997) Heterosynaptic LTD and depotentiation in the medial perforant path of the dentate gyrus in the freely moving rat. *J Neurophysiol* 77:571–578.
- Dragunow M, Robertson HA (1987) Kindling stimulation induces c-fos protein(s) in granule cells of the rat dentate gyrus. *Nature* 329:441–442.

References

- Dyhrfjeld-Johnsen J, Santhakumar V, Morgan RJ, Huerta R, Tsimring L, Soltesz I (2007) Topological determinants of epileptogenesis in large-scale structural and functional models of the dentate gyrus derived from experimental data. *J Neurophysiol* 97:1566–1587.
- Eichenbaum H (2016) Still searching for the engram. *Learn Behav* 44:209–222.
- Eichenbaum H, Schoenbaum G, Young B, Bunsey M (1996) Functional organization of the hippocampal memory system. *PNAS* 93:13500–13507.
- Eriksson PS, Perfilieva E, Björk-Eriksson T, Alborn a M, Nordborg C, Peterson D a, Gage FH (1998) Neurogenesis in the adult human hippocampus. *Nat Med* 4:1313–1317.
- Ermentrout B, David TH (2010) *Mathematical Foundations of Neuroscience*. Springer.
- Ernst A, Alkass K, Bernard S, Salehpour M, Perl S, Tisdale J, Possnert G, Druid H, Frisé J (2014) Neurogenesis in the striatum of the adult human brain. *Cell* 156:1072–1083.
- Escobar ML, Derrick B (2007) Long-Term Potentiation and Depression as Putative Mechanisms for Memory Formation.
- Espósito MS, Piatti VC, Laplagne DA, Morgenstern NA, Ferrari CC, Pitossi FJ, Schinder AF (2005) Neuronal differentiation in the adult hippocampus recapitulates embryonic development. *J Neurosci* 25:10074–10086.
- Evans RC, Morera-Herreras T, Cui Y, Du K, Sheehan T, Koteleski JH, Venance L, Blackwell KT (2012) The effects of NMDA subunit composition on calcium influx and spike timing-dependent plasticity in striatal medium spiny neurons. *PLoS Comput Biol* 8:e1002493.
- Fanselow MS, Dong H-W (2010) Are the Dorsal and Ventral Hippocampus Functionally Distinct Structures? *Neuron* 65:7–19.
- Farris S, Lewandowski G, Cox CD, Steward O (2014) Selective localization of arc mRNA in dendrites involves activity- and translation-dependent mRNA degradation. *J Neurosci* 34:4481–4493.
- Ferrante M, Migliore M, Ascoli GA (2009) Feed-forward inhibition as a buffer of the neuronal input-output relation. *PNAS* 106:18004–18009.
- Fink M, Noble D (2009) Markov models for ion channels: versatility versus identifiability and speed. *Philos Trans A Math Phys Eng Sci* 367:2161–2179.

References

- Fleischmann A, Hvalby O, Jensen V, Strekalova T, Zacher C, Layer LE, Kvello A, Reschke M, Spanagel R, Sprengel R, Wagner EF, Gass P (2003) Impaired long-term memory and NR2A-type NMDA receptor-dependent synaptic plasticity in mice lacking c-Fos in the CNS. *J Neurosci* 23:9116–9122.
- Förster E, Zhao S, Frotscher M (2006) Laminating the hippocampus. *Nat Rev Neurosci* 7:259–267.
- Freund TF, Buzsáki G (1998) Interneurons of the hippocampus. *Hippocampus* 6:347–470.
- Frey U, Morris RG (1998) Synaptic tagging: implications for late maintenance of hippocampal long-term potentiation. *Trends Neurosci* 21:181–188.
- Frotscher M (1991) Target cell specificity of synaptic connections in the hippocampus. *Hippocampus* 1:123–130.
- Fukazawa Y, Saitoh Y, Ozawa F, Ohta Y, Mizuno K, Inokuchi K (2003) Hippocampal LTP is accompanied by enhanced F-actin content within the dendritic spine that is essential for late LTP maintenance in vivo. *Neuron* 38:447–460.
- Gage FH (2000) Mammalian neural stem cells. *Science* (80-) 287:1433–1438.
- Ge S, Yang C-H, Hsu K-S, Ming G-L, Song H (2007) A critical period for enhanced synaptic plasticity in newly generated neurons of the adult brain. *Neuron* 54:559–566.
- Gheusi G, Lledo P-M (2014) Adult neurogenesis in the olfactory system shapes odor memory and perception. *Prog Brain Res* 208:157–175.
- Gidon A, Segev I (2009) Spike-timing-dependent synaptic plasticity and synaptic democracy in dendrites. *J Neurophysiol* 101:3226–3234.
- Glass R, Synowitz M, Kronenberg G, Walzlein J-H, Markovic DS, Wang L-P, Gast D, Kiwit J, Kempermann G, Kettenmann H (2005) Glioblastoma-induced attraction of endogenous neural precursor cells is associated with improved survival. *J Neurosci* 25:2637–2646.
- Gleeson JG, Lin PT, Flanagan LA, Walsh CA (1999) Doublecortin is a microtubule-associated protein and is expressed widely by migrating neurons. *Neuron* 23:257–271.
- Goldman DE (1943) Potential, impedance, and rectification in membranes. *J Gen Physiol* 27:37–60.
- Goldman SA, Nottebohm F (1983) Neuronal production, migration, and differentiation in a vocal control nucleus of the adult female canary brain. *PNAS* 80:2390–2394.

References

- Gonçalves JT, Bloyd CW, Shtrahman M, Johnston ST, Schafer ST, Parylak SL, Tran T, Chang T, Gage FH (2016) In vivo imaging of dendritic pruning in dentate granule cells. *Nat Neurosci*:5–10.
- Gonzales RB, DeLeon Galvan CJ, Rangel YM, Claiborne BJ (2001) Distribution of thorny excrescences on CA3 pyramidal neurons in the rat hippocampus. *J Comp Neurol* 430:357–368.
- Gordon E, Roepke TK, Abbott GW (2006) Endogenous KCNE subunits govern Kv2.1 K⁺ channel activation kinetics in *Xenopus* oocyte studies. *Biophys J* 90:1223–1231.
- Gould E, Beylin A, Tanapat P, Reeves A, Shors TJ (1999a) Learning enhances adult neurogenesis in the hippocampal formation. *Nat Neurosci* 2:260–265.
- Gould E, Reeves AJ, Fallah M, Tanapat P, Gross CG, Fuchs E (1999b) Hippocampal neurogenesis in adult Old World primates. *PNAS* 96:5263–5267.
- Gould E, Tanapat P, McEwen BS, Flügge G, Fuchs E (1998) Proliferation of granule cell precursors in the dentate gyrus of adult monkeys is diminished by stress. *PNAS* 95:3168–3171.
- Gould E, Vail N, Wagers M, Gross CG (2001) Adult-generated hippocampal and neocortical neurons in macaques have a transient existence. *PNAS* 98:10910–10917.
- Graupner M, Brunel N (2007) STDP in a bistable synapse model based on CaMKII and associated signaling pathways. *PLoS Comput Biol* 3:2299–2323.
- Guan J-S, Jiang J, Xie H, Liu K-Y (2016) How Does the Sparse Memory “Engram” Neurons Encode the Memory of a Spatial–Temporal Event? *Front Neural Circuits* 10.
- Harris KM (2001) Dendritic Spines. In: *Encyclopedia of Life Sciences*. Chichester, UK, UK: John Wiley & Sons, Ltd.
- Hart G (1983) The kinetics and temperature dependence of the pace-maker current in sheep Purkinje fibres. *J Physiol* 337:401–416.
- Hastings NB, Gould E (1999) Rapid extension of axons into the CA3 region by adult-generated granule cells. *J Comp Neurol* 413:146–154.
- Hayashi H, Nonaka Y (2011) Cooperation and competition between lateral and medial perforant path synapses in the dentate gyrus. *Neural networks* 24:233–246.
- Hebb DO (1949) *The Organization of Behavior*. New York: Wiley.

References

- Hendrickson PJ, Yu GJ, Dong Song, Berger TW (2015) A million-plus neuron model of the hippocampal dentate gyrus: Dependency of spatio-temporal network dynamics on topography. In: 37th Annual International Conference of the IEEE EMBC, pp 4713–4716.
- Henze D a, Urban NN, Barrioneuvo G (2000) The multifarious hippocampal mossy fiber pathway: A review. *Neuroscience* 98:407–427.
- Hille B (2001) *Ion Channels of Excitable Membranes*, 3rd ed. Sunderland, MA.: Sinauer Associates.
- Ho NF, Hooker JM, Sahay A, Holt DJ, Roffman JL (2013) In vivo imaging of adult human hippocampal neurogenesis: progress, pitfalls and promise. *Mol Psychiatry* 18:404–416.
- Hodgkin AL, Huxley AF (1952) A quantitative description of membrane current and its application to conduction and excitation in nerve. *J Physiol* 117:500.
- Hou S-W, Wang Y-Q, Xu M, Shen D-H, Wang J-J, Huang F, Yu Z, Sun F-Y (2008) Functional integration of newly generated neurons into striatum after cerebral ischemia in the adult rat brain. *Stroke* 39:2837–2844.
- Howard MW, Eichenbaum H (2015) Time and space in the hippocampus. *Brain Res* 1621:345–354.
- Huber L, Menzel R, Matsuzaki M, Honkura N, Ellis-Davies GCR, Kasai H (2004) Structural basis of long-term potentiation in single dendritic spines. *Nature* 429:761–766.
- Igarashi KM (2016) The entorhinal map of space. *Brain Res* 1637:177–187.
- Inta D, Alfonso J, von Engelhardt J, Kreuzberg MM, Meyer AH, van Hooft JA, Monyer H (2008) Neurogenesis and widespread forebrain migration of distinct GABAergic neurons from the postnatal subventricular zone. *PNAS* 105:20994–20999.
- Inta D, Cameron HA, Gass P (2015) New neurons in the adult striatum: from rodents to humans. *Trends Neurosci* 38:517–523.
- Jaffe DB, Carnevale NT (1999) Passive normalization of synaptic integration influenced by dendritic architecture. *J Neurophysiol* 82:3268–3285.
- Jaffe DB, Wang B, Brenner R (2011) Shaping of action potentials by type I and type II large-conductance Ca^{2+} -activated K^{+} channels. *Neuroscience* 192:205–218.
- Jagasia R, Steib K, Englberger E, Herold S, Faus-Kessler T, Saxe M, Gage FH, Song H, Lie DC (2009) GABA-cAMP response element-binding protein signaling regulates maturation and survival of newly generated neurons in the adult hippocampus. *J Neurosci* 29:7966–7977.

References

- Jedlicka P, Benuskova L, Abraham WC (2015) A voltage-based STDP rule combined with fast BCM-like metaplasticity accounts for LTP and concurrent “heterosynaptic” LTD in the dentate gyrus in vivo. *PLoS Comput Biol* 11:e1004588.
- Jedlicka P, Schwarzacher SW, Winkels R, Kienzler F, Frotscher M, Bramham CR, Schultz C, Bas Orth C, Deller T (2009) Impairment of in vivo theta-burst long-term potentiation and network excitability in the dentate gyrus of synaptopodin-deficient mice lacking the spine apparatus and the cisternal organelle. *Hippocampus* 19:130–140.
- Jiang Y, Lee A, Chen J, Ruta V, Cadene M, Chait BT, MacKinnon R (2003) X-ray structure of a voltage-dependent K⁺ channel. *Nature* 423:33–41.
- Jinde S, Zsiros V, Jiang Z, Nakao K, Pickel J, Kohno K, Belforte JE, Nakazawa K (2012) Hilar mossy cell degeneration causes transient dentate granule cell hyperexcitability and impaired pattern separation. *Neuron* 76:1189–1200.
- Jinde S, Zsiros V, Nakazawa K (2013) Hilar mossy cell circuitry controlling dentate granule cell excitability. *Front Neural Circuits* 7:14.
- Johansson CB, Svensson M, Wallstedt L, Janson AM, Frisé J (1999) Neural stem cells in the adult human brain. *Exp Cell Res* 253:733–736.
- Johnston D, Wu SM (1995) *Foundations of cellular neurophysiology*, 1st editio. Cambridge: MIT Press.
- Johnston ST, Shtrahman M, Parylak S, Gonçalves JT, Gage FH (2016) Paradox of pattern separation and adult neurogenesis: A dual role for new neurons balancing memory resolution and robustness. *Neurobiol Learn Mem* 129:60–68.
- Jow F, Zhang Z-H, Kopsco DC, Carroll KC, Wang K (2004) Functional coupling of intracellular calcium and inactivation of voltage-gated Kv1.1/Kvbeta1.1 A-type K⁺ channels. *PNAS* 101:15535–15540.
- Jung MW, McNaughton BL (1993) Spatial selectivity of unit activity in the hippocampal granular layer. *Hippocampus* 3:165–182.
- Jungenitz T, Radic T, Jedlicka P, Schwarzacher SW (2014) High-frequency stimulation induces gradual immediate early gene expression in maturing adult-generated hippocampal granule cells. *Cereb Cortex* 24:1845–1857.
- Kamada M, Li R-Y, Hashimoto M, Kakuda M, Okada H, Koyanagi Y, Ishizuka T, Yawo H (2004) Intrinsic and spontaneous neurogenesis in the postnatal slice culture of rat hippocampus. *Eur J Neurosci* 20:2499–2508.

References

- Kanda VA, Lewis A, Xu X, Abbott GW (2011) KCNE1 and KCNE2 provide a checkpoint governing voltage-gated potassium channel α -subunit composition. *Biophys J* 101:1364–1375.
- Kandel ER, Pittenger C (1999) The past, the future and the biology of memory storage. *Philos Trans R Soc B Biol Sci* 354:2027–2052.
- Karschin C, Dissmann E, Stühmer W, Karschin A (1996) IRK(1-3) and GIRK(1-4) inwardly rectifying K⁺ channel mRNAs are differentially expressed in the adult rat brain. *J Neurosci* 16:3559–3570.
- Kee N, Teixeira CM, Wang AH, Frankland PW (2007) Preferential incorporation of adult-generated granule cells into spatial memory networks in the dentate gyrus. *Nat Neurosci* 10:355–362.
- Kempermann G (2014) Off the beaten track: New neurons in the adult human striatum. *Cell* 156:870–871.
- Kempermann G (2015) Activity Dependency and Aging in the Regulation of Adult Neurogenesis. *Cold Spring Harb Perspect Biol* 7:a018929.
- Kempermann G, Kuhn HG, Gage FH (1997) More hippocampal neurons in adult mice living in an enriched environment. *Nature* 386:493–495.
- Kheirbek MA, Hen R (2011) Dorsal vs Ventral Hippocampal Neurogenesis: Implications for Cognition and Mood. *Neuropsychopharmacology* 36:373–374.
- Kim CH, Lisman JE (1999) A role of actin filament in synaptic transmission and long-term potentiation. *J Neurosci* 19:4314–4324.
- Kitamura T, Inokuchi K (2014) Role of adult neurogenesis in hippocampal-cortical memory consolidation. *Mol Brain* 7:13.
- Kleine Borgmann FB, Bracko O, Jessberger S (2013) Imaging neurite development of adult-born granule cells. *Development* 140:2823–2827.
- Kobayashi T, Ikeda K, Ichikawa T, Abe S, Togashi S, Kumanishi T (1995) Molecular cloning of a mouse G-protein-activated K⁺ channel (mGIRK1) and distinct distributions of three GIRK (GIRK1, 2 and 3) mRNAs in mouse brain. *Biochem Biophys Res Commun* 208:1166–1173.
- Kobayashi T, Washiyama K, Ikeda K (2003) Inhibition of G protein-activated inwardly rectifying K⁺ channels by fluoxetine (Prozac). *Br J Pharmacol* 138:1119–1128.

References

- Kohler SJ, Williams NI, Stanton GB, Cameron JL, Greenough WT (2011) Maturation time of new granule cells in the dentate gyrus of adult macaque monkeys exceeds six months. *PNAS* 108:10326–10331.
- Koketsu D, Furuichi Y, Maeda M, Matsuoka N, Miyamoto Y, Hisatsune T (2006) Increased number of new neurons in the olfactory bulb and hippocampus of adult non-human primates after focal ischemia. *Exp Neurol* 199:92–102.
- Koketsu D, Mikami A, Miyamoto Y, Hisatsune T (2003) Nonrenewal of neurons in the cerebral neocortex of adult macaque monkeys. *J Neurosci* 23:937–942.
- Koleske AJ (2013) Molecular mechanisms of dendrite stability. *Nat Rev Neurosci* 14:536–550.
- Kornack DR (2001) Cell Proliferation Without Neurogenesis in Adult Primate Neocortex. *Science* (80-) 294:2127–2130.
- Kornack DR, Rakic P (1999) Continuation of neurogenesis in the hippocampus of the adult macaque monkey. *PNAS* 96:5768–5773.
- Kowalski J, Gan J, Jonas P, Pernía-Andrade AJ (2016) Intrinsic membrane properties determine hippocampal differential firing pattern in vivo in anesthetized rats. *Hippocampus* 26:668–682.
- Kramer JW, Post MA, Brown AM, Kirsch GE (1998) Modulation of potassium channel gating by coexpression of Kv2.1 with regulatory Kv5.1 or Kv6.1 alpha-subunits. *Am J Physiol* 274:C1501–C1510.
- Krueppel R, Remy S, Beck H (2011) Dendritic integration in hippocampal dentate granule cells. *Neuron* 71:512–528.
- Kuipers SD, Tiron A, Soule J, Messaoudi E, Trentani A, Bramham CR (2009) Selective survival and maturation of adult-born dentate granule cells expressing the immediate early gene *Arc/Arg3.1*. *PLoS One* 4.
- Laplagne DA, Espósito MS, Piatti VC, Morgenstern NA, Zhao C, van Praag H, Gage FH, Schinder AF (2006) Functional convergence of neurons generated in the developing and adult hippocampus. *PLoS Biol* 4:e409.
- Lee H, Wang C, Deshmukh SSS, Knierim JJJ (2015) Neural Population Evidence of Functional Heterogeneity along the CA3 Transverse Axis: Pattern Completion versus Pattern Separation. *Neuron*:1–13.
- Lefebvre JL, Sanes JR, Kay JN (2015) Development of Dendritic Form and Function. *Annu Rev Cell Dev Biol* 31:741–777.

References

- Lemaire V, Tronel S, Montaron M-F, Fabre A, Dugast E, Abrous DN (2012) Long-Lasting Plasticity of Hippocampal Adult-Born Neurons. *J Neurosci* 32:3101–3108.
- Lepousez G, Valley MT, Lledo P-M (2013) The impact of adult neurogenesis on olfactory bulb circuits and computations. *Annu Rev Physiol* 75:339–363.
- Leuner B, Kozorovitskiy Y, Gross CG, Gould E (2007) Diminished adult neurogenesis in the marmoset brain precedes old age. *PNAS* 104:17169–17173.
- Leutgeb JK, Leutgeb S, Moser M-B, Moser EI (2007) Pattern Separation in the Dentate Gyrus and CA3 of the Hippocampus. *Science* (80-) 315:961–966.
- Lin C, Sim S, Ainsworth A, Okada M, Kelsch W (2010) Genetically increased cell-intrinsic excitability enhances neuronal integration into adult brain circuits. *Neuron* 65:32–39.
- Liu X, Ramirez S, Pang PT, Puryear CB, Govindarajan A, Deisseroth K, Tonegawa S (2012) Optogenetic stimulation of a hippocampal engram activates fear memory recall. *Nature* 484:381–385.
- Liu Z, Martin LJ (2003) Olfactory bulb core is a rich source of neural progenitor and stem cells in adult rodent and human. *J Comp Neurol* 459:368–391.
- Llorens-Martín M, Rábano A, Ávila J (2016) The Ever-Changing Morphology of Hippocampal Granule Neurons in Physiology and Pathology. *Front Neurosci* 9:1–20.
- Lois C, García-Verdugo JM, Alvarez-Buylla A (1996) Chain migration of neuronal precursors. *Science* (80-) 271:978–981.
- Long SB, Campbell EB, Mackinnon R (2005) Crystal structure of a mammalian voltage-dependent Shaker family K⁺ channel. *Science* (80-) 309:897–903.
- Loseva E, Yuan T-F, Karnup S (2009) Neurogliogenesis in the mature olfactory system: a possible protective role against infection and toxic dust. *Brain Res Rev* 59:374–387.
- Lu W-Y, Man H-Y, Ju W, Trimble WS, MacDonald JF, Wang YT (2001) Activation of Synaptic NMDA Receptors Induces Membrane Insertion of New AMPA Receptors and LTP in Cultured Hippocampal Neurons. *Neuron* 29:243–254.
- Lucassen PJ, Meerlo P, Naylor a S, van Dam a M, Dayer a G, Fuchs E, Oomen C a, Czéh B (2010) Regulation of adult neurogenesis by stress, sleep disruption, exercise and inflammation: Implications for depression and antidepressant action. *Eur Neuropsychopharmacol* 20:1–17.

References

- Luzzati F, De Marchis S, Fasolo A, Peretto P (2006) Neurogenesis in the caudate nucleus of the adult rabbit. *J Neurosci* 26:609–621.
- Lyford GL, Yamagata K, Kaufmann WE, Barnes CA, Sanders LK, Copeland NG, Gilbert DJ, Jenkins NA, Lanahan AA, Worley PF (1995) Arc, a growth factor and activity-regulated gene, encodes a novel cytoskeleton-associated protein that is enriched in neuronal dendrites. *Neuron* 14:433–445.
- Madsen TM, Kristjansen PEG, Bolwig TG, Wörtwein G (2003) Arrested neuronal proliferation and impaired hippocampal function following fractionated brain irradiation in the adult rat. *Neuroscience* 119:635–642.
- Magnusson JP, Göritz C, Tatarishvili J, Dias DO, Smith EMK, Lindvall O, Kokaia Z, Frisén J (2014) A latent neurogenic program in astrocytes regulated by Notch signaling in the mouse. *Science* (80-) 346:237–241.
- Mainen ZF, Sejnowski TJ (1996) Influence of dendritic structure on firing pattern in model neocortical neurons. *Nature* 382:363–366.
- Malberg JE, Eisch AJ, Nestler EJ, Duman RS (2000) Chronic Antidepressant Treatment Increases Neurogenesis in Adult Rat Hippocampus. *J Neurosci* 20:9104–9110.
- Malinow R (2003) AMPA receptor trafficking and long-term potentiation. *Philos Trans R Soc B Biol Sci* 358:707–714.
- Manahan-Vaughan D, Kulla A, Frey JU (2000) Requirement of translation but not transcription for the maintenance of long-term depression in the CA1 region of freely moving rats. *J Neurosci* 20:8572–8576.
- Marín-Burgin A, Mongiat LA, Pardi MB, Schinder AF (2012) Unique processing during a period of high excitation/inhibition balance in adult-born neurons. *Science* (80-) 335:1238–1242.
- Massey P V, Johnson BE, Moulton PR, Auberson YP, Brown MW, Molnar E, Collingridge GL, Bashir ZI (2004) Differential roles of NR2A and NR2B-containing NMDA receptors in cortical long-term potentiation and long-term depression. *J Neurosci* 24:7821–7828.
- Mateos-Aparicio P, Murphy R, Storm JF (2014) Complementary functions of SK and Kv7/M potassium channels in excitability control and synaptic integration in rat hippocampal dentate granule cells. *J Physiol* 592:669–693.
- Mattson MP, Bruce-Keller AJ (1999) Compartmentalization of signaling in neurons: evolution and deployment. *J Neurosci Res* 58:2–9.

References

- Mayford M (2013) The search for a hippocampal engram. *Philos Trans R Soc B Biol Sci* 369:20130161–20130161.
- Mayordomo-Cava J, Yajeya J, Navarro-López JD, Jiménez-Díaz L (2015) Amyloid- β (25-35) Modulates the Expression of GirK and KCNQ Channel Genes in the Hippocampus. *PLoS One* 10:e0134385.
- McAvoy KM et al. (2016) Modulating Neuronal Competition Dynamics in the Dentate Gyrus to Rejuvenate Aging Memory Circuits. *Neuron* 91:1356–1373.
- McCormick DA, Shu Y, Yu Y (2007) Neurophysiology: Hodgkin and Huxley model — still standing? *Nature* 445:E1–E2.
- McCrossan ZA, Lewis A, Panaghie G, Jordan PN, Christini DJ, Lerner DJ, Abbott GW (2003) MinK-related peptide 2 modulates Kv2.1 and Kv3.1 potassium channels in mammalian brain. *J Neurosci* 23:8077–8091.
- McKenzie S, Eichenbaum H (2011) Consolidation and Reconsolidation: Two Lives of Memories? *Neuron* 71:224–233.
- Ming G-L, Song H (2011) Adult neurogenesis in the Mammalian brain: significant answers and significant questions. *Neuron* 70:687–702.
- Mongiati LA, Espósito MS, Lombardi G, Schinder AF (2009) Reliable activation of immature neurons in the adult hippocampus. *PLoS One* 4:e5320.
- Moore KA, Lemischka IR (2006) Stem cells and their niches. *Science* (80-) 311:1880–1885.
- Moser EI, Kropff E, Moser M-B (2008) Place Cells, Grid Cells, and the Brain's Spatial Representation System. *Annu Rev Neurosci* 31:69–89.
- Moser EI, Moser M-B (2008) A metric for space. *Hippocampus* 18:1142–1156.
- Mullen RJ, Buck CR, Smith AM (1992) NeuN, a neuronal specific nuclear protein in vertebrates. *Development* 116:201–211.
- Myers CEC, Scharfman HE (2011) Pattern separation in the dentate gyrus: A role for the CA3 backprojection. *Hippocampus* 21:1190–1215.
- Nakashiba T, Cushman JD, Pelkey K a, Renaudineau S, Buhl DL, McHugh TJ, Barrera VR, Chittajallu R, Iwamoto KS, McBain CJ, Fanselow MS, Tonegawa S (2012) Young Dentate Granule Cells Mediate Pattern Separation, whereas Old Granule Cells Facilitate Pattern Completion. *Cell* 149:188–201.

References

- Nassirpour R, Bahima L, Lalive AL, Lüscher C, Luján R, Slesinger PA (2010) Morphine- and CaMKII-dependent enhancement of GIRK channel signaling in hippocampal neurons. *J Neurosci* 30:13419–13430.
- Naundorf B, Wolf F, Volgushev M (2006) Unique features of action potential initiation in cortical neurons. *Nature* 440:1060–1063.
- Neunuebel JP, Knierim JJ (2014) CA3 Retrieves Coherent Representations from Degraded Input: Direct Evidence for CA3 Pattern Completion and Dentate Gyrus Pattern Separation. *Neuron* 81:416–427.
- Nguyen P V, Abel T, Kandel ER (1994) Requirement of a critical period of transcription for induction of a late phase of LTP. *Science* (80-) 265:1104–1107.
- Nicola Z, Fabel K, Kempermann G (2015) Development of the adult neurogenic niche in the hippocampus of mice. *Front Neuroanat* 9:53.
- Nonaka M, Fujii H, Kim R, Kawashima T, Okuno H, Bito H (2013) Untangling the two-way signalling route from synapses to the nucleus, and from the nucleus back to the synapses. *Philos Trans R Soc Lond B Biol Sci* 369:20130150.
- O'Dell TJ, Kandel ER (1994) Low-frequency stimulation erases LTP through an NMDA receptor-mediated activation of protein phosphatases. *Learn Mem* 1:129–139.
- Oh WC, Parajuli LK, Zito K (2015) Heterosynaptic Structural Plasticity on Local Dendritic Segments of Hippocampal CA1 Neurons. *Cell Rep* 10:162–169.
- Ohkawa N, Saitoh Y, Tokunaga E, Nihonmatsu I, Ozawa F, Murayama A, Shibata F, Kitamura T, Inokuchi K (2012) Spine formation pattern of adult-born neurons is differentially modulated by the induction timing and location of hippocampal plasticity. *PLoS One* 7:e45270.
- Okamoto K-I, Nagai T, Miyawaki A, Hayashi Y (2004) Rapid and persistent modulation of actin dynamics regulates postsynaptic reorganization underlying bidirectional plasticity. *Nat Neurosci* 7:1104–1112.
- Okuno H, Akashi K, Ishii Y, Yagishita-Kyo N, Suzuki K, Nonaka M, Kawashima T, Fujii H, Takemoto-Kimura S, Abe M, Natsume R, Chowdhury S, Sakimura K, Worley PF, Bito H (2012) Inverse Synaptic Tagging of Inactive Synapses via Dynamic Interaction of Arc/Arg3.1 with CaMKII β . *Cell* 149:886–898.
- Pallotto M, Deprez F (2014) Regulation of adult neurogenesis by GABAergic transmission: signaling beyond GABAA-receptors. *Front Cell Neurosci* 8.

References

- Panama BK, McLerie M, Lopatin AN (2010) Functional consequences of Kir2.1/Kir2.2 subunit heteromerization. *Pflugers Arch Eur J Physiol* 460:839–849.
- Park S, Park JM, Kim S, Kim J-A, Shepherd JD, Smith-Hicks CL, Chowdhury S, Kaufmann W, Kuhl D, Ryazanov AG, Haganir RL, Linden DJ, Worley PF (2008) Elongation factor 2 and fragile X mental retardation protein control the dynamic translation of Arc/Arg3.1 essential for mGluR-LTD. *Neuron* 59:70–83.
- Paton JA, Nottebohm FN (1984) Neurons generated in the adult brain are recruited into functional circuits. *Science* (80-) 225:1046–1048.
- Payandeh J, Scheuer T, Zheng N, Catterall WA (2011) The crystal structure of a voltage-gated sodium channel. *Nature* 475:353–358.
- Peebles CL, Yoo J, Thwin MT, Palop JJ, Noebels JL, Finkbeiner S (2010) Arc regulates spine morphology and maintains network stability in vivo. *PNAS* 107:18173–18178.
- Perera TD, Coplan JD, Lisanby SH, Lipira CM, Arif M, Carpio C, Spitzer G, Santarelli L, Scharf B, Hen R, Rosoklija G, Sackeim HA, Dwork AJ (2007) Antidepressant-induced neurogenesis in the hippocampus of adult nonhuman primates. *J Neurosci* 27:4894–4901.
- Perera TD, Dwork AJ, Keegan KA, Thirumangalakudi L, Lipira CM, Joyce N, Lange C, Higley JD, Rosoklija G, Hen R, Sackeim HA, Coplan JD (2011a) Necessity of hippocampal neurogenesis for the therapeutic action of antidepressants in adult nonhuman primates. *PLoS One* 6:e17600.
- Perera TD, Lu D, Thirumangalakudi L, Smith ELP, Yaretskiy A, Rosenblum LA, Kral JG, Coplan JD (2011b) Correlations between hippocampal neurogenesis and metabolic indices in adult nonhuman primates. *Neural Plast* 2011:1–6.
- Pesold C, Impagnatiello F, Pisu MG, Uzunov DP, Costa E, Guidotti A, Caruncho HJ (1998) Reelin is preferentially expressed in neurons synthesizing gamma-aminobutyric acid in cortex and hippocampus of adult rats. *PNAS* 95:3221–3226.
- Piatti VC, Davies-Sala MG, Espósito MS, Mongiat L a, Trincherro MF, Schinder AF (2011) The timing for neuronal maturation in the adult hippocampus is modulated by local network activity. *J Neurosci* 31:7715–7728.
- Piatti VC, Ewell LA, Leutgeb JK (2013) Neurogenesis in the dentate gyrus: carrying the message or dictating the tone. *Front Neurosci* 7:50.
- Pierce AA, Xu AW (2010) De novo neurogenesis in adult hypothalamus as a compensatory mechanism to regulate energy balance. *J Neurosci* 30:723–730.

References

- Piwonska M, Wilczek E, Szewczyk a., Wilczynski GM (2008) Differential distribution of Ca²⁺-activated potassium channel β 4 subunit in rat brain: Immunolocalization in neuronal mitochondria. *Neuroscience* 153:446–460.
- Platschek S, Cuntz H, Vuksic M, Deller T, Jedlicka P (2016) A general homeostatic principle following lesion induced dendritic remodeling. *Acta Neuropathol Commun* 4:19.
- Polsky A, Mel BW, Schiller J (2004) Computational subunits in thin dendrites of pyramidal cells. *Nat Neurosci* 7:621–627.
- Pozo K, Goda Y (2010) Unraveling mechanisms of homeostatic synaptic plasticity. *Neuron* 66:337–351.
- Preston AR, Eichenbaum H (2013) Interplay of Hippocampus and Prefrontal Cortex in Memory. *Curr Biol* 23:R764–R773.
- Radic T, Al-Qaisi O, Jungenitz T, Beining M, Schwarzacher SW (2015) Differential Structural Development of Adult-Born Septal Hippocampal Granule Cells in the Thy1-GFP Mouse, Nuclear Size as a New Index of Maturation. *PLoS One* 10:e0135493.
- Raineteau O, Rietschin L, Gradwohl G, Guillemot F, Gähwiler BH (2004) Neurogenesis in hippocampal slice cultures. *Mol Cell Neurosci* 26:241–250.
- Rall W (1959) Branching dendritic trees and motoneuron membrane resistivity. *Exp Neurol* 1:491–527.
- Rall W (1962) Electrophysiology of a Dendritic Neuron Model. *Biophys J* 2:145–167.
- Rall W, Segev I (1985) Space clamp problems when voltage clamping branched neuron with intracellular microelectrodes. In: *Voltage and Patch Clamping with Microelectrodes* (Smith T, Lecar H, Redman SJ, Gage P, eds), pp 191–215. Springer New York.
- Restivo L, Niibori Y, Mercaldo V, Josselyn SA, Frankland PW (2015) Development of Adult-Generated Cell Connectivity with Excitatory and Inhibitory Cell Populations in the Hippocampus. *J Neurosci* 35:10600–10612.
- Rettig J, Heinemann SH, Wunder F, Lorra C, Parcej DN, Dolly JO, Pongs O (1994) Inactivation properties of voltage-gated K⁺ channels altered by presence of beta-subunit. *Nature* 369:289–294.
- Reymann KG, Frey JU (2007) The late maintenance of hippocampal LTP: requirements, phases, “synaptic tagging”, “late-associativity” and implications. *Neuropharmacology* 52:24–40.

References

- Ribak CE, Shapiro L a (2007) Dendritic development of newly generated neurons in the adult brain. *Brain Res Rev* 55:390–394.
- Rolls ET (2007) An attractor network in the hippocampus: theory and neurophysiology. *Learn Mem* 14:714–731.
- Rumbaugh G, Prybylowski K, Wang JF, Vicini S (2000) Exon 5 and spermine regulate deactivation of NMDA receptor subtypes. *J Neurophysiol* 83:1300–1306.
- Sahay A, Hen R (2007) Adult hippocampal neurogenesis in depression. *Nat Neurosci* 10:1110–1115.
- Sanai N, Berger MS, Garcia-Verdugo JM, Alvarez-Buylla A (2007) Comment on “Human neuroblasts migrate to the olfactory bulb via a lateral ventricular extension”. *Science* (80-) 318:393; author reply 393.
- Sanai N, Nguyen T, Ihrie RA, Mirzadeh Z, Tsai H-H, Wong M, Gupta N, Berger MS, Huang E, Garcia-Verdugo J-M, Rowitch DH, Alvarez-Buylla A (2011) Corridors of migrating neurons in the human brain and their decline during infancy. *Nature* 478:382–386.
- Santhakumar V, Aradi I, Soltesz I (2005) Role of mossy fiber sprouting and mossy cell loss in hyperexcitability: a network model of the dentate gyrus incorporating cell types and axonal topography. *J Neurophysiol* 93:437–453.
- Scharfman HE, Myers CE (2012) Hilar mossy cells of the dentate gyrus: a historical perspective. *Front Neural Circuits* 6:106.
- Schmidt-Hieber C, Jonas P, Bischofberger J (2004) Enhanced synaptic plasticity in newly generated granule cells of the adult hippocampus. *Nature* 429:184–187.
- Schmidt-Hieber C, Jonas P, Bischofberger J (2007) Subthreshold dendritic signal processing and coincidence detection in dentate gyrus granule cells. *J Neurosci* 27:8430–8441.
- Schmidt B, Marrone DF, Markus EJ (2012) Disambiguating the similar: the dentate gyrus and pattern separation. *Behav Brain Res* 226:56–65.
- Scoville WB, Milner B (1957) Loss of recent memory after bilateral hippocampal lesions. *J Neurol Neurosurg Psychiatry* 20:11–21.
- Seri B, García-Verdugo JM, McEwen BS, Alvarez-Buylla A (2001) Astrocytes give rise to new neurons in the adult mammalian hippocampus. *J Neurosci* 21:7153–7160.

References

- Shapiro LA, Korn MJ, Shan Z, Ribak CE (2005) GFAP-expressing radial glia-like cell bodies are involved in a one-to-one relationship with doublecortin-immunolabeled newborn neurons in the adult dentate gyrus. *Brain Res* 1040:81–91.
- Shors TJ (2004) Memory traces of trace memories: neurogenesis, synaptogenesis and awareness. *Trends Neurosci* 27:250–256.
- Shors TJ, Miesegaes G, Beylin A, Zhao M, Rydel T, Gould E (2001) Neurogenesis in the adult is involved in the formation of trace memories. *Nature* 410:372–376.
- Shruti S, Urban-Ciecko J, Fitzpatrick JA, Brenner R, Bruchez MP, Barth AL (2012) The brain-specific Beta4 subunit downregulates BK channel cell surface expression. *PLoS One* 7:e33429.
- Sibbe M, Förster E, Basak O, Taylor V, Frotscher M (2009) Reelin and Notch1 cooperate in the development of the dentate gyrus. *J Neurosci* 29:8578–8585.
- Sidiropoulou K, Pissadaki EK, Poirazi P (2006) Inside the brain of a neuron. *EMBO Rep* 7:886–892.
- Smith-Hicks C, Xiao B, Deng R, Ji Y, Zhao X, Shepherd JD, Posern G, Kuhl D, Hugarir RL, Ginty DD, Worley PF, Linden DJ (2010) SRF binding to SRE 6.9 in the Arc promoter is essential for LTD in cultured Purkinje cells. *Nat Neurosci* 13:1082–1089.
- Snyder JS, Choe JS, Clifford MA, Jeurling SI, Hurley P, Brown A, Kamhi JF, Cameron HA (2009) Adult-born hippocampal neurons are more numerous, faster maturing, and more involved in behavior in rats than in mice. *J Neurosci* 29:14484–14495.
- Snyder JS, Ferrante SC, Cameron H a. (2012) Late Maturation of Adult-Born Neurons in the Temporal Dentate Gyrus Migaud M, ed. *PLoS One* 7:e48757.
- Soom M, Schönherr R, Kubo Y, Kirsch C, Klinger R, Heinemann SH (2001) Multiple PIP 2 binding sites in Kir2.1 inwardly rectifying potassium channels. *FEBS Lett* 490:49–53.
- Soulé J, Penke Z, Kanhema T, Alme MN, Laroche S, Bramham CR (2008) Object-place recognition learning triggers rapid induction of plasticity-related immediate early genes and synaptic proteins in the rat dentate gyrus. *Neural Plast* 2008:269097.
- Spalding KL, Bergmann O, Alkass K, Bernard S, Salehpour M, Huttner HB, Boström E, Westerlund I, Vial C, Buchholz BA, Possnert G, Mash DC, Druid H, Frisén J (2013) Dynamics of Hippocampal Neurogenesis in Adult Humans. *Cell* 153:1219–1227.
- Spalding KL, Bhardwaj RD, Buchholz BA, Druid H, Frisén J (2005) Retrospective birth dating of cells in humans. *Cell* 122:133–143.

References

- Spruston N, Johnston D (1992) Perforated patch-clamp analysis of the passive membrane properties of three classes of hippocampal neurons. *J Neurophysiol* 67:508–529.
- Staley KJ, Otis TS, Mody I (1992) Membrane properties of dentate gyrus granule cells: comparison of sharp microelectrode and whole-cell recordings. *J Neurophysiol* 67:1346–1358.
- Steward O (1976) Topographic organization of the projections from the entorhinal area to the hippocampal formation of the rat. *J Comp Neurol* 167:285–314.
- Steward O, Farris S, Pirbhoy PS, Darnell J, Driesche SJ Van (2015) Localization and local translation of Arc/Arg3.1 mRNA at synapses: some observations and paradoxes. *Front Mol Neurosci* 7:1–15.
- Steward O, Wallace CS, Lyford GL, Worley PF (1998) Synaptic activation causes the mRNA for the IEG Arc to localize selectively near activated postsynaptic sites on dendrites. *Neuron* 21:741–751.
- Stocca G, Schmidt-Hieber C, Bischofberger J (2008) Differential dendritic Ca²⁺ signalling in young and mature hippocampal granule cells. *J Physiol* 586:3795–3811.
- Stone SSD, Teixeira CM, Zaslavsky K, Wheeler AL, Martinez-Canabal A, Wang AH, Sakaguchi M, Lozano AM, Frankland PW (2011) Functional convergence of developmentally and adult-generated granule cells in dentate gyrus circuits supporting hippocampus-dependent memory. *Hippocampus* 21:1348–1362.
- Stoppini L, Buchs P a, Muller D (1991) A simple method for organotypic cultures of nervous tissue. *J Neurosci Meth* 37:173–182.
- Sun GJ, Sailor KA, Mahmood QA, Chavali N, Christian KM, Song H, Ming G (2013) Seamless reconstruction of intact adult-born neurons by serial end-block imaging reveals complex axonal guidance and development in the adult hippocampus. *J Neurosci* 33:11400–11411.
- Sutula T, Steward O (1987) Facilitation of kindling by prior induction of long-term potentiation in the perforant path. *Brain Res* 420:109–117.
- Taffe MA, Kotzebue RW, Crean RD, Crawford EF, Edwards S, Mandyam CD (2010) Long-lasting reduction in hippocampal neurogenesis by alcohol consumption in adolescent nonhuman primates. *PNAS* 107:11104–11109.
- Tanaka KZ, Pevzner A, Hamidi AB, Nakazawa Y, Graham J, Wiltgen BJ (2014) Cortical Representations Are Reinstated by the Hippocampus during Memory Retrieval. *Neuron* 84:347–354.

References

- Tang YP, Shimizu E, Dube GR, Rampon C, Kerchner GA, Zhuo M, Liu G, Tsien JZ (1999) Genetic enhancement of learning and memory in mice. *Nature* 401:63–69.
- Tavosanis G (2012) Dendritic structural plasticity. *Dev Neurobiol* 72:73–86.
- Teixeira CM, Kron MM, Masachs N, Zhang H, Lagace DC, Martinez A, Reillo I, Duan X, Bosch C, Pujadas L, Brunso L, Song H, Eisch AJ, Borrell V, Howell BW, Parent JM, Soriano E (2012) Cell-Autonomous Inactivation of the Reelin Pathway Impairs Adult Neurogenesis in the Hippocampus. *J Neurosci* 32:12051–12065.
- Tejada J, Arisi GM, García-Cairasco N, Roque AC (2012) Morphological alterations in newly born dentate gyrus granule cells that emerge after status epilepticus contribute to make them less excitable. Cymbalyuk G, ed. *PLoS One* 7:e40726.
- Tejada J, Roque AC (2014) Computational models of dentate gyrus with epilepsy-induced morphological alterations in granule cells. *Epilepsy Behav* 38:63–70.
- Temprana SG, Mongiat LA, Yang SM, Trincherro MF, Alvarez DD, Kropff E, Giacomini D, Beltramone N, Lanuza GM, Schinder AF (2015) Delayed coupling to feedback inhibition during a critical period for the integration of adult-born granule cells. *Neuron* 85:116–130.
- Thompson RF, Kim JJ (1996) Memory systems in the brain and localization of a memory. *PNAS* 93:13438–13444.
- Thomson W (1854) On the Theory of the Electric Telegraph. *Proc R Soc London* 7:382–399.
- Tonchev AB, Yamashima T (2006) Differential neurogenic potential of progenitor cells in dentate gyrus and CA1 sector of the postischemic adult monkey hippocampus. *Exp Neurol* 198:101–113.
- Tonchev AB, Yamashima T, Sawamoto K, Okano H (2005) Enhanced proliferation of progenitor cells in the subventricular zone and limited neuronal production in the striatum and neocortex of adult macaque monkeys after global cerebral ischemia. *J Neurosci Res* 81:776–788.
- Tonchev AB, Yamashima T, Zhao L, Okano HJ, Okano H (2003) Proliferation of neural and neuronal progenitors after global brain ischemia in young adult macaque monkeys. *Mol Cell Neurosci* 23:292–301.
- Toni N, Laplagne DA, Zhao C, Lombardi G, Ribak CE, Gage FH, Schinder AF (2008) Neurons born in the adult dentate gyrus form functional synapses with target cells. *Nat Neurosci* 11:901–907.

References

- Toni N, Sultan S (2011) Synapse formation on adult-born hippocampal neurons. *Eur J Neurosci* 33:1062–1068.
- Toni N, Teng EM, Bushong E a, Aimone JB, Zhao C, Consiglio A, van Praag H, Martone ME, Ellisman MH, Gage FH (2007) Synapse formation on neurons born in the adult hippocampus. *Nat Neurosci* 10:727–734.
- Tønnesen J, Katona G, Rózsa B, Nägerl UV (2014) Spine neck plasticity regulates compartmentalization of synapses. *Nat Neurosci* 17:678–685.
- Tronel S, Lemaire V, Charrier V, Montaron M-F, Abrous DN (2015) Influence of ontogenetic age on the role of dentate granule neurons. *Brain Struct Funct* 220:645–661.
- Turrigiano GG (2008) The Self-Tuning Neuron: Synaptic Scaling of Excitatory Synapses. *Cell* 135:422–435.
- Ueki T, Tanaka M, Yamashita K, Mikawa S, Qiu Z, Maragakis NJ, Hevner RF, Miura N, Sugimura H, Sato K (2003) A novel secretory factor, Neurogenesis-1, provides neurogenic environmental cues for neural stem cells in the adult hippocampus. *J Neurosci* 23:11732–11740.
- van Praag H, Christie BR, Sejnowski TJ, Gage FH (1999) Running enhances neurogenesis, learning, and long-term potentiation in mice. *PNAS* 96:13427–13431.
- van Praag H, Schinder AF, Christie BR, Toni N, Palmer TD, Gage FH (2002) Functional neurogenesis in the adult hippocampus. *Nature* 415:1030–1034.
- Velasco MGM, Levene MJ (2014) In vivo two-photon microscopy of the hippocampus using glass plugs. *Biomed Opt Express* 5:1700–1708.
- Vicini S, Wang JF, Li JH, Zhu WJ, Wang YH, Luo JH, Wolfe BB, Grayson DR (1998) Functional and pharmacological differences between recombinant N-methyl-D-aspartate receptors. *J Neurophysiol* 79:555–566.
- Vivar C, Potter MC, Choi J, Lee J, Stringer TP, Callaway EM, Gage FH, Suh H, van Praag H (2012) Monosynaptic inputs to new neurons in the dentate gyrus. *Nat Commun* 3:1107.
- Vlachos A, Korkotian E, Schonfeld E, Copanaki E, Deller T, Segal M (2009) Synaptopodin regulates plasticity of dendritic spines in hippocampal neurons. *J Neurosci* 29:1017–1033.
- Vuksic M, Del Turco D, Vlachos A, Schuldt G, Müller CM, Schneider G, Deller T (2011) Unilateral entorhinal denervation leads to long-lasting dendritic alterations of mouse hippocampal granule cells. *Exp Neurol* 230:176–185.

References

- Wang B, Jaffe DB, Brenner R (2014) Current understanding of iberiotoxin-resistant BK channels in the nervous system. *Front Physiol* 5:382.
- Waung MW, Pfeiffer BE, Nosyreva ED, Ronesi JA, Huber KM (2008) Rapid Translation of Arc/Arg3.1 Selectively Mediates mGluR-Dependent LTD through Persistent Increases in AMPAR Endocytosis Rate. *Neuron* 59:84–97.
- Wei B, Nie Y, Li X, Wang C, Ma T, Huang Z, Tian M, Sun C, Cai Y, You Y, Liu F, Yang Z (2011) Emx1-expressing neural stem cells in the subventricular zone give rise to new interneurons in the ischemic injured striatum. *Eur J Neurosci* 33:819–830.
- Weisz VI, Argibay PF (2009) A putative role for neurogenesis in neuro-computational terms: inferences from a hippocampal model. *Cognition* 112:229–240.
- Wiskott L, Rasch MJ, Kempermann G (2006) A functional hypothesis for adult hippocampal neurogenesis: avoidance of catastrophic interference in the dentate gyrus. *Hippocampus* 16:329–343.
- Wosiski-Kuhn M, Stranahan AM (2012) Transient increases in dendritic spine density contribute to dentate gyrus long-term potentiation. *Synapse* 664:661–664.
- Wynne PM, Puig SI, Martin GE, Treistman SN (2009) Compartmentalized beta subunit distribution determines characteristics and ethanol sensitivity of somatic, dendritic, and terminal large-conductance calcium-activated potassium channels in the rat central nervous system. *J Pharmacol Exp Ther* 329:978–986.
- Yang SM, Alvarez DD, Schinder AF (2015) Reliable genetic labeling of adult-born dentate granule cells using *Ascl1CreERT2* and *GlastCreERT2* murine lines. *J Neurosci* 35:15379–15390.
- Yeckel MF, Berger TW (1990) Feedforward excitation of the hippocampus by afferents from the entorhinal cortex: redefinition of the role of the trisynaptic pathway. *PNAS* 87:5832–5836.
- Yeung LC, Shouval HZ, Blais BS, Cooper LN (2004) Synaptic homeostasis and input selectivity follow from a calcium-dependent plasticity model. *PNAS* 101:14943–14948.
- Yoganarasimha D, Rao G, Knierim JJ (2011) Lateral entorhinal neurons are not spatially selective in cue-rich environments. *Hippocampus* 21:1363–1374.
- Yu D, Fan W, Wu P, Deng J, Liu J, Niu Y, Li M, Deng J (2014) Characterization of hippocampal Cajal-Retzius cells during development in a mouse model of Alzheimer's disease (Tg2576). *Neural Regen Res* 9:394.

References

- Yuan T-F, Arias-Carrión O (2011) Adult neurogenesis in the hypothalamus: evidence, functions, and implications. *CNS Neurol Disord Drug Targets* 10:433–439.
- Yuen GL, Durand D (1991) Reconstruction of hippocampal granule cell electrophysiology by computer simulation. *Neuroscience* 41:411–423.
- Yuste R, Bonhoeffer T (2001) Morphological changes in dendritic spines associated with long-term synaptic plasticity. *Annu Rev Neurosci* 24:1071–1089.
- Zhao C, Jou J, Wolff LJ, Sun H, Gage FH (2014) Spine morphogenesis in newborn granule cells is differentially regulated in the outer and middle molecular layers. *J Comp Neurol* 0:1–11.
- Zhao C, Teng EM, Summers RG, Ming G-L, Gage FH (2006) Distinct morphological stages of dentate granule neuron maturation in the adult mouse hippocampus. *J Neurosci* 26:3–11.
- Zhao S, Förster E, Chai X, Frotscher M (2003) Different signals control laminar specificity of commissural and entorhinal fibers to the dentate gyrus. *J Neurosci* 23:7351–7357.
- Zhou Q, Homma KJ, Poo MM (2004) Shrinkage of dendritic spines associated with long-term depression of hippocampal synapses. *Neuron* 44:749–757.

8. *Publications*

8.1. Publication 1

Erklärung über Anteile der Autoren an der Publikation

“Adult-born dentate granule cells show a critical period of dendritic reorganization and are distinct from developmentally born cells”

in print @ Brain structure and function

	Entwicklung und Planung	Durchführung der einzelnen Experimente	Erstellung der Datensammlung und Abbildungen	Analyse / Interpretation der Daten	Verfassen des Manuskripts
Beining, Marcel	15 %	55 % Virale Injektion Schnitte Immunfärbung 2-Photon Konfok. Mikrosk Bildverarbeitung Rekonstruktion *Morph. Modell	70 % Fig. 1C-D, Fig. 2, Fig. 3, Fig. 4, Fig. 5, Suppl. Fig. 1-3	60 % Analyseskripte für Rekonstr. Interpretation	40 %
Jungenitz, Tassilo	10 %	35 % Wie M.B., nur ohne * zusätzl. HFS mit Ableitung	30 % Fig. 1A-B, Fig. 6	20 % Interpretation	10 %
Radic, Tijana	5 %	10 % Schnitte Immunfärbung	-	-	5 %
Deller, Thomas	5 %	-	-	-	10 %
Cuntz, Hermann	20 %	-	-	5 % Interpretation	10 %
Jedlicka, Peter	15 %	-	-	5 % Interpretation	10 %
Schwarzacher, Stephan W.	30 %	-	-	10 % Interpretation	15 %

Zustimmende Best. der Angaben:

Datum/Ort

Datum/Ort

Unterschrift Promovend

Unterschrift Betreuer

Adult-born dentate granule cells show a critical period of dendritic reorganization and are distinct from developmentally born cells

Short title: Dendritic morphology of abGCs

Keywords: Arc, dentate gyrus, HFS, morphological model, neurogenesis

Authors:

Beining Marcel^{*,1,2,3}, Jungenitz Tassilo^{*,1}, Radic Tijana¹, Deller Thomas¹, Cuntz Hermann^{+,2,3}, Jedlicka Peter^{+,1}, Schwarzacher Stephan Wolfgang^{+,1}

¹Institute of Clinical Neuroanatomy, Goethe University Frankfurt/Main, D-60528 Germany

²Ernst Strüngmann Institute (ESI) for Neuroscience in Cooperation with Max Planck Society, Frankfurt/Main, D-60528 Germany

³Frankfurt Institute for Advanced Studies (FIAS), Frankfurt/Main, D-60438 Germany

* Joint-first authors, + Joint-last authors

Corresponding author:

Marcel Beining,
Ernst-Strüngmann-Institute (ESI) for Neuroscience
Deutschordenstr. 46
D-60528 Frankfurt am Main
E-Mail: beining@fias.uni-frankfurt.de

Abstract

Adult-born dentate granule cells (abGCs) exhibit a critical developmental phase during functional integration. The time window of this phase is debated and whether abGCs become indistinguishable from developmentally born mature granule cells (mGCs) is uncertain. We analyzed complete dendritic reconstructions from abGCs and mGCs using viral labeling. AbGCs from 21–77 days post intrahippocampal injection (dpi) exhibited comparable dendritic arbors, suggesting that structural maturation precedes functional integration. In contrast, significant structural differences were found compared to mGCs: AbGCs had more curved dendrites, more short terminal segments, a different branching pattern, and more proximal terminal branches. Morphological modeling attributed these differences to developmental dendritic pruning and postnatal growth of the dentate gyrus. We further correlated GC morphologies with the responsiveness to unilateral medial perforant path stimulation using the immediate-early-gene *Arc* as a marker of synaptic activation. Only abGCs at 28 and 35 dpi but neither old abGCs nor mGCs responded to stimulation with a remodeling of their dendritic arbor. Summarized, abGCs stay distinct from mGCs and their dendritic arbor can be shaped by afferent activity during a narrow critical time window.

Introduction

In the hippocampal dentate gyrus (DG), granule cells (GCs) are continuously born and integrated into the neural network (for recent reviews, see Bergmann et al., 2015; Kempermann, 2015). Studies suggest that adult-born granule cells (abGCs) are crucial for certain forms of hippocampus-dependent spatial learning, i.e. they facilitate pattern separation, whereas perinatally born matured granule cells (mGCs) facilitate pattern completion (Clelland et al., 2009; Nakashiba et al., 2012). Pattern separation might be promoted between 4–6 weeks after mitosis, when young abGCs exhibit distinct functional properties compared to mature abGCs or mGCs, such as less inhibitory input (Marín-Burgin et al., 2012; Temprana et al., 2014), high excitability (Mongiat et al., 2009), enhanced synaptic plasticity (Ge et al., 2007; Gu et al., 2012), preferential recruitment into spatial memory networks (Kee et al., 2007), specific connectivity (Restivo et al., 2015), and experience-dependent remodeling of connections (Bergami et al., 2015). This critical phase is also delineated on the synaptic level since spinogenesis increases gradually starting at week 3 (van Praag et al., 2002; Espósito et al., 2005; Zhao et al., 2006; Sun et al., 2013).

As abGCs are selectively recruited by the network (e.g. reviewed in Li and Pleasure, 2010), it is important to elucidate whether abGCs remain a functionally distinctive subgroup, or rather transiently provide new plastic neurons to a spatial memory circuit and converge with perinatally born mGCs thereafter. Evidence for convergence was found by comparing synaptic properties and firing behavior of abGCs and mGCs (Espósito et al., 2005; Laplagne et al., 2006) and by analyzing their functional integration during behavioral tasks (Stone et al., 2011). In contrast, it has been proposed that abGCs form a specialized population of GCs because they are more plastic and are recruited for distinct spatial tasks even when they have fully matured (Lemaire et al., 2012; Tronel et al., 2014). Adding another level of complexity, it was recently shown that abGCs divide into two functionally distinguishable populations with different input integration properties independent of cell age (Brunner et al., 2014), suggesting that abGCs might partly converge and partly stay distinct from mGCs.

Importantly, the existence of different GC populations has so far not been studied in detail at the structural level, even though the dendrites generate the basic frame defining amount and specificity of inputs (recently reviewed in Lefebvre et al., 2015), shaping input-output behavior (Mainen and Sejnowski, 1996), and performing local computations (reviewed in Sidiropoulou et al., 2006; Branco and Häusser, 2010), thus defining most functions of the neuron. Interestingly, in a recent *in vivo* study pruning of dendritic terminal segments was found in 3–4 week old mouse abGCs, a time point when most of the cell's specific input is defined (Gonçalves et al., 2016). Hence, abGCs may go through a critical time window during which dendrites are altered in response to afferent input (reviewed in Tavosanis, 2012), changing its functional fate. In this study, we analyzed the dendritic morphology of abGCs during and after network integration in order to elucidate 1) whether we can find differences in dendritic arborization between abGCs and mGCs that indicate different subpopulations, and 2) whether there is any evidence for a phase of dendritic reorganization in response to activation of specific afferents.

To address these questions we used bilateral retrovirus (RV) -mediated GFP expression to selectively label abGCs at different time points (van Praag et al., 2002) and an adeno-associated viral (AAV) GFP expression system to label mGCs (Kügler et al., 2001, 2003). Combining this approach with ipsilateral *in vivo* high-frequency stimulation of the medial perforant path yielded unstimulated and stimulated GC populations in the same brain which could be reconstructed and analyzed (240 in total). Our data reveal that the dendritic development of abGCs is essentially complete before functional integration. Furthermore, mature abGCs remained structurally distinct from perinatally born mGCs and thus form a distinct subgroup. Using a morphological computer model, we provided an ontogenetic explanation for the observed differences. Finally, we detected activity-dependent loss of short distal dendrites exclusively in young abGCs, providing new evidence for the existence of a critical phase during which activity can shape the dendritic arbor of abGCs.

Material and Methods

Animals

Young adult male Sprague-Dawley rats (8–13 weeks, 220–450 g; Charles River, Sulzfeld, Germany) were housed under standard laboratory conditions in large rat cages (30 cm x 40 cm). All animal experiments conformed to the German guidelines for the use of laboratory animals. A total of 24 animals (4 RV-21 dpi, 5 RV-28 dpi, 5 RV-35 dpi, 5 RV-77 dpi and 5 AAV, for details see Tab. 1) were used.

Retrovirus production

We used Calcium-Phosphate precipitation to co-transfect HEK293T cells with pCAG-GFP, pCMV-GP and pCMV-VSV-G (3:2:1) helper plasmids that together reconstitute the full viral vector (van Praag et al., 2002). Retrovirus-containing supernatant was collected 48 h after transfection. Supernatant was cleared from cell debris by centrifugation at 3200 x g for 10 min, filtered through a 0.22 µm filter, concentrated by ultra-centrifugation at 65000 x g for 2 h, and resuspended in 200 µl phosphate buffered saline (PBS). Viral titer was 10⁵ colony forming units. Aliquots were stored at -80 °C.

Adeno-associated virus production

We used Calcium-Phosphate precipitation to co-transfect HEK293T cells with pDP1rs, pDG and GFP-vector helper plasmids (6:4:1) necessary for reproduction of the full viral vector (Kügler et al., 2001, 2003). Transfected HEK293T cells were collected 48 h after transfection. Cells were washed twice by centrifugation at 1500 x g for 5 min and resuspended in PBS. Multiple freeze thaw cycles (4x) were applied to set free the viral particles inside the cells. The supernatant was washed by centrifugation at 10000 rpm for 10 min. Aliquots were stored at -80 °C.

Intra-hippocampal viral injection *in vivo*

Surgical procedures were performed under deep anesthesia (150 µg Medetomidin, 2 mg Midazolam, 5 µg Fentanyl per kg body weight i.m. initially, additional injections as needed). Rats were placed in a Kopf stereotaxic device (Kopf instruments, Tujunga, CA, U.S.A.) and two small holes (1.5–2.0 mm diameter) were drilled in the skull at -3.8 mm from Bregma and 2.2 mm laterally at both hemispheres. RV- or AAV-containing solution (0.75 µl per hemisphere) was slowly injected bilaterally within the dentate gyrus (DG, 3.2 mm and 3.7 mm below the brain surface) using a NanoFil syringe (World Precision Instruments, Inc., Sarasota, FL, U.S.A.) with a 35 gauge beveled needle (NF35BV-2; World Precision Instruments, Inc., Sarasota, FL, U.S.A.). Animals were perfused 14 days post injection (dpi) in the case of AAV and 21, 28, 35 or 77 dpi in the case of RV injection.

Perforant path stimulation

Animals were anesthetized with Urethane (1.25 g/kg body weight s. c. initially and additional injections as needed; 250 mg urethane/ml 0.9 % saline). Surgery and stimulation procedures were performed as previously described (Schwarzacher et al., 2006; Jedlicka et al., 2009, 2015; Jungenitz et al., 2014). In short, a bipolar stainless steel stimulating electrode was placed in the angular bundle of the medial perforant path (coordinates from lambda: L: 4.5 mm; AP: +0.5 mm; V: -3.5 mm). Glass microelectrodes (1.5 mm outer diameter, filled with 0.9 % saline) were placed in the dorsal blade of the granule cell layer (coordinates from bregma: L: 2.0 mm, AP: -3.5 mm, V: -3.5 mm). 2 hours of high frequency stimulation (HFS) were performed that maximally evoked population spikes and induced robust LTP on the stimulated hemisphere (see Fig. 6A, C; Steward et al., 1998; Jungenitz et al., 2014). In three control animals, we put an additional stimulation and recording electrode on the opposite, contralateral hemisphere in order to estimate the effects of HFS of the medial perforant path on the contralateral DG (Fig. 6C). Only the early slope component of the evoked field potential was measured to avoid contamination by the population spike. Rats were transcardially perfused with a fixative containing 4 % paraformaldehyde in 0.1 M PBS (PFA), pH 7.4 immediately after

stimulation was finished. F-actin (Fig. 6B) and Arc (Fig. 6D1/2) staining was used to further evaluate the selectivity of our medial perforant path stimulation and the LTP induction (Fukazawa et al., 2003; Jungenitz et al., 2014).

Tissue preparation

Brains were postfixed up to 18 h in 4 % PFA. Serial frontal sections of the hippocampus (300 μ m) were cut with a vibratome, washed in 0.1 M TRIS-buffered saline (TBS), and stored at -20 °C in cryoprotectant-solution (30 % ethylene glycol, 25 % glycerin in PBS).

Immunohistochemistry

300 μ m sections were washed in TBS, blocked with 5 % bovine serum albumin (BSA, 1 h, room temperature), and incubated with an anti-GFP488 (mouse, 1:500, fluorescence-labeled Alexa 488, Sigma) primary antibody for 5 d at 4 °C. To further increase the signal-to-noise ratio, a secondary fluorescence-labeled Alexa 488 antibody (1:1000, Vector Labs., Burlingame, CA, U.S.A.) was applied for 3 d at 4 °C.

Image acquisition

Imaging of GFP-labeled GCs on both hemispheres was done with a custom-built two photon microscope based on Sutter Instruments Movable Objective Microscope (Sutter Instruments, Novato, CA, U.S.A.) and a 20x water immersion objective (Olympus XLUMPlan FI, NA 0.95). The excitation source was a MaiTai HP Ti-sapphire mode-locked laser (Spectra-Physics, Darmstadt, Germany) tuned to a wavelength of 890 nm to excite GFP. ScanImage 3.8.1 (Pologruto et al., 2003) was used for image acquisition. Multiple image stack tiles were imaged to fully cover areas with GFP-labeled cells in the DG. The obtained image stacks were further processed using Matlab (MathWorks, Natick, MA, U.S.A.) and ImageJ (e.g. for contrast normalization) and subsequently stitched together using XuvStitch 1.8.0 in order to obtain an image stack of the complete DG area comprising all GFP-labeled cells (composite stack, see Fig. 1A, B).

Cell ID Assignment

In order to re-identify one cell in all images and sections, each cell located in the composite stack was assigned a unique cell ID marker in the cell's soma using ImageJ (National Institutes of Health). Cells were re-identified in the Arc-immunostained thin sections based on their location, morphology, and neighboring cells (reidentification success of > 85 %).

Dendritic reconstruction and post-processing

Reconstruction of complete GC dendritic trees was done with a customized version of the TREES Toolbox (Cuntz et al., 2010, 2011) in Matlab (MathWorks, Natick, MA, U.S.A.). Dendritic trees of the supra- and infrapyramidal blades and of the contra- (unstimulated) and ipsilateral (stimulated) hemispheres were reconstructed. Since dendritic morphologies of GCs can vary along the pyramidal blade, we attempted not to reconstruct cells at the hilar crest and to choose equal numbers of medially and laterally localized cells in order to obtain a general and unbiased picture of GC morphologies in the DG. We identified granule cells in the AAV-labeled population by their morphology and location of the cell body within the GCL. Furthermore, since GCs localized superficially within the GCL can be different to deeply localized cells (Green and Juraska, 1985; Claiborne et al., 1990), we did not reconstruct AAV-labeled GCs from the two most superficial cell layers (for further criteria, see Results). RV-labeled GCs were always localized near to the hilar GCL border (see Fig. S3C). Even though we used 300 μm thick sections dendrites of GFP-labeled GCs were occasionally cut off. Therefore, cells with dendrites cut off in the proximal region (inner molecular layer (IML) or below) or cells with generally too many incomplete dendrites were excluded from reconstruction. The resulting numbers of reconstructed complete dendritic trees are summarized in Tab. 1.

Reconstruction was done by tracing the cell's dendrites to their end point, thereby placing nodes along the current dendrite section in 3D. Dendrites cut by the slicing process at the top or bottom of the stack were marked in order to rate completeness of the reconstructed tree post hoc. After reconstruction, all trees were resampled to an internode distance of 1 μm . Dendritic diameter and soma

thickness was adjusted semi-automatically to fit the image counterpart, while ignoring the fluorescence halo around the branches of the tree. Dendritic completeness was rated by considering the amount and location of cut or faint dendrites.

For a layer-specific analysis of dendritic trees, the anatomical borders of the DG were reconstructed in each composite stack (see example in Fig. 1C) using a self-written program in Matlab (MathWorks, Natick, MA, U.S.A.). Borders between the outer, middle, and inner ML (OML, MML, and IML respectively) were automatically calculated by dividing the area between the fissure and the GCL into three equal parts. This rough estimation was chosen because of its simplicity and to make the reconstruction of a large number of GCs feasible. Immunostainings of the real molecular sublayers in rats (e.g. defining the IML with VGlut2, data not shown) confirmed this approximation. Nodes of all reconstructed trees were then automatically assigned to one of the following regions according to the layer contours: subgranular zone (SGZ), GCL, IML, MML, or OML (Fig. 1D).

Reslicing and immunohistochemistry in imaged tissue sections

In a subsequent step, the 300 μm frontal sections of the hippocampus were resliced to 50 μm frontal sections with a vibratome, and stored at $-20\text{ }^{\circ}\text{C}$ in cryoprotectant solution (see above). Resliced sections were washed in TBS and blocked with 5 % bovine serum albumin (BSA, 1 h, room temperature) to reduce non-specific staining. To stain for the immediate-early-gene Arc (activity-regulated cytoskeleton-associated protein) as a marker of synaptic activation (Lyford et al., 1995), free floating sections were incubated with anti-Arc (rabbit, polyclonal, 1:1000, Synaptic Systems, Ctl. 156002) primary antibody for 48 h at room temperature and secondary fluorescence-labeled Alexa 568 antibodies (1:1000, Vector Labs., Burlingame, CA, U.S.A.) for 24 h at room temperature.

Image acquisition of Arc-stained sections

For expression analysis of Arc, all GFP-labeled granule cells located on a resliced section (ipsilateral and contralateral) were imaged using a confocal microscope (Nikon Eclipse 80i) and a 40x oil immersion objective (N.A. 1.3).

The general Arc staining pattern confirmed complete stimulation on the ipsilateral side (Fig. 6B1) whereas the lack of Arc expression on the contralateral hemisphere confirmed the absence of stimulation (Fig. 6B2). However, it was hard to obtain sufficient numbers of 77 dpi Arc-negative abGCs because the percentage of Arc-positive cells is already very high at this age (Jungenitz et al., 2014). We also found no Arc-negative AAV-GFP-labeled mGC in all 5 animals examined indicating that mGCs are fully functionally integrated into the DG.

Morphological analysis

Calculation of morphological parameters was done with Matlab (MathWorks, Natick, MA, U.S.A.), TREES Toolbox (Cuntz et al., 2010, 2011) and self-written algorithms. Only dendritic trees with a rated completeness of more than 70 % were further analyzed. For visualization purposes and cone fitting, dendritic trees were rotated and aligned automatically using principal component analysis. In detail, the somata centers were aligned first, followed by rotating the dendritic centers of mass onto the x-axis. Finally, the tree was rotated around the x-axis to have the tree's maximum variation within the xy-plane. Dendritic parameters (e.g. number of branch and termination points, dendritic length, and branching angle) were additionally analyzed in each anatomical layer separately (see above for reconstruction and assignment of layers).

The soma thickness was directly taken from the diameter information of the soma reconstruction. The relative soma position (depth) within the GCL was calculated using the reconstructed anatomical borders of each DG, where 0 μm denotes the hilar GCL border and negative values denote somata located in the hilus. Similarly, the relative location of termination points was calculated with 0 % denoting the GCL-ML border and 100 % the hippocampal fissure. Terminal segments were assigned to the region where most of its length was located. Cut and thus incomplete segments were excluded from analysis. According to the terminal segment length histograms (Fig. S1) revealing two overlapping groups of segments with different average lengths, segments shorter than 100 μm were defined as short terminal segments (STS). Terminal segment length histograms were not tested for significant differences.

We assumed that the dendritic tree of GCs has a cone-like shape, which is in line with literature (Desmond and Levy, 1982; Amaral et al., 2007). To obtain the cone shape the tree's nodes were projected to the cone's base and the soma was defined as the cone end. Subsequently, a 2D Gaussian distribution was fitted to the projected nodes. The distance of 6σ (i.e. $\approx 99\%$ of all nodes were enclosed by the cone) then represented the major and minor axes of the cone's base, respectively.

The 3D convex hull volume of each tree was calculated using the qhull algorithm in Matlab. Spatial density was calculated by subsampling the fitted cone into voxels ($10\times 10\times 10\ \mu\text{m}^3$) and calculating the Euclidian distance to the nearest dendrite. Spatial density in μm^{-1} was the inverse of this distance averaged over all voxels in the cone. The curvature was calculated as the mean of the second derivative of the unit direction vectors along all dendrites of the tree.

We analyzed the morphological differences between the supra- and the infrapyramidal blade and found only marginal differences in the Sholl distribution and the thickness of the molecular layer while the number of branching and termination points, STS length, mean location of topological points, total dendritic length, convex hull volume, curvature, soma position, soma thickness, branching angle, spatial density and length of the cone axis remained unchanged (Fig. S2). Since the differences found were negligible and the cell numbers in each blade were similar, cells were pooled together.

Statistical analysis of dendritic morphology

Data management, statistical analysis and visualization were done with Matlab. To test for statistical significance, we used an unpaired, two-tailed Student's t test or one-way ANOVA (if more than two groups were compared) with Tukey's honestly significant difference criterion to correct for multiple comparisons. Since we reconstructed equal numbers of GCs in each animal of one group/condition (3-5) we assumed that between-animal variations average out in each group. Significance levels were set at $P < 0.05$ (*), $P < 0.01$ (**) and $P < 0.001$ (***). Group values are reported as means \pm SEM.

Morphological Modeling

The morphological models of abGCs and mGCs were developed in Matlab (MathWorks, Natick, MA, U.S.A.) using a customized version of the TREES toolbox (Cuntz et al., 2010). Synthetic granule cell dendrite morphologies were generated by connecting target points using a minimum spanning tree (MST) algorithm based on wiring optimization principles as described previously (Cuntz et al., 2007, 2010). For the mGC model, first a postnatal (i.e. small) cubic DG volume was defined comprising the hilar region and GCL with a thickness of 45 μm each, as well as the inner, middle and outer molecular layer (IML, MML, OML) with a thickness of 50 μm each. The total ML thickness was therefore 150 μm . A cone shape was created by using fixed transverse and longitudinal angles of 33° and 22° starting at the hilar GCL border and reaching to the fissure. Target points were distributed in a cone-shaped volume with a relative distribution of 0 : 20 : 80 % (IML : MML : OML) that approximated dendritic targets such as reelin-gradients mainly established by Cajal-Retzius cells in the postnatal DG (Alcántara et al., 1998; Pesold et al., 1998). GC growth is always directed, which means a dendrite growing to the right will never turn to reach a distant point to the left. In order to consider this directed growth, the random target points in IML, MML and OML were complemented by directed target points that were placed at random depths between the soma and clusters of random target points with a ratio of 60 % random to 40 % directed target points. All target points were subsequently connected by the MST algorithm satisfying two wiring costs: (1) the total amount of wiring should be minimal and (2) the path length from any target point to the soma should be minimal. (Cuntz et al., 2007) These two constraints were applied using a balancing factor of 0.9, which weighted the second cost against the first cost. Resampling to 1 μm internode distance and node jittering (two times with length constants 10 and 4 μm and standard deviations of 0.4 and 0.23 μm , respectively, but see function `jitter_tree` in TREES toolbox) was applied to mimic the curving of real dendrites during growth. At last, a soma was added. We then applied a pruning step that deleted all terminal segments smaller than an absolute threshold of 35 μm mimicking developmental pruning (Fig. 5A, purple dendrites). The resulting morphology represented mGCs in the young postnatal DG. To mimic the growth

of DG, the DG and the tree was then stretched in z by a factor of 1.8 to obtain a final adult ML thickness of 270 μm , which approximates the average of the DG thickness in our slices from young adult rat ($273.69 \pm 1.82 \mu\text{m}$, s.e.m., $n = 240$). Furthermore, both structures were also stretched in x and y by a factor of 2.25 and 2 to simulate DG expansion in the transverse and longitudinal direction. This resulted in the final mGC morphology. In contrast, abGCs grow in the adult DG. Hence, for the abGC model we stretched the DG volume first with the mentioned x, y and z factors before creating the cone volume and target points. The random target point distribution here was 25 : 20 : 55 % (IML : MML : OML) in order to mimic reduction of reelin-expressing cells in the adult OML (Alcántara et al., 1998; Pesold et al., 1998) and appearance of commissural axons as targets in the adult IML (Alcántara et al., 1998; Förster et al., 2006; Yu et al., 2014). The other parameters as well as the post-processing (resampling, jittering, adding soma and a pruning threshold of 35 μm) were exactly the same as for the mGC model. With this method 10 abGC and 16 mGC morphologies were created to correspond to the numbers of contralateral reconstructions of 77 dpi abGCs and AAV-labeled mGCs, which the models should mimic. The subsequent morphological analysis and comparison of synthetic abGC and mGC morphologies was done in the same way as with the real morphologies.

Results

We utilized a retroviral vector (RV) expressing GFP under the CAG promoter that enabled us to label abGCs at their time of birth (Fig. 1A; van Praag et al., 2002). Young adult rats (8-13 weeks) were perfused at different time points after injection (21, 28, 35, and 77 dpi) to obtain abGCs of different cell ages. In order to keep the same definitions as other studies on adult neurogenesis, we continue using the term ‘adult-born’ as we did before (Jungenitz et al., 2014), even though new GCs at that animal age might be also called ‘juvenile-born’, since a recent careful comparison between rat and human life cycles eventually defined the beginning of adulthood in rat at the age of 6 months (Sengupta, 2013). For a structural analysis of perinatally born mGCs, we injected an adeno-associated viral vector expressing GFP under the Synapsin1 promoter (referred to as AAV, Fig. 1B), that labels synaptically matured hippocampal neurons (Fornasiero et al., 2010) and is strongly expressed in dentate GCs (Kuroda et al., 2008). In the first analysis, we assessed normal structural maturation of abGCs; hence we focused on the non-activated, contralateral hemisphere. Labeled dendritic trees of RV-labeled abGCs (21–77 dpi) and AAV-labeled mGCs in the supra- and infrapyramidal blades were reconstructed in 3D with the freely available TREES toolbox (Cuntz et al., 2010, 2011). Completeness of the dendritic reconstruction was determined for each cell (see Material & Methods) and complete dendritic trees were analyzed with respect to the inner, middle, and outer molecular layer (IML, MML, OML) (Fig. 1C–E).

Structural maturation of dendritic trees is completed between the third and the fourth week of cell age in adult born granule cells

We looked for cellular and layer-specific morphological differences between all observed abGC cell ages (for exemplary reconstructions, see Fig. 2A&B). When analyzing the distribution of terminal segment lengths we found that segments could be divided in long and short terminal segments (STS), the latter being smaller than 100 μm (Fig. 2C inset and Fig. S1). We recognized that young abGCs (21 dpi) had many distal STS (Fig. 2A cyan segments), a phenotype associated with immature neurons (Emoto, 2011). Interestingly, these STS were

substantially reduced one week later (28 dpi) and remained in low numbers until 77 dpi (Fig. 2C). In contrast, the total number of termination points and particularly their relative distribution in the molecular layer stayed rather constant over all investigated time points (Fig. 2D). Even though we performed extensive computer-aided morphological analyses on total and layer-specific dendritic lengths, branch points and angles, curvature, Sholl distribution, cone axes lengths, hull volumes, and spatial density (Fig. 3 and Fig. S3), we did not find any other significant differences between abGCs of different ages, except a higher dendritic length in the IML at 35 dpi compared to 28 dpi ($607.3 \pm 52.7 \mu\text{m}$ at 21 dpi, $565.2 \pm 33.1 \mu\text{m}$ at 28 dpi, $724.1 \pm 33.8 \mu\text{m}$ at 35 dpi, $597.7 \pm 38.2 \mu\text{m}$ at 77 dpi, mean and s.e.m.; Fig. 3C). The latter finding might indicate some ongoing dendritic dynamics that decrease until 77 dpi. However, as this transient increase was limited to the IML and total dendritic length at 35 dpi was not significantly increased, dendritic growth appears to be very limited beyond 28 dpi. Together, these findings demonstrate that the structural maturation of dendritic trees is largely completed between the third and the fourth week of cell age and thus precedes the critical phase of functional maturation and synaptic integration which has been reported to occur from the 4th to the 6th week after cell birth (Ge et al., 2007; Mongiat et al., 2009; Marín-Burgin et al., 2012; Temprana et al., 2014; Bergami et al., 2015; Restivo et al., 2015, see also Introduction).

Aged adult-born GCs stay structurally distinct from perinatally born GCs

Next we analyzed whether mature abGCs converge structurally to the same cell population as perinatally born mGCs or whether they form a distinct subpopulation even after the critical phase of integration has ended. As abGCs appeared to be structurally fully mature from 4 weeks on (see previous section), we could be confident that the reconstructed old (77 dpi) RV-labeled abGCs represent old matured abGCs, and thus could be compared with AAV-labeled mGCs (Typical morphologies are shown in Fig. 4 A and I). AAV-labeled GCs were identified by their characteristic GC morphology and the location of the soma within the GCL. Due to the outside-in layering of the DG, the

embryonically and perinatally born GCs occupy the upper parts of the GCL, whereas younger adult-born GCs are located near the SGZ (Muramatsu et al., 2007; Mathews et al., 2010; Radic et al., 2015). Hence, in order to increase the likelihood of selecting perinatally born mGCs we avoided the reconstruction of AAV-labeled GCs with somata located near the SGZ (Fig. 1B2&3). We also did not reconstruct superficial GCs as they are known to have several morphological differences compared to GCs located in deep layers (Claiborne et al., 1990). Using these restrictions and, due to the much higher incidence of perinatally born mGCs in comparison to mature abGCs (Mathews et al., 2010), we assumed that the vast majority of AAV-labeled reconstructed mGCs were indeed generated perinatally.

The most prominent difference between abGCs and AAV-labeled mGCs was that nearly all dendrites of the latter ended in the OML, consistent with literature (Desmond and Levy, 1982), whereas in abGCs, a subset of dendrites terminated in the proximal layers (Fig. 4B–D). Interestingly, we also found much less STS in AAV-labeled mGCs compared to abGCs (Fig. 4E, AAV: $32.14 \pm 15.90 \mu\text{m}$ vs. 77 dpi: $116.40 \pm 30.80 \mu\text{m}$ summed length STS, $p < 0.05$). Furthermore, AAV-labeled mGCs exhibited less curved dendrites (Fig. 4F and Fig. S4E) and had a different arborization pattern with more branch points in the MML and less in the IML and the OML (Fig. 4G). However, the total and layer-specific dendritic lengths were similar in mGCs and abGCs ($p > 0.05$, Fig. 4H), indicating that the higher curvature and more proximal branch points in abGCs might compensate for the more proximally terminating dendrites. Summarized, these results show that mature abGCs form a subpopulation structurally distinct from mGCs.

A morphological model accounts for structural differences between abGCs and mGCs

To explain the observed structural differences between abGCs and mGCs, we utilized a morphological model based on optimal wiring principles (Cuntz et al., 2007, 2008, 2010; Schneider et al., 2014). The morphological model uses the minimum spanning tree (MST) algorithm which generates realistic dendritic morphologies by connecting target points in space while minimizing total

dendrite length and conduction times in the dendritic tree (Cuntz et al., 2010). Fig. 5A shows our hypothesis which is based on the observation that the DG changes in size and composition during development. Perinatally born mGCs developed in the young DG which has a much thinner GCL and ML than the matured DG (Rihn and Claiborne, 1990). Furthermore, during development, the area close to the hippocampal fissure contains numerous Cajal-Retzius cells (Fig. 5A, upper left tree) that express reelin, a protein that plays a crucial role in guiding dendritic arborization of GCs in the DG (Förster et al., 2006; Frotscher, 2010; D’Arcangelo, 2014). Accordingly, for synthetic perinatally born mGCs we distributed target points for the MST algorithm mainly within the OML and within a volume that corresponds to the smaller dimensions of a young DG. A pruning step with an absolute threshold to mimic maturational dendrite pruning (Schuldiner and Yaron, 2014) was applied subsequently (Fig. 5A, purple dendrites). During and after maturation of perinatally born GCs, the dendritic tree becomes significantly stretched since the ML broadens massively between birth and adulthood (about 275 % from P4 to P60) due to the ingrowth of afferent fibers and GC dendrites (Loy et al., 1977; Claiborne et al., 1990; Rihn and Claiborne, 1990). To mimic this process, we stretched the developmentally grown dendritic trees of mGCs to the size of the adult DG (Fig. 5A, upper half).

In contrast to mGCs, abGCs grow within the already mature adult DG (lower left tree in Fig. 5A). Accordingly, to model abGCs, we distributed the target points in a DG of adult size. Furthermore, in the adult DG, reelin-expressing cells in the OML are drastically reduced (Alcántara et al., 1998; Pesold et al., 1998), whereas commissural axons have populated the IML (Alcántara et al., 1998; Förster et al., 2006; Yu et al., 2014). Therefore, in our model, target points were reduced in the OML and increased in the IML while keeping all other parameters and steps the same. Surprisingly, implementing these two differences was sufficient to produce realistic morphologies (Fig. 5B) and to reproduce the observed morphological differences and analogies of 77 dpi abGCs and AAV-labeled mGCs in almost all parameters and layers (Fig. 5C–H). In conclusion, morphological modeling suggests that the structural differences found between abGCs and mGCs originate from their particular

environmental constraints during growth and maturation within the adult or perinatal DG.

Young adult-born GCs exhibit a critical phase of dendritic reorganization following HFS

Using Arc (activity-regulated cytoskeleton-associated protein) as a marker of synaptic activation (Lyford et al., 1995; Jungenitz et al., 2014), we were interested whether we can find activity-related structural differences in abGCs (21–77 dpi) or mGCs in the ipsi- compared to the contralateral hemisphere. Two hour unilateral HFS (scheme as inset in Fig. 6A) of the medial perforant path induced strong LTP only in ipsilateral GCs, indicated by bilateral local field potential recordings and subsequent F-actin staining (Fig. 6A–C). We further found a strong Arc-expression in more than 90 % of all GCs that was restricted to the ipsilateral GCL (Fig. 6D) consistent with literature (Steward et al., 1998; Jungenitz et al., 2014). Notably, we were unable to detect ipsilateral Arc-expression in RV-labeled abGCs at 21 dpi (n=4 animals). This was expected because in our prior BrdU-study with identical stimulation conditions, the number of ipsilateral Arc-positive abGCs (21 dpi) after HFS was less than 10 % (Jungenitz et al., 2014). Thus, this group was excluded from comparison. At all other time-points, Arc-negative and Arc-positive RV- or AAV-labeled GCs on the ipsilateral side (see exemplary 35 dpi morphologies in Fig. 6E) were compared with RV- or AAV-labeled GCs on the contralateral side which served as the non-activated control. We found structural differences in ipsilateral Arc-positive abGCs at 28 and 35 dpi that proved to be a significant reduction of STS exclusively in the OML (Fig. 6F–H). This was not observed in Arc-negative abGCs of the same age (Fig. 6F–H), suggesting that Arc-negative ipsilateral GCs indeed had not been sufficiently activated during HFS. Importantly, old abGCs (77 dpi) and mGCs showed no stimulation- or Arc-correlated differences in STS length (Fig. 6F–H), thus revealing a critical time window for activity-induced dendritic reorganization at 28-35 dpi (Fig. 6I).

Discussion

Here we present a detailed structural study of young and old abGCs, as well as mGCs, based on complete 3D-reconstructions of RV-GFP- or AAV-GFP-labeled dendritic trees. Our analysis provides four major findings: First, dendritic maturation of abGCs is essentially complete by three weeks after birth. Second, abGCs form a subgroup that stays structurally distinct from mGCs even when fully matured (77 dpi). Third, the structural differences between abGCs and mGCs can be accounted for by different developmental conditions in the perinatal and adult dentate gyrus (DG), as indicated by our morphological model. Fourth, only young abGCs (28–35 dpi) but neither old abGCs nor mGCs responded to high-frequency perforant path stimulation (HFS) with a reduction of short distal dendrites. In sum, we conclude that abGCs stay distinct from mGCs and that their dendritic arbor can be shaped by afferent activity during a narrow critical phase/time window.

Complete reconstructions of abGCs and mGCs

As recently reviewed, detailed knowledge of the dendritic morphology of abGCs would be important for the understanding, prevention, and treatment of neuropathological alterations that emerge in conjunction with impaired adult hippocampal neurogenesis (Llorens-Martín et al., 2016). To our knowledge, this is the first report of 3D-reconstructed complete dendritic trees of rat abGCs. In earlier studies, rat abGCs had been reconstructed in 2D using flattened z-stacks of 40–50 μm thick slices (Rosenzweig and Wojtowicz, 2011; Teixeira et al., 2012; Lee et al., 2015). In our study the average total dendritic length of all reconstructed GCs was $2255 \pm 45 \mu\text{m}$ supra- and $2137 \pm 49 \mu\text{m}$ infrapyramidally (SupplFig. 2C, AAV-labeled mGCs only: $2347 \pm 120 \mu\text{m}$ and $2437 \pm 172 \mu\text{m}$, mean + s.e.m.). Using iontophoretic HRP-filling of GCs in adult rat hippocampal slices, Clairbone et al. (1990) reported a considerably higher total dendritic length of $3,478 \pm 88 \mu\text{m}$ and $2,793 \pm 74 \mu\text{m}$, respectively. Furthermore, when we compared the publicly available GCs (Rihn and Claiborne, 1990) to our AAV-labeled mGCs we found our GCs to have a lower number of branch points (*data not shown*). However, results from St John (1997) using biocytin-fillings of

hippocampal GCs in adult rats, were comparable to our data. Interestingly, they also found a tissue swelling of 35 % by the glycerol clearing step used by many former studies which might explain the reported higher dendritic lengths (Desmond and Levy, 1982; Claiborne et al., 1990; Rihn and Claiborne, 1990). A further explanation for discrepancies between different studies might be that GCs from the middle third (i.e. 30 to 70 % along HC) of the septotemporal axis were reconstructed in these studies, whereas we used only slices from the septal HC (i.e. 20 to 40 % along HC). It would be interesting to analyze if GCs generally become larger from septal to temporal HC.

Structural maturation of abGCs precedes the critical phase of functional integration

We found that maturation of the dendritic tree is largely completed at 21 dpi in RV-labeled rat abGCs, followed by only marginal structural changes identified as a reduction in number of short terminal segments (STS) between 21 and 28 dpi, and a transient increase of dendritic length that is restricted to week 5 (35 dpi) and to the IML. The end of major structural changes in abGCs at 4 weeks of age has also been shown in mouse (Zhao et al., 2006; Sun et al., 2013) arguing for a similar rate of maturation in mouse and rat. Interestingly, the reduction of STS in our study falls into the same phase when young mouse abGCs showed growth and pruning of terminal segments in a recent *in vivo* study (Gonçalves et al., 2016), suggesting similar dynamic processes in both species. Furthermore, in postnatal rat GCs, rapid dendritic growth followed by a reduction in distal primarily small segments was reported, arguing for a general intrinsic process in developing GCs (Rihn and Claiborne, 1990; Rahimi and Claiborne, 2007).

The critical phase of functional integration in abGCs has been determined to occur between the 4th and 6th week in mice (Ge et al., 2007; Mongiat et al., 2009; Restivo et al., 2015) which suggests that structural maturation of abGCs follows an endogenous program and might be mostly independent of specific functional synaptic input.

Structurally distinct populations of GCs in the dentate gyrus

Whether abGCs exhibit different functions as mGCs is currently a subject of strong debate. Whereas many studies indicate that after the critical time window, old abGCs and mGCs are functionally indistinguishable (Espósito et al., 2005; Laplagne et al., 2006; Nakashiba et al., 2012), others show that old abGCs still exert structural plasticity upon learning and are recruited during different learning tasks than mGCs (Lemaire et al., 2012; Tronel et al., 2014). However, until now, the structural divergence of old abGCs and old mGCs has not been analyzed in detail. Total dendritic length and number of branch points were reported to be similar (Vuksic et al., 2008; Sun et al., 2013) but postnatal GCs initially show multipolar morphologies compared to uni- or bipolar dendritic trees in immature abGCs (reviewed in Ribak and Shapiro, 2007). In the current study, we extended this knowledge and observed that abGCs have more dendrites ending in proximal regions, a higher amount of STS, and a higher curvature than mGCs. We proposed a morphological model explaining these differences by a stagnating growth of the ML, combined with a change of dendritic targets (a lower reelin-gradient, and more ingrown axonal fibers) of the adult compared to the postnatal DG. Similar to our model, pruning might occur prior to tissue growth in real perinatally born GCs, too, as they seem to maintain their total dendritic length despite massive DG expansion (Rihn and Claiborne, 1990), meaning that dendrites, most probably the shortest ones, must undergo pruning. However, another plausible explanation could be competition and space restriction: mGCs grow in a nearly unoccupied ML but subsequently lose their shorter branches to vacate space for newly ingrowing dendrites of abGCs, whereas the latter would not be able to fully extend their dendrites to the OML due to occupied space and only few free synaptic targets.

To estimate the functional impact of the structural disparities of abGCs and mGCs, combining both morphologies with a detailed biophysical model would be the next straight-forward step.

A novel form of dendritic reorganization in abGCs during the critical phase of synaptic integration

Following HFS of the medial perforant path, we found a reduction of distal STS exclusively in young abGCs (28–35 dpi) that responded with Arc expression (Fig. 6H). Notably, this cell age coincides with the steepest increase in HFS-induced Arc-positive cell numbers found in our earlier BrdU study (Jungenitz et al., 2014). Dendritic alterations following *in vivo* stimulation had been reported previously in neocortical layers 3 and 5 (Ivanco et al., 2000; Monfils and Teskey, 2004; Teskey et al., 2006), however this is the first report of activity-induced dendritic reorganization in the DG. Since short dendrites are often related to immature morphologies (Emoto, 2011), our observation could suggest that one population of abGCs was more mature than their Arc-negative counterparts and were therefore capable to exhibit IEG responsiveness. We argue that our findings rather indicate an activity-induced and Arc-correlated dendritic reorganization due to two reasons. First, whereas in mGCs the vast majority of STS was observed in the OML (Fig. 4E), this layer was nearly void of STS in Arc-positive young abGCs following HFS (Fig. 6E, H), indicating that the reduced STS cannot originate from intrinsic developmental pruning as in mGCs. Second, old abGCs (77 dpi) showed Arc expression without reduced STS, arguing against decreased STS being an indicator for maturity in abGCs. Interestingly, a recent *in vivo* time-lapse study reported accelerated pruning of young abGC dendrites in mice exposed to an enriched environment (Gonçalves et al., 2016) supporting the idea of young abGCs being amenable to activity-induced dendritic reorganization (illustrated in Fig. 6I).

We chose a study design where GCs of the contralateral unstimulated hemisphere served as the non-activated control in each animal which offers the advantage of direct comparison of stimulated and unstimulated cells within the same animal. However, contralateral GCs receive limited ipsilateral input via commissural entorhinal cortex or mossy cells axons. On the other side, the crossed temporo-dentate pathway from the ipsilateral entorhinal cortex to the contralateral DG was shown to be unable to evoke LTP under normal conditions (Wilson et al., 1979; Wilson, 1981; Reeves and Steward, 1986), To exclude

significant activation via commissural pathways, we performed contralateral LFP recordings during ipsilateral HFS and found no contralateral induction of LTP at the electrophysiological level or with the LTP marker F-actin (Fig. 6B, C). Furthermore, immediate-early-gene markers such as Arc (Fig. 6D), c-fos and zif-268 were expressed solely in the ipsilateral DG following HFS (Jungenitz et al., 2014) arguing against significant activation of the contralateral control GCs, that could lead to structural changes. In line with this, a recent study showed that activation of the hilar commissural pathway resulted in increased inhibition in contralateral GCs compared to increased excitation with perforant path stimulation from the same hemisphere (Hsu et al., 2015).

We used Arc to label GCs that had been synaptically activated during HFS. Could Arc also be mechanistically involved in the loss of STS in young abGCs? Arc had been shown to be involved in synaptic plasticity (reviewed in Bramham et al., 2010) and particularly in heterosynaptic LTD with a reduction of big mushroom, and formation of thin instable spines in unstimulated layers (Waung et al., 2008; Peebles et al., 2010; Okuno et al., 2012). Thus, one could speculate that destabilization of spines might lead to destabilization of the occupied dendrite, since dendritic and spine stability are tightly correlated (reviewed in Koleske, 2013). Spinogenesis in abGCs is starting during week 3 (van Praag et al., 2002; Espósito et al., 2005; Zhao et al., 2006; Ohkawa et al., 2012; Sun et al., 2013), thus dendrites in young abGCs, especially short ones, might be less stable and more amenable to reorganization, explaining the observed time window of 28–35 dpi (Fig. 6H). Interestingly, we previously showed that after entorhinal cortex lesion GCs not only lose spines but also dendrites located in denervated layers (Vuksic et al., 2011), suggesting that even old GCs show dendritic reorganization when a critical number of spines is lost.

What might be the functional consequence of such subtle changes as the loss of short distal dendrites in abGCs, whether developmentally- or activity-driven? Generally, dendritic morphology can substantially influence a neuron's information processing and excitability (Rall and Rinzel, 1973). Numerous studies have examined genetic deletions of key proteins and found aberrant

dendritic morphology together with substantial alterations of neuronal excitability (Duan et al., 2007; Fitzsimons et al., 2012; Šišková et al., 2014; Norkett et al., 2016). However, reduction in total dendritic length in our study was limited to ~5%, which would result in very limited changes of input resistance, and thus excitability. Alternatively, reduction of distal STS might help abGCs in their suggested role in pattern separation (Myers and Scharfman, 2011; Nakashiba et al., 2012; Deng et al., 2013; Johnston et al., 2015): When GCs prune dendritic segments in the OML, they receive less contextual input from the lateral entorhinal cortex and thereby might sharpen the group of context features that they are responding to, which is a key requirement for pattern separation. However, even though granule cells are electrotonically compact neurons and signal propagation from somata to dendrites is quite fast and efficient (Schmidt-Hieber et al., 2007), the impact of single synaptic inputs (that would be reduced distally through loss of short dendrites) was reported to be rather weak (Krueppel et al., 2011). Hence, further investigations are necessary to elucidate the putative functional impact of reduced short distal dendrites.

Conflict of interests

The authors declare that they have no conflict of interest.

Author contributions

HC, TD, PJ and SWS designed the study; MB, TJ, HC, PJ and SWS developed the methodology; MB, TJ and TR collected the data and performed the analysis; and MB, HC, TD, TJ, PJ, TR and SWS wrote the manuscript.

Data availability

Our reconstructions of dendritic morphologies will be made available on the widely-used NeuroMorpho data base (Ascoli et al., 2007).

Acknowledgement

This work was supported by the LOEWE-Program “Neuronal Coordination Research Focus Frankfurt” (NeFF), by the German Science Foundation (CRC 1180), by the Federal Ministry of Education and Research (BMBF, to PJ, No. 01GQ1203A), by a Young Investigators Grant (from the faculty of medicine Goethe-University to PJ), and by a BMBF grant (No. 01GQ1406 – Bernstein Award 2013) to HC. MB was further supported by the International Max Planck Research School (IMPRS) for Neural Circuits in Frankfurt. We thank Torsten Felske for help with GC reconstruction. We are indebted to Ute Fertig for technical assistance in preparing and staining of hippocampal slices. The authors declare no competing financial interests.

References

Alcántara S, Ruiz M, Arcangelo GD, Ezan F, Lecea L De, Curran T, Sotelo C, Soriano E (1998) Regional and cellular patterns of reelin mRNA expression in the forebrain of the developing and adult mouse. *J Neurosci* 18:7779–7799.

Amaral D, Scharfman H, Lavenex P (2007) The dentate gyrus: fundamental neuroanatomical organization (dentate gyrus for dummies). *Prog Brain Res* 153:390–394.

Ascoli G a., Donohue DE, Halavi M (2007) NeuroMorpho.Org: A Central Resource for Neuronal Morphologies. *J Neurosci* 27:9247–9251.

Bergami M, Masserdotti G, Temprana SG, Motori E, Eriksson TM, Göbel J, Yang SM, Conzelmann KK, Schinder AF, Götz M, Berninger B (2015) A critical period for experience-dependent remodeling of adult-born neuron connectivity. *Neuron* 85:710–717.

Bergmann O, Spalding KL, Frisén J (2015) Adult Neurogenesis in Humans. *Cold Spring Harb Perspect Biol* 7:1–12.

Bramham CR, Alme MN, Bittins M, Kuipers SD, Nair RR, Pai B, Panja D, Schubert M, Soule J, Tiron A, Wibrand K (2010) The Arc of synaptic memory. *Exp Brain Res* 200:125–140.

Branco T, Häusser M (2010) The single dendritic branch as a fundamental functional unit in the nervous system. *Curr Opin Neurobiol* 20:494–502.

Brunner J, Neubrandt M, Van-Weert S, András T, Kleine Borgmann FB, Jessberger S, Szabadics J (2014) Adult-born granule cells mature through two functionally distinct states. *Elife*:e03104.

Claiborne BJ, Amaral DG, Cowan WM (1990) Quantitative, three-dimensional analysis of granule cell dendrites in the rat dentate gyrus. *J Comp Neurol* 302:206–219.

Clelland CD, Choi M, Romberg C, Clemenson GD, Fagniere A, Tyers P, Jessberger S, Saksida LM, Barker R a, Gage FH, Bussey TJ (2009) A functional role for adult hippocampal neurogenesis in spatial pattern separation. *Science* (80-) 325:210–213.

Cuntz H, Borst A, Segev I (2007) Optimization principles of dendritic structure. *Theor Biol Med Model* 4:21.

Cuntz H, Forstner F, Borst A, Häusser M (2010) One rule to grow them all: a general theory of neuronal branching and its practical application. *PLoS Comput Biol* 6.

Cuntz H, Forstner F, Borst A, Häusser M (2011) The TREES Toolbox — Probing the Basis of Axonal and Dendritic Branching. *Neuroinformatics* 9:91–96.

Cuntz H, Forstner F, Haag J, Borst A (2008) The morphological identity of insect dendrites. *PLoS Comput Biol* 4:e1000251.

D’Arcangelo G (2014) Reelin in the Years: Controlling Neuronal Migration and Maturation in the Mammalian Brain. *Adv Neurosci* 2014:1–19.

Deng W, Mayford M, Gage FH (2013) Selection of distinct populations of dentate granule cells in response to inputs as a mechanism for pattern separation in mice. *Elife* 2:e00312.

Desmond NL, Levy WB (1982) A quantitative anatomical study of the granule cell dendritic fields of the rat dentate gyrus using a novel probabilistic method. *J Comp Neurol* 212:131–145.

Duan X, Chang JH, Ge S, Faulkner RL, Kim JY, Kitabatake Y, Liu X bo, Yang CH, Jordan JD, Ma DK, Liu CY, Ganesan S, Cheng HJ, Ming G li, Lu B, Song H (2007) Disrupted-In-Schizophrenia 1 Regulates Integration of Newly Generated Neurons in the Adult Brain. *Cell* 130:1146–1158.

Emoto K (2011) Dendrite remodeling in development and disease. *Dev Growth Differ* 53:277–286.

Espósito MS, Piatti VC, Laplagne DA, Morgenstern NA, Ferrari CC, Pitossi FJ, Schinder AF (2005) Neuronal differentiation in the adult hippocampus recapitulates embryonic development. *J Neurosci* 25:10074–10086.

Fitzsimons CP, van Hooijdonk LW a, Schouten M, Zalachoras I, Brinks V, Zheng T, Schouten TG, Saaltink DJ, Dijkmans T, Steindler D a, Verhaagen J, Verbeek FJ, Lucassen PJ, de Kloet ER, Meijer OC, Karst H, Joels M, Oitzl MS, Vreugdenhil E (2012) Knockdown of the glucocorticoid receptor alters functional integration of newborn neurons in the adult hippocampus and impairs fear-motivated behavior. *Mol Psychiatry* 18:993–1005.

Fornasiero EF, Bonanomi D, Benfenati F, Valtorta F (2010) The role of synapsins in neuronal development. *Cell Mol Life Sci* 67:1383–1396.

Förster E, Zhao S, Frotscher M (2006) Laminating the hippocampus. *Nat Rev Neurosci* 7:259–267.

Frotscher M (2010) Role for Reelin in stabilizing cortical architecture. *Trends Neurosci* 33:407–414.

Fukazawa Y, Saitoh Y, Ozawa F, Ohta Y, Mizuno K, Inokuchi K (2003) Hippocampal LTP is accompanied by enhanced F-actin content within the dendritic spine that is essential for late LTP maintenance in vivo. *Neuron* 38:447–460.

Ge S, Yang C-H, Hsu K-S, Ming G-L, Song H (2007) A critical period for enhanced synaptic plasticity in newly generated neurons of the adult brain. *Neuron* 54:559–566.

Gonçalves JT, Bloyd CW, Shtrahman M, Johnston ST, Schafer ST, Parylak SL, Tran T, Chang T, Gage FH (2016) In vivo imaging of dendritic pruning in dentate granule cells. *Nat Neurosci*:5–10.

Green EJ, Juraska JM (1985) The dendritic morphology of hippocampal dentate granule cells varies with their position in the granule cell layer: a quantitative Golgi study. *Exp Brain Res* 59:582–586.

Gu Y, Arruda-Carvalho M, Wang J, Janoschka SR, Josselyn SA, Frankland PW, Ge S (2012) Optical controlling reveals time-dependent roles for adult-born dentate granule cells. *Nat Neurosci* 15:1700–1706.

Hsu T-T, Lee C-T, Tai M-H, Lien C-C (2015) Differential Recruitment of Dentate Gyrus Interneuron Types by Commissural Versus Perforant Pathways. *Cereb Cortex*:bhv127 – .

Ivanco TL, Racine RJ, Kolb B (2000) Morphology of layer III pyramidal neurons is altered following induction of LTP in sensorimotor cortex of the freely moving rat. *Synapse* 37:16–22.

Jedlicka P, Schwarzacher SW, Winkels R, Kienzler F, Frotscher M, Bramham CR, Schultz C, Bas Orth C, Deller T (2009) Impairment of in vivo theta-burst long-term potentiation and network excitability in the dentate gyrus of synaptopodin-deficient mice lacking the spine apparatus and the cisternal organelle. *Hippocampus* 19:130–140.

Jedlicka P, Vnencak M, Krueger DD, Jungenitz T, Brose N, Schwarzacher SW (2015) Neuroligin-1 regulates excitatory synaptic transmission, LTP and EPSP-spike coupling in the dentate gyrus in vivo. *Brain Struct Funct* 220:47–58.

Johnston ST, Shtrahman M, Parylak S, Gonçalves JT, Gage FH (2015) Paradox of Pattern Separation and Adult Neurogenesis: A Dual Role for New Neurons Balancing Memory Resolution and Robustness. *Neurobiol Learn Mem*.

Jungenitz T, Radic T, Jedlicka P, Schwarzacher SW (2014) High-frequency stimulation induces gradual immediate early gene expression in maturing adult-generated hippocampal granule cells. *Cereb Cortex* 24:1845–1857.

Kee N, Teixeira CM, Wang AH, Frankland PW (2007) Preferential incorporation of adult-generated granule cells into spatial memory networks in the dentate gyrus. *Nat Neurosci* 10:355–362.

Kempermann G (2015) Activity Dependency and Aging in the Regulation of Adult Neurogenesis. *Cold Spring Harb Perspect Biol* 7:a018929.

Koleske AJ (2013) Molecular mechanisms of dendrite stability. *Nat Rev Neurosci* 14:536–550.

Krueppel R, Remy S, Beck H (2011) Dendritic integration in hippocampal dentate granule cells. *Neuron* 71:512–528.

Kügler S, Kilic E, Bähr M (2003) Human synapsin 1 gene promoter confers highly neuron-specific long-term transgene expression from an adenoviral vector in the adult rat brain depending on the transduced area. *Gene Ther* 10:337–347.

Kügler S, Meyn L, Holzmüller H, Gerhardt E, Isenmann S, Schulz JB, Bähr M (2001) Neuron-specific expression of therapeutic proteins: evaluation of different cellular promoters in recombinant adenoviral vectors. *Mol Cell Neurosci* 17:78–96.

Kuroda H, Kutner RH, Bazan NG, Reiser J (2008) A comparative analysis of constitutive and cell-specific promoters in the adult mouse hippocampus using lentivirus vector-mediated gene transfer. *J Gene Med* 10:1163–1175.

Laplagne DA, Espósito MS, Piatti VC, Morgenstern NA, Zhao C, van Praag H, Gage FH, Schinder AF (2006) Functional convergence of neurons generated in the developing and adult hippocampus. *PLoS Biol* 4:e409.

Lee H, Kang E, Goodsmith D, Yoon DY, Song H, Knierim JJ, Ming G, Christian KM (2015) DISC1-mediated dysregulation of adult hippocampal neurogenesis in rats. *Front Syst Neurosci* 9:1–8.

Lefebvre JL, Sanes JR, Kay JN (2015) Development of Dendritic Form and Function. *Annu Rev Cell Dev Biol* 31:741–777.

Lemaire V, Tronel S, Montaron M-F, Fabre A, Dugast E, Abrous DN (2012) Long-Lasting Plasticity of Hippocampal Adult-Born Neurons. *J Neurosci* 32:3101–3108.

- Li G, Pleasure SJ (2010) Ongoing interplay between the neural network and neurogenesis in the adult hippocampus. *Curr Opin Neurobiol* 20:126–133.
- Llorens-Martín M, Rábano A, Ávila J (2016) The Ever-Changing Morphology of Hippocampal Granule Neurons in Physiology and Pathology. *Front Neurosci* 9:1–20.
- Loy R, Lynch G, Cotman CW (1977) Development of afferent lamination in the fascia dentata of the rat. *Brain Res* 121:229–243.
- Lyford GL, Yamagata K, Kaufmann WE, Barnes CA, Sanders LK, Copeland NG, Gilbert DJ, Jenkins NA, Lanahan AA, Worley PF (1995) Arc, a growth factor and activity-regulated gene, encodes a novel cytoskeleton-associated protein that is enriched in neuronal dendrites. *Neuron* 14:433–445.
- Mainen ZF, Sejnowski TJ (1996) Influence of dendritic structure on firing pattern in model neocortical neurons. *Nature* 382:363–366.
- Marín-Burgin A, Mongiat L a, Pardi MB, Schinder AF (2012) Unique processing during a period of high excitation/inhibition balance in adult-born neurons. *Science* 335:1238–1242.
- Mathews EA, Morgenstern NA, Piatti VC, Zhao C, Jessberger S, Schinder AF, Gage FH (2010) A distinctive layering pattern of mouse dentate granule cells is generated by developmental and adult neurogenesis. *J Comp Neurol* 518:4479–4490.
- Monfils M-H, Teskey GC (2004) Induction of long-term depression is associated with decreased dendritic length and spine density in layers III and V of sensorimotor neocortex. *Synapse* 53:114–121.
- Mongiat L a, Espósito MS, Lombardi G, Schinder AF (2009) Reliable activation of immature neurons in the adult hippocampus. *PLoS One* 4:e5320.
- Muramatsu R, Ikegaya Y, Matsuki N, Koyama R (2007) Neonatally born granule cells numerically dominate adult mice dentate gyrus. *Neuroscience* 148:593–598.

Myers CEC, Scharfman HE (2011) Pattern separation in the dentate gyrus: A role for the CA3 backprojection. *Hippocampus* 21:1190–1215.

Nakashiba T, Cushman JD, Pelkey K a, Renaudineau S, Buhl DL, McHugh TJ, Barrera VR, Chittajallu R, Iwamoto KS, McBain CJ, Fanselow MS, Tonegawa S (2012) Young Dentate Granule Cells Mediate Pattern Separation, whereas Old Granule Cells Facilitate Pattern Completion. *Cell* 149:188–201.

Norkett R, Modi S, Birsa N, Atkin TA, Ivankovic D, Pathania M, Trossbach S V., Korth C, Hirst WD, Kittler JT (2016) DISC1-dependent regulation of mitochondrial dynamics controls the morphogenesis of complex neuronal dendrites. *J Biol Chem* 291:613–629.

Ohkawa N, Saitoh Y, Tokunaga E, Nihonmatsu I, Ozawa F, Murayama A, Shibata F, Kitamura T, Inokuchi K (2012) Spine formation pattern of adult-born neurons is differentially modulated by the induction timing and location of hippocampal plasticity. *PLoS One* 7:e45270.

Okuno H, Akashi K, Ishii Y, Yagishita-Kyo N, Suzuki K, Nonaka M, Kawashima T, Fujii H, Takemoto-Kimura S, Abe M, Natsume R, Chowdhury S, Sakimura K, Worley PF, Bito H (2012) Inverse Synaptic Tagging of Inactive Synapses via Dynamic Interaction of Arc/Arg3.1 with CaMKII β . *Cell* 149:886–898.

Peebles CL, Yoo J, Thwin MT, Palop JJ, Noebels JL, Finkbeiner S (2010) Arc regulates spine morphology and maintains network stability in vivo. *Proc Natl Acad Sci U S A* 107:18173–18178.

Pesold C, Impagnatiello F, Pisu MG, Uzunov DP, Costa E, Guidotti A, Caruncho HJ (1998) Reelin is preferentially expressed in neurons synthesizing gamma-aminobutyric acid in cortex and hippocampus of adult rats. *Proc Natl Acad Sci U S A* 95:3221–3226.

Pologruto T a TT a, Sabatini BLB, Svoboda K (2003) ScanImage: flexible software for operating laser scanning microscopes. *Biomed Eng Online* 2:13.

- Radic T, Al-Qaisi O, Jungenitz T, Beining M, Schwarzacher SW (2015) Differential Structural Development of Adult-Born Septal Hippocampal Granule Cells in the Thy1-GFP Mouse, Nuclear Size as a New Index of Maturation. *PLoS One* 10:e0135493.
- Rahimi O, Claiborne BJ (2007) Morphological development and maturation of granule neuron dendrites in the rat dentate gyrus. *Prog Brain Res* 163:167–181.
- Rall W, Rinzel J (1973) Branch input resistance and steady attenuation for input to one branch of a dendritic neuron model. *Biophys J* 13:648–687.
- Reeves TM, Steward O (1986) Emergence of the capacity for LTP during reinnervation of the dentate gyrus: evidence that abnormally shaped spines can mediate LTP. *Exp Brain Res* 65:167–175.
- Restivo L, Niibori Y, Mercaldo V, Josselyn SA, Frankland PW (2015) Development of Adult-Generated Cell Connectivity with Excitatory and Inhibitory Cell Populations in the Hippocampus. *J Neurosci* 35:10600–10612.
- Ribak CE, Shapiro L a (2007) Dendritic development of newly generated neurons in the adult brain. *Brain Res Rev* 55:390–394.
- Rihn LL, Claiborne BJ (1990) Dendritic growth and regression in rat dentate granule cells during late postnatal development. *Dev Brain Res* 54:115–124.
- Rosenzweig S, Wojtowicz JM (2011) Analyzing dendritic growth in a population of immature neurons in the adult dentate gyrus using laminar quantification of disjointed dendrites. *Front Neurosci* 5:34.
- Schmidt-Hieber C, Jonas P, Bischofberger J (2007) Subthreshold dendritic signal processing and coincidence detection in dentate gyrus granule cells. *J Neurosci* 27:8430–8441.
- Schneider CJ, Cuntz H, Soltesz I (2014) Linking Macroscopic with Microscopic Neuroanatomy Using Synthetic Neuronal Populations. *PLoS Comput Biol* 10:e1003921.

Schuldiner O, Yaron A (2014) Mechanisms of developmental neurite pruning. *Cell Mol Life Sci* 72:101–119.

Schwarzacher S, Vuksic M, Haas C, Burbach G, Sloviter RS, Deller T (2006) Neuronal hyperactivity induces astrocytic expression of neurocan in the adult rat hippocampus. *Glia* 714:704–714.

Sengupta P (2013) The Laboratory Rat: Relating Its Age With Human's. *Int J Prev Med* 4:624–630.

Sidiropoulou K, Pissadaki EK, Poirazi P (2006) Inside the brain of a neuron. *EMBO Rep* 7:886–892.

Šišková Z, Justus D, Kaneko H, Friedrichs D, Henneberg N, Beutel T, Pitsch J, Schoch S, Becker A, von der Kammer H, Remy S (2014) Dendritic structural degeneration is functionally linked to cellular hyperexcitability in a mouse model of Alzheimer's disease. *Neuron* 84:1023–1033.

St John JL, Rosene DL, Luebke JI (1997) Morphology and electrophysiology of dentate granule cells in the rhesus monkey: comparison with the rat. *J Comp Neurol* 387:136–147.

Steward O, Wallace CS, Lyford GL, Worley PF (1998) Synaptic activation causes the mRNA for the IEG Arc to localize selectively near activated postsynaptic sites on dendrites. *Neuron* 21:741–751.

Stone SSD, Teixeira CM, Zaslavsky K, Wheeler AL, Martinez-Canabal A, Wang AH, Sakaguchi M, Lozano AM, Frankland PW (2011) Functional convergence of developmentally and adult-generated granule cells in dentate gyrus circuits supporting hippocampus-dependent memory. *Hippocampus* 21:1348–1362.

Sun GJ, Sailor KA, Mahmood QA, Chavali N, Christian KM, Song H, Ming G (2013) Seamless reconstruction of intact adult-born neurons by serial end-block imaging reveals complex axonal guidance and development in the adult hippocampus. *J Neurosci* 33:11400–11411.

Tavosanis G (2012) Dendritic structural plasticity. *Dev Neurobiol* 72:73–86.

Teixeira CM, Kron MM, Masachs N, Zhang H, Lagace DC, Martinez A, Reillo I, Duan X, Bosch C, Pujadas L, Brunso L, Song H, Eisch AJ, Borrell V, Howell BW, Parent JM, Soriano E (2012) Cell-Autonomous Inactivation of the Reelin Pathway Impairs Adult Neurogenesis in the Hippocampus. *J Neurosci* 32:12051–12065.

Temprana SG, Mongiat LA, Yang SM, Trincherro MF, Alvarez DD, Kropff E, Giacomini D, Beltramone N, Lanuza GM, Schinder AF (2014) Delayed Coupling to Feedback Inhibition during a Critical Period for the Integration of Adult-Born Granule Cells. *Neuron*:1–15.

Teskey GC, Monfils M-HH, Silasi G, Kolb B, Young NA, Van Rooyen F, Larson SEM, Flynn C, Monfils M-HH, Kleim JA, Henry LC, Goertzen CD, Silasi G, Kolb B (2006) Neocortical kindling is associated with opposing alterations in dendritic morphology in neocortical layer V and striatum from neocortical layer III. *Synapse* 59:1–9.

Tronel S, Lemaire V, Charrier V, Montaron M-F, Abrous DN (2014) Influence of ontogenetic age on the role of dentate granule neurons. *Brain Struct Funct*:1–17.

van Praag H, Schinder AF, Christie BR, Toni N, Palmer TD, Gage FH (2002) Functional neurogenesis in the adult hippocampus. *Nature* 415:1030–1034.

Vuksic M, Del Turco D, Bas Orth C, Burbach GJ, Feng G, Müller CM, Schwarzacher SW, Deller T (2008) 3D-reconstruction and functional properties of GFP-positive and GFP-negative granule cells in the fascia dentata of the Thy1-GFP mouse. *Hippocampus* 18:364–375.

Vuksic M, Del Turco D, Vlachos A, Schuldt G, Müller CM, Schneider G, Deller T (2011) Unilateral entorhinal denervation leads to long-lasting dendritic alterations of mouse hippocampal granule cells. *Exp Neurol* 230:176–185.

Waung MW, Pfeiffer BE, Nosyreva ED, Ronesi JA, Huber KM (2008) Rapid Translation of Arc/Arg3.1 Selectively Mediates mGluR-Dependent LTD through Persistent Increases in AMPAR Endocytosis Rate. *Neuron* 59:84–97.

Wilson RC (1981) Changes in translation of synaptic excitation to dentate granule cell discharge accompanying long-term potentiation. I. Differences between normal and reinnervated dentate gyrus. *J Neurophysiol* 46:324–338.

Wilson RC, Levy WB, Steward O (1979) Functional effects of lesion-induced plasticity: long term potentiation in formal and lesion-induced temporodentate connections. *Brain Res* 176:65–78.

Yu D, Fan W, Wu P, Deng J, Liu J, Niu Y, Li M, Deng J (2014) Characterization of hippocampal Cajal-Retzius cells during development in a mouse model of Alzheimer's disease (Tg2576). *Neural Regen Res* 9:394.

Zhao C, Teng EM, Summers RG, Ming G-L, Gage FH (2006) Distinct morphological stages of dentate granule neuron maturation in the adult mouse hippocampus. *J Neurosci* 26:3–11.

Tables

Table 1 Summary of cell and animal numbers

Groups	Cells			Animals		
	Arc ⁺ (ipsi)	Arc ⁻ (ipsi)	contra	Arc ⁺ (ipsi)	Arc ⁻ (ipsi)	contra
abGC (21 dpi)	– ^a	23	9	– ^a	4	3
abGC (28 dpi)	21	25	21	5	5	5
abGC (35 dpi)	24	22	20	5	5	5
abGC (77 dpi)	17	15	10	5	4	3
mGC (AAV)	17	– ^a	16	5	– ^a	5
Total	79	85	76	20	18	21

^a No corresponding cells could be found (see Material & Methods).

Figures

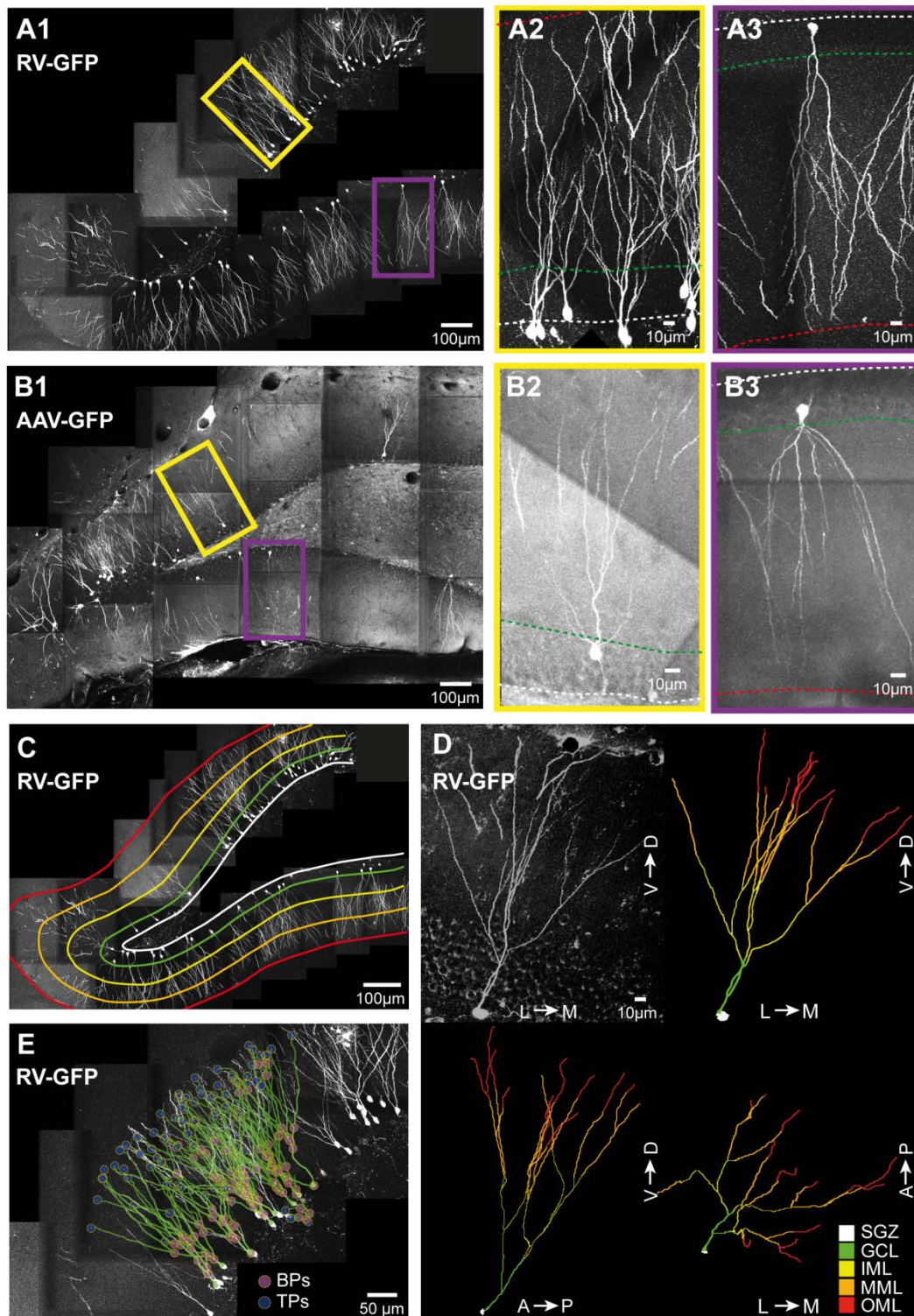


Fig. 1. Reconstruction of RV-labeled adult-born granule cells (abGCs) and AAV-labeled mature granule cells (mGCs) in the dentate gyrus (DG).

A, abGCs (28 dpi) labeled with the RV-CAG-GFP vector. **A1**, Maximum intensity projection of a stitched, two-photon, composite stack showing GFP-positive abGCs. **A2–3**, High magnification of **A1** showing suprapyramidal (yellow frame, **A2**) and infrapyramidal (violet frame, **A3**) abGCs. Borders of the GCL to the hilus (white) and to the IML (green) as well as the fissure (red) are illustrated as dashed lines. **B**, mGCs labeled with the AAV-Syn1-GFP vector. Same layout as in **A**. **C**, Reconstructed DG layers from **A1** (border colors: white: hilus-GCL, green: GCL-ML, yellow: IML-MML, orange: MML-OML, red: hippocampal fissure). **D**, Representative fluorescence image of an abGC (28 dpi, upper left panel) with a corresponding 3D-reconstruction (3 different views: combinations of L → M **lateral**-medial, V → D ventral-dorsal, A → P anterior-posterior). The reconstructed DG layers were mapped onto the 3D-reconstruction of GCs to assign the respective layers (see legend). **E**, Overlay of dendritic reconstructions (green) and the fluorescence image of suprapyramidal abGCs from **A1** with automatically marked branching (magenta, BPs) and termination (blue, TPs) points. Abbreviations: subgranular zone (SGZ); granule cell layer (GCL); inner, middle and outer molecular layer (IML, MML, and OML).

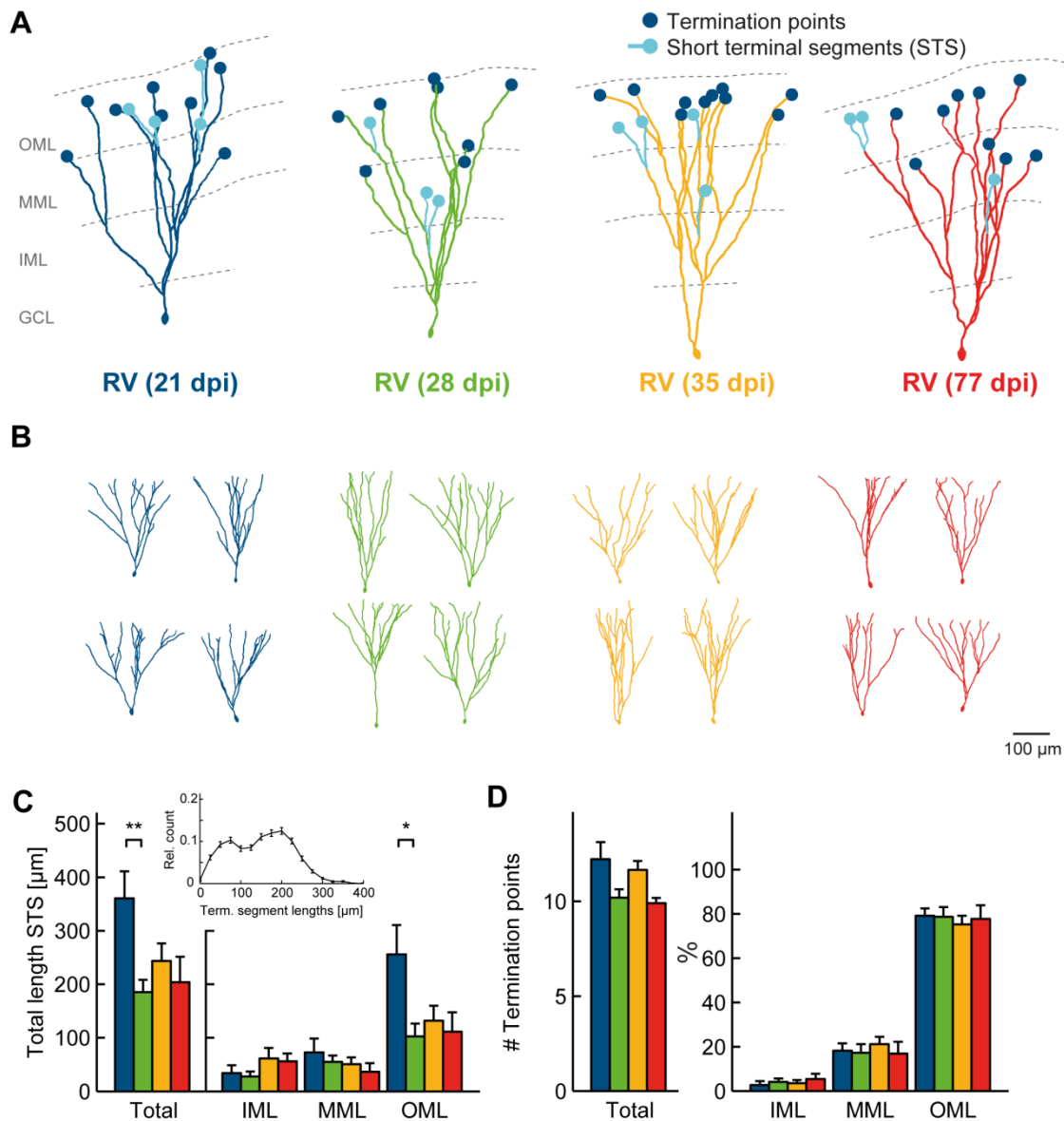


Fig. 2. Loss of short terminal segments (STS) in the dendrites of abGCs 3–4 weeks after cell birth.

A, Representative examples of abGC reconstructions (21–77 dpi) with marked termination points (blue) and short terminal segments (STS, cyan). **B**, More examples illustrating the variation in dendritic morphology. **C**, Mean summed length of STS. Inset: Distribution of terminal segment lengths in RVs showing two populations of segment lengths. **D**, The number of termination points and their relative distribution in the molecular layer. Abbreviations: IML, inner molecular layer; MML, middle molecular layer; OML, outer molecular layer. Error bars represent mean + s.e.m. P values are $P < 0.05$ (*) and $P < 0.01$ (**).

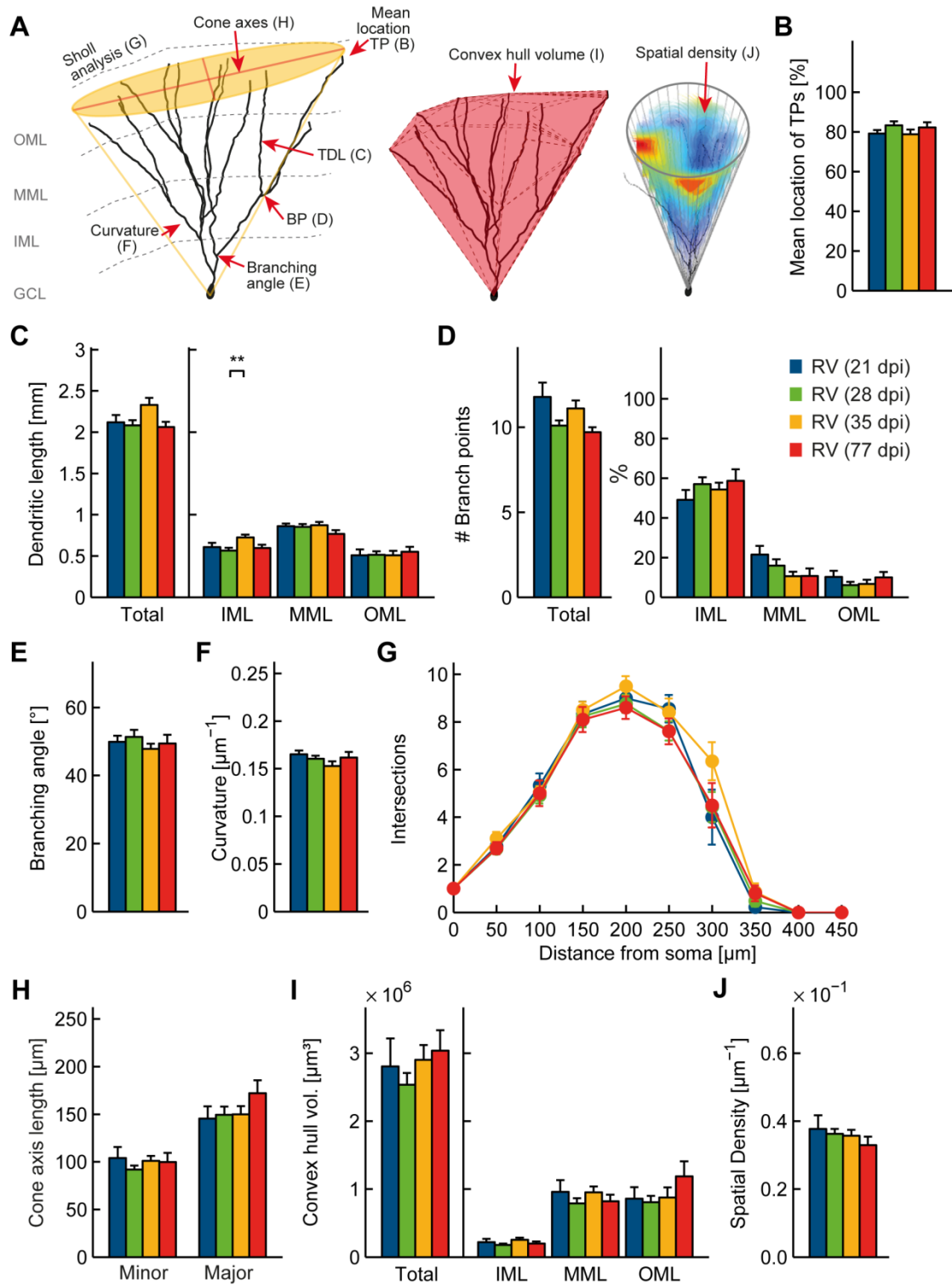


Fig. 3. Detailed morphological analysis reveals that structural maturation of developing abGCs is completed by 3 weeks after cell birth.

A, Schematic illustrating morphological parameters analyzed in **B–J** (see Supplementary Methods for more details). **B**, Mean location of termination points. **C**, Dendritic length. **D**, Branch points and their relative distribution in the molecular layer. **E**, Branching angle. **F**, Curvature. **G**, Sholl intersections. **H**, Length of major and minor axis of the fitted Gaussian cone. **I**, Volume of the tree's convex hull. **J**, Spatial density of the tree within its cone-shaped space. Error bars represent mean + s.e.m. P values are $P < 0.01$ (**). Abbreviations: branch point (BP), termination point (TP), total dendritic length (TDL), inner molecular layer (IML), middle molecular layer (MML), outer molecular layer (OML).

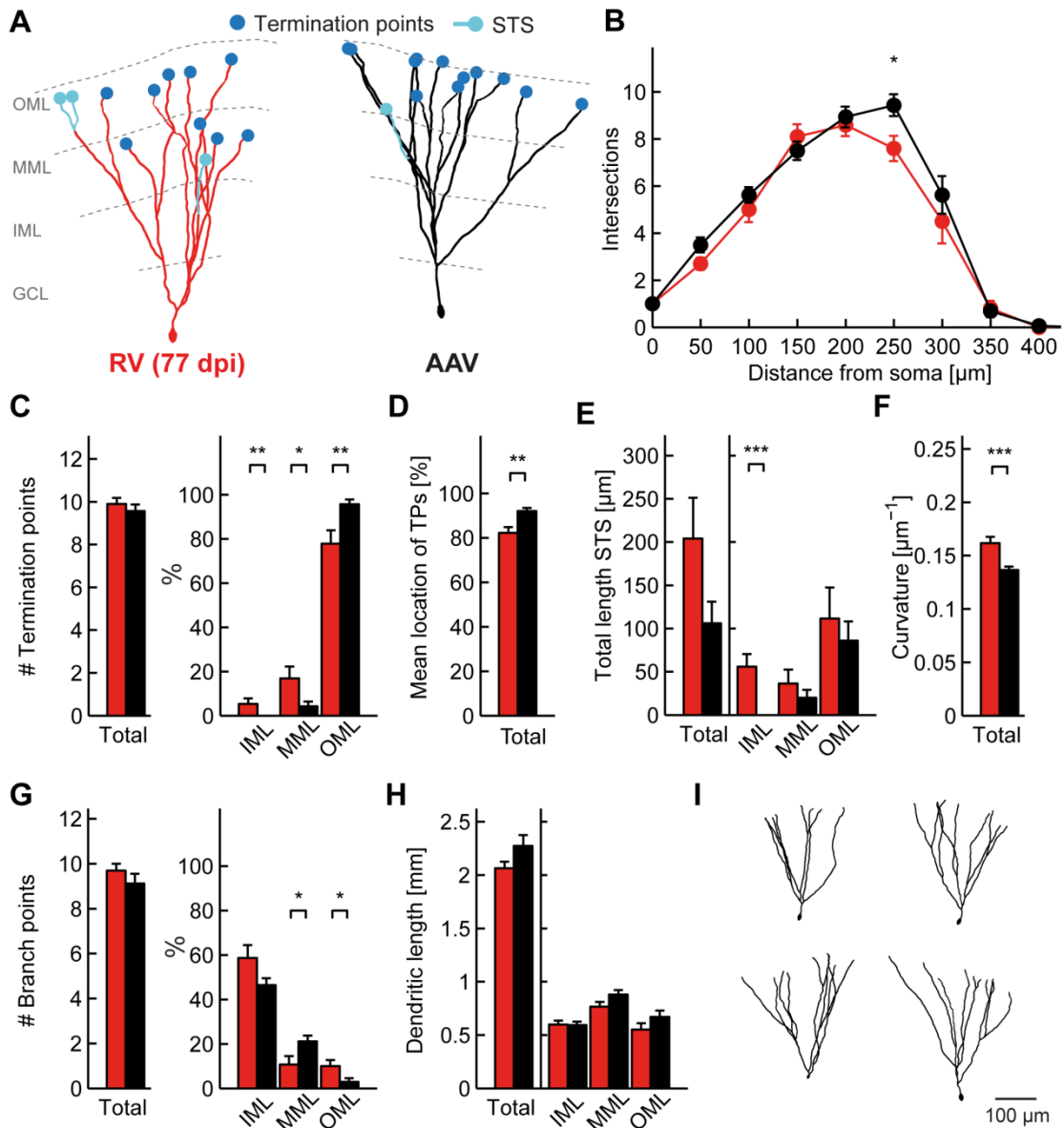


Fig. 4. Old abGCs remain structurally distinct from mGCs.

A, Representative reconstruction of an 77 dpi old abGCs (red) and a AAV-labeled mGC (black) with marked termination points (blue) and STS (cyan). **B**, Sholl intersections. **C**, Termination points and their relative distribution in the molecular layer. **D**, Mean location of termination points. **E**, Mean summed length of STS. **F**, Curvature. **G**, Branch points and their relative distribution in ML. **H**, Dendritic length. **I**, More examples of AAV-labeled mGCs illustrating the variation in dendritic morphology. Error bars are mean + s.e.m. P values are $P < 0.05$ (*), $P < 0.01$ (**) and $P < 0.005$ (***).

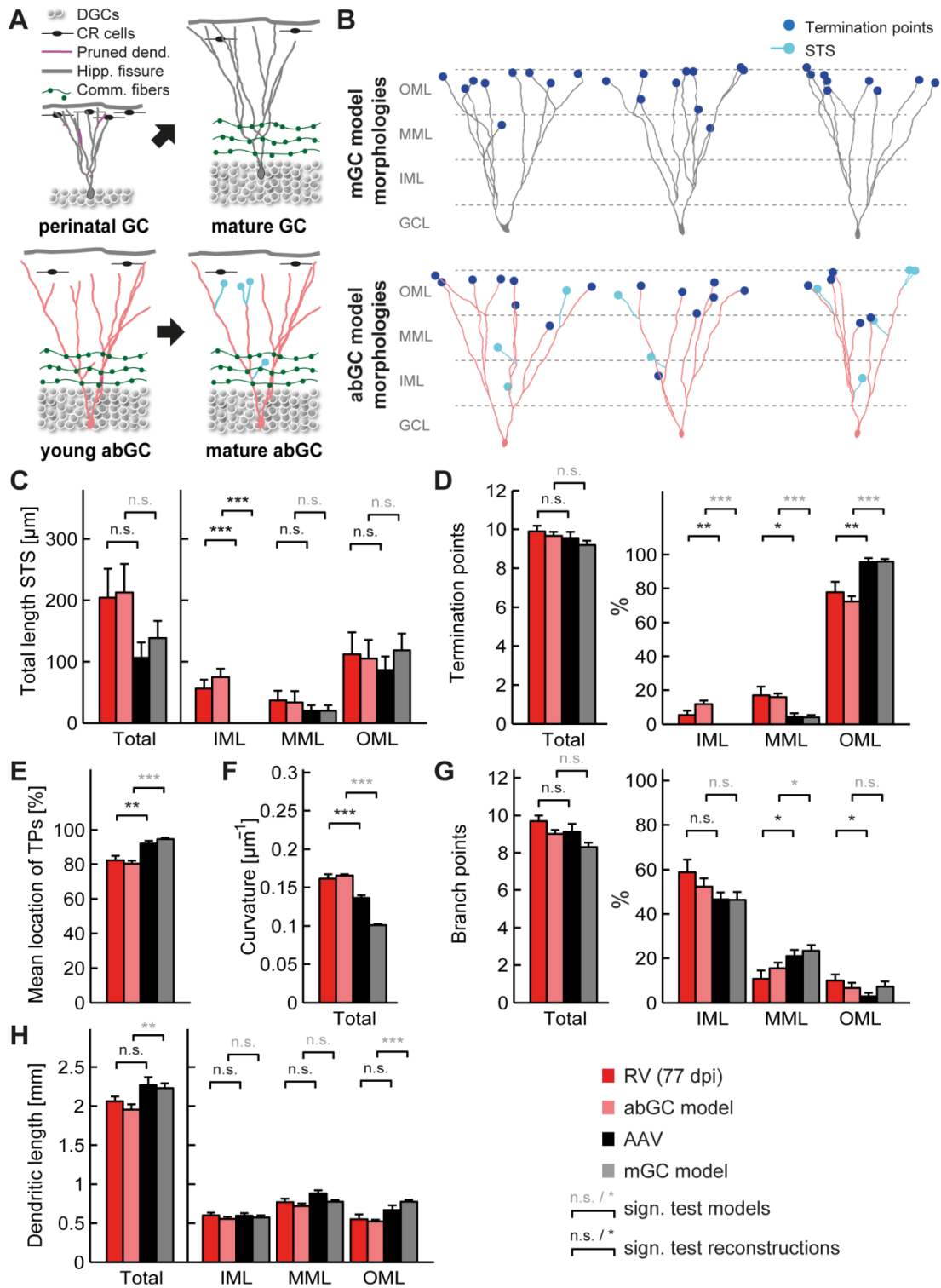


Fig. 5. Morphological model shows that dendritic pruning and developmental growth of the dentate gyrus (DG) can account for experimental data.

A, Schematic explaining the difference between the morphological model of abGCs and mGCs. AAV-positive mGCs grow in the young small DG with a high reelin gradient produced by Cajal-Retzius (CR) and other cells (upper left panel), and are stretched subsequently when the DG matures (upper right panel). RV-positive abGCs grow in the already stretched, mature DG with a lower reelin gradient but commissural fibers as targets in the IML (lower panels). Short dendritic segments that are pruned during maturation are depicted in purple, non-pruned STS in cyan. **B**, Representative examples of synthetic morphologies for both RV-labeled abGCs and AAV-labeled mGCs created with the morphological model (see Supplementary Methods for details). **C–H**, Morphological comparison of synthetic and reconstructed morphologies (AAV: black, mGC model: gray, RV 77 dpi: red, abGC model bright red). Test for significance was only done between RV (77 dpi) and AAV (lower row, black text) as well as between the abGC and mGC model (upper row, gray text) in order to illustrate where experimental and model data are comparable. No differences in both cases imply consensus between experiment and model, too. Note that consensus was found in all parameters except for the number of branch points in the OML (G), and the total dendritic length and dendritic length in the OML (H). Error bars are mean + s.e.m.

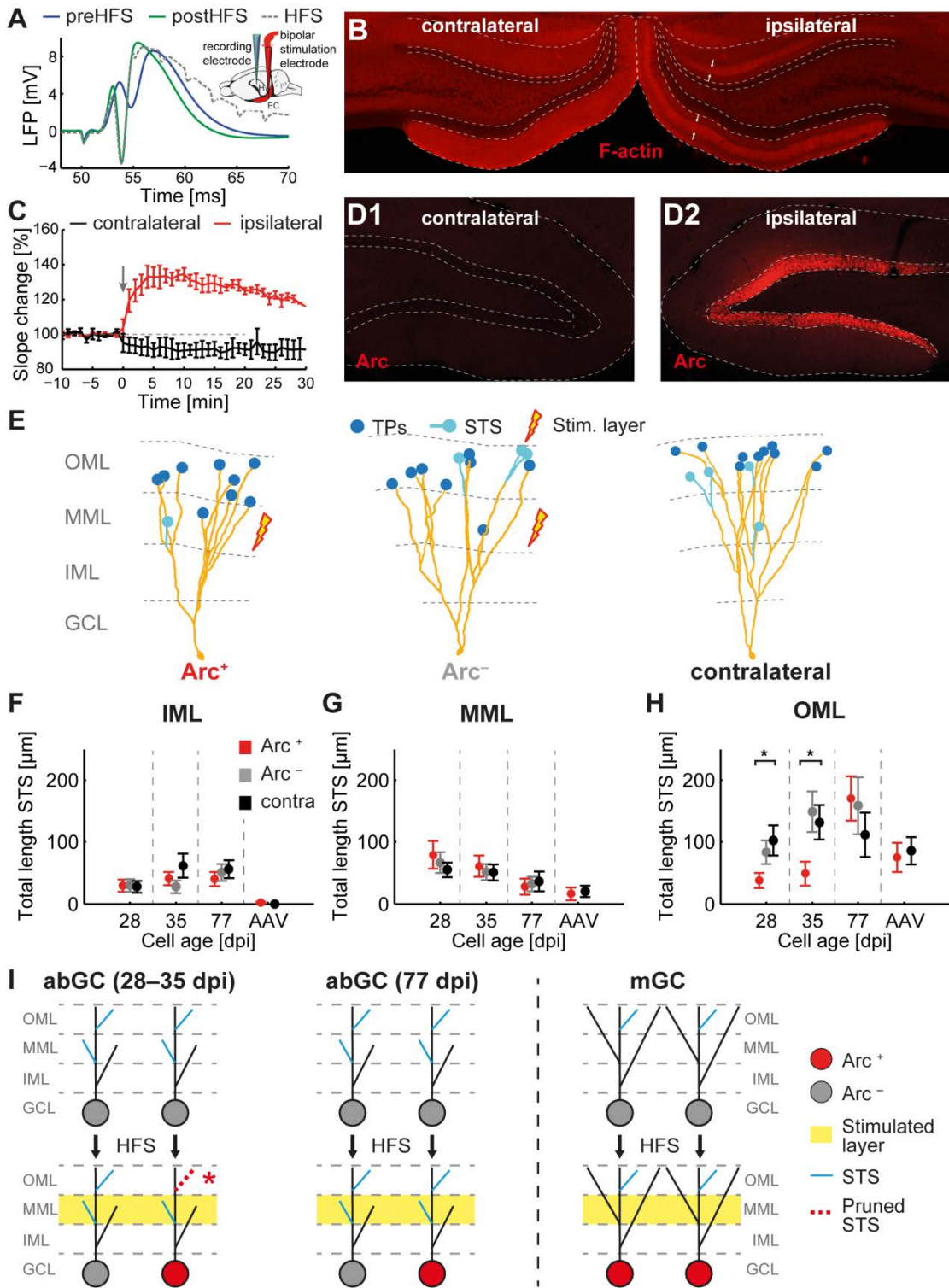
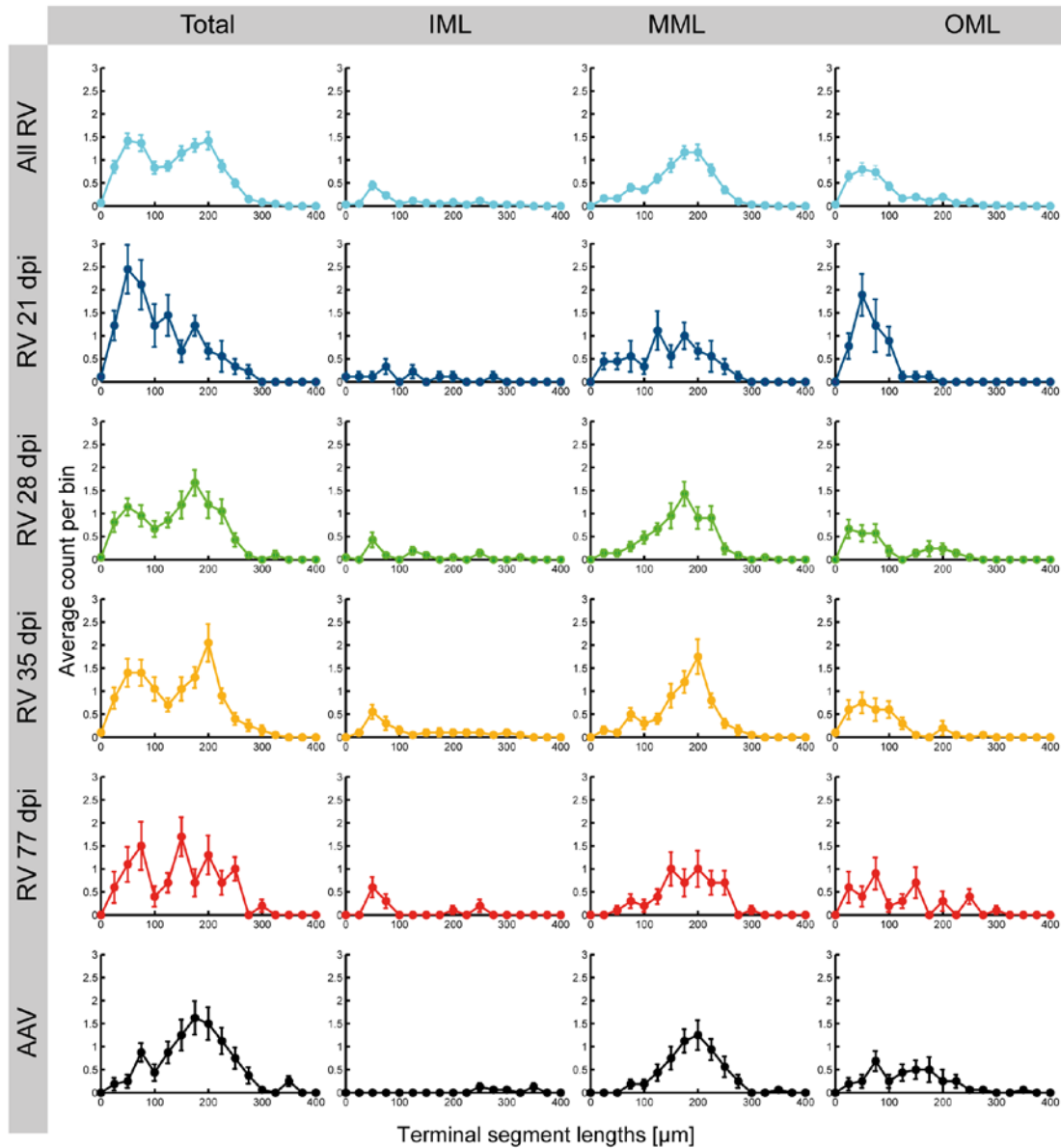


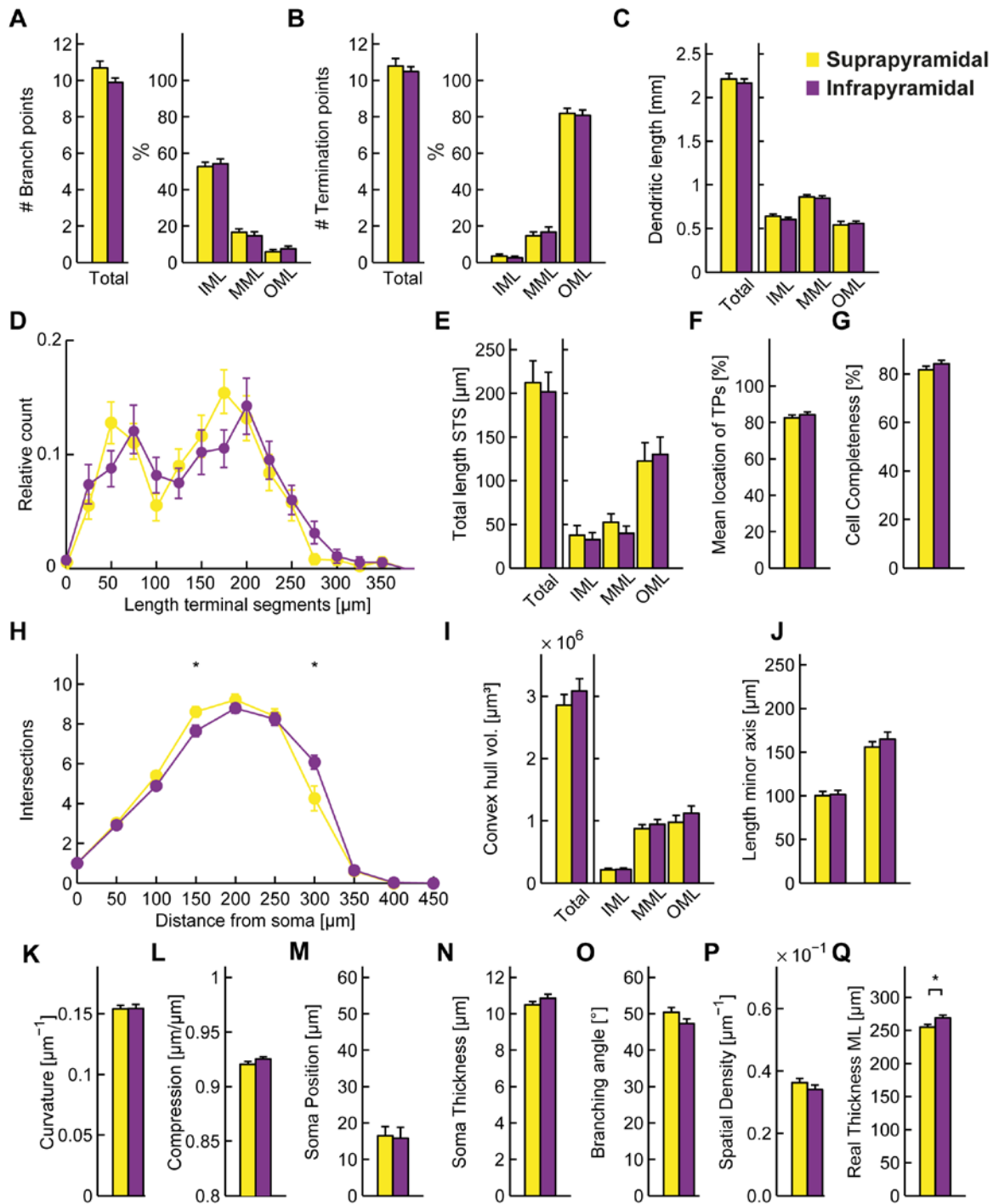
Fig. 6. Arc expression correlates with reduced short terminal segments in the OML of young abGCs following HFS.

A, Local field potentials recorded in the ipsilateral DG before (blue) and after (green) 2 h HFS (test pulse to the ipsilateral medial perforant path, 5 traces averaged). Inset: Schematic of rat brain with bipolar stimulation electrode (red) in the medial perforant path of the entorhinal cortex (EC) and a recording electrode (blue) in the DG of the hippocampus (H). **B**, Epifluorescence images of a 50 μm frontal section showing enrichment of F-actin in the ipsilateral MML (white arrows) compared to homogenous F-actin distribution in the contralateral ML. **C**, Change of the early local field potential slope following a test pulse (500 μA) to the corresponding medial perforant path (red: ipsilateral, black: contralateral, $n = 3$). The start of the HFS protocol is indicated (gray arrow). **D**, Confocal images (maximum intensity z projection) of a 50 μm frontal section showing absence of Arc expression in the contralateral hemisphere (D1) compared to robust Arc expression in the granule cell layer of the ipsilateral side (D2). **E**, Representative dendritic reconstructions of an Arc-positive (left tree) and Arc-negative (middle tree) ipsilateral abGC (35 dpi) compared to a contralateral (right tree) abGC (35 dpi). **F–G**, Mean summed lengths of STS in the MML (**F**) and OML (**G**) after 2 h of medial perforant path stimulation (HFS) are shown for the RV-labeled abGC (28–77 dpi) groups and the AAV-labeled mGCs. Gray values denote Arc-negative cells, red values denote Arc-positive cells, and black values denote the contralateral side as the unstimulated control. Note that in the stimulated hemisphere, there were no Arc-negative mGCs as all mGCs were Arc-positive (see Methods). **H**, Schematic illustrating that abGCs exhibit a critical phase (28–35 dpi) when medial perforant path stimulation of the middle molecular layer (yellow band, lower row) can induce dendritic reorganization in the OML as observed by the loss of STS (dashed red segment and asterisk). STS in other layers or cells of different ages (cyan segments) were not affected by the stimulation. Error bars are mean + s.e.m. P values are $P < 0.05$ (*) and $P < 0.01$ (**). Abbreviations: short terminal segment (STS), inner molecular layer (IML), middle molecular layer (MML), outer molecular layer (OML).

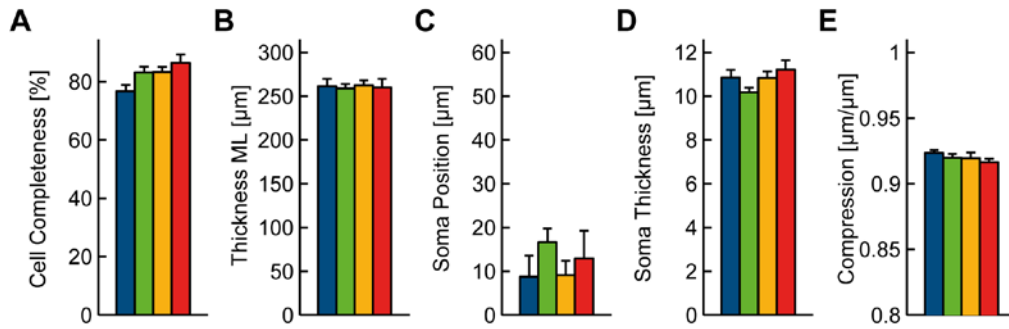
Supplementary Figures

**Supplementary Figure 1: Terminal segments change in length at different ages.**

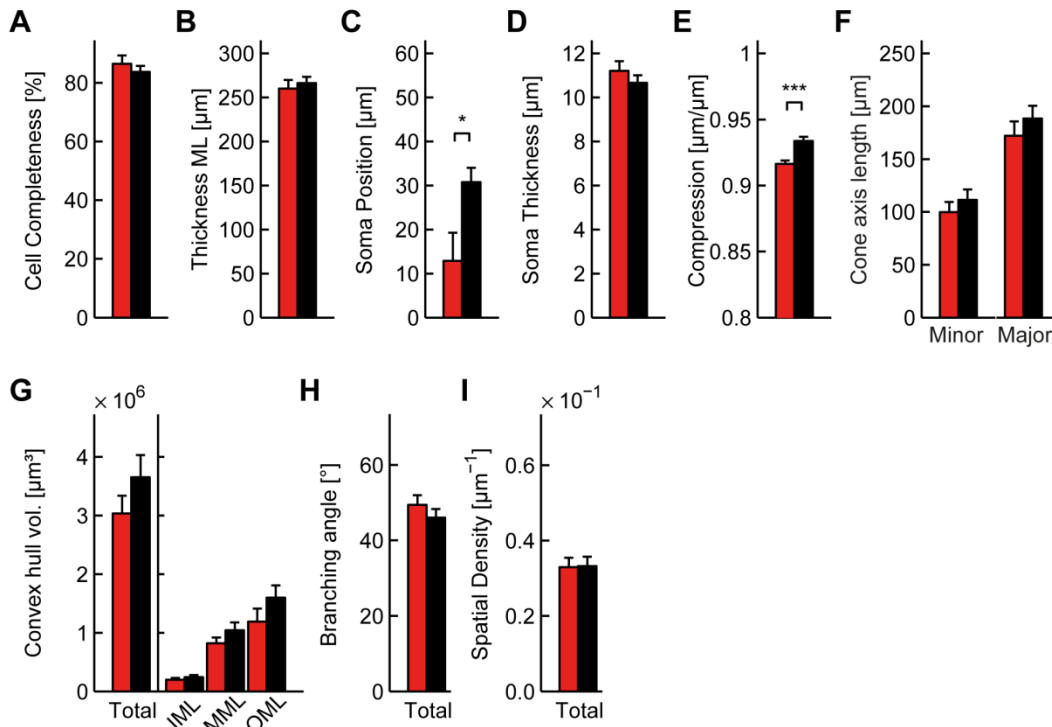
Absolute histograms of terminal dendritic segments in abGCs (RV 21-77 dpi) and mGCs (AAV) of the complete dendritic arbor ("Total", left column) or in the inner, middle and outer molecular layer (IML, MML, OML), respectively. Note the bimodal distribution of shorter and larger terminal segments and the shift from mainly short terminal segments (STS, < 100 μm) at 21 dpi to mainly large terminal segments in AAV-labeled mGCs in the left column. The few STS which are left in mGCs are located in the OML. Since the binning dilutes the differences (which can affect as much as 10 % of the total dendritic length as from RV 21 to 28 dpi), we summed the length of STS for the main figures.



Supplementary Figure 2: Supra- and infrapyramidal GCs are structurally similar and thus were pooled. All reconstructed cells were pooled according to their supra- or infrapyramidal location to analyze difference arising only from location on the pyramidal blade **A-P**, Same morphological analyses as in Figures 2-6 and Suppl. Fig. 2-4 showing only small differences in the Sholl distribution (H) and the thickness of the ML (Q) which might both be correlated due to different GCL and ML thicknesses.



Supplementary Figure 3: Remaining morphological comparisons in the developing abGC groups (21-77 dpi). **A**, Rated cell completeness (see Material & Methods). **B**, Thickness of molecular layer (ML). **C**, Vertical position of somata. **D**, Thickness of somata. **E**, Compression (euclidean length of each dendritic segment endings divided by path length along the segment) as another measure of dendritic curvature.



Supplementary Figure 4: Remaining morphological comparisons between abGCs (77 dpi) and AAV-labeled mGCs. **A**, Rated cell completeness (see Material & Methods). **B**, Thickness of molecular layer (ML). **C**, Vertical position of somata showing abGCs are located near to the hilus even at 77 dpi. **D**, Thickness of somata. **E**, Compression (euclidean length of each dendritic segment endings divided by path length along the segment) shows same result as curvature. **F**, Length of major and minor axis of the fitted Gaussian cone. **G**, Volume of the dendritic arbor's convex hull. **H**, Branching angle. **I**, Spatial density of the dendritic arbor within its cone-shaped space. Error bars are mean + s.e.m.

8.2. Publication 2

Erklärung über Anteile der Autoren an der Publikation

“Structural homo- and heterosynaptic plasticity in adult newborn hippocampal granule cells”

submitted

	Entwicklung und Planung	Durchführung der einzelnen Experimente	Erstellung der Datensammlung und Abbildungen	Analyse / Interpretation der Daten	Verfassen des Manuskripts
Jungenitz, Tassilo	20 %	55 % Virale Injektion Schnitte Immunfärbung 2-Photon Konfok. Mikrosk Bildverarbeitung Spinerekonstr. *HFS+Ableitung *Spinezählung *EM Bilder	70 % Fig. 1A-E, Fig. 2D-G, Fig. 4, Fig. 5, Fig. 6, Fig. S1	60 % Analyseskripte für Spines Interpretation	40 %
Beining, Marcel	10 %	35 % Wie T.J., nur ohne *	30 % Fig. 1 F-K, Fig. 3	20 % Interpretation	15 %
Radic, Tijana	10 %	10 % Schnitte Immunfärbung	-	-	5 %
Deller, Thomas	5 %	-	-	-	10 %
Cuntz, Hermann	5 %	-	-	5 % Interpretation	10 %
Jedlicka, Peter	15 %	-	-	5 % Interpretation	5 %
Schwarzacher, Stephan W.	35 %	-	-	10 % Interpretation	15 %

Zustimmende Best. der Angaben:

Datum/Ort

Datum/Ort

Unterschrift Promovend

Unterschrift Betreuer

Structural homo- and heterosynaptic plasticity in adult newborn rat hippocampal granule cells

Tassilo Jungenitz*^{#1,2}, Marcel Beining*^{1,2,3,4}, Tijana Radic^{1,2}, Thomas Deller¹, Hermann Cuntz^{3,4}, Peter Jedlicka¹, Stephan W. Schwarzacher¹

¹*Institute of Clinical Neuroanatomy, Goethe-University Frankfurt, Frankfurt am Main, Germany*

²*Faculty of biosciences, Goethe University, Frankfurt/Main, Germany*

³*Ernst Strüngmann Institute (ESI) for Neuroscience in Cooperation with Max Planck Society, Frankfurt/Main, Germany*

⁴*Frankfurt Institute for Advanced Studies (FIAS), Frankfurt/Main, Germany*

*These Authors contributed equally to this work (joint-first coauthors)

Author for correspondence: Tassilo Jungenitz, Institute of Clinical Neuroanatomy, Goethe-University, Theodor-Stern-Kai 7, D-60590 Frankfurt am Main, Phone: +49 (0)69 6301 6914, Fax: +49 (0)69 6301 6425, E-mail: tassilo.j@gmx.de

Number of figures and tables: 7

Number of pages: 43

Keywords: adult neurogenesis, hippocampus, spines, murine moloney leukemia virus, retrovirus, adeno-associated virus

Abstract

Adult newborn hippocampal granule cells (abGCs) contribute to spatial learning and memory. AbGCs are thought to play a specific role in pattern separation, distinct from developmentally born mature GCs (mGCs) that enable completion of stored patterns. During the time course of synaptic integration in the adult network abGCs undergo a critical phase of enhanced synaptic activity. Here we examine on the level of individual structurally analyzed cells at which exact cell age abGCs are synaptically integrated in the adult network and which forms of synaptic plasticity are expressed. We used virus-mediated labeling of abGCs and (mGCs) to analyze changes in spine morphology as indicator of plasticity in rats in vivo. High-frequency stimulation of the medial perforant path induced LTP in the middle molecular layer (MML) and LTD in the non-stimulated outer molecular layer (OML). Stimulation elicited homosynaptic spine enlargement in the MML and heterosynaptic spine shrinkage in the inner and OML. Both processes were concurrently present on individual dendritic trees of mGCs and abGCs. Spine shrinkage counteracted spine enlargement and thus could play a homeostatic role, normalizing synaptic weights. Spine plasticity appeared gradually from 21 dpi on, with a sharp increase at 28-35 dpi. This is the first demonstration of structural homo- and heterosynaptic plasticity in mGCs and abGCs and defines the critical phase for abGCs integration between 21-35 dpi.

Statement of significance

The lifelong genesis of hippocampal granule cells (abGCs) enables specific forms of spatial learning. Learning and memory are mediated by LTP and LTD of synaptic strength, called synaptic plasticity. Following LTP and LTD induction, three week old abGCs show spine enlargement in stimulated dendritic segments and spine shrinkage in non-stimulated segments of the same cell. This concurrent structural homo- and heterosynaptic plasticity increases at 4-5 weeks of cell age, defining a critical phase of abGCs integration. Structural homo- and heterosynaptic plasticity is also present in mature granule cells, confirming a general form of synaptic plasticity and homeostasis. The presence of increasing structural plasticity on abGCs provides novel evidence on their direct involvement in synaptic plasticity underlying learning.

Introduction

Hippocampal granule cells (GCs) are generated throughout life in the mammalian dentate gyrus (DG) (Gage, 2000) and are considered to be important for spatial learning and memory (Cameron and Glover, 2015). AbGCs are thought to play a distinct role in separation and identification of new patterns, whereas mature GCs (mGCs), born during development, enable completion of stored patterns upon partial activation (Clelland et al., 2009; Nakashiba et al., 2012). Generation and maturation of GCs follows a course of differentiation, structural growth, and functional integration (Kempermann et al., 2015). Within 3-11 weeks of age, adult newborn granule cells (abGCs) become increasingly integrated into the hippocampal network (Deshpande et al., 2013; Denny et al., 2014). This particular function of abGCs might depend on a critical time window at 3-6 weeks when abGCs exhibit enhanced synaptic plasticity (Schmidt-Hieber et al., 2004; Ge et al., 2007), an increased excitation to inhibition balance (Marín-Burgin et al., 2012; Temprana et al., 2014), and the capability for experience-dependent remodeling of their connectivity (Martínez-Canabal, 2015).

Dendritic spines of abGCs appear during the third week (Zhao et al., 2006), forming first glutamatergic contacts at perforant path synapses (Toni et al., 2007; Toni and Sultan, 2011). Spine morphology is activity-dependent, and correlated with changes in synaptic strength (Alvarez and Sabatini, 2007). Spine size has been reported to match the size of the postsynaptic density (PSD) and number of glutamate receptors, and therefore is directly correlated with synaptic strength (Reymann and Frey, 2007). Numerous studies demonstrated that induction of LTP is associated with spine enlargement (Huber et al., 2004), and conversely, LTD is associated with shrinkage (Zhou et al., 2004). Thus, change in spine size can be seen as structural equivalent of LTP and LTD. These two opposing types of synaptic plasticity (Oh et al., 2015) can be further classified into homosynaptic and heterosynaptic plasticity. Homosynaptic plasticity can be induced at synapses that are directly stimulated, while heterosynaptic plasticity takes place at inactive synapses neighboring stimulated synapses (Oh et al., 2015).

Excitatory synaptic contacts impinge on GC dendrites in the molecular layer (ML) of the DG. The ML is highly laminated and receives inputs via the medial perforant path (MPP) in the middle molecular layer (MML), inputs via the lateral perforant path (LPP) in the outer molecular layer (OML) and inputs from associated and commissural fibers of mossy cells in the inner molecular layer (IML) (Amaral et al., 2007).

In previous studies, selective stimulation of either the MPP or LPP revealed homosynaptic LTP (Steward et al., 1998) and heterosynaptic LTD (Abraham et al., 2007) in the respective MML or OML. Heterosynaptic LTD has been discussed recently as a homeostatic mechanism for normalizing the overall synaptic weights and maintaining synaptic competition (Chistiakova et al., 2015). Furthermore, computational modelling showed that homosynaptically induced LTP would strengthen heterosynaptic LTD at neighboring dendritic segments (Jedlicka et al., 2015) and thus could lead to effective and long-lasting changes of synaptic weights as a requisite for learning and memory. How and when heterosynaptic plasticity emerges during development and contributes to integration of abGCs into the hippocampal network is currently not known.

We performed intra-hippocampal injections of viral vectors for GFP-labeling of abGCs and mGCs to study the time course of development and structural plasticity of dendritic spines. *In vivo* high-frequency stimulation (HFS) of the MPP revealed enlargement of spines located in the MML in abGCs from 21 dpi on. Furthermore, neighboring spines in the unstimulated IML and OML of the same dendritic tree exhibited shrinkage. Thus, we could demonstrate for the first time the occurrence of homo- and heterosynaptic structural plasticity in abGCs.

Results

High-frequency stimulation of the perforant path induced expression of Arc in newborn and mature dentate granule cells

The population of abGCs was transduced with a GFP-expressing murine leukemia retroviral vector (RV-GFP) by an intra-hippocampal injection followed by HFS of the MPP at distinct time points between 21-77 dpi, in order to analyze the time course of development and structural plasticity of spines (Fig. 1a, f-i). Furthermore, we used intra-hippocampal injections of an adeno-associated viral vector to express GFP under the control of a synapsin promoter in order to study developmentally born mGCs (Fig. 1a, j, k). We refer to RV-GFP and AAV-GFP labeled cells as abGCs and mGCs respectively in the remaining text, although it is worth noting that AAV-GFP labeling does not exclude mature adult-born GCs (see Methods). We then performed 2 h HFS of the MPP with a protocol that induced robust LTP as well as a strong expression of immediate early genes (IEGs) in more than 90% of all granule cells (Fig. 1b, d; Steward et al., 1998; Jungenitz et al., 2014). In addition, 2h HFS resulted in enhanced expression of the LTP-markers F-actin and synaptopodin (Fukazawa et al., 2003) in the ipsilateral MML, i.e. the lamina of MPP fiber projection (see later, Fig. 3). Following 2 h HFS, expression of the synaptic plasticity-related IEG Arc was detected in the vast majority of GCs in the ipsilateral DG, including abGCs and mGCs (Fig. 1g, i, k). LTP induction at the MPP is known to generate a concurrent heterosynaptic LTD of the LPP input (Abraham et al., 1985, 2007). In order to evaluate the occurrence of heterosynaptic LTD following HFS of the MPP we placed a second stimulation electrode in the LPP in control experiments. Stimulation of the LPP was discriminated from the concurrent MPP stimulation by characteristic differences in the shape of the evoked local GC field potentials and in the latency of the population spike (Fig. 1b, Abraham et al. 2007, Petersen et al. 2013). Furthermore, low intensity paired pulse stimulation typically exhibited paired pulse facilitation at 20 ms interpulse-interval following LPP but not MPP stimulation, as has been described earlier (Fig. 1c, Petersen et al. 2013). Following 2h HFS, homosynaptic LTP at the MPP was accompanied by heterosynaptic LTD at the LPP following 2 h HFS

(Fig. 1d). The contralateral, non-stimulated DG showed no LTP induction following HFS in control recordings, and no enhancement of Arc-expression in the GCL as well as no enhancement of the LTP-marker F-actin and synaptopodin in all stimulation experiments. The contralateral DG therefore served as a control and was used to study the general time course of spine development in abGCs (Fig. 1e, f, h, j).

Time course of spine development in adult newborn granule cells

Dendritic segments of abGCs (Fig. 2a, top) and mGCs (Fig. 2a, bottom) were sampled from the IML, MML, and OML of the contralateral, unstimulated dentate gyrus (Fig. 2c). Only segments with a direct traceable connection to the soma were used. Time points for the analysis of abGC spines were chosen based on previous findings from rat *in vivo* (Jungenitz et al., 2014), starting at 21 dpi (n = 3 animals), with additional time points at 28 (n = 6), 35 (n = 5), and 77 dpi (n = 4) and compared to mGCs (n = 5). Dendritic segments in GCs showed a high diversity of spine sizes and shapes. Spines were classified into small (< 0.2 μm^2) and large spines (> 0.2 μm^2) using a grid based approach (Fig. 2b, for details see Methods). The density of spines, irrespective of size, increased gradually in all layers (IML, MML, and OML) between 21-77 dpi: starting at 21 dpi with $0.84 \pm 0.02 \mu\text{m}^{-1}$ in the IML, $0.99 \pm 0.01 \mu\text{m}^{-1}$ in the MML, $0.95 \pm 0.18 \mu\text{m}^{-1}$ in the OML and reaching mature levels with $1.41 \pm 0.09 \mu\text{m}^{-1}$ in the IML, $1.58 \pm 0.04 \mu\text{m}^{-1}$ in the MML and $1.77 \pm 0.13 \mu\text{m}^{-1}$ in the OML at 77 dpi (Fig. 2d₁). At 77 dpi, spine density in abGCs showed no significant differences to mGCs in all layers (IML: $1.29 \pm 0.20 \mu\text{m}^{-1}$, MML: $1.49 \pm 0.16 \mu\text{m}^{-1}$, OML: $1.56 \pm 0.17 \mu\text{m}^{-1}$). Both small (Fig. 2e₁) and large spines (Fig. 2f₁) exhibited a similar gradual age-dependent increase in density throughout all MLs, reaching the density of mGCs at 77 dpi. The density of small spines in abGCs increased from $0.81 \pm 0.04 \mu\text{m}^{-1}$ at 21 dpi to $1.35 \pm 0.07 \mu\text{m}^{-1}$ at 77 dpi with no significant difference to mGCs with $1.18 \pm 0.11 \mu\text{m}^{-1}$. Large spine density in mGCs increased from $0.10 \pm 0.02 \mu\text{m}^{-1}$ (21 dpi) to $0.22 \pm 0.03 \mu\text{m}^{-1}$ (77 dpi) with large spine density in mGCs being $0.18 \pm 0.03 \mu\text{m}^{-1}$. Thus, large spines formed about 15 % of the spine density, and there was no significant change in the percentage of large spines over the entire time period that we analyzed

(Fig. 2g₁). Data from all analyzed animals were pooled to perform a layer-specific, cell age-independent comparison. The spine density (including small and large spines) found in the MML and OML was significantly higher than in the IML (Fig. 2d₂-f₂). However, the MML showed a higher percentage of large spines in contrast to the IML and the OML (Fig. 2g₂).

We conclude from these results that a gradual development of spines occurs in abGCs between 21 dpi and 77 dpi, when spine size and density reach the levels found in mGCs.

High-frequency stimulation of the perforant path induced a layer specific expression of F-actin and synaptopodin

F-actin and synaptopodin are located in dendritic spines and are involved in processes regulating structural modifications of spines related to changes in synaptic plasticity (Deller et al., 2003; Fukazawa et al., 2003). F-actin and synaptopodin expression has been described as a valuable tool to measure layer-specific synaptic activation and plasticity following LTP induction *in vivo* (Fukazawa et al., 2003). Following 2 h HFS of the MPP, F-actin (Fig. 3a, b) and synaptopodin (Fig. 3e) expression was increased in the MML, i.e. the lamina of MPP fiber projection. The distribution of F-actin fluorescence intensity in the IML, MML, and OML was measured along the granule cell layer (GCL)-hippocampal fissure axis, starting from the border between GCL and IML up to the hippocampal fissure (Fig. 3d). Following HFS, F-actin fluorescence intensity showed a significant elevation in the stimulated MML and a significant reduction in the unstimulated IML and OML, whereas the fluorescence intensity of the total ML was not altered compared to the unstimulated side (Fig. 3c).

Taken together, these results show stimulation-dependent and layer-specific accumulation of F-actin within the MML and a concurrent decrease of signal intensity in the adjacent IML and OML following HFS of the MPP. These data indicate a stimulation-induced homosynaptic LTP in the MML (Fukazawa et al., 2003) and a concurrent depression in the IML and OML, which could correspond to heterosynaptic LTD in the OML (Abraham et al., 2007) and a possible similar effect in the IML.

Structural plasticity of dendritic spines in adult newborn granule cells following 2 h high-frequency perforant path stimulation

We then took advantage of existing correlations between spine size and synaptic strength (Alvarez and Sabatini, 2007) to study the effects of HFS on structural spine plasticity we used the same grid-based spine size classification as in Figure 2b to discriminate between small ($< 0.2 \mu\text{m}^2$) and large ($> 0.2 \mu\text{m}^2$) spines and again analyzed only those dendritic compartments that could be traced until the cell soma. Using this approach, we were able to study layer-specific changes of spines in the same dendritic tree at the level of individual cells (see Methods). Within the MML, following 2 h HFS, the spine density remained unchanged at any age, both in abGCs and mGCs (Fig. 4c). However, we observed a decrease in the density of small spines (Fig. S1c) and an increase in density of large spines (Fig. S1d) in stimulated abGCs. The result was a significant gain in the percentage of large spines within the ipsilateral MML of abGCs (Fig. 4d) at 28 dpi (from $15.55 \pm 1.32 \%$ to $24.50 \pm 1.35 \%$), 35 dpi (from $15.83 \pm 0.89 \%$ to $22.39 \pm 2.35 \%$), and 77 dpi (from $15.90 \pm 2.93 \%$ to $26.48 \pm 1.70 \%$), as well as in mGCs (from $15.49 \pm 1.42 \%$ to $30.86 \pm 5.61 \%$). Thus, HFS of the MPP induced structural plasticity and spine enlargement in the MML in abGCs from 28 dpi on as well as in mGCs.

While the total number of spines of abGCs and mGCs also remained unchanged in the adjacent OML (Fig. 4a), the density of small spines increased (Fig. S1a) and the density of large spines decreased (Fig. S1b), resulting in a significant decline in the percentage of large spines in the OML from 35 dpi on (at 35 dpi from $14.31 \pm 0.82 \%$ to $8.22 \pm 0.33 \%$, at 77 dpi from $15.73 \pm 1.39 \%$ to $8.80 \pm 1.28 \%$ and in mGCs from $12.65 \pm 1.55 \%$ to $7.02 \pm 2.59 \%$; Fig. 4b). Although a similar trend of a decline of large spines was observed in the IML, we found no significant changes in the percentage of large versus small spine size in the IML of abGCs and mGCs (Fig. 4e, f and Fig. S1e, f).

These results indicate that HFS of the MPP leads to a robust homosynaptic spine enlargement in the (directly activated) MML in abGCs from 28 dpi on and mGCs. Furthermore, concurrent heterosynaptic spine shrinkage was found in the adjacent OML in abGCs starting at 35 dpi and in mGCs. Interestingly,

stimulation-induced spine enlargement in the MML and spine shrinkage in the OML were found on adjacent dendritic segments of the same identified GCs, providing structural evidence for activity-dependent localized spine plasticity in the same neuron under *in vivo* conditions.

We found a sharp increase of structural spine plasticity between 28 dpi and 35 dpi indicating a critical time window for synaptic integration of abGCs. In order to elucidate the gradual changes of spine size following HFS in more detail, we performed a direct measurement of the largest cross-sectional area of all spine heads in confocal z-stacks of dendritic segments from RV-GFP labeled abGCs at 28 dpi and 35 dpi (Fig. 5).

The average area of spine heads in the MML increased from $0.13 \pm 0.01 \mu\text{m}^2$ (28 dpi) to $0.160 \pm 0.002 \mu\text{m}^2$ (35 dpi) in abGCs contralateral to the stimulation. We applied thresholds of $0.15 \mu\text{m}^2$, $0.2 \mu\text{m}^2$, and $0.25 \mu\text{m}^2$ to these datasets to differentiate between small and large spines and to analyze the size changes of larger spines (Fig. 5 insets). At 28 dpi, spines in the MML were affected by 2 h HFS (Fig. 5c) as indicated by an increase from $14.09 \pm 1.65 \%$ to $22.01 \pm 1.66 \%$ (threshold of $0.2 \mu\text{m}^2$). There were no significant changes in the OML (Fig. 5a) and the IML (Fig. 5e) following HFS. At 35 dpi, abGCs showed an increase of spine head size in the MML at a threshold of $0.25 \mu\text{m}^2$ from $12.45 \pm 0.51 \%$ to $18.24 \pm 3.62 \%$ (Fig. 5d). In contrast, spines in the OML and IML (Fig. 5 b and f) showed a decrease in size at a threshold of $0.2 \mu\text{m}^2$ (OML: $20.19 \pm 2.90 \%$ to $10.51 \pm 0.70 \%$; IML: from $11.66 \pm 1.08 \%$ to $5.02 \pm 0.72 \%$). The existence of synaptic contacts on labeled abGCs spines within the MML were verified with ultrastructural examination of abGCs at 35 dpi (Fig. 5g, h).

In summary, the detailed spine head size measurements (Fig. 5) confirmed the grid-based size classification with a chosen threshold of $0.2 \mu\text{m}^2$ (Fig. 4) and showed once more the suitability of this method to detect homosynaptic structural plasticity in the MML and heterosynaptic plasticity in the OML. Furthermore, the detailed analysis provided significant evidence for additional heterosynaptically induced shrinkage of spines in the IML following HFS in abGCs at 35 dpi.

Cell-specific homeostatic effect of homo- and heterosynaptic changes in spine size

In order to investigate the cell-specific manifestation of homo- and heterosynaptic plasticity-related changes of spines, we analyzed individual cells labeled ipsilaterally following HFS (i.e. fully activated cells, Fig. 6a, b) and compared them to GCs within their respective cell age group (abGCs or mGCs) on the contralateral, non-stimulated side. The percentage of large spines in the MML was elevated ipsilaterally in comparison with the percentage on the contralateral side. In addition, the proportion of large spines was decreased in the IML and OML. Some abGCs already exhibited homo- and heterosynaptic structural plasticity at 21 dpi and 28 dpi following HFS on the ipsilateral side (21 dpi: 18.75 ± 3.61 %, 28 dpi: 19.82 ± 2.39 %; Fig. 6c). The percentage of homo- and heterosynaptic plasticity-positive cells increased with cell age (35 dpi: 51.28 ± 6.60 %), and reached mature levels in abGCs at 77 dpi (61.67 ± 8.33 %). No further increase (62.22 ± 2.22 %) was found in mGCs (Fig. 6c). The relative change in percentage of large spines across all groups showed an average increase of 169.50 ± 8.88 % in the MML, a decrease to 39.95 ± 4.59 % in the IML, and to 49.84 ± 5.72 % in the OML. There were no significant differences between abGCs of different cell ages or between abGCs and mGCs (Fig. 6d).

Percentages of large spines from the IML, MML, and OML of the same dendritic tree were averaged in order to estimate the total structural spine changes of individual abGCs (Fig. 6a, b). Interestingly, age-matched comparison between ipsilateral and contralateral GCs revealed no significant relative differences, indicating that the overall percentage of large spines remained stable (Fig. 6e; see also Fig. 4b, d, f). Thus, the elevation in the percentage of large spines in the ipsilateral MML by homosynaptic structural plasticity was counteracted by heterosynaptic structural plasticity in the adjacent IML and OML and normalized the degree of structural changes along the dendritic tree.

These findings demonstrate that homo- and heterosynaptic plasticity is present in some abGCs from 21 dpi on and gradually increases to mature levels at 77 dpi.

Discussion

In this study we show for the first time homosynaptic and heterosynaptic structural plasticity of dendritic spines in abGCs following 2 h stimulation of the perforant path *in vivo*. This provides novel structural evidence for synaptic plasticity in abGCs, consistent with an active role of abGCs in hippocampal learning and memory (Cameron and Glover, 2015).

Two hour HFS of the MPP led to LTP, associated with a strong Arc expression in the granule cell layer. The stimulated MML exhibited an increase of F-actin and synaptopodin expression as well as a significant enlargement of dendritic spines in abGCs from 28 dpi on, thus revealing robust and layer-specific molecular and structural correlates of a homosynaptic LTP in young abGCs. In addition, LTP following 2 h HFS of the MPP was accompanied by LTD as shown by control stimulation of the LPP. Furthermore, the expression of F-actin was reduced in the adjacent unstimulated OML, the termination site of the LPP, as well as the unstimulated IML. Dendritic spines of abGCs in the IML and OML showed a significant reduction in size from 35 dpi on, indicating heterosynaptic structural plasticity. In addition, homo- and heterosynaptic structural plasticity was also found on the level of individual abGCs from 21 dpi on, as well as in mature abGCs at 77 dpi, and at similar intensities in developmentally-born GCs.

We conclude that synaptic integration of abGCs into the entorhino-hippocampal pathway is a gradual process and requires at least 4-5 weeks until abGCs exhibit structural plasticity with a capacity comparable to mGCs in response to synaptic activation. The finding of layer-specific homo- and heterosynaptic plasticity within the same dendritic tree of individual GCs can be explained as a homeostatic mechanism on the cellular level in both abGCs and mGCs.

General spine development of abGCs

We analyzed the number and morphology of dendritic spines in RV-GFP-labeled abGCs at 21 dpi, 28 dpi, 35 dpi, and 77 dpi and compared them to AAV-GFP-labeled mGCs located in the contralateral, unstimulated DG. The number of spines increased from 21 dpi on, reaching a maximum density at 77 dpi with

no significant differences to mGCs (Fig 2). The percentage of large spines was almost constant between 10-15 % throughout all analyzed age groups, indicating that the rate of *de novo* formation of spines is proportional to their morphological development. Our data is consistent with earlier reports from rats and mice on the time course of spinogenesis in abGCs. The earliest time point of spine formation in abGCs was reported at 16 dpi for rats (Ohkawa et al., 2012) and mice (Zhao et al., 2006). An early sharp increase in spine density was observed between 16-18 dpi in rats (Ohkawa et al., 2012) and about one week later in mice (Zhao et al., 2006; Toni et al., 2007), supporting the general idea that abGCs mature faster in rats than in mice (Snyder et al., 2009). Reports in mice further showed a continuous increase during the following 8 weeks until abGCs reach a plateau at about 70 dpi. Spines can show a prolonged structural maturation, which is modulated by a variety of stimuli (Zhao et al., 2006; Toni et al., 2007, 2008). Because in our study abGCs at 77 dpi exhibited spine shapes and numbers comparable to mGCs, we conclude that in rats, spine maturation is completed by 11 weeks.

The characterization of spine formation in maturing abGCs is based on the analysis of dendritic segments located in the contralateral DG. The contralateral DG receives limited input from the ipsilateral entorhinal cortex (EC) via direct commissural and indirect multi-synaptic projections. The first pathway is known for only a sparse activation of GCs and lacking the capacity of LTP induction under normal, physiological conditions (Wilson et al., 1979, 1981; Wilson, 1981; Alvarez-Salvado et al., 2014). Our electrophysiological data showed a strong LTP induction of the ipsilateral EC-DG pathway, and no LTP-induction on the contralateral EC-DG pathway (Fig. 1c). Furthermore, The contralateral, non-stimulated DG showed no enhancement of Arc-expression in the GCL (Fig. 1) as well as no enhancement of the LTP-markers F-actin and synaptopodin (Fig. 3) in all stimulation experiments, which clearly indicates the absence of any direct or indirect (multi-synaptic) stimulation strong enough to induce LTP resulting in relevant changes in spine size. However, any possible indirect stimulation of the contralateral DG would likely lead to a potential overestimation of contralateral spine sizes, and thus would lead to an underestimation of the documented effects on the ipsilateral side. We therefore

chose the contralateral DG as a valuable control that allowed a direct comparison of the non-stimulated and stimulated side in each animal.

Induction of homo- and heterosynaptic plasticity following 2 h HFS of the medial perforant path

Two types of synaptic plasticity are in the focus of this paper: homosynaptic plasticity and potentiation, which is input-specific and occurs only at directly activated synapses, and heterosynaptic plasticity and depression, which can be induced at synapses that were not active during the induction of homosynaptic plasticity (Abraham et al., 2007). Both forms of plasticity have been well-studied in the DG and can be induced by stimulation of the perforant path *in vivo* (Abraham et al., 1985; Benuskova and Abraham, 2007; Jedlicka et al., 2015). Heterosynaptic plasticity has been discussed as a homeostatic mechanism for normalization of synaptic weights and maintenance of synaptic competition (Chistiakova et al., 2015).

In our experiments, HFS of the MPP induced a robust homosynaptic LTP and heterosynaptic LTD of the LPP (also reported by Abraham et al., 2007). LTP induction was accompanied by a layer-specific accumulation of F-actin and synaptopodin in the stimulated MML, which is in agreement with the observations described by Fukazawa and colleagues (Fukazawa et al., 2003) indicating that the applied stimulation protocol and procedure were specific in targeting fibers of the MPP and activated mainly synapses located in the MML. Fukuzawa et al. (2003) showed that LTP induction in the DG by stimulating the perforant path *in vivo* leads to a long-lasting NMDA receptor-dependent reorganization of F-actin. In addition, they found a layer-specific increase of several marker proteins of synaptic activity, including synaptopodin. Synaptopodin is an actin-binding protein, which is functionally linked to the formation of the spine apparatus and it was demonstrated that synaptopodin deficiency leads to an impairment of LTP (Deller et al., 2003; Jedlicka et al., 2009).

Intriguingly, we also found a significant decrease of F-actin in the adjacent unstimulated IML and OML after stimulation of the MML. F-actin, as a component of the cytoskeleton, is associated with the plasma membrane and organization of the postsynaptic density (PSD) in dendritic spines and plays a crucial role in synaptic plasticity and the definition of spine morphology (Bosch and Hayashi, 2012). Polymerization of actin filaments is required for stable LTP (Kim and Lisman, 1999; Huber et al., 2004) whereas LTD is accompanied by depolymerization of F-actin (Okamoto et al., 2004). Thus, our data suggest that actin could be involved not only in the regulation of homosynaptic LTP, but also heterosynaptic LTD.

Given the well-described role of F-actin and synaptopodin in synaptic plasticity, we conclude that the applied HFS protocol in our study was suitable to induce a robust input-specific homosynaptic structural LTP at directly stimulated GC-synapses of the MML (Fukazawa et al., 2003) and likely a concurrent heterosynaptic structural LTD at the unstimulated GC-synapses in the OML (Abraham et al., 2007) and possibly also in the IML (Benuskova and Abraham, 2007; Beňušková and Jedlička, 2012).

Homo- and heterosynaptic structural changes of spines in abGCs following 2 h HFS

We observed an enlargement of spines in dendritic segments located in the stimulated MML in abGCs from 28 dpi on and shrinkage of spines in the adjacent non-stimulated IML and OML from 35 dpi on. Spine size is positively correlated to the size of the postsynaptic density (PSD) and the number of glutamate receptors, and thus with synaptic strength (Reymann and Frey, 2007). Induction of LTP is associated with spine enlargement (Huber et al., 2004), and LTD with spine shrinkage (Zhou et al., 2004). Induction of homosynaptic LTP and heterosynaptic LTD at the perforant path synapse should consequently manifest in a change of spine size, as found in our study. It is heavily debated if LTP is accompanied by a *de novo* formation of spines or morphological changes of pre-existing spines (Popov et al., 2004; Wosiski-Kuhn and Stranahan, 2012). In fact, this may depend on the plasticity-inducing protocols used in different studies. We could not see a change in the overall

number of spines following stimulation, indicating that our LTP protocol did not induce changes in spine density. Importantly, tracing dendritic segments from the cell soma to the hippocampal fissure allowed us to study structural changes following HFS in the IML, MML, and OML within the same cell. GCs with induced heterosynaptic plasticity were identified by showing an enlargement of spines in the MML and shrinkage of spines in the IML and OML in comparison to the contralateral, non-stimulated hemisphere. Heterosynaptic plasticity has been reported previously only in the MML and OML, but not in the IML of the DG. Therefore, to our knowledge, these results provide not only the first evidence for heterosynaptic plasticity in abGCs but also the first experimental evidence for heterosynaptic plasticity at commissural/associational IML synapses, as it has been predicted by computational modeling (Beňušková and Jedlička, 2012). We found stimulation-induced layer-specific homo- and heterosynaptic plasticity on neighboring IML, MML, and OML segments of the dendritic tree in individual abGCs and mGCs. About 20 % of abGCs exhibited heterosynaptic plasticity from 21 dpi on, and starting at 35 dpi, there was a sharp increase to ~60 %, with no further change at 77 dpi or in comparison to developmentally-born GCs. The effective relative change of structural spine plasticity was equal between all groups. Interestingly, our data revealed that heterosynaptic shrinkage of spines counteracted homosynaptic spine enlargement. The percentage of large spines in abGCs and mGCs showed no net change along the dendritic tree compared to unstimulated control GCs. These findings support the idea of heterosynaptic plasticity as a homeostatic mechanism for normalization of synaptic weights (Chistiakova et al., 2015) and no *de novo* formation of spines.

A critical time period for integration of abGCs

Various lines of evidence from several studies point to a critical phase for integration of abGCs in the hippocampal network between 4-6 weeks of cell age (Schmidt-Hieber et al., 2004; Ge et al., 2007; Mongiat et al., 2009; Marín-Burgin et al., 2012; Temprana et al., 2014; Martínez-Canabal, 2015). In this study, the majority of abGCs showed a transition from homo- without heterosynaptic plasticity at 28 dpi to homosynaptic together with concurrent heterosynaptic

plasticity from 35 dpi on. In a previous study, we analyzed the time course of LTP induction by expression of IEGs in abGCs following 2 h HFS of the perforant path in adult rats (Jungenitz et al., 2014). *De novo* transcription of IEGs (e.g. c-fos and Arc) has been shown to be required for long-lasting LTP and synaptic plasticity (Fleischmann et al., 2003; Bramham et al., 2008). We identified a sharp increase in the ability of abGCs to respond to LTP stimulation with expression of IEGs between 28 dpi and 35 dpi (Jungenitz et al., 2014). Taken together, our findings imply a rapid period of synaptic integration of abGCs between 28 dpi and 35 dpi.

Between 4-6 weeks of age, abGCs pass through a critical time window that is characterized by an enhanced synaptic plasticity with a lowered threshold for LTP (Schmidt-Hieber et al., 2004; Ge et al., 2007). During this critical phase, coupling and response to feedback inhibition through GABAergic interneurons is weak, but during maturation GCs become gradually integrated into inhibitory circuits (Temprana et al., 2014). This transition may support a higher excitability in immature, but an increased inhibition in mature GCs. Using rabies virus-mediated retrograde tracing, evidence of early local connections to the hippocampal network has been reported, as well as long range afferent projections from the entorhinal cortex via the perforant path in a rapidly increasing quantity from 21 dpi on, providing evidence for increasing connectivity through the critical phase of 4-6 weeks (Vivar et al., 2012; Deshpande et al., 2013).

We conclude that during their development, abGCs pass through a process of structural maturation until the 3rd week, followed by a gradual integration into the hippocampal network at a critical time period between 4-5 weeks of age, and a further synaptic maturation until 11 weeks when abGCs appear to be comparable to developmentally born mGCs. The finding of robust homo- and heterosynaptic structural plasticity during the critical time period of synaptic integration is consistent with the general view that abGCs contribute to hippocampus-specific forms of learning and memory (Cameron and Glover, 2015).

Material and Methods

Animals

Adult male Sprague-Dawley rats (8-13 weeks, 220-450 g; Charles River, Sulzfeld, Germany) were housed under standard laboratory conditions in large rat cages (30 cm x 40 cm). All animal experiments were performed in conformance with German guidelines for the use of laboratory animals.

Retrovirus production

HEK293T cells were co-transfected with pCAG-GFP, pCMV-GP and pCMV-VSV-G (3:2:1) plasmids by Calcium-Phosphate precipitation. The media containing retrovirus was collected 48 h after transfection. Cell debris was removed from the supernatant by centrifugation at 3200 x g for 10 min and filtration through a 0.22 µm filter. The retrovirus was concentrated by ultracentrifugation at 160000 x g for 2 h (Sorvall WX Ultracentrifuge and SureSpin 630 swinging bucket rotor; Thermo Fisher Scientific, Waltham, MA, U.S.A.). The retroviral pellet was resuspended in 200 µl phosphate buffered saline (PBS; Sigma-Aldrich, St. Louis, MO, U.S.A.), aliquoted and stored at -80 °C. The titer was at 10⁵ colony forming units.

Adeno-associated virus production

HEK293T cells were co-transfected with pDP1rs, pDG and GFP-vector-plasmid (6:4:1) by Calcium-Phosphate precipitation. The transfected cells were collected 48 h after transfection. Cells were washed (2 times) by centrifugation at 1500 x g for 5 min and resuspended in PBS. The viral particles inside the cells were set free by multiple freeze thaw cycles (4 times). The supernatant was collected and washed by centrifugation at 3200 x g for 10 min. The AAV containing supernatant was aliquoted and stored at -80 °C.

Intra-hippocampal viral in vivo injection

All surgical procedures were performed under deep Medetomidin (Domitor; Pfizer, New York City, NY, U.S.A.), Midazolam (Dormicum; Roche, Basel, Switzerland) and Fentanyl (Janssen Pharmaceutica, Beerse, Belgium)

anesthesia (150 µg Medetomidin, 2 mg Midazolam, 5 µg Fentanyl per kg body weight i.m. initially and additional injections as needed), in agreement with the German law on the use of laboratory animals. Animals were placed in a Kopf stereotaxic device (Kopf instruments, Tujunga, CA, U.S.A.). Two small holes (1.5-2.0 mm diameter) were drilled in the skull at -3.8 mm from Bregma and 2.2 mm laterally at both hemispheres. A NanoFil syringe (World Precision Instruments, Inc., Sarasota, FL, U.S.A.) with a 35 gauge beveled needle (NF35BV-2; World Precision Instruments) was used to slowly inject 0.75 µl of the viral solution at 3.2 mm and 3.7 mm below the brain surface into the dentate gyrus (both hemispheres).

Retrovirally-mediated labeling of abGCs is a well-established method (van Praag et al., 2002) utilized by an increasing number of publications characterizing adult neurogenesis. GFP expression of AAV-transduced GCs was controlled by a Synapsin I promotor. Synapsin I is increasingly active when synapse formation starts (Valtorta et al., 2011). The AAV lacks cell type specificity in general, but expression of GFP is limited to mature neurons with established synapses only. AAV-GFP-labeled GCs were identified by their morphology, and to further ensure that predominantly developmentally and perinatally born GCs were analyzed, we selected AAV-GFP-labeled GCs based on their location in the upper half of the GCL, as it has been shown that abGCs remain located in the inner part of the GCL (Radic et al., 2015). Therefore, and because perinatally born GCs form the dominant population of GCs, we assume that AAV-GFP-labeled GCs represent the pool of developmentally-born GCs (mGCs).

Perforant path stimulation *in vivo*

All surgical procedures for perforant path stimulation were performed under deep urethane anesthesia (1.25 g/kg body weight s. c. initially and additional injections as needed; 250 mg urethane/ml 0.9 % saline; Sigma-Aldrich), in agreement with the German law on the use of laboratory animals. Surgery and stimulation procedures were performed as previously described (Jungenitz et al., 2014). In short, animals were placed in a Kopf stereotaxic device (Kopf instruments). Rectal temperature was maintained at 37.0±0.5 °C. Two small

holes (1.5-2.0 mm diameter) were drilled in the skull and a bipolar stainless steel stimulating electrode (NE-200; Rhodes Medical, Woodland Hills, CA, U.S.A.) was placed in the angular bundle of the MPP (coordinates from lambda: L: 4.5 mm; AP: +0.5 mm; V: -3.5 mm measured from the surface of the brain). Glass microelectrodes (1.5 mm outer diameter) were pulled on a Zeitz (München, Germany) electrode puller, filled with 0.9 % saline, and placed in the dorsal blade of the granule cell layer (coordinates from bregma: L: 2.0 mm, AP: -3.5 mm, V: -3.5 mm). The vertical tip position of the recording electrode was optimized under low voltage perforant path control stimulation pulses (500 μ A, 0.1 ms pulse duration, 10 s interpulse interval) using the characteristic shape of the evoked field potentials.

Subsequently, high-frequency stimulation (HFS) maximally evoked population spikes and induced robust long-term potentiation (LTP) as has been described in detail before (Steward et al., 1998; Jungenitz et al., 2014). HFS was applied for 2 h at the MPP. One HFS train consisted of 8 pulses (500 μ A, 0.1 ms pulse duration) of 400 Hz once per 10 s. Two hour HFS was applied in RV-GFP transduced animals 21 dpi (n = 4), 28 dpi (n = 6), 35 dpi (n = 5) and 77 dpi (n = 4) and in AAV-GFP (n = 3) transduced animals 14 dpi. Directly after 2 h of HFS, rats were deeply anesthetized with urethane, and transcardially perfused with a fixative containing 4 % PFA in 0.1 M PBS, pH 7.4. Brains were removed and postfixed for up to 18 h.

LTP induction at the MPP is known to generate heterosynaptic LTD at the LPP (Abraham et al., 1985, 2007). In a separate experimental group (n = 6 animals), a second concentric stimulation electrode was placed in the LPP (coordinates from lambda: L: 5.5 mm; AP: +0.5 mm; V: -3.5 mm measured from the surface of the brain) to concurrently record evoked field potentials in the DG by stimulation of the LPP or MPP. The medio-lateral position of the lateral stimulation electrode in the LPP was optimized and confirmed by low intensity paired pulse stimulation at 20 ms interpulse interval, which is known to result in paired pulse facilitation and increase of the second slope by LPP and not by MPP stimulation (Petersen et al., 2013). HFS was applied to the MPP as described above. Control stimulation pulses were applied separately either to

the MPP (500 μ A, 0.1 ms pulse duration, 10 s interpulse interval) or the LPP (800 μ A, 0.1 ms pulse duration, 10 s interpulse interval) to evoke and record field potentials before, during and after HFS.

In order to estimate the effects of HFS of the MPP on the contralateral EC-DG pathway, an additional stimulation and recording electrode were placed on the opposite, contralateral hemisphere at laterally-inversed positions mentioned above ($n = 3$ animals). Control stimulation pulses (500 μ A, 0.1 ms pulse duration, 10 s interpulse interval) were applied separately either to the ipsilateral or the contralateral MPP to evoke and record field potentials before, during and after HFS. For the analysis of the slope of evoked field potential, only the early component of the response was measured to avoid contamination by the population spike.

Tissue preparation

Serial frontal sections of the hippocampus (300 μ m) were cut with a vibratome, washed in 0.1 M TRIS buffered saline (TBS; AppliChem, Darmstadt, Germany), and stored at -20°C in cryoprotectant solution (30 % ethylene glycol, 25 % glycerin in PBS). 300 μ m serial frontal sections were used to allow reconstructions of complete GC dendritic trees (not in the focus of this study). Subsequently, sections were cut to 50 μ m with a vibratome, washed in 0.1 M TBS, and stored at -20°C in cryoprotectant solution. All histological examinations were performed on 50 μ m sections.

Immunohistochemistry

Free-floating sections were washed in TBS, blocked with 5 % bovine serum albumin (BSA; New England BioLabs, Ipswich, MA, U.S.A.) containing 0.1 % Triton X-100 for 1 h at room temperature to reduce non-specific staining and incubated in primary antibody solution containing 2 % BSA, 0.25 % Triton X-100, 0.1 % NaN_3 in 0.1 M TBS for 48 h at room temperature. The following primary antibodies were used: anti-Arc (rabbit, polyclonal, 1:1000; Synaptic Systems, Göttingen, Germany), anti-GFP488 (mouse, 1:500, fluorescence-labeled Alexa 488; Sigma-Aldrich), anti-Synaptopodin (guinea pig, polyclonal, 1:1000; Synaptic Systems). For fluorescence-immunohistochemical detection,

sections were incubated with secondary fluorescence-labeled antibodies (1:1000; Alexa 488, 568; Vector Labs., Burlingame, CA, U.S.A.) for 24 h at room temperature.

For detection of F-actin, free-floating sections were washed in TBS, blocked with 5 % BSA for 1 h at room temperature, and incubated with Phalloidin-Alexa 568 (1:200; MoBiTec, Göttingen, Germany) for 24 h at room temperature.

Immunohistochemical quantification

For expression analysis of Arc expression, all GFP-labeled granule cells located on a section (ipsilateral and contralateral) were imaged using a confocal microscope (Nikon Eclipse80i; Nikon, Shinagawa, Tokyo, Japan) and a 40x oil immersion objective (N.A. 1.3; Nikon) with a step distance of 2 μm .

For analysis of F-actin expression, image stacks (step distance of 5 μm , 6 images) were acquired from 2 frontal sections of the ipsilateral and contralateral dentate gyrus molecular layer (3 image stacks per section, suprapyramidal and infrapyramidal blade) using a confocal microscope (Nikon Eclipse 80i; Nikon) and a 20x objective (N.A. 1.3; Nikon). The field zoom was adjusted to include the molecular layer from the granule cell-inner molecular layer-border to the hippocampal fissure. Image stacks were rotated and cropped to align samples using ImageJ (website: imagej.nih.gov/ij/). Profiles of the mean fluorescence-intensity were measured from the first image (showing the section surface) of each image stack using ImageJ. Due to differences in the length between molecular layer samples, fluorescence-intensity profiles were resampled to 100 data points using Matlab (MathWorks, Natick, MA, U.S.A.). The mean fluorescence-intensity of the complete molecular layer showed no significant differences between the ipsilateral and contralateral hemispheres and was therefore used to normalize the fluorescence-intensity profiles. Profiles were divided into the inner, middle and outer molecular layer (IML: 1-27, MML: 28-64, OML: 65-100) and further averaged into two data points per layer, which were used for statistical analysis.

Image acquisition and analysis of dendritic spines

For dendritic spine analysis, segments of GFP-labeled granule cells were imaged using a confocal microscope (Nikon Eclipse 80i; Nikon) and a 60x oil immersion objective (N.A. 1.3; Nikon) with a 5x field zoom and a step distance of 0.5 μm . Only dendritic segments with a visual connection to the cell soma were used for imaging, to ensure a reliable analysis of layer specific differences within the same cell. Only GFP-labeled cells located in a section with robust Arc expression were used. The imaging window for IML located dendritic segments was set adjacent to the GCL, for the OML close to the hippocampal fissure (with a distance of 5 to 10 μm from the fissure), and the MML in the center between the IML and the OML. 2-4 segments were imaged per cell and layer.

The length of a sampled dendritic segment was measured in a z-projection by manual tracing the center of the dendritic shaft (the mean length was approximately 42 μm). Spines were counted in the image stack. Only spines exhibiting a visible spine neck and head were used for the analysis. Spine morphology and size is highly dynamic and correlated to the size of the postsynaptic density (PSD) and the number of glutamate receptors (Alvarez and Sabatini, 2007). Small spines exhibit the ability to potentiate, whereas large spines are more stable and associated with larger synapses. In the literature, large spines with bulbous heads and head diameters $> 0.6 \mu\text{m}$ are also referred to as mushroom-spines (Sorra and Harris, 2000). Accordingly, we classified spines into small and large spines using a grid overlay with a grid element size set to $0.2 \mu\text{m}^2$ (square diagonal $\sim 0.6 \mu\text{m}$, see Fig. 2b). Spines were assigned to the class of small spines when the spine head appeared visually smaller than a grid element or to the class of large spines when visually larger than a grid element. The number of spines was normalized to the length of the dendritic segment ($\#/\mu\text{m}$).

The specific spine size was measured by manually tracing the largest cross-sectional area of the spine head using Fiji (Schindelin et al., 2012) and a graphic tablet (Wacom, Kazo, Saitama, Japan). In average, 60 spines per ABGC and layer were measured from 3 ipsi- and 3 contralateral cells at 28 dpi and 5 ipsi- and 5 contralateral cells at 35 dpi.

GFP-labeled GCs shown in Fig. 2a and Fig. 6a were edited in order to isolate the cells from surrounding fluorescent structures.

Electron Microscopy

Deeply anesthetized rats were transcidentally perfused with a fixative containing 4 % PFA (in 0.1 M PBS, pH 7.4), 2 % glutaraldehyde (Polysciences Europe GmbH, Eppelheim, Germany) and 0.1 M sodium cacodylate buffer (Science Services, München, Germany). Brains were removed and postfixed for up to 18 h. Serial frontal sections of the hippocampus (50 μ m) were cut with a vibratome.

Sections were washed in TBS, incubated in 0.1 % NaBH₄ (Sigma-Aldrich) and blocked with 5 % BSA containing 0.1 % Triton X-100 for 1 h at room temperature to reduce non-specific staining. Antibody solutions contained 2 % BSA, 0.25 % Triton X-100 in 0.1 M TBS. For detection of GFP-labeled cells, anti-GFP (goat, 1:500, 18 h, room temperature; Acris, Herford, Germany) was used as primary antibody and a biotinylated anti-Goat IgG (1:200, 60 min room temperature; Vector Laboratories, Burlingame, CA) as secondary antibody. After washing in TBS, sections were incubated in avidin-biotin-peroxidase complex (ABC-Elite, Vector Laboratories) for 90 min (room temperature) and reacted with nickel-diaminobenzidine solution (Vector Laboratories) for 2-15 min (room temperature). Sections were silver-intensified by the following steps: incubation in 3 % hexamethylenetetramine (Sigma-Aldrich), 5 % silvernitrate (AppliChem) and 2.5 % di-sodiumtetraborate (Sigma-Aldrich) for 10 min (60 °C); 1 % tetrachlorogold (AppliChem) solution for 3 min and 2.5 % sodiumthiosulfate (Sigma-Aldrich) for 3 min. Between each step, sections were washed thoroughly in distilled water.

After staining, the sections were washed in cacodylate buffer, osmicated (0.5 % OsO₄ (Plano, Wetzlar, Germany) in cacodylate buffer), dehydrated (1 % uranyl acetate (Serva, Heidelberg, Germany) in 70 % ethanol), and embedded in durcupan (Sigma-Aldrich). Sections were collected on single-slot Formavar-coated copper grids and examined using a Zeiss electron microscope (Zeiss EM 900).

Statistical analysis

Data management, statistical analysis, and visualization were done with Microsoft Excel (Microsoft, Redmond, Washington, U.S.A.) and GraphPad Prism 6 (Graphpad Software, San Diego, CA, U.S.A.). Statistical comparisons were calculated with the two-sided Wilcoxon rank-sum test (Fig. 3, 4, 5, 6, S1), the Kruskal-Wallis with Dunn's comparison test (Fig. 2, 6), the two-way ANOVA with Bonferroni correction (Fig. 3), or the Friedman with Dunn's multiple comparison test (Fig. 2). Significance level was set at $P < 0.05$. Group values are reported as means \pm SEM.

Acknowledgements

We are indebted to Ute Fertig and Anke Biczysko for technical assistance in preparing and staining of hippocampal slices and electron microscopy. This work was supported by the DFG (CRC 1180), the LOWE-Program "Neuronal Coordination Research Focus Frankfurt" (NeFF), the International Max-Planck Research School (IMPRS) for Neural Circuits in Frankfurt, and a BMBF grant (No. 01GQ1406 - Bernstein Award 2013) to HC.

References

Abraham WC, Bliss TVP, Goddard G V (1985) Heterosynaptic changes accompany long-term but not short-term potentiation of the perforant path in the anaesthetized rat. *J Physiol* 363:335–349.

Abraham WC, Logan B, Wolff A, Benuskova L (2007) “Heterosynaptic” LTD in the dentate gyrus of anesthetized rat requires homosynaptic activity. *J Neurophysiol* 98:1048–1051.

Alvarez V a, Sabatini BL (2007) Anatomical and Physiological Plasticity of Dendritic Spines. *Annu Rev Neruoscience* 30:79–97.

Alvarez-Salvado E, Pallarés V, Moreno A, Canals S (2014) Functional MRI of long-term potentiation: imaging network plasticity. *Philos Trans R Soc Lond B Biol Sci* 369:20130152.

Amaral D, Scharfman H, Lavenex P (2007) The dentate gyrus: fundamental neuroanatomical organization (dentate gyrus for dummies). *Prog Brain Res* 153:390–394.

Beňušková Ľ., Jedlička P. (2012) Computational modeling of long-term depression of synaptic weights: Insights from stdp, metaplasticity and spontaneous activity. *Neural Netw World* 22:161–180.

Benuskova L, Abraham WC (2007) STDP rule endowed with the BCM sliding threshold accounts for hippocampal heterosynaptic plasticity. *J Comput Neurosci* 22:129–133.

Bosch M, Hayashi Y (2012) Structural plasticity of dendritic spines. *Curr Opin Neurobiol* 22:383–388.

Bramham CR, Worley PF, Moore MJ, Guzowski JF (2008) The immediate early gene *arc/arg3.1*: regulation, mechanisms, and function. *J Neurosci* 28:11760–11767.

Cameron HA, Glover LR (2015) Adult Neurogenesis: Beyond Learning and Memory. *Annu Rev Psychol* 66:53–81.

Chistiakova M, Bannon NM, Chen J-Y, Bazhenov M, Volgushev M (2015) Homeostatic role of heterosynaptic plasticity: models and experiments. *Front Comput Neurosci* 9:89.

Clelland CD, Choi M, Romberg C, Clemenson GD, Fragniere A, Tyers P, Jessberger S, Saksida LM, Barker R a, Gage FH, Bussey TJ (2009) A functional role for adult hippocampal neurogenesis in spatial pattern separation. *Science* (80-) 325:210–213.

Deller T, Korte M, Chabanis S, Drakew A, Schwegler H, Stefani GG, Zuniga A, Schwarz K, Bonhoeffer T, Zeller R, Frotscher M, Mundel P (2003) Synaptopodin-deficient mice lack a spine apparatus and show deficits in synaptic plasticity. *Proc Natl Acad Sci U S A* 100:10494–10499.

Denny CA, Kheirbek MA, Alba EL, Tanaka KF, Brachman RA, Laughman KB, Tamm NK, Turi GF, Losonczy A, Hen R (2014) Hippocampal Memory Traces Are Differentially Modulated by Experience, Time, and Adult Neurogenesis. *Neuron* 83:189–201.

Deshpande A, Bergami M, Ghanem A, Conzelmann K-K, Lepier A, Götz M, Berninger B (2013) Retrograde monosynaptic tracing reveals the temporal evolution of inputs onto new neurons in the adult dentate gyrus and olfactory bulb. *Proc Natl Acad Sci U S A* 110:E1152-61.

Fleischmann A, Hvalby O, Jensen V, Strekalova T, Zacher C, Layer LE, Kvello A, Reschke M, Spanagel R, Sprengel R, Wagner EF, Gass P (2003) Impaired long-term memory and NR2A-type NMDA receptor-dependent synaptic plasticity in mice lacking c-Fos in the CNS. *J Neurosci* 23:9116–9122.

Fukazawa Y, Saitoh Y, Ozawa F, Ohta Y, Mizuno K, Inokuchi K (2003) Hippocampal LTP is accompanied by enhanced F-actin content within the dendritic spine that is essential for late LTP maintenance in vivo. *Neuron* 38:447–460.

- Gage FH (2000) Mammalian neural stem cells. *Science* 287:1433–1438.
- Ge S, Yang C-H, Hsu K-S, Ming G-L, Song H (2007) A critical period for enhanced synaptic plasticity in newly generated neurons of the adult brain. *Neuron* 54:559–566.
- Huber L, Menzel R, Matsuzaki M, Honkura N, Ellis-Davies GCR, Kasai H (2004) Structural basis of long-term potentiation in single dendritic spines. *Nature* 429:761–766.
- Jedlicka P, Benuskova L, Abraham WC (2015) A Voltage-Based STDP Rule Combined with Fast BCM-Like Metaplasticity Accounts for LTP and Concurrent “Heterosynaptic” LTD in the Dentate Gyrus In Vivo. *PLoS Comput Biol* 11:e1004588.
- Jedlicka P, Schwarzacher SW, Winkels R, Kienzler F, Frotscher M, Bramham CR, Schultz C, Bas Orth C, Deller T (2009) Impairment of in vivo theta-burst long-term potentiation and network excitability in the dentate gyrus of synaptopodin-deficient mice lacking the spine apparatus and the cisternal organelle. *Hippocampus* 19:130–140.
- Jungenitz T, Radic T, Jedlicka P, Schwarzacher SW (2014) High-frequency stimulation induces gradual immediate early gene expression in maturing adult-generated hippocampal granule cells. *Cereb Cortex* 24:1845–1857.
- Kempermann G, Song H, Gage FH (2015) Neurogenesis in the Adult Hippocampus. *Cold Spring Harb Perspect Biol* 7:a018812.
- Kim CH, Lisman JE (1999) A role of actin filament in synaptic transmission and long-term potentiation. *J Neurosci* 19:4314–4324.
- Marín-Burgin A, Mongiat L a, Pardi MB, Schinder AF (2012) Unique processing during a period of high excitation/inhibition balance in adult-born neurons. *Science* 335:1238–1242.

Martínez-Canabal A (2015) Rewiring, forgetting and learning. Commentary: A critical period for experience-dependent remodeling of adult-born neuron connectivity. *Front Neurosci* 9:710–717.

Mongiati L a, Espósito MS, Lombardi G, Schinder AF (2009) Reliable activation of immature neurons in the adult hippocampus. *PLoS One* 4:e5320.

Nakashiba T, Cushman JD, Pelkey K a, Renaudineau S, Buhl DL, McHugh TJ, Barrera VR, Chittajallu R, Iwamoto KS, McBain CJ, Fanselow MS, Tonegawa S (2012) Young Dentate Granule Cells Mediate Pattern Separation, whereas Old Granule Cells Facilitate Pattern Completion. *Cell* 149:188–201.

Oh WC, Parajuli LK, Zito K (2015) Heterosynaptic Structural Plasticity on Local Dendritic Segments of Hippocampal CA1 Neurons. *Cell Rep* 10:162–169.

Ohkawa N, Saitoh Y, Tokunaga E, Nihonmatsu I, Ozawa F, Murayama A, Shibata F, Kitamura T, Inokuchi K (2012) Spine formation pattern of adult-born neurons is differentially modulated by the induction timing and location of hippocampal plasticity. *PLoS One* 7:e45270.

Okamoto K-I, Nagai T, Miyawaki A, Hayashi Y (2004) Rapid and persistent modulation of actin dynamics regulates postsynaptic reorganization underlying bidirectional plasticity. *Nat Neurosci* 7:1104–1112.

Petersen RP, Moradpour F, Eadie BD, Shin JD, Kannangara TS, Delaney KR, Christie BR (2013) Electrophysiological identification of medial and lateral perforant path inputs to the dentate gyrus. *Neuroscience* 252:154–168.

Popov VI, Davies H a., Rogachevsky V V., Patrushev I V., Errington ML, Gabbott PL a, Bliss TVP, Stewart MG (2004) Remodelling of synaptic morphology but unchanged synaptic density during late phase long-term potentiation (LTP): A serial section electron micrograph study in the dentate gyrus in the anaesthetised rat. *Neuroscience* 128:251–262.

Radic T, Al-Qaisi O, Jungenitz T, Beining M, Schwarzacher SW (2015) Differential Structural Development of Adult-Born Septal Hippocampal Granule Cells in the Thy1-GFP Mouse, Nuclear Size as a New Index of Maturation. *PLoS One* 10:e0135493.

Reymann KG, Frey JU (2007) The late maintenance of hippocampal LTP: requirements, phases, “synaptic tagging”, “late-associativity” and implications. *Neuropharmacology* 52:24–40.

Schindelin J, Arganda-Carreras I, Frise E, Kaynig V, Longair M, Pietzsch T, Preibisch S, Rueden C, Saalfeld S, Schmid B, Tinevez J-Y, White DJ, Hartenstein V, Eliceiri K, Tomancak P, Cardona A (2012) Fiji: an open-source platform for biological-image analysis. *Nat Methods* 9:676–682.

Schmidt-Hieber C, Jonas P, Bischofberger J (2004) Enhanced synaptic plasticity in newly generated granule cells of the adult hippocampus. *Nature* 429:184–187.

Snyder JS, Choe JS, Clifford MA, Jeurling SI, Hurley P, Brown A, Kamhi JF, Cameron HA (2009) Adult-born hippocampal neurons are more numerous, faster maturing, and more involved in behavior in rats than in mice. *J Neurosci* 29:14484–14495.

Sorra KE, Harris KM (2000) Overview on the structure, composition, function, development, and plasticity of hippocampal dendritic spines. *Hippocampus* 10:501–511.

Steward O, Wallace CS, Lyford GL, Worley PF (1998) Synaptic activation causes the mRNA for the IEG Arc to localize selectively near activated postsynaptic sites on dendrites. *Neuron* 21:741–751.

Temprana SG, Mongiat LA, Yang SM, Trincherro MF, Alvarez DD, Kropff E, Giacomini D, Beltramone N, Lanuza GM, Schinder AF (2014) Delayed Coupling to Feedback Inhibition during a Critical Period for the Integration of Adult-Born Granule Cells. *Neuron* 85:1–15.

- Toni N, Laplagne DA, Zhao C, Lombardi G, Ribak CE, Gage FH, Schinder AF (2008) Neurons born in the adult dentate gyrus form functional synapses with target cells. *Nat Neurosci* 11:901–907.
- Toni N, Sultan S (2011) Synapse formation on adult-born hippocampal neurons. *Eur J Neurosci* 33:1062–1068.
- Toni N, Teng EM, Bushong E a, Aimone JB, Zhao C, Consiglio A, van Praag H, Martone ME, Ellisman MH, Gage FH (2007) Synapse formation on neurons born in the adult hippocampus. *Nat Neurosci* 10:727–734.
- Valtorta F, Pozzi D, Benfenati F, Fornasiero EF (2011) The synapsins: Multitask modulators of neuronal development. *Semin Cell Dev Biol* 22:378–386.
- van Praag H, Schinder AF, Christie BR, Toni N, Palmer TD, Gage FH (2002) Functional neurogenesis in the adult hippocampus. *Nature* 415:1030–1034.
- Vivar C, Potter MC, Choi J, Lee J, Stringer TP, Callaway EM, Gage FH, Suh H, van Praag H (2012) Monosynaptic inputs to new neurons in the dentate gyrus. *Nat Commun* 3:1107.
- Wilson RC (1981) Changes in translation of synaptic excitation to dentate granule cell discharge accompanying long-term potentiation. I. Differences between normal and reinnervated dentate gyrus. *J Neurophysiol* 46:324–338.
- Wilson RC, Levy WB, Steward O (1979) Functional Effects of Lesio-Induced Plasticity: Long Term Potentiation in Normal and Lesion-Induced Temporodentate Connections. *Brain Res* 176:65–78.
- Wilson RC, Levy WB, Steward O (1981) Changes in translation of synaptic excitation to dentate granule cell discharge accompanying long-term potentiation. II. An evaluation of mechanisms utilizing dentate gyrus dually innervated by surviving ipsilateral and sprouted crossed temporodentate inp. *J Neurophysiol* 46:339–355.

Wosiski-Kuhn M, Stranahan AM (2012) Transient increases in dendritic spine density contribute to dentate gyrus long-term potentiation. *Synapse* 66:661–664.

Zhao C, Teng EM, Summers RG, Jr. M, G.I, Gage FH (2006) Distinct morphological stages of dentate granule neuron maturation in the adult mouse hippocampus. *J Neurosci* 26:3–11.

Zhou Q, Homma KJ, Poo MM (2004) Shrinkage of dendritic spines associated with long-term depression of hippocampal synapses. *Neuron* 44:749–757.

Figures

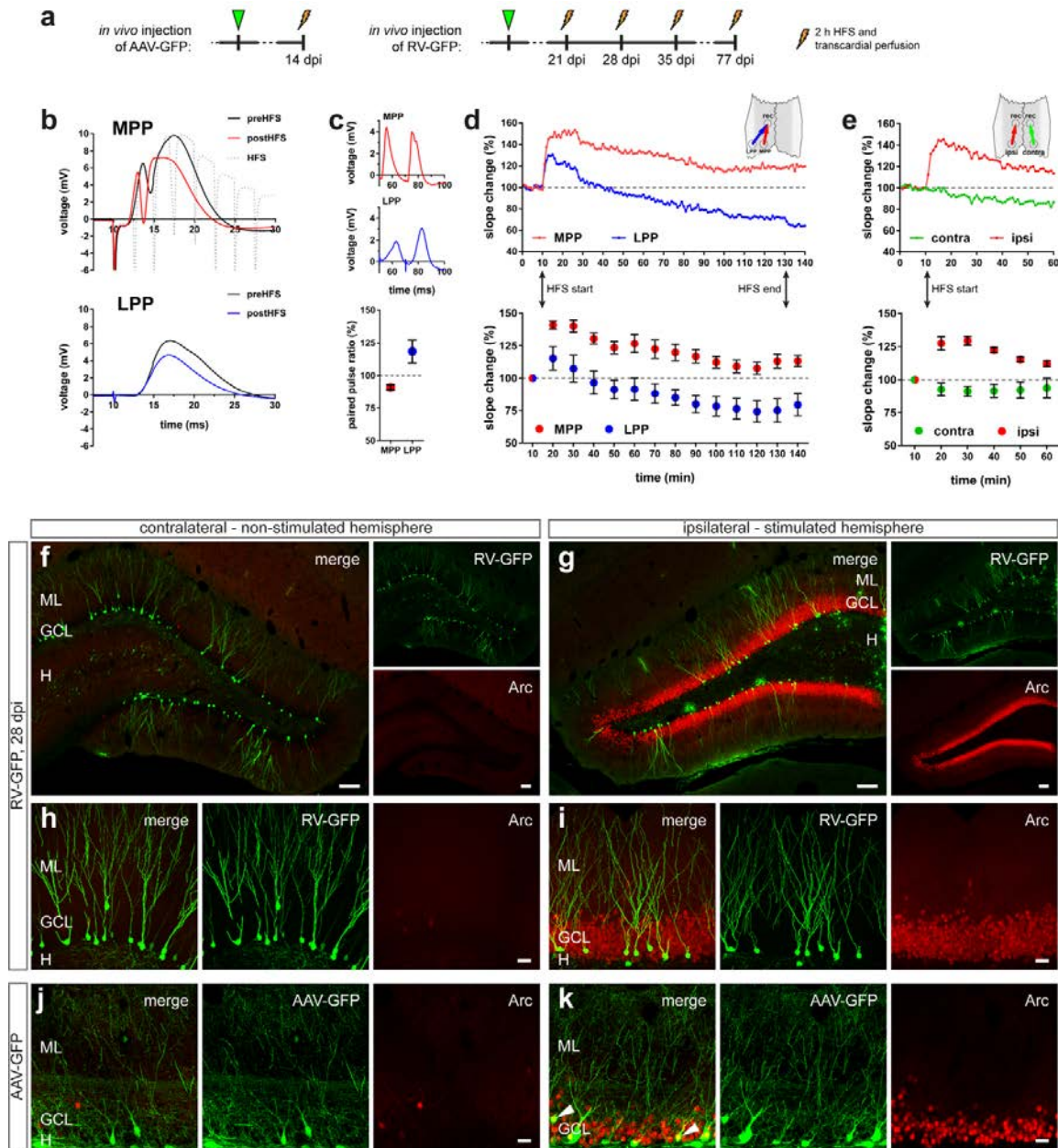


Figure 1 Expression of Arc in GFP-labeled young (RV-GFP) and mature (AAV-GFP) GCs following 2 h HFS.

(a) Local bilateral intra-hippocampal injections of a murine leukemia virus (RV-GFP, CAG promotor) or an adeno-associated virus (AAV-GFP, synapsin promotor) were performed for GFP-labeling (green) of abGCs (**f-i**) or mature neurons (**j, k**), respectively. Subsequently, HFS was applied (8 pulses at 400 Hz) to the medial perforant path (MPP). **(b)** In order to estimate homosynaptic induced LTP and heterosynaptic induced LTD, evoked local field potentials of GCS by MPP stimulation and lateral perforant path (LPP) stimulation were recorded in the DG before application of MPP HFS (black), during MPP HFS (grey dotted line) and following MPP HFS (MPP: red, LPP: blue). **(c)** Low intensity paired pulse stimulation with 20 ms interpulse-interval of the LPP resulted in paired pulse disinhibition and enlargement of the second pulse. **(d)** HFS of the MPP induced LTP via the MPP and LTD via the LPP (top: single animal time course, bottom: group time course). **(e)** Unilateral MPP HFS induced a strong LTP, which was restricted to the ipsilateral hemisphere (top: single animal time course, bottom: group time course). **(g, i, k)** Induction of LTP was accompanied by strong expression of Arc (red) in the ipsilateral granule cell layer (GCL) of the DG, including RV-GFP- and AAV-GFP-labeled GCs. **(f, h, j)** In contrast, the contralateral GCL showed only very sparse Arc labeling. White arrows indicate AAV-GFP- and Arc-labeled GCs. Number of animals: **(c, d)** n = 6, **(e)** n = 3. Scale bars: **(f, g)** 100 μ m, **(h-k)** 25 μ m. EC, entorhinal cortex; H, hilus; ML, molecular layer.

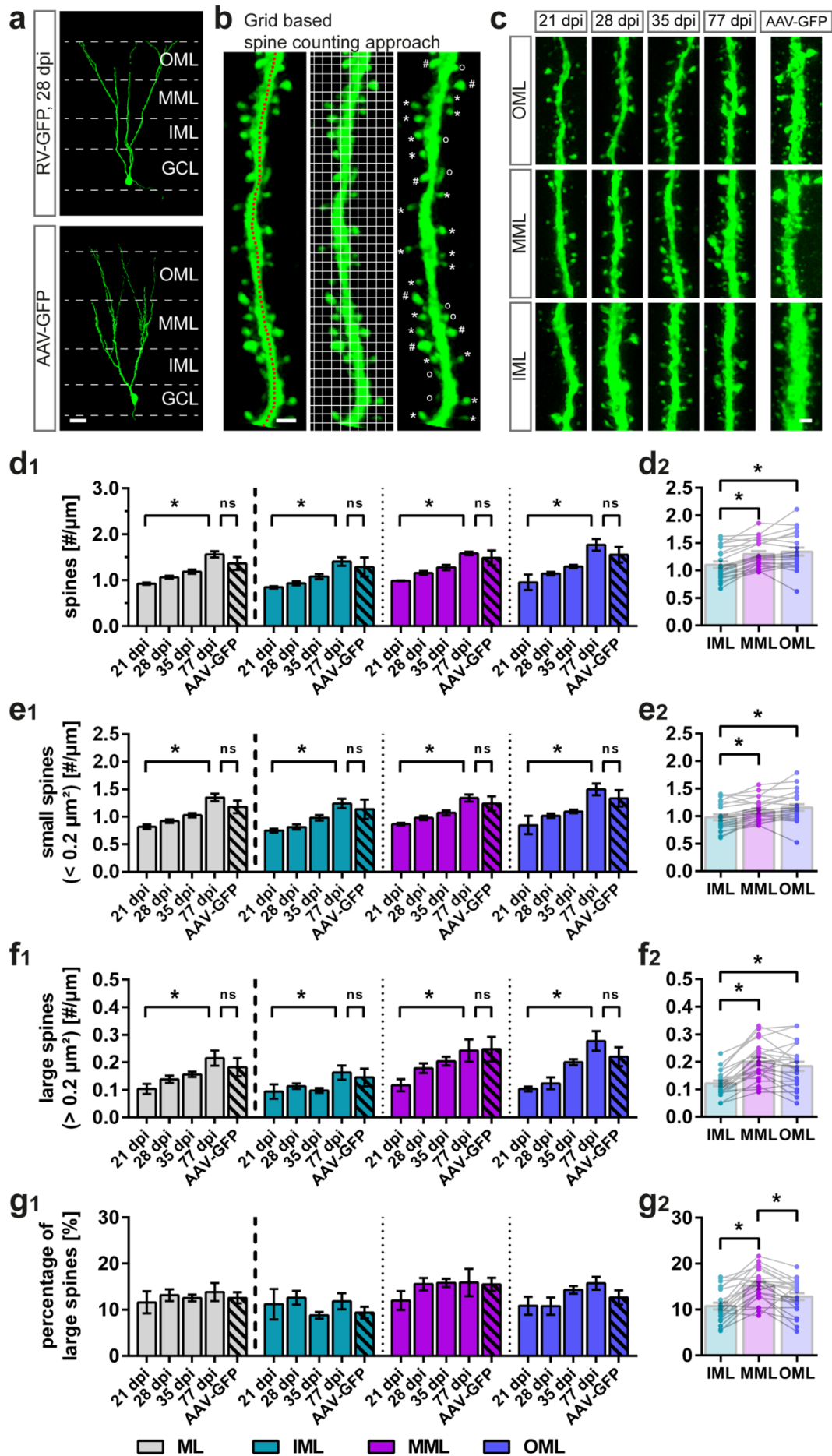


Figure 2 Time course of dendritic spine development in abGCs.

(a) Sample RV-GFP-labeled abGC at 28 dpi and AAV-GFP-labeled mGC, used to quantify dendritic spines in the inner (IML), middle (MML), and outer (OML) molecular layer during the development of abGCs and in mGCs. (b) The length of a dendritic segment was measured in a z-projection (left image, red dotted line), and a grid-based approach (middle image, grid size $0.2 \mu\text{m}^2$) was used to determine the density of spines in general and to differentiate between small ($< 0.2 \mu\text{m}^2$, indicated by stars) and large ($> 0.2 \mu\text{m}^2$, indicated by dashes) spines (right image). Spines without a spine neck and head were excluded from analysis (indicated by open circles). (c) Samples of dendritic segments from 21-77 dpi abGCs and mGCs showing spines in the IML, MML, and OML. (d₁) Density of spines in RV-GFP-labeled abGCs in the complete ML from 21-77 dpi and in AAV-GFP-labeled mGCs. (d₂) Density of spines per layer. (e₁) Density of small spines. (e₂) Density of small spines per layer. (f₁) Density of large spines. (f₂) Density of large spines per layer. (g₁) Percentage of large spines was calculated as relative amount of large spines from spine density. (g₂) Overall percentage of large spines per layer. Number of animals: $n_{21 \text{ dpi}} = 3$, $n_{28 \text{ dpi}} = 6$, $n_{35 \text{ dpi}} = 5$, $n_{77 \text{ dpi}} = 4$, $n_{\text{AAV-GFP}} = 4$. (d₁-g₁) Kruskal-Wallis with Dunn's multiple comparisons test (21 dpi vs. 77 dpi, 77 dpi vs. mGCs): * $P < 0.05$. (d₂-g₂) Friedman with Dunn's multiple comparisons test (IML vs. MML, IML vs. OML, MML vs. OML): * $P < 0.05$. Scale bars: (a) $25 \mu\text{m}$, (b, c) $1 \mu\text{m}$. GCL, granule cell layer; H, hilus.

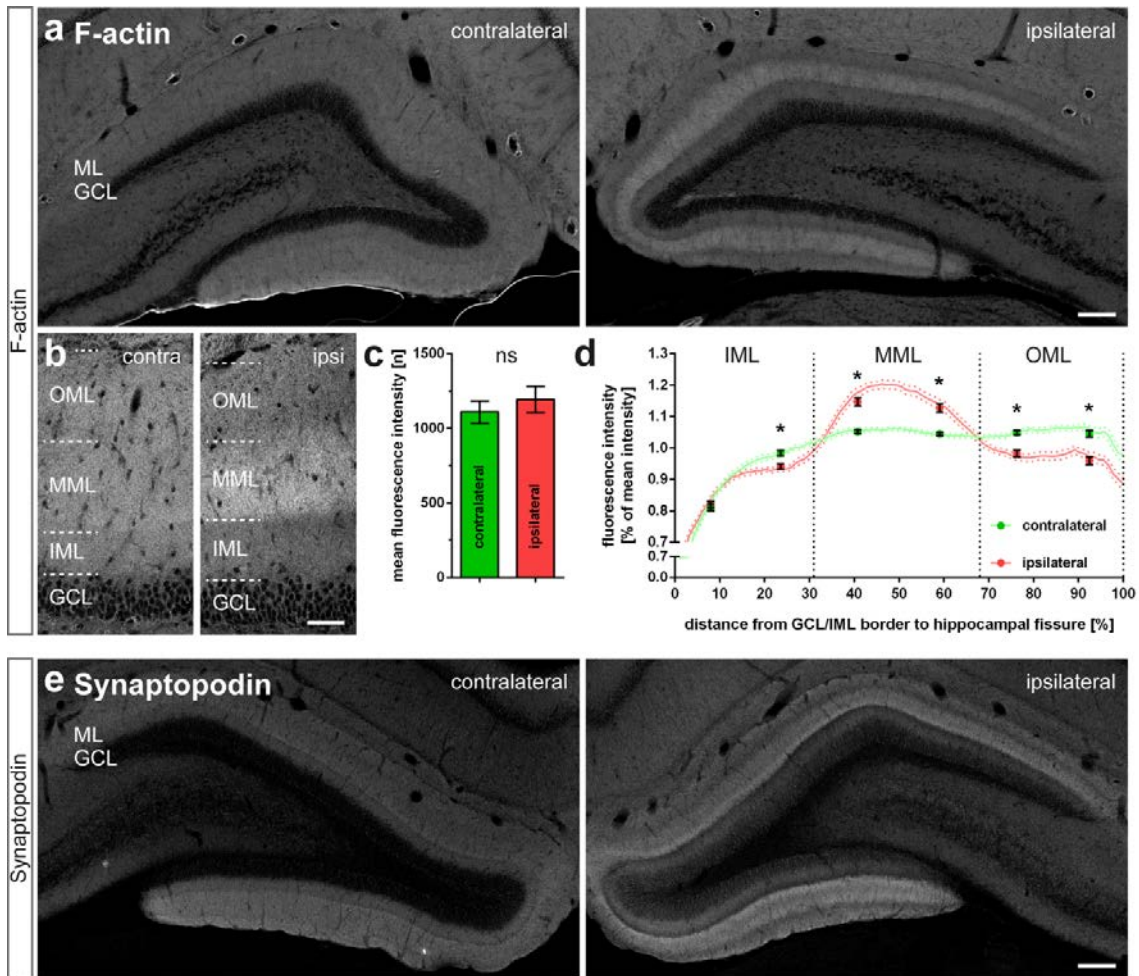


Figure 3 F-actin and synaptopodin are enhanced in the MML following 2 h HFS of the medial perforant path.

(a, b) Expression of F-actin following 2 h HFS. (c) Immunofluorescence intensity of the entire ML was not altered following HFS in the stimulated (ipsilateral, red) versus unstimulated (contralateral, green) side. (d) Normalized intensity profiles obtained across the ML (from the GCL-IML-border to the hippocampal fissure) revealed layer-specific changes of F-actin expression on the stimulated (ipsilateral, red line) side compared to the contralateral side (green line). (e) Note layer-specific changes of synaptopodin expression on the stimulated (ipsilateral) side. Number of animals: $n_{\text{F-actin}} = 21$. (c) Two-sided Wilcoxon rank-sum test: $*P < 0.05$. (d) Two-way ANOVA with Bonferroni correction: $*P < 0.05$. Scale bars: (a, e) $100 \mu\text{m}$, (b) $50 \mu\text{m}$. ipsi, ipsilateral; contra, contralateral; GCL, granule cell layer; H, hilus; ML, molecular layer.

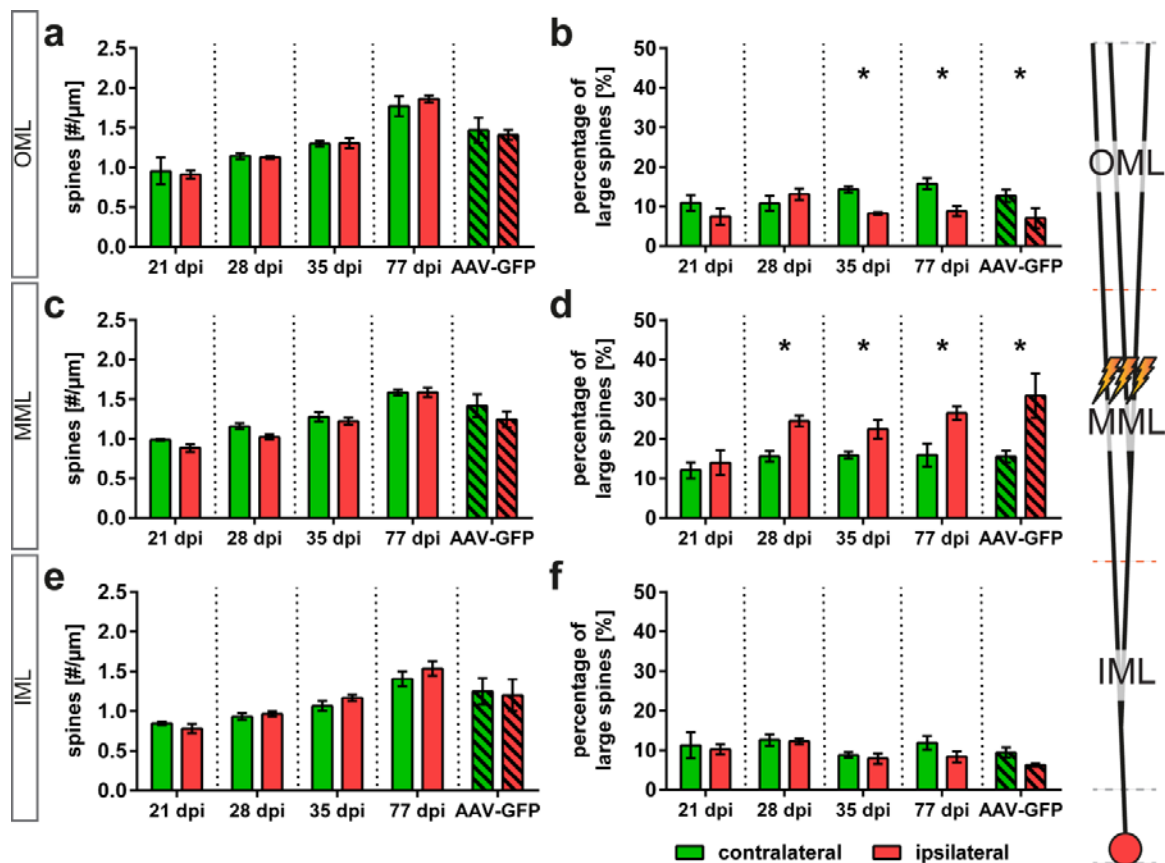


Figure 4 Percentage of large spines is increased in the MML and decreased in the OML following 2 h HFS of the medial perforant path.

The medial perforant path was stimulated with a strong HFS protocol for 2 h to induce LTP in the ipsilateral middle molecular layer (MML). Dendritic spines of RV-GFP-labeled abGCs (21-77 dpi), or AAV-GFP-labeled mGCs were analyzed in a layer-specific approach. The contralateral, non-stimulated hemisphere was used as a control. (a) Spine density in the outer molecular layer (OML) was not altered following HFS. (b) The percentage of large spines showed a significant decrease in abGCs from 28 dpi on and in mGCs. (c) Spine density in the MML did not change following stimulation at any age neither in abGCs, nor in mGCs. (d) The percentage of large spines significantly increased in abGCs from 28 dpi on and in mGCs. (e, f) In this analysis, spines in the inner molecular layer (IML) were not significantly affected by HFS (but see also Fig. 5b). Number of animals: $n_{21 \text{ dpi}} = 3$, $n_{28 \text{ dpi}} = 6$, $n_{35 \text{ dpi}} = 5$, $n_{77 \text{ dpi}} = 4$, $n_{\text{AAV-GFP}} = 4$. Two-sided Wilcoxon rank-sum test: * $P < 0.05$.

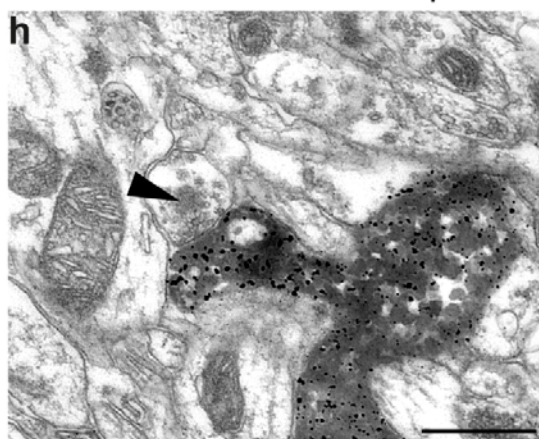
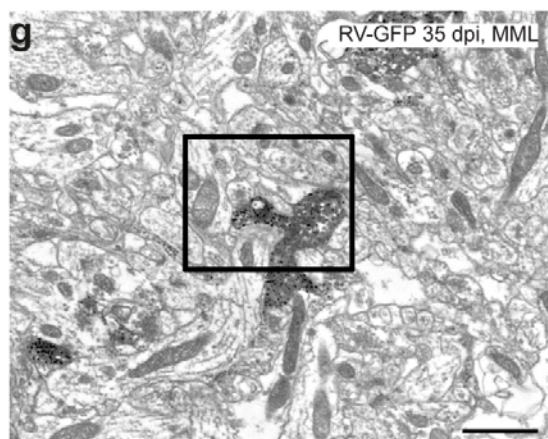
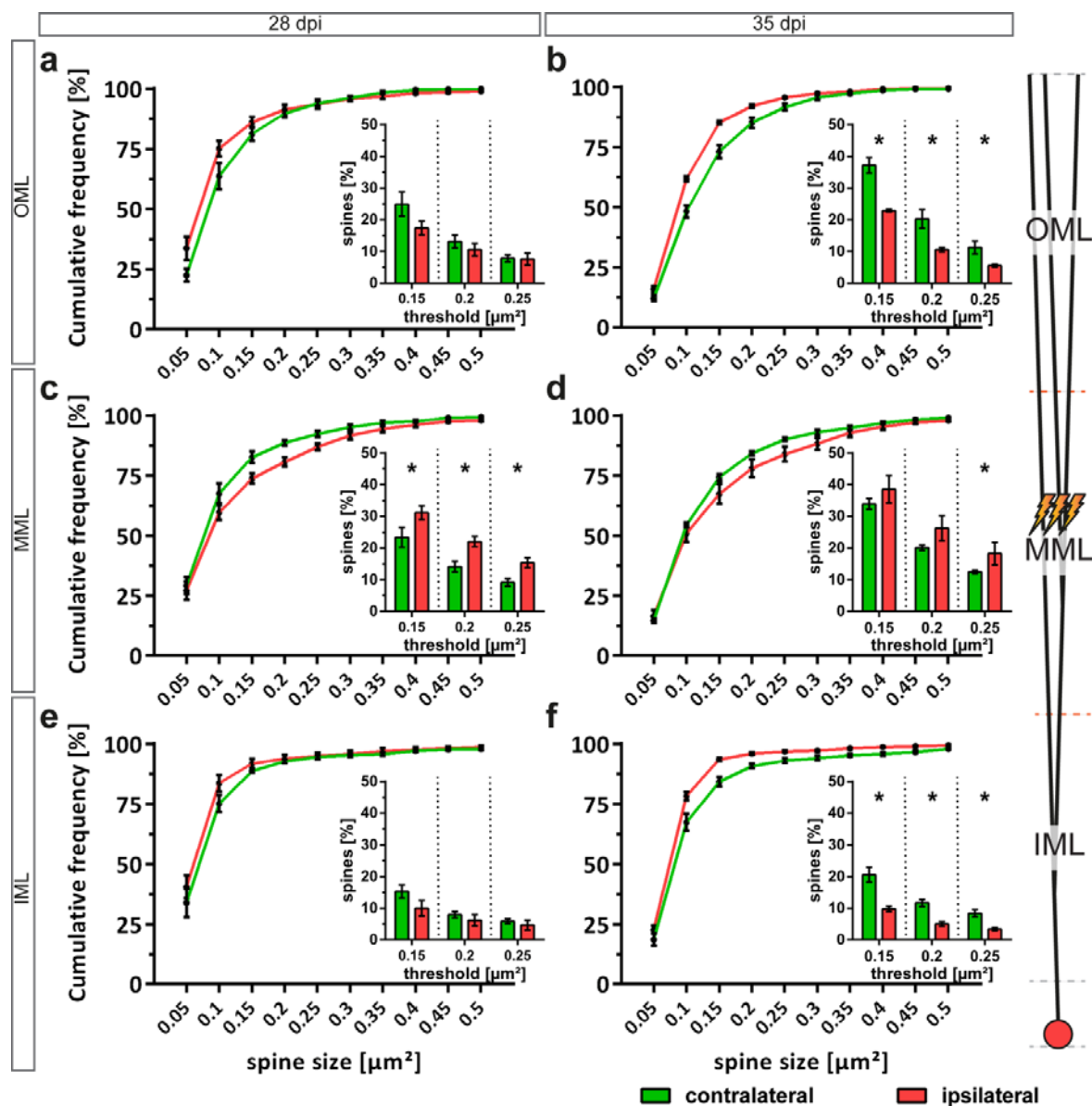


Figure 5 Layer-specific spine size histograms confirm HFS-induced spine plasticity in 28 dpi and 35 dpi abGCs.

(a-f) Cumulative fractions of spine head sizes (largest cross-sectional areas) with HFS (red, ipsilateral) and without HFS (green, contralateral) in OML (a, b), MML (c, d), and IML (e, f). Insets identify the amount of spines larger than the following thresholds: $0.15 \mu\text{m}^2$, $0.2 \mu\text{m}^2$, and $0.25 \mu\text{m}^2$. Significant homosynaptic structural plasticity in the MML of 28 dpi (c) and 35 dpi (d) abGCs, as well as significant heterosynaptic plasticity in the IML (f) and OML (b) of 35 dpi abGCs. (g) Electron micrograph illustrating an immuno-labeled cross-section of a dendritic segment located in the MML with a spine of a RV-GFP-labeled abGC (35 dpi). (h) Enlarged area from g (black rectangle). The spine forms a synapse with an unlabeled axon terminal (black arrow). Number of animals: $n_{28 \text{ dpi}} = 6$, $n_{35 \text{ dpi}} = 5$. Two-sided Wilcoxon rank-sum test: $*P < 0.05$. Scale bars: (g) 1000 nm, (h) 500 nm.

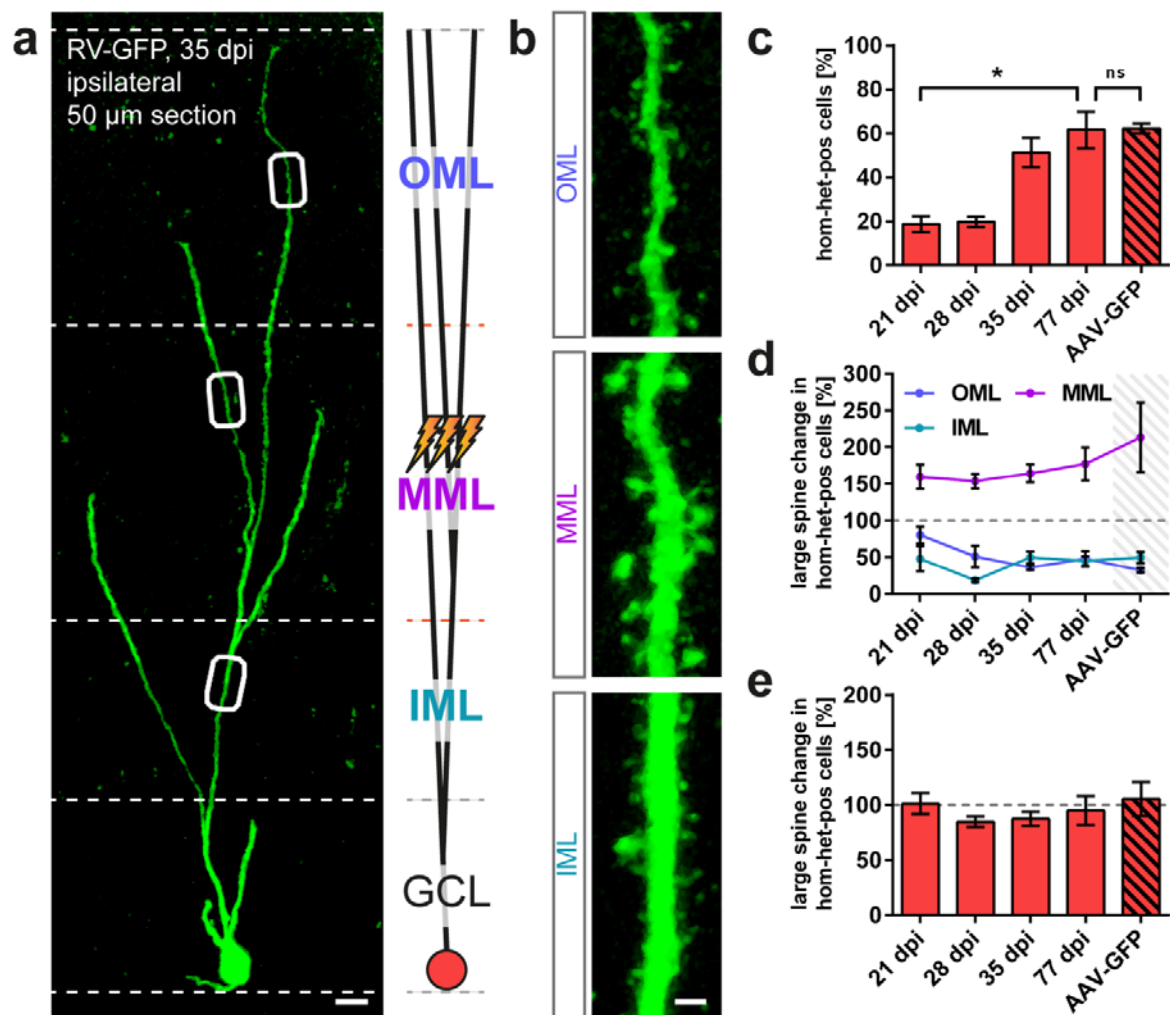


Figure 6 Homo- and concurrent heterosynaptic structural plasticity is induced within the same dendritic tree of individual GCs following 2 h HFS.

(a) Homo- and heterosynaptic structural remodeling of spines was analyzed in dendritic segments of the same GC. **(b)** GCs exhibiting homosynaptic structural plasticity in the MML, heterosynaptic structural plasticity in the IML and OML following HFS were identified from the entire population of analyzed cells. **(c)** Fraction of abGCs exhibiting structural homosynaptic spine enlargement and heterosynaptic spine shrinkage (hom-het-pos cells). **(d)** Similar changes in large spines of hom-het-pos GCs in the MML, IML, and OML in all age groups. **(e)** Overall percentage of large spines along the entire dendritic tree (comprising IML, MML, and OML) in relation to the contralateral side, indicating that structural heterosynaptic spine shrinkage in the IML and OML counteracted induction of homosynaptic spine enlargement in the MML. Number of animals: $n_{21 \text{ dpi}} = 3$, $n_{28 \text{ dpi}} = 6$, $n_{35 \text{ dpi}} = 5$, $n_{77 \text{ dpi}} = 4$, $n_{\text{AAV-GFP}} = 4$. **(c, d)** Kruskal-Wallis with Dunn's multiple comparisons test (21 dpi vs. 77 dpi, 77 dpi vs. AAV-GFP): * $P < 0.05$. **(e)** Two-sided Wilcoxon rank-sum test: * $P < 0.05$. Scale bars: **(a)** 10 μm , **(b)** 1 μm . GCL, granule cell layer.

Supplementary Figures

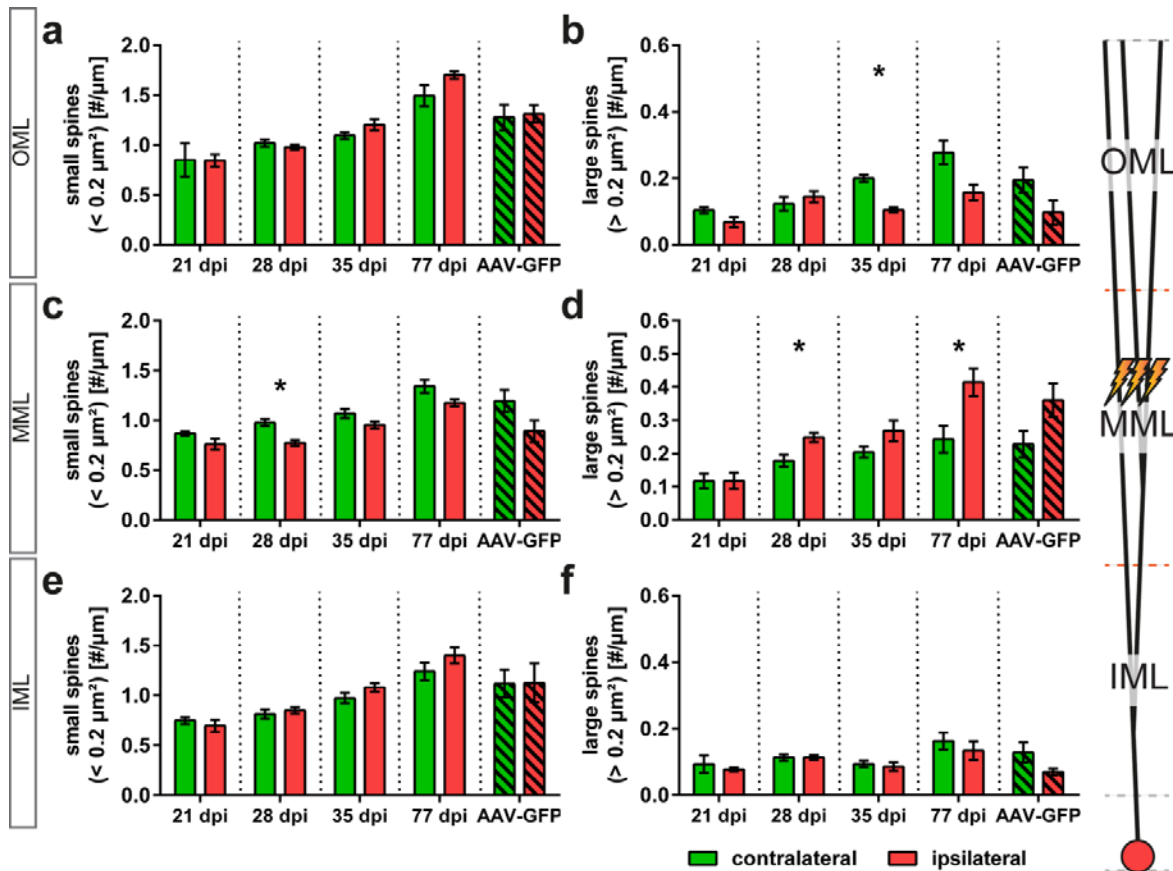


Figure S1 The number of large spines is increased in the MML and decreased in the OML following 2 h HFS of the medial perforant path.

(a) Small spines in the outer molecular layer (OML) were not affected by stimulation at any age. **(b)** Large spines were significantly increased at 35 dpi. **(c)** Small spines decreased in the middle molecular layer (MML) at 28 dpi following stimulation. **(d)** Large spines were significantly increased at 28 dpi and 77 dpi. **(e, f)** Spines in the inner molecular layer (IML) were not affected by HFS and showed no structural changes. $n_{21 \text{ dpi}} = 3$, $n_{28 \text{ dpi}} = 6$, $n_{35 \text{ dpi}} = 5$, $n_{77 \text{ dpi}} = 4$, $n_{\text{AAV-GFP}} = 4$. Two-sided Wilcoxon rank-sum test: * $P < 0.05$.

8.3. Publication 3

Erklärung über Anteile der Autoren an der Publikation

“A comprehensive and consistent electrophysiological model of dentate granule cells”
submitted

	Entwicklung und Planung	Durchführung der einzelnen Experimente	Erstellung der Datensammlung und Abbildungen	Analyse / Interpretation der Daten	Verfassen des Manuskripts
Beining, Marcel	30 %	95 % Literatursuche Erstellen und Anpassen des comp. Modells, Erstellung+Durchf. aller Simulationen, Morph. Modell	100 % Alle Tabellen, Abbildungen und Ergänzungsabbildungen (Supplementary Figures)	70 % Analyseskripte Interpretation	65 %
Mongiat, Lucas	5 %	5 % Bereitstellung der elektrophys. Daten aus Mongiat 2009	-	5 % Interpretation	5 %
Schwarzacher Stephan W.	10 %	-	-	5 % Interpretation	10 %
Cuntz, Hermann	25 %	-	-	10 % Interpretation	10 %
Jedlicka, Peter	30 %	-	-	10 % Interpretation	10 %

Zustimmende Best. der Angaben:

Datum/Ort

Datum/Ort

Unterschrift Promovend

Unterschrift Betreuer

A novel comprehensive and consistent electrophysiological model of dentate granule cells

*Marcel Beining^{a,b,c,d}, Lucas A. Mongiat^e, Stephan W. Schwarzacher^c, Hermann Cuntz^{a,b,1}, Peter Jedlicka^{c,1}

^a*Ernst Strüngmann Institute (ESI) for Neuroscience in Cooperation with Max Planck Society, Frankfurt/Main, Germany*

^b*Frankfurt Institute for Advanced Studies, Frankfurt/Main, Germany*

^c*Institute of Clinical Neuroanatomy, Neuroscience Center, Goethe University, Frankfurt/Main, Germany*

^d*Faculty of biosciences, Goethe University, Frankfurt/Main, Germany*

^e*Instituto de Investigación en Biodiversidad y Medioambiente, Universidad Nacional del Comahue-CONICET, San Carlos de Bariloche, Argentina.*

¹*Joint senior authors*

**To whom correspondence should be addressed*

Short title: Granule cell model

Keywords: compartmental modeling, dentate gyrus granule cell, electrophysiology, electrotonic properties, adult neurogenesis, epilepsy

***Corresponding Author:**

Marcel Beining

Ernst Strüngmann Institute (ESI) for Neuroscience

Deutschordenstraße 46

60528 Frankfurt/Main

Germany

Tel.: +49 (69) 96769 544

E-mail: beining@fias.uni-frankfurt.de

Abstract

Compartmental models have become the theoretical tool of choice for understanding single neuron computations. However, many models are built *ad hoc*, are unstable, incomplete, and require sensitive tuning for each novel condition rendering them of limited usability. Here, based on the currently known ion channel composition and detailed morphology, we present an active model of rodent dentate granule cells (GCs) that replicates a wide palette of experimental results from various labs. The model is stable over a broad range of reconstructed as well as synthetic morphologies of both mouse and rat GCs. It is therefore suitable for large-scale network models as well as for making novel predictions. Moreover, our model also reproduces the GC behavior under various pharmacological as well as epileptic conditions. Finally, since the dentate gyrus is subjected to adult neurogenesis, we have implemented experimentally observed changes in ionic conductances to accurately simulate young adult-born GCs.

Introduction

Traditionally, neurons have long been interpreted as passive integrators of input signals that fire action potentials when a threshold is reached (Knight, 1972). This paradigm has meanwhile changed as the output of neurons was shown to depend on many intrinsic cellular mechanisms (e.g. voltage-gated channels, dendritic architecture, synaptic plasticity, active dendrites, axon initial segment) indicating that single neuron computation is rather complex (Brunel, Hakim, & Richardson, 2014; Softky & Koch, 1993; Volgushev, 2016). Consequently, detailed compartmental models have found their way into the set of tools for neuroscientists to understand, test or predict mechanisms underlying neuronal function (de Schutter, 1994). Compartmental models are easy to manipulate and models of cellular mechanisms such as ion channels and synapses can be incorporated in arbitrary detail. Many recent models include reconstructed morphologies which are often available online through specialized databases. As these models seem to become more and more realistic, the hope arises that one will soon be able to simulate entire circuits or even the brain itself simply by including more and more details (Markram, 2006, 2012; Markram et al., 2015). However, most published models behave poorly when used outside of the scope for which they were created. A recent review on cortical layer 5 pyramidal cells counted several reasons for this, such as bona fide adaptation of other models without knowing their limitations, too few target constraints because of using a low number of target parameters, no scientific rationale for setting the parameters, missing axon initial segments and a lack of data from pharmacology to fit and test the model's individual components (Almog & Korngreen, 2016).

Similar issues and problems can be found in many other compartmental models, including models of dentate granule cells (GCs). Due to the central role of GCs in the hippocampal circuit, e.g. their function in transforming input information into sparse code (Jung & McNaughton, 1993), attempts to construct compartmental models of mature GCs have been made early on (Yuen & Durand, 1991). In the meantime, many models were generated and have been modified and extended multiple times (Chiang et al., 2012; Ferrante et al., 2009;

Jaffe et al., 2011; Jedlicka et al., 2015; Krueppel et al., 2011; Mateos-Aparicio et al., 2014; Platschek et al., 2016; Tejada et al., 2012). This has been instrumental for studying the large-scale network of the dentate gyrus (DG), e.g. to analyze the origins of DG hyperexcitability in temporal lobe epilepsy (Dyhrfjeld-Johnsen et al., 2007; Hendrickson, Yu, Dong Song, & Berger, 2015; Santhakumar, Aradi, & Soltesz, 2005; Tejada & Roque, 2014). However, these models were based on the very first GC models, when simplified morphologies were used, detailed knowledge of the ion channel distribution and kinetics was lacking and missing parameters were often adopted from other cell types or species. Probably due to these factors, more recent GC models needed to be modified or created *ad hoc* to reproduce single experiments (Chiang et al., 2012; Jaffe et al., 2011; Mateos-Aparicio et al., 2014; Platschek et al., 2016; Stegen et al., 2012; Yim, Hanuschkin, & Wolfart, 2015). Since many new insights from more recent studies on GC electrophysiology and protein expression are accumulating and more complete GC morphologies have become available, we aimed here to create a novel GC model that (1) is solely based on ion channel isoforms known to exist in GCs, (2) is robust over many different real and synthetic dendritic morphologies and (3) reproduces experimental results from various different studies.

Results

We assembled a set of ion channels and their compartment-specific distributions that have been reliably characterized experimentally by immunohistochemical labeling with light or electron microscopy as well as electrophysiology and modeling (Table 1 and Figure 1A, see Materials and methods for a full description of all ion channels). The corresponding ion channel models were obtained from literature or developed based on known channel kinetics and incorporated in reconstructed morphologies of eight mature mouse GCs (Schmidt-Hieber, Jonas, & Bischofberger, 2007) to set the channel densities for our biophysical model (Figure 1A). In order to make sure that our compartmental model was stable over a large set of GC morphologies we also adapted a previously published morphological model for rat GCs (Beining et al., 2016) to mature mouse GCs (Figure 1B). The resulting synthetic dendritic trees were morphologically comparable to the reconstructed trees from Schmidt-Hieber et al. (Figure 1C), and were introduced into the compartmental model as a further validation of the fitted passive and active properties.

Passive mouse GC model

The channel densities of the passive channels (the leak and the inward-rectifying Kir2 channel) were fitted to experimentally measured steady-state currents in mature GCs during voltage clamp steps from -130 to -60 mV (I-V curve, Figure 2A) (Mongiat, Espósito, Lombardi, & Schinder, 2009). We further used I-V curves obtained after application of 200 μ M BaCl to the extracellular medium to selectively block Kir channels and thereby estimate their contribution to passive currents (Figure 2A). Interestingly, a further block of the passive channel by 30 % was necessary in the Ba²⁺ simulations to match the data. This is consistent with the observed moderate Ba²⁺ sensitivity in K2P channels (Goldstein et al., 2005; Lesage et al., 1997; Ma et al., 2011; Meadows et al., 2000).

The model was also fitted to reproduce passive properties such as the membrane time constant and capacitance (Table 2). The resulting input resistance (R_{in}) was consistent with electrophysiological measurements by

Mongiati et al. (2009). Furthermore, our model was also consistent with R_{in} measurements from other mouse studies (Brenner et al., 2005; Schmidt-Hieber, Jonas, & Bischofberger, 2008). By considering the current or voltage steps applied in each of these studies (Figure 2A, colored arrows) we could show that due to the inward rectification, the measured R_{in} can vary substantially depending on the holding voltage and the current or voltage step that is applied. Interestingly, in electrophysiological traces, the current dynamics of the cells showed a slowly activating outward current at holding voltages below -100 mV (Figure 2—figure supplement 1). This current was reproduced by our GC model as Kir channels were partly blocked at resting potential and had a slow recovery time when being unblocked by hyperpolarization. In addition, the outward current might be mediated by hyperpolarization-activated cyclic nucleotide-gated (HCN) channels which open at hyperpolarized potentials, too. However, HCN channels are strongly expressed in GCs only in temporal lobe epilepsy (TLE) patients (Stegen et al., 2012) or animal models of TLE (Bender et al., 2003) but not in preparations of healthy subjects or animals. Thus, Kir channels more likely underlie the observed slowly activating outward current.

Fully active mouse GC model

In order to fit our active GC model, we used raw traces from current clamp measurements of eight mature GCs (Mongiati et al., 2009) to reproduce action potential (AP) shape and spiking properties in detail. The spiking frequency vs. current (F–I) curve, relating somatic current injections to the amount of elicited APs is an important measure of a neuron's excitability, and therefore a crucial feature to be replicated. Our active model was able to reproduce the F–I curve in both conditions, control and pharmacological blockade of Kir channels with BaCl (Figure 2B, experiment: gray lines on the left; model: blue lines in the middle column). The spiking behavior closely matched the experimental data (Figure 2C), which was validated by comparing the AP properties such as the AP width, threshold, amplitude, fast afterhyperpolarization (AHP) as well as the voltage phase plot (Figure 2D–F). Importantly, replacing the reconstructed with synthetic mouse morphologies produced similar electrophysiological results (Figure 2A–F right column, model data shown in green) indicating a strong

robustness of our model against morphological changes. This further renders our morphological mouse model suitable for large-scale network modeling of the DG. Interestingly, the different morphologies exhibited different variants, e.g. of AHPs and depolarizing afterpotentials (DAPs), similarly to what was observed in experiments (Althaus, Sagher, Parent, & Murphy, 2015). We analyzed the morphological origin of the electrophysiological variability and found a moderate negative correlation between dendritic surface and AP threshold (correlation coefficient $R = -0.42$) or AP number (correlation coefficient $R = -0.40$) indicating reduced excitability in larger dendritic trees (Figure 2—figure supplement 2, left). This is consistent with previous experimental and modeling studies showing that larger dendritic trees exhibit reduced excitability due to the larger dendritic leak (Krichmar et al., 2002; Šišková et al., 2014; Platschek et al. 2016). The size of the soma was also of relevance since it shaped AP characteristics such as fast AHP (correlation coefficient $R = -0.33$) and AP width (correlation coefficient $R = -0.45$) in the GC models (Figure 2—figure supplement 2, right). Thus, some of the variance observed in electrophysiological studies might be explained by the morphological variability of GCs.

Rat GC model

Next, since many GC experiments are performed in rats instead of mice we further developed a rat GC model. In order to reproduce rat GC electrophysiology, we replaced the mouse morphologies with reconstructions of mature rat GCs (Figure 3A, left) as well as a corresponding morphological model (Figure 3A, right), both reported previously by our lab (Beining et al., 2016). Rat GCs have generally longer dendrites but only marginally higher total dendritic length since they are less branched than mouse GCs (Beining et al., 2016). Furthermore, rat GCs have a larger mean dendritic diameter. However, even with the altered morphologies, experimental rat GC R_{in} measurements (average $218 \pm 30 \text{ M}\Omega$, Figure 3B, colored arrows) were only matched when increasing the K_{ir} conductance by a factor of $\times 2.5$ ($204 \pm 16 \text{ M}\Omega$, solid blue curve, Figure 3B), and not when passive channel densities were kept as in the mouse model ($313 \pm 21 \text{ M}\Omega$ dashed line, Figure 3B). Also, when the K_{ir}

conductance was not adjusted, ongoing spiking failed at high current injections. These results suggest that a higher expression of Kir channels might account for the major species difference in passive properties. With the adjustments, our rat GC model then reproduced the F–I curve reported from a study (Pourbadie et al., 2015), for which similar intracellular solutions were used as for the mouse GC electrophysiology (Mongiat et al., 2009) (Figure 3C). Consequently, after aforementioned minor adjustments, active channel properties and densities from mouse GCs reliably reproduce the spiking behavior of rat GCs. This result indicates that both rodent species might share a similar GC ionic channel density pattern, conferring to these neurons their electrophysiological identity. Similarly to the mouse GC model, real and synthetic rat morphologies could be interchanged without affecting the spiking behavior (Figure 3B–D, left vs. right), indicating an inherent robustness of our active model and thus validating its usefulness for large-scale network simulations of the rat DG, too.

Dendritic signal propagation and Ca²⁺ signaling in mouse and rat

To further analyze the usefulness of our mouse and rat active models, we next investigated dendritic signal propagation and Ca²⁺ signaling. Speed and attenuation of backpropagating APs (bAPs) that were previously measured in rats at various distances from the soma (Krueppel et al., 2011) were matched by our rat GC model (Figure 4A, left, blue curves) with a relative attenuation at 185 μm of $24.0 \pm 2.8 \%$, compared to $24.5 \pm 3.6 \%$ in experiments (Figure 4A, left, black dots). Since we did not implement voltage-gated sodium (Na_v) channels in the dendritic region of our morphologies, our simulations strengthen the notion that, as suggested previously (Krueppel et al., 2011), GC dendrites are virtually void of Na_v channels. This is particularly important since earlier GC models comprised dendritic Na_v channels (Aradi & Holmes, 1999; Mateos-Aparicio et al., 2014; Santhakumar et al., 2005; Schmidt-Hieber & Bischofberger, 2010) thereby strongly affecting synaptic integration and calcium- or voltage-dependent plasticity. It is important to note, that the delay between the somatic AP and the maximum bAP at distal dendrites could not be well reproduced without adjusting the specific axial resistance R_a and the passive membrane conductance to the higher temperature of 33 °C that was

used in experiments by Krueppel and colleagues (Figure 4B, left) with Q10 values taken from Trevelyan and Jack (2002). This provides further evidence for the consistency of our model with experimental data. We therefore conclude that faster dendritic voltage propagation at higher temperatures should be considered in models that simulate *in vivo* conditions. Applying the same protocols to the mouse GC model revealed a significantly lower relative bAP attenuation of $35.6 \pm 3.2\%$ at $185\ \mu\text{m}$ ($p = 0.028$, Kruskal-Wallis test, $n = 5$ rat GCs vs. $n = 8$ mouse GCs) but a similar delay (1.81 ± 0.08 ms in mouse vs. 1.68 ± 0.05 ms at $185\ \mu\text{m}$, $p = 0.188$, Kruskal-Wallis test, $n = 5$ rat GCs vs. $n = 8$ mouse GCs) compared to the rat model (Figure 4A, B, right). This predicts species-specific differences in bAP attenuation that remain to be examined experimentally.

As Ca^{2+} is an important cellular signal, we also analyzed the bAP-induced Ca^{2+} peak and decay in various compartments (axon, soma, proximal and distal dendrite) in the mouse and rat model and compared it to known experimental data. The Ca^{2+} peak levels were found to be slightly but not significantly higher in mouse ($n = 8$) than in rat ($n = 5$) dendrites (Figure 4C, proximal: $216.4 \pm 16.5\ \mu\text{M}$ in mouse vs. $152.0 \pm 39.4\ \mu\text{M}$ in rat, $p = 0.305$ Kruskal-Wallis test; distal: $102.6 \pm 12.1\ \mu\text{M}$ in mouse vs. $76.8 \pm 11.9\ \mu\text{M}$ in rat, $p = 0.305$, Kruskal-Wallis test). Provided that Ca^{2+} buffering and extrusion mechanisms are comparable between mouse and rat GCs (Stocca, Schmidt-Hieber, & Bischofberger, 2008), this suggests that dendritic Ca^{2+} signaling is relatively similar in both species despite differences in backpropagating dendritic voltage spread. Interestingly, Ca^{2+} dynamics in synthetic morphologies (Figure 4C, green bars) matched Ca^{2+} signals from experiments (black bars) as well as those from reconstructed morphologies (blue bars). Thus, our GC model generated realistic and stable intracellular Ca^{2+} dynamics over a broad range of different morphologies in rat and mouse (Figure 4).

Sensitivity analysis reveals critical ion channels in mouse and rat GCs

Since our GC model exhibited biophysical accuracy and comprised exclusively ion channel isoforms that were demonstrated to exist in GCs, it can be useful for making novel predictions and to identify parameters that critically influence neural computation in GCs. Figure 5A shows a sensitivity matrix in which the relative effects on physiological features of GCs were measured when ion channel conductances or other model parameters were up- or downregulated. A number of predictions can be drawn from this matrix. Reducing the passive leak and Kir2.1 channels critically influenced R_{in} , the membrane time constant, the interspike interval (ISI), and the number of APs at 100 pA. In contrast, the number of APs at 200 pA was only marginally affected, indicating that as the membrane is steadily depolarized at high current injections other channels such as $K_v2.1$ and K_v7 dominate the hyperpolarizing potassium influx, as Kir2.1 channels close. The 8-state sodium channel model (na8st) which represents $Na_v1.2$ and 1.6 was critically involved in excitability, AP shape and threshold as well as in the propagation speed along the dendrites and axon. As in nature, R_a and C_m of a neuron stay relatively constant since they depend on the composition of the membrane and cytoplasm, our matrix suggests that Na_v channels, Na^+ concentration and temperature (besides anatomical properties such as diameter and branching) are the only components influencing propagation speed. Interestingly, $K_v2.1$ (A-current) blockade reduced ISI but increased ISI adaptation, as the higher number of APs recruited more K_v7 channels. The blockade of K_v7 shows that this channel gains relevance as membrane depolarizes, as it contributes more and more to the slow AHP. As was expected, altering the reversal potential of the Na^+ and K^+ had complementary effects: A 10 mV increase of E_K (from -90 to -80 mV) influenced mainly the passive properties such as R_{in} and excitability, whereas a reduction of E_{Na} by -20 mV reduced AP amplitude (and propagation along the axon) and therefore increased AP width due to reduced activation of repolarizing K-channels. Interestingly, corresponding increases (doubling) of each model parameter led to opposite effects (Figure 5—figure supplement 1), except that the doubling of C_m partly showed paradoxical results arising from its effect on the dynamics of activation of dendritic channels.

Even though only five channels were modeled as being temperature-sensitive in our model ($Ca_v3.2$, SK, $K_v4.2$, $K_v7.2/3$ and HCN), increasing or decreasing the temperature by 10 °C from 24°C to 34°C or to 14°C had a significant influence on the cell's excitability and spiking behavior (34°C: Figure 5A; 14°C: Figure 5—figure supplement 1). From these predictions, we conclude that, as different recording temperatures are used in different studies, the influence of temperature on the contribution of specific channels to electrophysiological properties, e.g. to the slow AHP, can therefore be quite important and should be considered.

Finally, we tested some experimentally suggested relationships of ion channels and AP features. Firstly, we tested whether our model could reproduce the experimentally documented dominant contribution of BK and K_v3 channels to AP repolarization in GCs (Brenner et al., 2005; Riazanski et al., 2001) with BK governing somatic (Müller, Kukley, Uebachs, Beck, & Dietrich, 2007) and K_v3 axonic repolarization (Alle, Kubota, & Geiger, 2011). To this goal, we conducted simulations with low (90 pA) and high (250 pA) current injections to analyze the contribution of BK and K_v3 channels to AP repolarization. We found that K_v3 blocking had no major effects on somatic AP shape, whereas a blockade of BK channels increased AP width, especially when the cell has to elicit several short-interval APs (Figure 5B, 250 pA). For both stimulation intensities, the relative contribution of $K_v3.4$ and BK stayed the same in the model with BK contributing considerably more to somatic repolarization, consistent with literature (data from rat; Müller et al., 2007; Riazanski et al., 2001; compared with our rat GC model in Figure 5B). Secondly, we found that in our GC model K_v7 (M-current) contributed to spiking adaptation whereas calcium-dependent SK channels did not (Figure 5C). This is different from experimental data measured in rat GCs (Mateos-Aparicio et al., 2014). This discrepancy might originate from the manually adjusted size of injected current during spiking adaptation measurements under different pharmacological blockers (Mateos-Aparicio et al., 2014) from the different intracellular potassium source (K-Gluconate in our experiments vs. $KMeSO_4$ in their experiment, where the latter is known to induce larger slow AHPs (Zhang et al., 1994) and to slowly reduce R_{in} by up to 70 % (Kaczorowski, Disterhoft, & Spruston, 2007), from the putative

partial permeability of SK for Na^+ which would drastically increase E_{Na} to ~ 50 mV (Shin, Soh, Chang, Kim, & Park, 2005), or from the very complex interaction between K_v7 channels, KATP channels and neuronal Ca^{2+} sensors such as hippocalcin (Andrade, Foehring, & Tzingounis, 2012) of which all are further affected by temperature (note the 10°C higher temperature in Mateos-Aparicio et al., 2014), phosphorylation (Andrade et al., 2012) and ATP (Baukrowitz & Fakler, 2000).

Taken together, our sensitivity mapping of ion channel changes opens a number of insights that help to understand the contribution of each ion channel isoform to the electrophysiological behavior of GCs.

Compensatory ion channel alterations in temporal lobe epilepsy (TLE)

To test the predictive power of our model under pathological changes in the GC ion channel composition we analyzed the impact of ion channel changes reported to occur during TLE (Bender et al., 2003; Kirchheim, Tinnes, Haas, Stegen, & Wolfart, 2013; Stegen et al., 2012; Young et al., 2009). Overexpression of HCN and Kir (by doubling the channel densities in the model) reduced the intrinsic excitability of our model GCs by decreasing R_{in} (133 ± 11 M Ω vs. 204 ± 16 M Ω , Figure 5D). This was consistent with patch-clamp recordings from murine and human GCs in TLE revealing a compensatory reduction of GC excitability due to protective enhanced expression of HCN and Kir channels (Stegen et al., 2012; Young et al., 2009). In addition, in line with these experiments, our normal GC model shows a very low resonant behavior when oscillating currents between 1 and 15 Hz were injected (Figure 5—figure supplement 2), indicating that the low HCN channel density in GCs under normal conditions is not sufficient to induce resonant behavior as observed in CA1 pyramidal cells (Stegen et al., 2012). Similarly, we further showed that protective overexpression of $\text{K}_v1.1$ found in animal models of TLE increased spike delays and decreased GC excitability (Figure 5E) although the spike delay effect in our model was not as prominent as in experiments (Kirchheim et al., 2013), which might, similar to the discrepancy found in the spiking adaptation experiments, originate from the different intracellular potassium source (K-Gluconate in our experiments vs. KMeSO_4 in

the experiment, see above). Taken together, our model appears useful to analyze GC spiking behavior following compensatory channel regulation due to pathological conditions such as TLE and thus could be integrated in available dentate network models that aim to model such conditions (Yim et al., 2015).

Adult-born GC model

Dentate GCs are continuously produced throughout life, a process called adult neurogenesis. Young adult-born GCs (abGCs) possess unique electrophysiological features and numerous studies have pointed out their special role in hippocampal memory formation (Ming and Song, 2011; Aimone et al., 2014; Johnston et al., 2016). In particular, young abGCs display a critical phase starting at about four weeks of cell age when they exhibit increased excitability, enhanced synaptic and dendritic plasticity, and receive less inhibitory input (Beining et al., 2016; Bergami et al., 2015; Ge, Yang, Hsu, Ming, & Song, 2007; Marín-Burgin, Mongiat, Pardi, & Schinder, 2012; Mongiat et al., 2009; Temprana et al., 2015). As no compartmental model of young abGCs existed so far, we aimed to investigate the capability of our biophysical GC model to replicate the electrophysiology of abGCs when differences in channel expression are considered.

In order to fit the passive and active properties of the young abGC model we used raw voltage and current traces that have been acquired under the same conditions as in the mature mouse GC experiments (Mongiat et al., 2009). The I-V relationship and other passive properties were well matched by reducing the Kir2 channel density by 73 % (Figure 6A). This was consistent with previously reported reduced Kir channel currents and increased excitability in young abGCs (Mongiat et al., 2009). Since other channels have not been studied in young abGCs so far, altered channel expression for our abGC model was inspired from channel distribution studies in postnatal developing GCs (Table 3) as their development was reported to be similar to that of abGCs (Laplagne et al., 2006; Urbán & Guillemot, 2014).

Since young abGCs have a much lower membrane capacitance consistent with a lower spine density at 28 dpi (Mongiat et al., 2009; Yang, Alvarez, & Schinder,

2015), we reduced the spine scaling factor (see Materials and Methods) by a factor of $\times 0.3$ compared to the mature GC model. Even with this low value, the membrane capacitance of our model (46.95 ± 3.21 pF) did not match the experimental values of 30.6 ± 1.0 pF (Mongiat et al., 2009). This resulted in longer spike delays compared to exemplary spike traces (compare columns in Figure 6B). However, the acute slice recordings might have slightly underestimated the capacitance values due to ineffective voltage clamping of distal dendritic regions or due to dendritic branches that were cut during slice preparation. Moreover, other studies showed capacitances for young abGCs of around 40 pF (Piatti et al., 2011; Yang et al., 2015). Despite the differences in capacitance, our young abGC model was capable of reproducing the experimental F–I relationship (Figure 6C), AP characteristics (Figure 6D–E), and AP dynamics (Figure 6F) when spine densities and expression of ion channels were reduced as mentioned above.

Synaptic signal integration in young abGCs

Young abGCs have been attributed a special role in hippocampal pattern separation and integration due to their broader tuning to input activity (see reviews Aimone et al., 2010; Rangel et al., 2013; Johnston et al., 2016). Therefore, to further test our model and to generate quantitative predictions concerning synaptic integration of abGCs, we compared the temporal processing of synaptic inputs in the young abGC and the mature GC model considering only intrinsic differences (i.e. no additional inhibitory input). We first randomly and equally distributed 30 excitatory synapses over the middle (MML) and outer molecular layer (OML), the termination side of the major afferent input from the medial and lateral entorhinal cortex, respectively. Next, we synaptically activated the GCs synchronously at different frequencies (Figure 7A). Interestingly, when we used the same number and strength of synapses in the mature and young abGC model, the young abGCs could follow the input even at high frequencies (Figure 7A, right panel, dashed pink line) whereas the mature GCs could only follow frequencies below 20 Hz, mainly due to the activation of slow AHP currents. However, it is known, that young abGCs have a lower number of synapses than mature GCs as indicated by lower spine

densities (Zhao, Teng, Summers, Ming, & Gage, 2006) and lower miniature excitatory post-synaptic current (mEPSC) frequencies but similar amplitudes (Mongiat et al., 2009). Therefore, we reduced the number of synapses in the young abGC model accordingly by a factor of two (15 synapses, same strength). Interestingly, in this reduced input configuration, abGCs had a similar synaptic input/output relation as the mature GCs (Figure 7A, right panel, solid pink line compare with solid blue line). This suggests that (1) the higher intrinsic excitability of abGCs compensates for their lower numbers of synaptic inputs and (2) both young abGCs and mature GCs are tuned to follow input frequencies in the theta range (< 10 Hz). This result is consistent with studies showing that diminished glutamatergic input is compensated by the enhanced excitability when GABAergic inhibition is blocked (Mongiat et al., 2009; Pardi, Ogando, Schinder, & Marin-Burgin, 2015).

In order to test the input tuning of young abGCs we then investigated their integration of temporally delayed inputs. In these simulations, the phase of the distal inputs (OML) was shifted with respect to the proximal synapses (MML) by a time difference Δt , and the more realistic “reduced input” (15 synapses) configuration was used for young abGCs. Interestingly, we found that whereas mature GCs were not able to integrate considerably delayed inputs ($\Delta t > 15$ ms), young abGCs performed better (Figure 7B, upper graph), despite receiving input from less synapses. However, when the frequency exceeded 20 Hz young abGCs performed slightly worse than mature GCs in following the input frequency (Figure 7B lower right graphs). The higher the frequency, the worse was the performance correlated with Δt as the young cells’ activity became saturated. In summary, at low frequencies in the theta range, young abGCs were able to integrate synaptic inputs with a broader time window than mature GCs. This mechanism would be consistent with the proposed special role in hippocampal pattern separation/integration due to their broader tuning to input activity (Aimone et al., 2010; Johnston et al., 2016; Rangel et al., 2013). In conclusion, our model reproduces the activation patterns of young and mature granule cells under conditions when inhibition is not present.

Discussion

In this study we developed a new compartmental model simulating detailed electrophysiological behavior of mature GCs and young abGCs in mouse and rat. The model has five important advantages and improvements when compared to previous published models: (1) The model is robust across a wide range of reconstructed and synthetic morphologies. (2) The model contains only conductances of channel isoforms that are currently known to exist in GCs and accurately implements their kinetics. (3) The model is capable of reproducing findings and experiments from many different studies. (4) After adjustment of passive channels, the model reproduces electrophysiological behavior of both rat and mouse GCs indicating that these species might share similar active channels. (5) The adapted model for abGCs represents the first available data-driven compartmental model of these neurons. With this consistent model at hand, we were able to reproduce the effects of compensatory ion channel changes under epileptic conditions in mature GCs. Furthermore, the model predicted the impact of differences in intrinsic properties between young abGCs and mature GCs on the temporal summation of synaptic input. We found that the higher intrinsic excitability allows young abGCs to integrate synaptic inputs in a broader time window compared to mature GCs.

T2N, a new interface between Matlab/TREES and NEURON

The model framework and easy switching between morphologies and different biophysics was achieved with T2N, a new interface between the TREES toolbox (Cuntz, Forstner, Borst, & Häusser, 2010, 2011) and NEURON (Carnevale & Hines, 2006) allowing an easy and clear definition and control of the NEURON compartmental model (morphologies, channel distributions, simulations etc.) as well as a subsequent analysis with Matlab and TREES. Moreover, the automatic parallelization of simulations reduces simulation time without the need of rewriting code for the NEURON parallel computing feature (Migliore, Cannia, Lytton, Markram, & Hines, 2006). The clear structure of defining the biophysics and the automatically produced stereotyped hoc code improves readability and mergeability of models developed with T2N. Thus, T2N is a new

valuable tool highly recommended for extensive *in silico* structure-function analyses in NEURON.

Mouse and rat model

A source of possible issues in former GC modeling studies lies in the fact that morphologies, biophysical mechanisms and electrophysiological data were not always used together in a consistent way in regard to the animal/cell age or the species, i.e. mouse or rat. The widely used model from Aradi and Holmes (Aradi & Holmes, 1999) had originally been fitted on a mature rat morphology and rat experiments. However, since then it has been used with newborn GC morphologies (Julián Tejada et al., 2012), fitted on mouse data (Ferrante et al., 2009) or used with mouse morphologies to reproduce mouse (Platschek et al., 2016) or even rat experiments (Chiang et al., 2012; Krueppel et al., 2011). Thus, there was a need for developing a consistent compartmental GC model, which would be specific for a given species and GC maturation phase. We took great care to fit and use our mature mouse GC model only with mature mouse morphologies and corresponding electrophysiological experiments. As the resulting detailed compartmental model provided accurate results by mimicking mature mouse GC behavior, we used it to develop a young mouse abGC and a mature rat GC model by implementing differences suggested by literature in regard to ion channel expression and electrophysiology as compared to mature mouse GCs.

Interestingly, despite the thicker ML in the rat DG, the total dendritic length and surface of reconstructed mouse (Schmidt-Hieber et al., 2007) and rat (Beining et al., 2016) GCs were not significantly different from each other. This phenomenon can be explained by the increased branching in mouse GCs (~16 branch points in mouse vs ~10 in rat). We first challenged our model to reproduce electrophysiological data from rat by simply replacing the mouse with rat morphologies. However, the combined rat R_{in} measurements from literature implied a steeper I-V relationship than in mouse (Mateos-Aparicio et al., 2014; Pourbadie et al., 2015; Schmidt-Hieber, Jonas, & Bischofberger, 2004; Staley, Otis, & Mody, 1992) and this difference could not be explained by morphology alone. Increasing the K_{ir} conductance resulted in F-I curves matching

experimental data. These results suggest that rat GCs display a reduced excitability due to incorporation of additional Kir channels. As an alternative, this could also be achieved by other leak channels such as K2P channels, however the rat I-V curve from experimental data in Figure 3B showed pronounced inward rectification, further supporting Kir channels as an underlying mechanism. In line with this, the increased leak conductance in the rat GC model improved the fitting of simulated bAP attenuation to physiological recordings obtained from rat experiments (Krueppel et al., 2011), as the attenuation was too weak in the unmodified rat model (data not shown).

Young abGC model

As the neuronal circuit of the DG is continuously remodeled by adult neurogenesis, the role of adult-born neurons in hippocampal processing gains relevance (Johnston et al., 2016; Rangel et al., 2013). As these neurons transiently exhibit unique intrinsic and synaptic properties they are subject to many studies (see reviews Aimone et al., 2010; Rangel et al., 2013; Johnston et al., 2016). Many special features have been associated with abGCs, such as increased excitability due to reduced Kir2 channel expression (Mongiat et al., 2009), increased synaptic plasticity due to higher NMDAR-2b expression (Ge et al., 2007), low inhibition due to developmentally delayed input from both feedforward and feedback GABAergic inhibitory loops (Marín-Burgin et al., 2012; Pardi et al., 2015; Temprana et al., 2015) and prolonged calcium transients due to different buffering capacities (Stocca et al., 2008). However, these special features of abGCs are most prominent during a critical time window (4-6 weeks after cell birth), when abGCs are supposed to exert their special role in learning and memory. In our attempt to create the first compartmental model of abGCs, we focused on their special intrinsic, non-synaptic properties known to exist at the start of the critical time window, namely increased input resistance and weaker Na/K peak conductances (Mongiat et al., 2009). To implement these changes we used data on ion channels which are known to be upregulated during postnatal development (Table 3) assuming that adult-born is similar, delayed at the most, as postnatal GC development (Espósito et al., 2005; Snyder, Ferrante, & Cameron, 2012;

Zhao et al., 2006). Even though a lower expression (or alternative splicing) of BK channels is only visible at P14 or earlier, we also had to reduce BK channels in our young abGC model because the fast AHP which is mainly regulated by BK channels in GCs was reported to be reduced in young abGCs (Yang et al., 2015), an observation we also found in our raw traces (Figure 6B, left) from Mongiat et al. (2009). The parameters of the young abGC model were fitted best when we reduced the beta4-subunit associated BK current (gabk) by 100 %. Thus, the abGC model predicts that the beta4 subunit is less expressed or not associated with BK channels in young abGCs.

To investigate the impact of the special intrinsic properties of young abGCs on their synaptic integration, we subjected both young and mature GC models to a broad range of synaptic input stimulation frequencies ranging from 10 to 75 Hz. In line with experimental data (Mongiat et al., 2009; Pardi et al., 2015) we found that diminished glutamatergic input onto abGCs was compensated by their enhanced excitability when GABAergic inhibition was absent. Both populations of GCs responded in a similar fashion over a wide range of stimuli, which is also in agreement with electrophysiological recordings (Pardi et al., 2015). Furthermore, despite their weaker excitatory input, we found that young abGCs were more efficiently activated by temporally separated (> 15 ms) incoming activity from medial and lateral perforant path inputs as compared to mature GCs. In future models, both feedforward and feedback inhibitory GABAergic inputs as well as realistic proportional numbers of immature and mature GCs could be incorporated to obtain a comprehensive realistic model of the DG network.

Wide diversity of realistic morphologies

Many previous compartmental models were based on a very simplified representation of GC morphology comprising two cylinders representing cell dendrites (e.g. Jedlicka et al., 2015; Santhakumar et al., 2005). Furthermore, models that did not use such simplified compartments were mostly tested in single morphologies (Aradi & Holmes, 1999; Ferrante et al., 2009). Therefore, there was a need for a new biophysical model which would be transferable to further morphologies. In our study, we introduced electrophysiological variability

(Figure 2—figure supplement 2) to the compartmental model by using diverse realistic and synthetic morphologies while keeping the channel densities the same. We developed a morphological mouse model capable of reproducing detailed morphological parameters of reconstructed mouse GCs (Schmidt-Hieber et al., 2007). We also created synthetic rat GCs using our recently published morphological model fitted on fully reconstructed rat morphologies (Beining et al., 2016). The morphological variability produced by each model was similar to the biological variability in the reconstructions. Interestingly, the resulting electrophysiological variability was in the range of experimental data indicating that morphological variability is able to account for a large part of electrophysiological variability. Hence, our model provides a valuable tool to create a DG network model with thousands of different but realistic GC morphologies (c.f. Schneider et al., 2014) and data-driven GC spiking behavior.

Biological ion channel composition

Most existing GC models did not implement specific ion channels but instead used equations describing ion currents (A-, M-, T-type, L-type, N-type, delayed rectifier etc.) that had been measured in GCs, but which are formed by the combined action of several differently distributed ion channels in the real cell (e.g. K_v1 and K_v4 form the A-type current in GCs but are localized in the axon or dendrite, respectively). By incorporating the contributions of different ion channel isoforms, our model can be used to analyze and predict the impact of different channelopathies or compensatory ion channel adaptations onto the cell's active and passive behavior. This might be of special interest since specific isoforms dynamically control excitability (e.g. $K_v2.1$; Misonou, Mohapatra, & Trimmer, 2005) and alter their expression under pathological conditions such as epilepsy (e.g. $K_v1.1$; Kirchheim et al., 2013; or Kir2.1 and HCN; Stegen et al., 2012) or oxidative stress (e.g. K_v4 ; Rüschemschmidt, Chen, Becker, Riazanski, & Beck, 2006). Indeed, our model was able to reproduce qualitatively the effects of a compensatory upregulation of Kir, HCN and $K_v1.1$ channels reported in TLE (Kirchheim et al., 2013; Stegen et al., 2012) demonstrating its predictive power there. Thus, the model might further be used to predict single or combined effects of other TLE-induced hippocampal

alterations such as the reduction of BK channels in GCs (Pacheco Otalora et al., 2008), the aberrant connectivity (see review by Sharma et al., 2007; and network model by Santhakumar et al., 2005), as well as the impact of therapeutic gene transfer approaches, such as the transfer of the K2P leak channel TREK-1 to ameliorate status epilepticus (Dey et al., 2014).

Model limitations and outlook

Kir channels significantly shape the resting membrane potential (M. Day et al., 2005; Stegen et al., 2012). A portion of the current that is described by our Kir2 model is probably also mediated by G-protein coupled Kir channels (Kir3 or GIRK) and by ATP-sensitive Kir channels (Kir6 or KATP) in real GCs. Both are expressed and functional in GCs (Karschin, Dissmann, Stühmer, & Karschin, 1996; Pelletier, Pahapill, Pennefather, & Carlen, 2000; Tanner, Lutas, Martínez-François, & Yellen, 2011) but are not part of our GC model as this would have required models of the G-protein and ATP molecular machinery (Enkvetchakul, Loussouarn, Makhina, Shyng, & Nichols, 2000; Proks & Ashcroft, 2009). GIRKs might be involved in neuromodulation through their activation by G-protein coupled receptors (e.g. 5-HT_{1A} serotonin, GABA_B and D₂ dopamine receptors). KATP channels are involved in controlling the resting membrane potential (Baukrowitz & Fakler, 2000) and a part of the slow AHP (Andrade et al., 2012) due to their opening upon ATP depletion after long-lasting spiking phases, which might explain the vulnerability of our model to high and prolonged current injections. Furthermore, in experiments, the Na⁺ ionic drive drops during strong and prolonged current injections as the Na⁺/K⁺ pump activity becomes saturated (Forrest, Wall, Press, & Feng, 2012; Norby, 1983; Zahler, Zhang, Manor, & Boron, 1997). Hence, an implementation of models for the Na⁺/K⁺ pump, KATP channels and cellular ATP handling might further improve the GC model.

To model sodium channel isoforms Na_v1.2 and Na_v1.6, which are expressed in GCs, we used a unifying Na_v model which had been developed based on AP measurements in mouse GCs (Schmidt-Hieber & Bischofberger, 2010). In the experimental data on which we fitted our mouse GC models (Mongiati et al., 2009), GCs displayed an initial high maximal rate of voltage rise during an AP which slowly decreased with increasing current injections whereas in the model

the rate was low at the beginning and increased with higher current injections (Figure 2—figure supplement 3, mature GCs and young abGCs in mouse). Furthermore, in the model, the amplitude of the second spike was lower indicating only partial recovery from inactivation (Fig. 2D). Developing detailed models of $\text{Na}_v1.2$ and 1.6 and their controlling mechanisms might help improving this aspect of the GC model.

An important issue is disentangling the different mechanisms of Ca^{2+} buffering and thereby the interdependency of Ca^{2+} channels, Ca^{2+} internal stores and Ca^{2+} -dependent potassium channels since Ca^{2+} influences AP repolarization (through BK channels) and ISIs (through SK and the slow AHP). We implemented a phenomenological Ca^{2+} buffer model reproducing measured concentrations and kinetics of free Ca^{2+} at different subcellular levels as well as measured GC Ca^{2+} currents (Eliot & Johnston, 1994; Jackson & Redman, 2003; Stocca et al., 2008). By incorporating realistic local Ca^{2+} dynamics we avoided using unphysiologically high BK or Ca^{2+} channel densities (Aradi & Holmes, 1999; Hayashi & Nonaka, 2011; Jaffe et al., 2011; Santhakumar et al., 2005) or adding unknown Ca^{2+} - and voltage-dependent channels (Mateos-Aparicio et al., 2014). This represents a significant improvement over former GC models. However, we have not explicitly modeled Ca^{2+} from the internal Ca^{2+} stores. The implementation of such an internal store mechanism might be important for modeling synaptic plasticity (Jedlicka & Deller, 2016) but also for detailed modeling of fast, medium and slow AHP generating potassium channels (Kaufmann et al., 2010; Piwonska et al., 2008; Shruti et al., 2012; Wang et al., 2016).

Another useful extension of the model would be an implementation of explicit spines. Spines are especially important during synaptic activation generating strong local depolarization (Gulledge, Carnevale, & Stuart, 2012; Tønnesen et al., 2014). Therefore, their explicit model will be needed to simulate realistically the effects of the depolarization on spine-localized ion channels and plasticity mechanisms.

As we did not investigate the entire parameter space of our electrophysiological models (especially in the young abGC model), e.g. using a genetic algorithm, we cannot exclude that a different channel density distribution would result in a similar reproduction of experimental results (Achard & De Schutter, 2006). We took great care to compare the expression and subcellular distribution data of ion channels in immunohistochemical studies with different studies by other labs or with electrophysiological evidence (e.g. pharmacological blockade). However, previous work in other cell types and animals has shown that similar electrical behavior might arise from different combinations and parameters of ion channels (Achard and De Schutter, 2006; Günay et al., 2008; Prinz et al., 2004; for review see Marder, 2011; Marder and Goaillard, 2006). Thus, our biophysical and morphological model provides a basis for future studies determining how cell-to-cell and animal-to-animal variability of ion channel expression combined with morphological and synaptic variability affects the robustness of GC passive and active behavior. As an example, our model can now be used to address the exciting question whether ion channel degeneracy in GCs exists in terms of compensatory interactions between multiple ion channels (Drion, O'Leary, & Marder, 2015) and how it contributes to the homeostasis of GC function.

In summary, we developed a new compartmental model of mouse and rat GCs that is biologically and physiologically consistent and thus of high predictive value for studies on the single-cell and network behavior of mature GCs and young abGCs, as well as under pathological conditions of synaptic, morphological or physiological alterations of GCs.

Materials and Methods

Compartmental modeling was done in the NEURON (Carnevale & Hines, 2006) environment (V7.3). The programming environment Matlab (Mathworks, versions 2014a–2015b) was used together with the freely-available TREES toolbox (Cuntz et al., 2010, 2011) with a self-developed interface to set simulation parameters, adjust morphologies and launch parallel NEURON simulations directly. Individual figure panels were generated with Matlab and combined in Adobe Illustrator CS6.

Reconstructed dendritic morphologies

Eight morphologies of mature mouse GCs (Schmidt-Hieber et al., 2007) were converted to NEURON models using the TREES toolbox (Cuntz et al., 2010). To each morphology a synthetic axon (length: 1,350 μm , diameter 0.45 μm) was added where no axon was provided. Three of those morphologies are shown in Figure 1A. The biophysical model for mouse mature GCs was first fitted on the basis of these morphologies. In order to accommodate the layer dependent mechanisms of the biophysical model, it was necessary to define the following dendritic regions: the granule cell layer (GCL), and the inner, middle and outer molecular layer (IML, MML and OML, respectively). We assumed a molecular layer (ML) thickness of 188 μm (Dokter et al., 2015; Zhou et al., 2009) and subdivided it with a ratio of (0.2 : 0.4 : 0.4) as the IML is smaller compared to MML and OML in mouse due to the lack of commissural fibers. We rotated the morphologies to align the distal dendritic tips and assigned all dendrites within 75 μm of the tips to the OML, all dendrites within 75 μm of the OML border to the MML and the dendrites within 38 μm of the MML border to the IML. The remaining dendritic segments between the IML border and the soma were assigned to the GCL. For the rat GC model, reconstructed morphologies from a previous study were used (Beining et al., 2016). We only chose reconstructions that belonged to the mature population, were untreated (contralateral side) and had a completeness of over 90 % resulting in five morphologies. Dendritic regions in these morphologies were anatomically

assigned based on the slices they were reconstructed from (see Beining et al., 2016).

Morphological models

To further test the robustness of the biophysical model against morphological variations, 15 synthetic mouse and rat morphologies of mature GCs were generated with a self-written morphological GC model based on the minimum spanning tree algorithm available in the TREES toolbox (Cuntz et al., 2010). The rat morphological model has already been published (Beining et al., 2016) and reproduces morphological data of mature rat GCs with great detail (Figure 3A, right side). For the mouse model (Figure 1B), we used the GC morphologies mentioned above (Schmidt-Hieber et al., 2007) to fit the parameters, which resulted in several changes compared to the rat model. Since the volume of the mouse DG is considerably smaller, the thickness of the ML was reduced to 188 μm in the model to mimic the ML thickness of the real morphologies including the ratios between the layers (38 : 75 : 75 μm). In parallel, the threshold for pruning short terminal segments was reduced to 20 μm . Furthermore, mouse GCs were much more branched (compare morphologies in Figure 2 and 3), reaching a similar total dendritic length despite a smaller ML. Hence, we doubled the total number of target points (50), and changed their distribution to obtain more points in the MML, where branching was extensive in real mouse morphologies (Schmidt-Hieber et al., 2007). Fitting a quadratic diameter taper function to the morphologies of Schmidt-Hieber (Schmidt-Hieber et al., 2007) resulted in an offset of 0.396 μm and a scaling factor of 0.1, which was used to taper the dendritic diameter of the synthetic trees. The soma diameter was set to $10.25 \pm 0.5 \mu\text{m}$. Analog to the real morphologies, a synthetic axon was added.

Ion channels

We performed an extensive literature research on the existence and subcellular distribution of different channel isoforms in mature GCs and found 16 ion channel isoforms (Figure 1A) together with their coarse subcellular distribution. Briefly, an 8-state sodium (Na_v) channel model from (Schmidt-Hieber & Bischofberger, 2010) was adapted, a leaky inward-rectifier channel (Kir) model was developed based on experimental data (Dhamoon et al., 2004; Ishihara & Yan, 2007; T.-A. Liu, Chang, & Shieh, 2012; Lopatin, Makhina, & Nichols, 1995; Panama & Lopatin, 2006; Yan & Ishihara, 2005), A-type potassium channels were represented by models of $\text{K}_v1.1$ (Christie, Adelman, Douglass, & North, 1989), $\text{K}_v1.4$ (Wissmann et al., 2003) and $\text{K}_v4.2$ (Barghaan, Tozakidou, Ehmke, & Bähring, 2008) channel isoforms, the delayed-rectifier channel $\text{K}_v3.4$ was fitted on data from (Desai, Kronengold, Mei, Forman, & Kaczmarek, 2008; Rettig et al., 1992; Riazanski et al., 2001; Rudy et al., 1991; Schröter et al., 1991; Vega-Saenz de Miera, Moreno, Fruhling, Kentros, & Rudy, 1992), and the M-type potassium channel $\text{K}_v7.2/3$ was taken from (Mateos-Aparicio et al., 2014). Furthermore, we included an HCN channel (Stegen et al., 2012) adapted to a lower threshold for activation, a $\text{Ca}_v2.2$ (N-type) calcium (Ca^{2+}) channel (Fox, Nowycky, & Tsien, 1987) adapted to a more realistic, slower inactivation time constant (100 ms instead of 1–10 ms), a T-type $\text{Ca}_v3.2$ Ca^{2+} channel model from (Burgess, Crawford, Delisle, & Satin, 2002), two L-type $\text{Ca}_v1.2$ and $\text{Ca}_v1.3$ Ca^{2+} channel models (Evans, Maniar, & Blackwell, 2013) transferred from GENESIS (Bower & Beeman, 1998), the Ca^{2+} -dependent big and small conductance potassium channels BK and SK from (Jaffe et al., 2011) and (Solinas et al., 2007) with modifications (see Materials and methods), and an improved Ca^{2+} buffering model (see Materials and methods). We then looked for the kinetics of these channels and chose ion channel models that followed these kinetics (or could be modified appropriately) or, if not available, fitted own channel models to this data. Generally, all channels were incorporated according to their expression strength found by protein immune staining followed by fine-tuning of the channel densities to fit the active properties of mature GCs. The original literature, the incorporated channel densities and the origin of the channel models are summarized in Table 1. A general review on

axonal targeting of voltage-dependent potassium channels can be found in (Gu & Barry, 2011). The reversal potentials for potassium and sodium were calculated from the solutions which were used in the experiments (Mongiati et al., 2009) ($E_K = -93$ mV, $E_{Na} = 87.76$ mV) and were kept constant throughout the simulations.

Passive membrane properties

The axial resistance was chosen to be 200 Ω cm in the dendrites and the soma and 100 Ω cm in the axon. The specific membrane capacitance C_m was 0.9 pF/cm². Spines were implicitly modeled by scaling the passive conductance and C_m in the IML by a factor of 1.45, and in the MML and OML by a factor of 1.9 (mature mouse and rat GC model). We combined the function of two-pore channel potassium (K2P) channels such as TWIK and TREK into a single passive channel as they behave in a voltage-independent manner (i.e. linearly) over a wide voltage range and are expressed in GCs (Aller & Wisden, 2008; Gabriel, Abdallah, Yost, Winegar, & Kindler, 2002; Hervieu et al., 2001; Lesage et al., 1997; Talley, Solorzano, Lei, Kim, & Bayliss, 2001; Yarishkin et al., 2014). However, it should be noted that modeling leak currents exactly (i.e. non-linearly) may affect the output of neurons (Huang, Hong, & De Schutter, 2015).

Passive leak channel and Kir channel

For the passive GC model, a passive leak channel model was introduced representing the cell's channels with linear current-voltage relationships, such as 2-pore potassium (K2P) channels that are known to be strongly expressed in GCs (Gabriel et al., 2002; Hervieu et al., 2001; Yarishkin et al., 2014). Moreover, we incorporated a model of the inward-rectifying Kir2 channel, which also contributes to the cell's passive properties. Kir channels in GCs are expressed as several variants (Kir2.1-4) (Karschin et al., 1996; Prüss et al., 2005), which can assemble to heteromeric channels with mixed properties (Dhamoon et al., 2004). Hence, because the stoichiometry of Kir channel subunits is not known in GCs yet, we aimed to incorporate a unifying Kir2.x model. We used a model for a Kir 2.1 channel that described low- and high-affinity spermine block as well as Mg²⁺ block modes (Yan & Ishihara, 2005).

Since later studies showed that both modes exist in parallel with the high-affinity block being a substate of the channel that still shows low conductance (Liu et al., 2012), we first changed the high-affinity block state to be a substate. To account for other Kir2 isoforms and putative Kir2.1–3 heteromers, which have different sensitivities to spermine block and are thus less rectifying (especially Kir2.3) (Panama & Lopatin, 2006), we set the high-affinity fractional subconductance to 0.25 (which corresponds to the fractional conductance being susceptible to the low-affinity spermine block) compared to 0.09–0.15 in the original studies with homomeric Kir2.1 (Ishihara & Yan, 2007; Yan & Ishihara, 2005). Then, we added the low-affinity state as another substate to the model (6 states in total) and fitted an exponential back and forward rate as the low-affinity mode had originally been described without kinetics, being assumed to be instantaneous (Yan & Ishihara, 2005). Furthermore, the unblock rates of the high-affinity states were slowed down to match the values measured by (Lopatin et al., 1995; Panama & Lopatin, 2006). Another issue with the original Kir2.1 model was that it was based on measurements in equal extra- and intracellular potassium (i.e. $E_K = 0$ mV) and different Mg^{2+} concentrations, two factors which strongly influence Kir rectification. As the dependence between E_K and $V_{1/2}$ of the Kir channel block has a slope of exactly 1 (Panama & Lopatin, 2006) we shifted the activation and inactivation of the model by -93 mV, which was the E_K in our biophysical model. Furthermore, as the Mg^{2+} block of the Kir channel was weakened in our experiments due to a drastic difference in the Mg^{2+} driving force ($E_{Mg} = -14.38$ mV and $E_K = -93$ mV vs. $E_{Mg} = -88$ mV and $E_K = 0$ mV in the original study), we adapted the Mg^{2+} block in the Kir model by shifting the Mg^{2+} inactivation by only $0.5 * E_K$ and reducing the influence of intracellular Mg^{2+} concentration by a factor of 8. The resulting model could well reproduce the steady-state I–V relationships (Figure 2A, Figure 3B and Figure 6B) as well as the slow unblock at hyperpolarized potentials (Figure 2—figure supplement 1).

Sodium channels

We implemented the 8-state sodium (Na_v) channel model from Schmidt-Hieber as it had been directly fitted on mature GCs (Schmidt-Hieber & Bischofberger,

2010) However, we found that distributing the densities according to the spatial functions used in the model was not compatible with our morphologies since the spiking behavior depended strongly on the somatic and axonal geometry, which varied significantly between cells. Thus, we chose region-dependent densities with the highest density in the axon initial segment (Schmidt-Hieber & Bischofberger, 2010). The dendritic sodium channel was removed because GC dendrites were reported to only exhibit passive properties (Krueppel et al., 2011; Schmidt-Hieber et al., 2007). In order to compensate for the resulting smaller excitatory drive, somatic and axonal channel densities were increased compared to the original. Also, the Na_v channel activation curve was shifted by +10 mV in order to reproduce the spike threshold from the electrophysiology data (see Figure 2E). Furthermore, the inactivation kinetics had originally only been fitted between -50 and 20 mV thereby omitting the reproduction of deinactivation kinetics between -120 and -50 mV, which were slower than the reported values in literature (Mercer, Chan, Tkatch, Held, & Surmeier, 2007; Rush, Dib-Hajj, & Waxman, 2005). Hence, we adapted the inactivation rates to fit the recovery kinetics from inactivation, too.

K_v channels

Table 1 summarizes the literature that the different K_v models were taken from or fitted onto. Importantly, K_v1 channels at the axon initial segment control action potential (AP) waveforms and synaptic efficacy (Kole, Letzkus, & Stuart, 2007) and form heteromers comprising α - and auxiliary subunits. In the DG $\text{K}_v1.1/1.4$, heteromers are formed together with $\text{K}_v\beta1/2$ (Monaghan, Trimmer, & Rhodes, 2001; K J Rhodes et al., 1997) and KCNE1/2 (Kanda, Lewis, Xu, & Abbott, 2011; Tinel et al., 2000) subunits. However, these interactions have only been modeled in detail in the K_v4 channel (Amarillo et al., 2008; Barghaan et al., 2008); we therefore implemented a standard $\text{K}_v1.1$ and $\text{K}_v1.4$ model from (Christie et al., 1989) and (Wissmann et al., 2003), which might ignore functional impacts such as the calcium-dependent modification of inactivation kinetics through $\text{K}_v\beta1$ (Jow, Zhang, Kopsco, Carroll, & Wang, 2004).

HCN channels

The existence of HCN channels in GCs remains controversial (Stegen et al., 2012) which might partly be explained by the use of different species and by the fact, that HCN channels are blocked differentially by the Mg^{2+} present in the pipette in various concentrations (Vemana, Pandey, & Larsson, 2008). We implemented an HCN channel (Stegen et al., 2012) but left-shifted the voltage-dependence by 10 mV since $V_{1/2}$ was more hyperpolarized than -90 mV for all HCN channel isoforms found in the literature (Altomare et al., 2001; Bräuer et al., 2001; Chen, Wang, & Siegelbaum, 2001; Postea & Biel, 2011; Surges et al., 2006).

Calcium channels

For the $Ca_v2.2$ (N-type) Ca-channel we used the activation and inactivation kinetics from (Fox et al., 1987), but set the inactivation time constant to 100 ms (compared to 1–10 ms between 0 and 50 mV in the original model). The resulting inactivation kinetics of $Ca_v2.2$ at these voltages were then more similar to experimental results (Fox et al., 1987; X. Huang, Senatore, Dawson, Quan, & Spafford, 2010) and were in the range of inactivation time constants of other models (Evans et al., 2013; Hemond et al., 2008; Papoutsis, Sidiropoulou, Cutsuridis, & Poirazi, 2013; Wolf et al., 2005). However, it should be noted that the deinactivation kinetics (below 0 mV) are much slower in real channels being in the range of seconds (Zhu, McDavid, & Currie, 2015), which might be important when $Ca_v2.2$ is inactivated by a long depolarization and then reactivated shortly thereafter.

The expression and distribution of T-type Ca-channels ($Ca_v3.1-3$) was controversial in the literature: Whereas Martinello et al. (EM immune stainings) reported $Ca_v3.2$ to be mainly expressed in GC dendrites (Martinello et al., 2015), McKay et al. (fluorescent immune staining) found $Ca_v3.2$ to be expressed exclusively in the soma (McKay et al., 2006). Similarly, McKay et al. found $Ca_v3.3$ strongly expressed in GC somata (McKay et al., 2006), whereas Talley et al. reported very weak $Ca_v3.3$ mRNA expression in the DG and McRory et al. reported a complete lack of $Ca_v3.3$ in the hippocampus (McRory

et al., 2001). Since one explanation might be that $\text{Ca}_v3.3$ expression is largely reduced from juvenile to the adult age (McRory et al., 2001; Yunker et al., 2003), we decided to only implement a $\text{Ca}_v3.2$ model from (Burgess et al., 2002) to model T-type Ca^{2+} currents. We did not use a separate $\text{Ca}_v3.1$ channel as it has kinetics similar to $\text{Ca}_v3.2$ (Cain & Snutch, 2010). Moreover, since no consensus could be found about the subcellular distribution, we incorporated the model into all compartments with increased densities in the soma and dendrite (Martinello et al., 2015; McKay et al., 2006).

Calcium buffer

Since calcium (Ca^{2+}) activates small-conductance and big potassium (SK and BK) channels and plays a crucial role for synaptic plasticity, we developed an improved Ca^{2+} buffering model. Submembrane shell models of Ca^{2+} buffering and dynamics in neurons were used in previous compartmental models of granule cells (Aradi & Holmes, 1999; Hayashi & Nonaka, 2011; Mateos-Aparicio et al., 2014; Santhakumar et al., 2005; Yuen & Durand, 1991). They were based on the assumption that Ca^{2+} is mainly active within a thin shell beneath the cell membrane but rapidly buffered outside of that shell. However, as recently reported (Anwar et al., 2014), many of these shell models were found to contain an error that was introduced in early GC models and led to incorrect Ca^{2+} levels in thin dendrites. Hence, we implemented a Ca^{2+} shell model (using a shell depth of $0.05 \mu\text{m}$) corrected to varying diameters in the morphology (Anwar et al., 2014).

Furthermore, earlier compartmental models of GCs used shell models with fast exponential Ca^{2+} decay times of 9 ms (Aradi & Holmes, 1999; Mateos-Aparicio et al., 2014; Santhakumar et al., 2005; Yuen & Durand, 1991). This was an estimate originally implemented into the compartmental GC model of Yuen and Durand (1991) to reproduce spike adaptation and represents averaged and simplified Ca^{2+} dynamics which, in reality, extends over several time scales in nerve cells (Blaustein, 1988; Yuen & Durand, 1991). Slower dynamics of 100 ms have only been used in motoneurons so far (Traub & Llinás, 1977), but a carefully calibrated Ca^{2+} imaging study in rat and mouse mature GCs revealed decay time constants of 230 ± 30 ms and 280 ± 30 ms, respectively,

as well as considerably lower Ca^{2+} peak levels (Stocca et al., 2008) as compared to former models (Aradi & Holmes, 1999; Hayashi & Nonaka, 2011; Mateos-Aparicio et al., 2014; Santhakumar et al., 2005). Furthermore, other studies have reported that the membrane of GCs comprises micro- and nanodomains of Ca^{2+} channels clustered with SK or BK channels at distances between 13 and 150 nm and showed that the Ca^{2+} rise and decay can be very large and nearly instantaneous in these domains (Fakler & Adelman, 2008; Kaufmann et al., 2010; Marrion & Tavalin, 1998; Müller et al., 2007). In our model we aimed to reproduce overall Ca^{2+} increase and decay on the one side, but also the local Ca^{2+} increase in micro- and nanodomains. Hence, we introduced a phenomenological model of Ca^{2+} buffering by dividing the Ca^{2+} influx with a constant, which was analog to the so called Ca^{2+} binding ratio representing the ratio of buffer-bound Ca^{2+} ions versus free ions. Following the literature we assumed a lower Ca^{2+} binding ratio of 10 in the axon compared to 50 in the dendrite (Jackson & Redman, 2003; Stocca et al., 2008). A somatic Ca^{2+} binding ratio has not been reported, yet, but might be high due to a high amount of fixed and mobile buffers such as mitochondria (Duchen, 1999). Hence, we set the Ca^{2+} binding ratio to 200 in the soma. To model the clustering of Ca^{2+} channels with BK and SK channels, we additionally supplied BK and SK channels with unmodified (i.e. no Ca^{2+} binding ratio) instantaneous local $[\text{Ca}^{2+}]_i$ from the respective clustered Ca^{2+} channel (N-type Ca^{2+} channels for BK and L-type Ca^{2+} channels for SK channels; see Marrion and Tavalin, 1998). In this way the model was taking into account that these channels are in close proximity to Ca^{2+} channels and therefore their Ca^{2+} -activation is not affected by the intracellular Ca^{2+} buffers (Fakler & Adelman, 2008; Müller et al., 2007).

We set the Ca^{2+} decay time constant to 43 ms in the axon (Jackson & Redman, 2003) and to 240 ms in all other compartments (Stocca et al., 2008). To fine-tune the Ca^{2+} channel density distributions of the four used Ca^{2+} channels ($\text{Ca}_v1.2$, $\text{Ca}_v1.3$, $\text{Ca}_v2.2$ and $\text{Ca}_v3.2$) we additionally considered the contribution of each isoform to the Ca^{2+} current at 100 mV (Eliot & Johnston, 1994) and peak Calcium levels following an AP (Jackson & Redman, 2003; Stocca et al., 2008).

Calcium-dependent potassium channels

Ca²⁺-dependent potassium channels such as BK and SK form micro- and nanodomains with specific Ca²⁺ channels in GCs (reviewed in (Fakler & Adelman, 2008)): N-type Ca²⁺ channels form nanodomains with BK (Loane, Lima, & Marrion, 2007; Marrion & Tavalin, 1998) and L-type Ca²⁺ channels form microdomains with SK channels (Marrion & Tavalin, 1998). In these clusters, the local Ca²⁺ concentration can be very fast and high during Ca²⁺ channel opening. Thus, as aforementioned, an additional local [Ca²⁺] was directly calculated for BK and SK channels from the respective locally clustered Ca²⁺ channel without applying the Ca²⁺ binding ratio. For simplification and fast computation this local [Ca²⁺] was assumed to be instantaneous, i.e. without a rise or decay time. To account for SK having a higher distance of ~150 nm to its L-type Ca²⁺ channels in the microdomains, compared to 13-50 nm for BK channels we divided the local SK [Ca²⁺] by 3.

The BK channel model from (Jaffe et al., 2011) simulated BK α -subunits with or without β 4-subunits which make the channel kinetics much slower and resistant against the BK blocker iberiotoxin. Pharmacological studies with iberiotoxin suggest that wildtype GCs do not contain pure α -BK channels (Shruti et al., 2012), but prolonged application of high toxin concentrations were shown to also block wildtype GC BK channels (Müller et al., 2007), suggesting that BK channels might be expressed with different stoichiometries of α - and β 4-subunits resulting in partial iberiotoxin-resistances and intermediate kinetics (Wang, Jaffe, & Brenner, 2014). As there exist no studies on such intermediate kinetics, we implemented both the α - and $\alpha\beta$ 4-subunit model of BK.

We adapted the SK2 channel model from Solinas et al. (Solinas et al., 2007) which is based on the kinetic model by (Hirschberg, Maylie, Adelman, & Marrion, 1998) to model all SK channel isoforms expressed in GCs (SK1-3) as they have similar kinetics and calcium-dependencies. We found that the activation kinetics of the model following Ca²⁺ transients were too fast and the inactivation kinetics too slow, compared to experimental measurements (Hirschberg et al., 1998; Xia et al., 1998), hence we refitted the constant and the Ca²⁺-dependent rates to the experimental data.

Fine-tuning of the models' passive and active channel densities was done with Matlab using raw voltage and current traces (Mongiat et al., 2009) (control vs. BaCl application) and further experimental data on GC physiology from literature (Krueppel et al., 2011; Müller et al., 2007; Riazanski et al., 2001; Schmidt-Hieber & Bischofberger, 2010; Schmidt-Hieber et al., 2007; Stocca et al., 2008).

Young abGC model

We turned our biophysical model of mature GCs into a model of young (28 dpi) abGCs by reducing several channel densities that have been reported to be less expressed in developing GCs (Table 3). By reducing the Na_v channel density, a smaller Na^+ drive was achieved similar as it was found in the phase plots of young abGCs (Figure 6F). Reducing $\text{K}_v2.1$ and $\text{K}_v4.2$ in the model decreased the medium AHP that otherwise would induce too long and hyperpolarized ISIs. Consequently, $\text{Ca}_v1.3$ also had to be reduced to avoid unrealistically strong dendritic depolarization caused by the lacking hyperpolarization mediated by $\text{K}_v4.2$. Furthermore, we reduced BK channel density to eliminate the prominent fast AHP not found in the experimental data from abGCs (Mongiat et al., 2009; Yang et al., 2015).

Synaptic integration in adult-born granule cells (abGCs)

For these simulations we randomly distributed 30 synapses equally distributed over dendrites in the MML and OML (schemes in Figure 7). The synapses had an exponential rise and decay with dynamics mimicking that of real EC-GC synapses (exponential rise time constant: 0.2 ms, exponential decay time constant: 2.5 ms, reversal potential at 0 mV, synaptic weight 0.65 nS each). All synapses were either activated synchronously (Figure 7A) with a frequency ranging from 10 to 100 Hz or with a delay between MML and OML synapses (Figure 7B) ranging from -25 to +25 ms. The relation between input and output was analyzed by calculating the ratio of the output versus the input frequency. Hence a ratio of 1 means the cell having the same spiking frequency as the input and 0 meaning the cell does not spike at all.

Data sharing

Upon publication, all compartmental models along with all simulation protocols that have been performed in this study will be made available on the ModelDB public database (<http://senselab.med.yale.edu/ModelDB/default.asp>). The T2N interface will also be available separately on the TREES homepage (<http://treestoolbox.org>).

Acknowledgements

We would like to thank J. Kasper and S. Krischok for performing preliminary analyses and T. Deller for useful discussions and continuous support.

Author contributions

M.B., H.C., L.A.M., P.J. and S.W.S. conceived the study and wrote the paper. M.B. implemented the model and performed the numerical simulations and L.A.M. performed the experiments.

References

- Achard, P., & De Schutter, E. (2006). Complex parameter landscape for a complex neuron model. *PLoS Computational Biology*, *2*(7), e94. <https://doi.org/10.1371/journal.pcbi.0020094>
- Aimone, J. B., Deng, W., & Gage, F. H. (2010). Adult neurogenesis: integrating theories and separating functions. *Trends in Cognitive Sciences*, *14*(7), 325–337. <https://doi.org/10.1016/j.tics.2010.04.003>
- Aimone, J. B., Li, Y., Lee, S. W., Clemenson, G. D., Deng, W., & Gage, F. H. (2014). Regulation and function of adult neurogenesis: from genes to cognition. *Physiol Rev*, *94*(4), 991–1026. <https://doi.org/10.1152/physrev.00004.2014>
- Alle, H., Kubota, H., & Geiger, J. R. P. (2011). Sparse But Highly Efficient Kv3 Outpace BKCa Channels in Action Potential Repolarization at Hippocampal Mossy Fiber Boutons. *Journal of Neuroscience*, *31*(22), 8001–8012. <https://doi.org/10.1523/JNeurosci.0972-11.2011>
- Aller, M. I., & Wisden, W. (2008). Changes in expression of some two-pore domain potassium channel genes (KCNK) in selected brain regions of developing mice. *Neuroscience*, *151*(4), 1154–1172. <https://doi.org/10.1016/j.neuroscience.2007.12.011>
- Almog, M., & Korngreen, A. (2016). Is realistic neuronal modeling realistic? *Journal of Neurophysiology*, *2*(1), jn.00360.2016. <https://doi.org/10.1152/jn.00360.2016>
- Althaus, A. L., Sagher, O., Parent, J. M., & Murphy, G. G. (2015). Intrinsic neurophysiological properties of hilar ectopic and normotopic dentate granule cells in human temporal lobe epilepsy and a rat model. *Journal of Neurophysiology*, *113*(4), 1184–1194. <https://doi.org/10.1152/jn.00835.2014>
- Altomare, C., Bucchi, A., Camatini, E., Baruscotti, M., Viscomi, C., Moroni, A., & DiFrancesco, D. (2001). Integrated allosteric model of voltage gating of HCN channels. *Journal of General Physiology*, *117*(6), 519–532. <https://doi.org/10.1085/jgp.117.6.519>

- Amarillo, Y., De Santiago-Castillo, J. A., Dougherty, K., Maffie, J., Kwon, E., Covarrubias, M., & Rudy, B. (2008). Ternary Kv4.2 channels recapitulate voltage-dependent inactivation kinetics of A-type K⁺ channels in cerebellar granule neurons. *Journal of Physiology*, *586*(8), 2093–2106. <https://doi.org/10.1113/jphysiol.2007.150540>
- An, W. F., Bowlby, M. R., Betty, M., Cao, J., Ling, H. P., Mendoza, G., ... Rhodes, K. J. (2000). Modulation of A-type potassium channels by a family of calcium sensors. *Nature*, *403*(6769), 553–556. <https://doi.org/10.1038/35000592>
- Andrade, R., Foehring, R. C., & Tzingounis, A. V. (2012). The calcium-activated slow AHP: cutting through the Gordian knot. *Frontiers in Cellular Neuroscience*, *6*, 47. <https://doi.org/10.3389/fncel.2012.00047>
- Antonucci, D. E., Lim, S. T., Vassanelli, S., & Trimmer, J. S. (2001). Dynamic localization and clustering of dendritic Kv2.1 voltage-dependent potassium channels in developing hippocampal neurons. *Neuroscience*, *108*(1), 69–81. [https://doi.org/10.1016/S0306-4522\(01\)00476-6](https://doi.org/10.1016/S0306-4522(01)00476-6)
- Anwar, H., Roome, C. J., Nedeleescu, H., Chen, W., Kuhn, B., & De Schutter, E. (2014). Dendritic diameters affect the spatial variability of intracellular calcium dynamics in computer models. *Frontiers in Cellular Neuroscience*, *8*, 168. <https://doi.org/10.3389/fncel.2014.00168>
- Aradi, I., & Holmes, W. R. (1999). Role of multiple calcium and calcium-dependent conductances in regulation of hippocampal dentate granule cell excitability. *Journal of Computational Neuroscience*, *6*(3), 215–235.
- Bähring, R., Boland, L. M., Varghese, A., Gebauer, M., & Pongs, O. (2001). Kinetic analysis of open- and closed-state inactivation transitions in human Kv4.2 A-type potassium channels. *Journal of Physiology*, *535*(1), 65–81. <https://doi.org/10.1111/j.1469-7793.2001.00065.x>

- Ballesteros-Merino, C., Watanabe, M., Shigemoto, R., Fukazawa, Y., Adelman, J. P., & Luján, R. (2014). Differential subcellular localization of SK3-containing channels in the hippocampus. *European Journal of Neuroscience*, *39*(6), 883–892. <https://doi.org/10.1111/ejn.12474>
- Barghaan, J., Tozakidou, M., Ehmke, H., & Bähring, R. (2008). Role of N-terminal domain and accessory subunits in controlling deactivation-inactivation coupling of Kv4.2 channels. *Biophysical Journal*, *94*(4), 1276–1294. <https://doi.org/10.1529/biophysj.107.111344>
- Baukrowitz, T., & Fakler, B. (2000). K(ATP) channels gated by intracellular nucleotides and phospholipids. *European Journal of Biochemistry*, *267*(19), 5842–5848. <https://doi.org/10.1046/j.1432-1327.2000.01672.x>
- Beining, M., Jungenitz, T., Radic, T., Deller, T., Cuntz, H., Jedlicka, P., & Schwarzacher, S. W. (2016). Adult-born dentate granule cells show a critical period of dendritic reorganization and are distinct from developmentally born cells. *Brain Structure & Function*. <https://doi.org/10.1007/s00429-016-1285-y>
- Bender, R. A., Soleymani, S. V, Brewster, A. L., Nguyen, S. T., Beck, H., Mathern, G. W., & Baram, T. Z. (2003). Enhanced expression of a specific hyperpolarization-activated cyclic nucleotide-gated cation channel (HCN) in surviving dentate gyrus granule cells of human and experimental epileptic hippocampus. *Journal of Neuroscience*, *23*(17), 6826–6836.
- Bergami, M., Masserdotti, G., Temprana, S. G. G., Motori, E., Eriksson, T. M. M., Göbel, J., ... Berninger, B. (2015). A critical period for experience-dependent remodeling of adult-born neuron connectivity. *Neuron*, *85*(4), 710–717. <https://doi.org/10.1016/j.neuron.2015.01.001>
- Blaustein, M. P. (1988). Calcium transport and buffering in neurons. *Trends in Neurosciences*, *11*(10), 438–443. [https://doi.org/10.1016/0166-2236\(88\)90195-6](https://doi.org/10.1016/0166-2236(88)90195-6)
- Bower, J. M., & Beeman, D. (1998). *The book of GENESIS: exploring realistic neural models with the GEneral NEural Simulation System (2nd Ed.)*. New York: Springer-Verlag.

- Bräuer, A. U., Savaskan, N. E., Kole, M. H., Plaschke, M., Monteggia, L. M., Nestler, E. J., ... Nitsch, R. (2001). Molecular and functional analysis of hyperpolarization-activated pacemaker channels in the hippocampus after entorhinal cortex lesion. *FASEB Journal*, *15*(14), 2689–2701. <https://doi.org/10.1096/fj.01-0235com>
- Brenner, R., Chen, Q. H., Vilaythong, A., Toney, G. M., Noebels, J. L., & Aldrich, R. W. (2005). BK channel beta4 subunit reduces dentate gyrus excitability and protects against temporal lobe seizures. *Nature Neuroscience*, *8*(12), 1752–1759. <https://doi.org/10.1038/nn1573>
- Brunel, N., Hakim, V., & Richardson, M. J. E. (2014). Single neuron dynamics and computation. *Current Opinion in Neurobiology*, *25*, 149–155. <https://doi.org/10.1016/j.conb.2014.01.005>
- Burgess, D. E., Crawford, O., Delisle, B. P., & Satin, J. (2002). Mechanism of inactivation gating of human T-type (low-voltage activated) calcium channels. *Biophysical Journal*, *82*(4), 1894–1906. [https://doi.org/10.1016/S0006-3495\(02\)75539-2](https://doi.org/10.1016/S0006-3495(02)75539-2)
- Cain, S. M., & Snutch, T. P. (2010). Contributions of T-type calcium channel isoforms to neuronal firing. *Channels (Austin, Tex.)*, *4*(6), 475–482. <https://doi.org/10.4161/chan.4.6.14106>
- Carnevale, N. T., & Hines, M. L. (2006). *The NEURON Book*. Cambridge, UK: Cambridge University Press.
- Chang, S. Y., Zaghera, E., Kwon, E. S., Ozaita, A., Bobik, M., Martone, M. E., ... Rudy, B. (2007). Distribution of Kv3.3 potassium channel subunits in distinct neuronal populations of mouse brain. *Journal of Comparative Neurology*, *502*(6), 953–972. <https://doi.org/10.1002/cne.21353>
- Chen, S., Wang, J., & Siegelbaum, S. A. (2001). Properties of hyperpolarization-activated pacemaker current defined by coassembly of HCN1 and HCN2 subunits and basal modulation by cyclic nucleotide. *Journal of General Physiology*, *117*(5), 491–504. <https://doi.org/10.1085/jgp.117.5.491>

Chiang, P.-H., Wu, P.-Y., Kuo, T.-W., Liu, Y.-C., Chan, C.-F., Chien, T.-C., ... Lien, C.-C. (2012). GABA is depolarizing in hippocampal dentate granule cells of the adolescent and adult rats. *Journal of Neuroscience*, *32*(1), 62–67. <https://doi.org/10.1523/JNeurosci.3393-11.2012>

Christie, M. J., Adelman, J. P., Douglass, J., & North, R. A. (1989). Expression of a cloned rat brain potassium channel in *Xenopus* oocytes. *Science*, *244*(4901), 221–224. <https://doi.org/10.1126/science.2539643>

Chung, Y. H., Shin, C. M., Kim, M. J., Shin, D. H., Yoo, Y. B., & Cha, C. I. (2001). Spatial and temporal distribution of N-type Ca(2+) channels in gerbil global cerebral ischemia. *Brain Research*, *902*(2), 294–300. <https://doi.org/10.1126/science.2539643>

Cooper, E. C., Harrington, E., Jan, Y. N., & Jan, L. Y. (2001). M channel KCNQ2 subunits are localized to key sites for control of neuronal network oscillations and synchronization in mouse brain. *Journal of Neuroscience*, *21*(24), 9529–9540.

Cooper, E. C., Milroy, A., Jan, Y. N., Jan, L. Y., & Lowenstein, D. H. (1998). Presynaptic localization of Kv1.4-containing A-type potassium channels near excitatory synapses in the hippocampus. *Journal of Neuroscience*, *18*(3), 965–974.

Craig, P. J., Beattie, R. E., Folly, E. A., Banerjee, M. D., Reeves, M. B., Priestley, J. V., ... Volsen, S. G. (1999). Distribution of the voltage-dependent calcium channel alpha1G subunit mRNA and protein throughout the mature rat brain. *European Journal of Neuroscience*, *11*(8), 2949–2964.

Cuntz, H., Forstner, F., Borst, A., & Häusser, M. (2010). One rule to grow them all: a general theory of neuronal branching and its practical application. *PLoS Computational Biology*, *6*(8), e1000877. <https://doi.org/10.1371/journal.pcbi.1000877>

Cuntz, H., Forstner, F., Borst, A., & Häusser, M. (2011). The TREES toolbox--probing the basis of axonal and dendritic branching. *Neuroinformatics*, *9*(1), 91–96. <https://doi.org/10.1007/s12021-010-9093-7>

- Day, M., Carr, D. B., Ulrich, S., Ilijic, E., Tkatch, T., & Surmeier, D. J. (2005). Dendritic excitability of mouse frontal cortex pyramidal neurons is shaped by the interaction among HCN, Kir2, and K_{leak} channels. *Journal of Neuroscience*, *25*(38), 8776–8787. <https://doi.org/10.1523/JNeurosci.2650-05.2005>
- Day, N. C., Shaw, P. J., McCormack, A. L., Craig, P. J., Smith, W., Beattie, R., ... Volsen, S. G. (1996). Distribution of alpha 1A, alpha 1B and alpha 1E voltage-dependent calcium channel subunits in the human hippocampus and parahippocampal gyrus. *Neuroscience*, *71*(4), 1013–1024. [https://doi.org/10.1016/0306-4522\(95\)00514-5](https://doi.org/10.1016/0306-4522(95)00514-5)
- de Schutter, E. (1994). Modelling the cerebellar Purkinje cell: experiments in computo. *Progress in Brain Research*, *102*, 427–441.
- Desai, R., Kronengold, J., Mei, J., Forman, S. A., & Kaczmarek, L. K. (2008). Protein kinase C modulates inactivation of Kv3.3 channels. *Journal of Biological Chemistry*, *283*(32), 22283–22294. <https://doi.org/10.1074/jbc.M801663200>
- Dey, D., Eckle, V.-S., Vitko, I., Sullivan, K. A., Lasiecka, Z. M., Winckler, B., ... Perez-Reyes, E. (2014). A potassium leak channel silences hyperactive neurons and ameliorates status epilepticus. *Epilepsia*, *55*(2), 203–213. <https://doi.org/10.1111/epi.12472>
- Dhamoon, A. S., Pandit, S. V., Sarmast, F., Parisian, K. R., Guha, P., Li, Y., ... Anumonwo, J. M. B. (2004). Unique Kir2.x properties determine regional and species differences in the cardiac inward rectifier K⁺ current. *Circulation Research*, *94*(10), 1332–1339. <https://doi.org/10.1161/01.Res.0000128408.66946.67>
- Dokter, M., Busch, R., Poser, R., Vogt, M. A., von Bohlen Und Halbach, V., Gass, P., ... von Bohlen Und Halbach, O. (2015). Implications of p75NTR for dentate gyrus morphology and hippocampus-related behavior revisited. *Brain Structure & Function*, *220*(3), 1449–1462. <https://doi.org/10.1007/s00429-014-0737-5>

Drion, G., O'Leary, T., & Marder, E. (2015). Ion channel degeneracy enables robust and tunable neuronal firing rates. *PNAS*, *112*(38), E5361-5370. <https://doi.org/10.1073/pnas.1516400112>

Duchen, M. R. (1999). Contributions of mitochondria to animal physiology: from homeostatic sensor to calcium signalling and cell death. *Journal of Physiology*, *516*, 1–17. <https://doi.org/10.1111/j.1469-7793.1999.001aa.x>

Dyhrfjeld-Johnsen, J., Santhakumar, V., Morgan, R. J., Huerta, R., Tsimring, L., & Soltesz, I. (2007). Topological determinants of epileptogenesis in large-scale structural and functional models of the dentate gyrus derived from experimental data. *Journal of Neurophysiology*, *97*(2), 1566–1587. <https://doi.org/10.1152/jn.00950.2006>

Eliot, L. S., & Johnston, D. (1994). Multiple components of calcium current in acutely dissociated dentate gyrus granule neurons. *Journal of Neurophysiology*, *72*(2), 762–777.

Enkvetchakul, D., Loussouarn, G., Makhina, E., Shyng, S. L., & Nichols, C. G. (2000). The kinetic and physical basis of K(ATP) channel gating: toward a unified molecular understanding. *Biophysical Journal*, *78*(5), 2334–2348. [https://doi.org/10.1016/S0006-3495\(00\)76779-8](https://doi.org/10.1016/S0006-3495(00)76779-8)

Espósito, M. S., Piatti, V. C., Laplagne, D. A., Morgenstern, N. A., Ferrari, C. C., Pitossi, F. J., & Schinder, A. F. (2005). Neuronal differentiation in the adult hippocampus recapitulates embryonic development. *Journal of Neuroscience*, *25*(44), 10074–10086. <https://doi.org/10.1523/JNeurosci.3114-05.2005>

Evans, R. C., Maniar, Y. M., & Blackwell, K. T. (2013). Dynamic modulation of spike timing-dependent calcium influx during corticostriatal upstates. *Journal of Neurophysiology*, *110*(7), 1631–1645. <https://doi.org/10.1152/jn.00232.2013>

Fakler, B., & Adelman, J. P. (2008). Control of K(Ca) channels by calcium nano/microdomains. *Neuron*, *59*(6), 873–881. <https://doi.org/10.1016/j.neuron.2008.09.001>

- Ferrante, M., Migliore, M., & Ascoli, G. A. (2009). Feed-forward inhibition as a buffer of the neuronal input-output relation. *PNAS*, *106*(42), 18004–18009. <https://doi.org/10.1073/pnas.0904784106>
- Forrest, M. D., Wall, M. J., Press, D. A., & Feng, J. (2012). The sodium-potassium pump controls the intrinsic firing of the cerebellar Purkinje neuron. *PLoS ONE*, *7*(12), e51169. <https://doi.org/10.1371/journal.pone.0051169>
- Fox, A. P., Nowycky, M. C., & Tsien, R. W. (1987). Kinetic and pharmacological properties distinguishing three types of calcium currents in chick sensory neurones. *Journal of Physiology*, *394*, 149–172. <https://doi.org/10.1113/jphysiol.1987.sp016864>
- Gabriel, A., Abdallah, M., Yost, C. S., Winegar, B. D., & Kindler, C. H. (2002). Localization of the tandem pore domain K⁺ channel KCNK5 (TASK-2) in the rat central nervous system. *Molecular Brain Research*, *98*(1–2), 153–163. [https://doi.org/10.1016/S0169-328X\(01\)00330-8](https://doi.org/10.1016/S0169-328X(01)00330-8)
- Ge, S., Yang, C.-H., Hsu, K.-S., Ming, G.-L., & Song, H. (2007). A critical period for enhanced synaptic plasticity in newly generated neurons of the adult brain. *Neuron*, *54*(4), 559–566. <https://doi.org/10.1016/j.neuron.2007.05.002>
- Geiger, J., Weber, Y. G., Landwehrmeyer, B., Sommer, C., & Lerche, H. (2006). Immunohistochemical analysis of KCNQ3 potassium channels in mouse brain. *Neuroscience Letters*, *400*(1–2), 101–104. <https://doi.org/10.1016/j.neulet.2006.02.017>
- Goldstein, S. A. N., Bayliss, D. A., Kim, D., Lesage, F., Plant, L. D., & Rajan, S. (2005). International Union of Pharmacology. LV. Nomenclature and molecular relationships of two-P potassium channels. *Pharmacological Reviews*, *57*(4), 527–540. <https://doi.org/10.1124/pr.57.4.12>
- Gordon, E., Roepke, T. K., & Abbott, G. W. (2006). Endogenous KCNE subunits govern Kv2.1 K⁺ channel activation kinetics in *Xenopus* oocyte studies. *Biophysical Journal*, *90*(4), 1223–1231. <https://doi.org/10.1529/biophysj.105.072504>

- Grosse, G., Draguhn, A., Höhne, L., Tapp, R., Veh, R. W., & Ahnert-Hilger, G. (2000). Expression of Kv1 potassium channels in mouse hippocampal primary cultures: development and activity-dependent regulation. *Journal of Neuroscience*, *20*(5), 1869–1882.
- Gu, C., & Barry, J. (2011). Function and mechanism of axonal targeting of voltage-sensitive potassium channels. *Progress in Neurobiology*, *94*(2), 115–132. <https://doi.org/10.1016/j.pneurobio.2011.04.009>
- Guan, D., Horton, L. R., Armstrong, W. E., & Foehring, R. C. (2011). Postnatal development of A-type and Kv1- and Kv2-mediated potassium channel currents in neocortical pyramidal neurons. *Journal of Neurophysiology*, *105*(6), 2976–2988. <https://doi.org/10.1152/jn.00758.2010>
- Gulledge, A. T., Carnevale, N. T., & Stuart, G. J. (2012). Electrical advantages of dendritic spines. *PLoS ONE*, *7*(4), e0036007. <https://doi.org/10.1371/journal.pone.0036007>
- Gunay, C., Edgerton, J. R., & Jaeger, D. (2008). Channel Density Distributions Explain Spiking Variability in the Globus Pallidus: A Combined Physiology and Computer Simulation Database Approach. *Journal of Neuroscience*, *28*(30), 7476–7491. <https://doi.org/10.1523/JNEUROSCI.4198-07.2008>
- Hayashi, H., & Nonaka, Y. (2011). Cooperation and competition between lateral and medial perforant path synapses in the dentate gyrus. *Neural Networks*, *24*(3), 233–246. <https://doi.org/10.1016/j.neunet.2010.12.004>
- Hemond, P., Epstein, D., Boley, A., Migliore, M., Ascoli, G. A., & Jaffe, D. B. (2008). Distinct classes of pyramidal cells exhibit mutually exclusive firing patterns in hippocampal area CA3b. *Hippocampus*, *18*(4), 411–424. <https://doi.org/10.1002/hipo.20404>
- Hendrickson, P. J., Yu, G. J., Dong Song, & Berger, T. W. (2015). A million-plus neuron model of the hippocampal dentate gyrus: Dependency of spatio-temporal network dynamics on topography. In *37th Annual International Conference of the IEEE EMBC* (Vol. 2015, pp. 4713–4716). <https://doi.org/10.1109/EMBC.2015.7319446>

- Hervieu, G. J., Cluderay, J. E., Gray, C. W., Green, P. J., Ranson, J. L., Randall, A. D., & Meadows, H. J. (2001). Distribution and expression of TREK-1, a two-pore-domain potassium channel, in the adult rat CNS. *Neuroscience*, *103*(4), 899–919. [https://doi.org/10.1016/S0306-4522\(01\)00030-6](https://doi.org/10.1016/S0306-4522(01)00030-6)
- Hirschberg, B., Maylie, J., Adelman, J. P., & Marrion, N. V. (1998). Gating of recombinant small-conductance Ca-activated K⁺ channels by calcium. *Journal of General Physiology*, *111*(4), 565–581. <https://doi.org/10.1085/jgp.111.4.565>
- Hirschberg, B., Maylie, J., Adelman, J. P., & Marrion, N. V. (1999). Gating properties of single SK channels in hippocampal CA1 pyramidal neurons. *Biophysical Journal*, *77*(4), 1905–1913. [https://doi.org/10.1016/S0006-3495\(99\)77032-3](https://doi.org/10.1016/S0006-3495(99)77032-3)
- Huang, S., Hong, S., & De Schutter, E. (2015). Non-linear leak currents affect mammalian neuron physiology. *Frontiers in Cellular Neuroscience*, *9*, 432. <https://doi.org/10.3389/fncel.2015.00432>
- Huang, X., Senatore, A., Dawson, T. F., Quan, Q., & Spafford, J. D. (2010). G-proteins modulate invertebrate synaptic calcium channel (LCav2) differently from the classical voltage-dependent regulation of mammalian Cav2.1 and Cav2.2 channels. *Journal of Experimental Biology*, *213*(Pt 12), 2094–2103. <https://doi.org/10.1242/jeb.042242>
- Ishihara, K., & Yan, D.-H. (2007). Low-affinity spermine block mediating outward currents through Kir2.1 and Kir2.2 inward rectifier potassium channels. *Journal of Physiology*, *583*(Pt 3), 891–908. <https://doi.org/10.1113/jphysiol.2007.136028>
- Jackson, M. B., & Redman, S. J. (2003). Calcium dynamics, buffering, and buffer saturation in the boutons of dentate granule-cell axons in the hilus. *Journal of Neuroscience*, *23*(5), 1612–1621.
- Jaffe, D. B., Wang, B., & Brenner, R. (2011). Shaping of action potentials by type I and type II large-conductance Ca²⁺-activated K⁺ channels. *Neuroscience*, *192*, 205–218. <https://doi.org/10.1016/j.neuroscience.2011.06.028>

Jedlicka, P., Benuskova, L., & Abraham, W. C. (2015). A voltage-based STDP rule combined with fast BCM-like metaplasticity accounts for LTP and concurrent “heterosynaptic” LTD in the dentate gyrus in vivo. *PLoS Computational Biology*, *11*(11), e1004588.

<https://doi.org/10.1371/journal.pcbi.1004588>

Jedlicka, P., & Deller, T. (2016). Understanding the role of synaptopodin and the spine apparatus in Hebbian synaptic plasticity - New perspectives and the need for computational modeling. *Neurobiology of Learning and Memory*.

<https://doi.org/10.1016/j.nlm.2016.07.023>

Jerng, H. H., Kunjilwar, K., & Pfaffinger, P. J. (2005). Multiprotein assembly of Kv4.2, KCHIP3 and DPP10 produces ternary channel complexes with ISA-like properties. *Journal of Physiology*, *568*(Pt 3), 767–788.

<https://doi.org/10.1113/jphysiol.2005.087858>

Jerng, H. H., Shahidullah, M., & Covarrubias, M. (1999). Inactivation gating of Kv4 potassium channels: molecular interactions involving the inner vestibule of the pore. *Journal of General Physiology*, *113*(5), 641–660.

<https://doi.org/10.1085/jgp.113.5.641>

Johnston, S. T., Shtrahman, M., Parylak, S., Gonçalves, J. T., & Gage, F. H. (2016). Paradox of pattern separation and adult neurogenesis: A dual role for new neurons balancing memory resolution and robustness. *Neurobiology of Learning and Memory*, *129*, 60–68. <https://doi.org/10.1016/j.nlm.2015.10.013>

Jones, O. T., Bernstein, G. M., Jones, E. J., Jugloff, D. G., Law, M., Wong, W., & Mills, L. R. (1997). N-Type calcium channels in the developing rat hippocampus: subunit, complex, and regional expression. *Journal of Neuroscience*, *17*(16), 6152–6164.

Jow, F., Zhang, Z.-H., Kopsco, D. C., Carroll, K. C., & Wang, K. (2004). Functional coupling of intracellular calcium and inactivation of voltage-gated Kv1.1/Kvbeta1.1 A-type K⁺ channels. *PNAS*, *101*(43), 15535–15540.

<https://doi.org/10.1073/pnas.0402081101>

- Jung, M. W., & McNaughton, B. L. (1993). Spatial selectivity of unit activity in the hippocampal granular layer. *Hippocampus*, 3(2), 165–182. <https://doi.org/10.1002/hipo.450030209>
- Kaczorowski, C. C., Disterhoft, J., & Spruston, N. (2007). Stability and plasticity of intrinsic membrane properties in hippocampal CA1 pyramidal neurons: effects of internal anions. *Journal of Physiology*, 578(Pt 3), 799–818. <https://doi.org/10.1113/jphysiol.2006.124586>
- Kanda, V. A., Lewis, A., Xu, X., & Abbott, G. W. (2011). KCNE1 and KCNE2 provide a checkpoint governing voltage-gated potassium channel α -subunit composition. *Biophysical Journal*, 101(6), 1364–1375. <https://doi.org/10.1016/j.bpj.2011.08.014>
- Karschin, C., Dissmann, E., Stühmer, W., & Karschin, A. (1996). IRK(1-3) and GIRK(1-4) inwardly rectifying K⁺ channel mRNAs are differentially expressed in the adult rat brain. *Journal of Neuroscience*, 16(11), 3559–3570.
- Kaufmann, W. A., Kasugai, Y., Ferraguti, F., & Storm, J. F. (2010). Two distinct pools of large-conductance calcium-activated potassium channels in the somatic plasma membrane of central principal neurons. *Neuroscience*, 169(3), 974–986. <https://doi.org/10.1016/j.neuroscience.2010.05.070>
- Kaulin, Y. A., De Santiago-Castillo, J. A., Rocha, C. A., & Covarrubias, M. (2008). Mechanism of the modulation of Kv4:KChIP-1 channels by external K⁺. *Biophysical Journal*, 94(4), 1241–1251. <https://doi.org/10.1529/biophysj.107.117796>
- Kerschensteiner, D., & Stocker, M. (1999). Heteromeric assembly of Kv2.1 with Kv9.3: effect on the state dependence of inactivation. *Biophysical Journal*, 77, 248–257. [https://doi.org/10.1016/S0006-3495\(99\)76886-4](https://doi.org/10.1016/S0006-3495(99)76886-4)
- Kim, J., Nadal, M. S., Clemens, A. M., Baron, M., Jung, S.-C., Misumi, Y., ... Hoffman, D. A. (2008). Kv4 accessory protein DPPX (DPP6) is a critical regulator of membrane excitability in hippocampal CA1 pyramidal neurons. *Journal of Neurophysiology*, 100(4), 1835–1847. <https://doi.org/10.1152/jn.90261.2008>

- Kirchheim, F., Tinnes, S., Haas, C. A., Stegen, M., & Wolfart, J. (2013). Regulation of action potential delays via voltage-gated potassium Kv1.1 channels in dentate granule cells during hippocampal epilepsy. *Frontiers in Cellular Neuroscience*, 7, 248. <https://doi.org/10.3389/fncel.2013.00248>
- Klinger, F., Gould, G., Boehm, S., & Shapiro, M. S. (2011). Distribution of M-channel subunits KCNQ2 and KCNQ3 in rat hippocampus. *NeuroImage*, 58(3), 761–769. <https://doi.org/10.1016/j.neuroimage.2011.07.003>
- Knaus, H. G., Schwarzer, C., Koch, R. O., Eberhart, A., Kaczorowski, G. J., Glossmann, H., ... Sperk, G. (1996). Distribution of high-conductance Ca(2+)-activated K⁺ channels in rat brain: targeting to axons and nerve terminals. *Journal of Neuroscience*, 16(3), 955–963.
- Knight, B. W. (1972). Dynamics of encoding in a population of neurons. *Journal of General Physiology*, 59(6), 734–766.
- Kole, M. H. P., Letzkus, J. J., & Stuart, G. J. (2007). Axon Initial Segment Kv1 Channels Control Axonal Action Potential Waveform and Synaptic Efficacy. *Neuron*, 55(4), 633–647. <https://doi.org/10.1016/j.neuron.2007.07.031>
- Kramer, A. a., Ingraham, N. E., Sharpe, E. J., & Mynlieff, M. (2012). Levels of 1.2 L-type channels peak in the first two weeks in rat hippocampus whereas 1.3 channels steadily increase through development. *Journal of Signal Transduction*, 2012, 597214. <https://doi.org/10.1155/2012/597214>
- Kramer, J. W., Post, M. A., Brown, A. M., & Kirsch, G. E. (1998). Modulation of potassium channel gating by coexpression of Kv2.1 with regulatory Kv5.1 or Kv6.1 alpha-subunits. *American Journal of Physiology*, 274(6 Pt 1), C1501–C1510.
- Kress, G. J., Dowling, M. J., Eisenman, L. N., & Mennerick, S. (2010). Axonal sodium channel distribution shapes the depolarized action potential threshold of dentate granule neurons. *Hippocampus*, 20(4), 558–571. <https://doi.org/10.1002/hipo.20667>

- Krichmar, J. L., Nasuto, S. J., Scorcioni, R., Washington, S. D., & Ascoli, G. a. (2002). Effects of dendritic morphology on CA3 pyramidal cell electrophysiology: A simulation study. *Brain Research*, *941*(1–2), 11–28. [https://doi.org/10.1016/S0006-8993\(02\)02488-5](https://doi.org/10.1016/S0006-8993(02)02488-5)
- Krueppel, R., Remy, S., & Beck, H. (2011). Dendritic integration in hippocampal dentate granule cells. *Neuron*, *71*(3), 512–528. <https://doi.org/10.1016/j.neuron.2011.05.043>
- Laplagne, D. A., Espósito, M. S., Piatti, V. C., Morgenstern, N. A., Zhao, C., van Praag, H., ... Schinder, A. F. (2006). Functional convergence of neurons generated in the developing and adult hippocampus. *PLoS Biology*, *4*(12), e409. <https://doi.org/10.1371/journal.pbio.0040409>
- Leitch, B., Szostek, A., Lin, R., & Shevtsova, O. (2009). Subcellular distribution of L-type calcium channel subtypes in rat hippocampal neurons. *Neuroscience*, *164*(2), 641–657. <https://doi.org/10.1016/j.neuroscience.2009.08.006>
- Lesage, F., Lauritzen, I., Duprat, F., Reyes, R., Fink, M., Heurteaux, C., & Lazdunski, M. (1997). The structure, function and distribution of the mouse TWIK-1 K⁺ channel. *FEBS Letters*, *402*(1), 28–32. [https://doi.org/10.1016/S0014-5793\(96\)01491-3](https://doi.org/10.1016/S0014-5793(96)01491-3)
- Li, L., Bischofberger, J., & Jonas, P. (2007). Differential gating and recruitment of P/Q-, N-, and R-type Ca²⁺ channels in hippocampal mossy fiber boutons. *Journal of Neuroscience*, *27*(49), 13420–13429. <https://doi.org/10.1523/JNeurosci.1709-07.2007>
- Liu, T.-A., Chang, H.-K., & Shieh, R.-C. (2012). Revisiting inward rectification: K ions permeate through Kir2.1 channels during high-affinity block by spermidine. *Journal of General Physiology*, *139*(3), 245–259. <https://doi.org/10.1085/jgp.201110736>
- Liu, Y. B., Lio, P. a, Pasternak, J. F., & Trommer, B. L. (1996). Developmental changes in membrane properties and postsynaptic currents of granule cells in rat dentate gyrus. *Journal of Neurophysiology*, *76*(2), 1074–1088.

- Loane, D. J., Lima, P. A., & Marrion, N. V. (2007). Co-assembly of N-type Ca²⁺ and BK channels underlies functional coupling in rat brain. *Journal of Cell Science*, *120*(Pt 6), 985–995. <https://doi.org/10.1242/jcs.03399>
- Lopatin, A. N., Makhina, E. N., & Nichols, C. G. (1995). The mechanism of inward rectification of potassium channels: “long-pore plugging” by cytoplasmic polyamines. *Journal of General Physiology*, *106*(5), 923–955. <https://doi.org/10.1085/jgp.106.5.923>
- Ma, X. Y., Yu, J. M., Zhang, S. Z., Liu, X. Y., Wu, B. H., Wei, X. L., ... Zheng, J. Q. (2011). External Ba²⁺ block of the two-pore domain potassium channel TREK-1 defines conformational transition in its selectivity filter. *Journal of Biological Chemistry*, *286*(46), 39813–39822. <https://doi.org/10.1074/jbc.M111.264788>
- MacDonald, S. H.-F., Ruth, P., Knaus, H.-G., & Shipston, M. J. (2006). Increased large conductance calcium-activated potassium (BK) channel expression accompanied by STREX variant downregulation in the developing mouse CNS. *BMC Developmental Biology*, *6*, 37. <https://doi.org/10.1186/1471-213X-6-37>
- Maciaszek, J. L., Soh, H., Walikonis, R. S., Tzingounis, A. V., & Lykotrafitis, G. (2012). Topography of native SK channels revealed by force nanoscopy in living neurons. *Journal of Neuroscience*, *32*(33), 11435–11440. <https://doi.org/10.1523/JNeurosci.1785-12.2012>
- Maletic-Savatic, M., Lenn, N. J., & Trimmer, J. S. (1995). Differential spatiotemporal expression of K⁺ channel polypeptides in rat hippocampal neurons developing in situ and in vitro. *Journal of Neuroscience*, *15*(5 Pt 2), 3840–3851.
- Marder, E. (2011). Variability, compensation, and modulation in neurons and circuits. *PNAS*, *108*, 15542–15548. <https://doi.org/10.1073/pnas.1010674108>
- Marder, E., & Goaillard, J.-M. (2006). Variability, compensation and homeostasis in neuron and network function. *Nature Reviews Neuroscience*, *7*(7), 563–574. <https://doi.org/10.1038/nrn1949>

- Marín-Burgin, A., Mongiat, L. A., Pardi, M. B., & Schinder, A. F. (2012). Unique processing during a period of high excitation/inhibition balance in adult-born neurons. *Science*, *335*(6073), 1238–1242.
<https://doi.org/10.1126/science.1214956>
- Markram, H. (2006). The blue brain project. *Nature Reviews. Neuroscience*, *7*(2), 153–160. <https://doi.org/10.1038/nrn1848>
- Markram, H. (2012). The human brain project. *Scientific American*, *306*(6), 50–55.
- Markram, H., Muller, E., Ramaswamy, S., Reimann, M. W., Abdellah, M., Sanchez, C. A., ... Schürmann, F. (2015). Reconstruction and simulation of neocortical microcircuitry. *Cell*, *163*(2), 456–492.
<https://doi.org/10.1016/j.cell.2015.09.029>
- Marrion, N. V., & Tavalin, S. J. (1998). Selective activation of Ca²⁺-activated K⁺ channels by co-localized Ca²⁺ channels in hippocampal neurons. *Nature*, *395*(6705), 900–905. <https://doi.org/10.1038/27674>
- Martinello, K., Huang, Z., Lujan, R., Tran, B., Watanabe, M., Cooper, E. C., ... Shah, M. M. (2015). Cholinergic Afferent Stimulation Induces Axonal Function Plasticity in Adult Hippocampal Granule Cells. *Neuron*, *85*(2), 346–363.
<https://doi.org/10.1016/j.neuron.2014.12.030>
- Mateos-Aparicio, P., Murphy, R., & Storm, J. F. (2014). Complementary functions of SK and Kv7/M potassium channels in excitability control and synaptic integration in rat hippocampal dentate granule cells. *Journal of Physiology*, *592*(Pt 4), 669–693. <https://doi.org/10.1113/jphysiol.2013.267872>
- McCrossan, Z. A., Lewis, A., Panaghie, G., Jordan, P. N., Christini, D. J., Lerner, D. J., & Abbott, G. W. (2003). MinK-related peptide 2 modulates Kv2.1 and Kv3.1 potassium channels in mammalian brain. *Journal of Neuroscience*, *23*(22), 8077–8091.

McKay, B. E., McRory, J. E., Molineux, M. L., Hamid, J., Snutch, T. P., Zamponi, G. W., & Turner, R. W. (2006). CaV3 T-type calcium channel isoforms differentially distribute to somatic and dendritic compartments in rat central neurons. *European Journal of Neuroscience*, *24*(9), 2581–2594. <https://doi.org/10.1111/j.1460-9568.2006.05136.x>

McRory, J. E., Santi, C. M., Hamming, K. S., Mezeyova, J., Sutton, K. G., Baillie, D. L., ... Snutch, T. P. (2001). Molecular and functional characterization of a family of rat brain T-type calcium channels. *Journal of Biological Chemistry*, *276*(6), 3999–4011. <https://doi.org/10.1074/jbc.M008215200>

Meadows, H. J., Benham, C. D., Cairns, W., Gloger, I., Jennings, C., Medhurst, A. D., ... Chapman, C. G. (2000). Cloning, localisation and functional expression of the human orthologue of the TREK-1 potassium channel. *Pflugers Archiv European Journal of Physiology*, *439*(6), 714–722. <https://doi.org/10.1007/s004240050997>

Menegola, M., & Trimmer, J. S. (2006). Unanticipated region- and cell-specific downregulation of individual KChIP auxiliary subunit isoforms in Kv4.2 knock-out mouse brain. *Journal of Neuroscience*, *26*(47), 12137–12142. <https://doi.org/10.1523/JNeurosci.2783-06.2006>

Mercer, J. N., Chan, C. S., Tkatch, T., Held, J., & Surmeier, D. J. (2007). Nav1.6 sodium channels are critical to pacemaking and fast spiking in globus pallidus neurons. *Journal of Neuroscience*, *27*(49), 13552–13566. <https://doi.org/10.1523/JNeurosci.3430-07.2007>

Migliore, M., Cannia, C., Lytton, W. W., Markram, H., & Hines, M. L. (2006). Parallel network simulations with NEURON. *Journal of Computational Neuroscience*, *21*(2), 119–129. <https://doi.org/10.1007/s10827-006-7949-5>

Ming, G.-L., & Song, H. (2011). Adult neurogenesis in the Mammalian brain: significant answers and significant questions. *Neuron*, *70*(4), 687–702. <https://doi.org/10.1016/j.neuron.2011.05.001>

- Misonou, H., Menegola, M., Buchwalder, L., Park, E. W., Meredith, A., Rhodes, K. J., ... Trimmer, J. S. (2006). Immunolocalization of the Ca²⁺-activated K⁺ channel Slo1 in axons and nerve terminals of mammalian brain and cultured neurons. *Journal of Comparative Neurology*, 496(3), 289–302. <https://doi.org/10.1002/cne.20931>
- Misonou, H., Mohapatra, D. P., & Trimmer, J. S. (2005). Kv2.1: A voltage-gated K⁺ channel critical to dynamic control of neuronal excitability. *NeuroToxicology*, 26(5), 743–752. <https://doi.org/10.1016/j.neuro.2005.02.003>
- Miyashita, T., & Kubo, Y. (1997). Localization and developmental changes of the expression of two inward rectifying K⁺-channel proteins in the rat brain. *Brain Research*, 750(1–2), 251–263. [https://doi.org/10.1016/S0006-8993\(96\)01365-0](https://doi.org/10.1016/S0006-8993(96)01365-0)
- Monaghan, M. M., Trimmer, J. S., & Rhodes, K. J. (2001). Experimental localization of Kv1 family voltage-gated K⁺ channel alpha and beta subunits in rat hippocampal formation. *Journal of Neuroscience*, 21(16), 5973–5983.
- Mongiati, L. A., Espósito, M. S., Lombardi, G., & Schinder, A. F. (2009). Reliable activation of immature neurons in the adult hippocampus. *PLoS ONE*, 4(4), e5320. <https://doi.org/10.1371/journal.pone.0005320>
- Müller, A., Kukley, M., Uebachs, M., Beck, H., & Dietrich, D. (2007). Nanodomains of single Ca²⁺ channels contribute to action potential repolarization in cortical neurons. *Journal of Neuroscience*, 27(3), 483–495. <https://doi.org/10.1523/JNeurosci.3816-06.2007>
- Murakoshi, H., & Trimmer, J. S. (1999). Identification of the Kv2.1 K⁺ channel as a major component of the delayed rectifier K⁺ current in rat hippocampal neurons. *Journal of Neuroscience*, 19(5), 1728–1735.
- Norby, J. G. (1983). Kinetics of Na-ATPase activity by the Na,K pump. Interactions of the phosphorylated intermediates with Na⁺, Tris⁺, and K⁺. *Journal of General Physiology*, 82(6), 725–759. <https://doi.org/10.1085/jgp.82.6.725>

- Notomi, T., & Shigemoto, R. (2004). Immunohistochemical localization of Ih channel subunits, HCN1-4, in the rat brain. *Journal of Comparative Neurology*, 471(3), 241–276. <https://doi.org/10.1002/cne.11039>
- Obermair, G. J., Kaufmann, W. A., Knaus, H. G., & Flucher, B. E. (2003). The small conductance Ca²⁺-activated K⁺ channel SK3 is localized in nerve terminals of excitatory synapses of cultured mouse hippocampal neurons. *European Journal of Neuroscience*, 17(4), 721–731. <https://doi.org/10.1046/j.1460-9568.2003.02488.x>
- Pacheco Otalora, L. F., Hernandez, E. F., Arshadmansab, M. F., Francisco, S., Willis, M., Ermolinsky, B., ... Garrido-Sanabria, E. R. (2008). Down-regulation of BK channel expression in the pilocarpine model of temporal lobe epilepsy. *Brain Research*, 1200, 116–131. <https://doi.org/10.1016/j.brainres.2008.01.017>
- Panama, B. K., & Lopatin, A. N. (2006). Differential polyamine sensitivity in inwardly rectifying Kir2 potassium channels. *Journal of Physiology*, 571(Pt 2), 287–302. <https://doi.org/10.1113/jphysiol.2005.097741>
- Papoutsis, A., Sidiropoulou, K., Cutsuridis, V., & Poirazi, P. (2013). Induction and modulation of persistent activity in a layer V PFC microcircuit model. *Frontiers in Neural Circuits*, 7, 161. <https://doi.org/10.3389/fncir.2013.00161>
- Pardi, M. B., Ogando, M. B., Schinder, A. F., & Marin-Burgin, A. (2015). Differential inhibition onto developing and mature granule cells generates high-frequency filters with variable gain. *eLife*, 4, e08764. <https://doi.org/10.7554/eLife.08764>
- Patel, S. P., Parai, R., Parai, R., & Campbell, D. L. (2004). Regulation of Kv4.3 voltage-dependent gating kinetics by KCHIP2 isoforms. *Journal of Physiology*, 557(Pt 1), 19–41. <https://doi.org/10.1113/jphysiol.2003.058172>
- Pedroni, A., Minh, D. D., Mallamaci, A., & Cherubini, E. (2014). Electrophysiological characterization of granule cells in the dentate gyrus immediately after birth. *Frontiers in Cellular Neuroscience*, 8, 44. <https://doi.org/10.3389/fncel.2014.00044>

- Pelletier, M. R., Pahapill, P. a, Pennefather, P. S., & Carlen, P. L. (2000). Analysis of single K(ATP) channels in mammalian dentate gyrus granule cells. *Journal of Neurophysiology*, *84*(5), 2291–2301.
- Piatti, V. C., Davies-Sala, M. G., Espósito, M. S., Mongiat, L. a, Trincherro, M. F., & Schinder, A. F. (2011). The timing for neuronal maturation in the adult hippocampus is modulated by local network activity. *Journal of Neuroscience*, *31*(21), 7715–7728. <https://doi.org/10.1523/JNeurosci.1380-11.2011>
- Piwonska, M., Wilczek, E., Szewczyk, a., & Wilczynski, G. M. (2008). Differential distribution of Ca²⁺-activated potassium channel β 4 subunit in rat brain: Immunolocalization in neuronal mitochondria. *Neuroscience*, *153*(2), 446–460. <https://doi.org/10.1016/j.neuroscience.2008.01.050>
- Platschek, S., Cuntz, H., Vuksic, M., Deller, T., & Jedlicka, P. (2016). A general homeostatic principle following lesion induced dendritic remodeling. *Acta Neuropathologica Communications*, *4*(1), 19. <https://doi.org/10.1186/s40478-016-0285-8>
- Postea, O., & Biel, M. (2011). Exploring HCN channels as novel drug targets. *Nature Reviews Drug Discovery*, *10*, 903–914. <https://doi.org/10.1038/nrd3576>
- Pourbadie, H. G., Naderi, N., Mehranfard, N., Janahmadi, M., Khodaghali, F., & Motamedi, F. (2015). Preventing effect of L-type calcium channel blockade on electrophysiological alterations in dentate gyrus granule cells induced by entorhinal amyloid pathology. *PLoS ONE*, *10*(2), e0117555. <https://doi.org/10.1371/journal.pone.0117555>
- Prinz, A. A., Bucher, D., & Marder, E. (2004). Similar network activity from disparate circuit parameters. *Nature Neuroscience*, *7*(12), 1345–1352. <https://doi.org/10.1038/nn1352>
- Proks, P., & Ashcroft, F. M. (2009). Modeling KATP channel gating and its regulation. *Progress in Biophysics and Molecular Biology*, *99*(1), 7–19. <https://doi.org/10.1016/j.pbiomolbio.2008.10.002>

- Prüss, H., Derst, C., Lommel, R., Veh, R. W., Pru, H., Derst, C., ... Veh, W. (2005). Differential distribution of individual subunits of strongly inwardly rectifying potassium channels (Kir2 family) in rat brain. *Molecular Brain Research*, *139*(1), 63–79. <https://doi.org/10.1016/j.molbrainres.2005.05.006>
- Prüss, H., Wenzel, M., Eulitz, D., Thomzig, A., Karschin, A., & Veh, R. W. (2003). Kir2 potassium channels in rat striatum are strategically localized to control basal ganglia function. *Molecular Brain Research*, *110*(2), 203–219. [https://doi.org/10.1016/S0169-328X\(02\)00649-6](https://doi.org/10.1016/S0169-328X(02)00649-6)
- Rangel, L. M., Quinn, L. K., Chiba, A. A., Gage, F. H., & Aimone, J. B. (2013). A hypothesis for temporal coding of young and mature granule cells. *Frontiers in Neuroscience*, *7*, 75. <https://doi.org/10.3389/fnins.2013.00075>
- Rettig, J., Wunder, F., Stocker, M., Lichtinghagen, R., Mastiaux, F., Beckh, S., ... Ruppersberg, J. P. (1992). Characterization of a Shaw-related potassium channel family in rat brain. *EMBO Journal*, *11*(7), 2473–86.
- Rhodes, K. J., Carroll, K. I., Sung, M. A., Doliveira, L. C., Monaghan, M. M., Burke, S. L., ... Trimmer, J. S. (2004). KChIPs and Kv4 alpha subunits as integral components of A-type potassium channels in mammalian brain. *Journal of Neuroscience*, *24*(36), 7903–7915. <https://doi.org/10.1523/JNeurosci.0776-04.2004>
- Rhodes, K. J., Strassle, B. W., Monaghan, M. M., Bekele-Arcuri, Z., Matos, M. F., & Trimmer, J. S. (1997). Association and colocalization of the Kvbeta1 and Kvbeta2 beta-subunits with Kv1alpha-subunits in mammalian brain K⁺ channel complexes. *Journal of Neuroscience*, *17*(21), 8246–8258.
- Riazanski, V., Becker, A., Chen, J., Sochivko, D., Lie, A., Wiestler, O. D., ... Beck, H. (2001). Functional and molecular analysis of transient voltage-dependent K⁺ currents in rat hippocampal granule cells. *Journal of Physiology*, *537*(Pt 2), 391–406. <https://doi.org/10.1111/j.1469-7793.2001.00391.x>

Rudy, B., Sen, K., Vega-Saenz De Miera, E., Lau, D., Ried, T., & Ward, D. C. (1991). Cloning of a human cDNA expressing a high voltage-activating, TEA sensitive, type-A K⁺ channel which maps to chromosome 1 band p21. *Journal of Neuroscience Research*, 29(3), 401–412.

<https://doi.org/10.1002/jnr.490290316>

Rüschenschmidt, C., Chen, J., Becker, A., Riazanski, V., & Beck, H. (2006). Functional properties and oxidative modulation of A-type K⁺ currents in hippocampal granule cells of control and chronically epileptic rats. *European Journal of Neuroscience*, 23(3), 675–685. <https://doi.org/10.1111/j.1460-9568.2006.04608.x>

Rush, A. M., Dib-Hajj, S. D., & Waxman, S. G. (2005). Electrophysiological properties of two axonal sodium channels, Nav1.2 and Nav1.6, expressed in mouse spinal sensory neurones. *Journal of Physiology*, 564(Pt 3), 803–815. <https://doi.org/10.1113/jphysiol.2005.083089>

Safiulina, V. F., Zacchi, P., Taglialatela, M., Yaari, Y., & Cherubini, E. (2008). Low expression of Kv7/M channels facilitates intrinsic and network bursting in the developing rat hippocampus. *Journal of Physiology*, 586(Pt 22), 5437–5453. <https://doi.org/10.1113/jphysiol.2008.156257>

Sailer, C. A., Kaufmann, W. A., Kogler, M., Chen, L., Sausbier, U., Ottersen, O. P., ... Knaus, H. G. (2006). Immunolocalization of BK channels in hippocampal pyramidal neurons. *European Journal of Neuroscience*, 24(2), 442–454. <https://doi.org/10.1111/j.1460-9568.2006.04936.x>

Sailer, C. a., Kaufmann, W. a., Marksteiner, J., & Knaus, H. G. (2004). Comparative immunohistochemical distribution of three small-conductance Ca²⁺-activated potassium channel subunits, SK1, SK2, and SK3 in mouse brain. *Molecular and Cellular Neuroscience*, 26(3), 458–469. <https://doi.org/10.1016/j.mcn.2004.03.002>

Santhakumar, V., Aradi, I., & Soltesz, I. (2005). Role of mossy fiber sprouting and mossy cell loss in hyperexcitability: a network model of the dentate gyrus incorporating cell types and axonal topography. *Journal of Neurophysiology*, *93*(1), 437–453. <https://doi.org/10.1152/jn.00777.2004>

Schmidt-Hieber, C., & Bischofberger, J. (2010). Fast sodium channel gating supports localized and efficient axonal action potential initiation. *Journal of Neuroscience*, *30*(30), 10233–10242. <https://doi.org/10.1523/JNeurosci.6335-09.2010>

Schmidt-Hieber, C., Jonas, P., & Bischofberger, J. (2004). Enhanced synaptic plasticity in newly generated granule cells of the adult hippocampus. *Nature*, *429*(6988), 184–187. <https://doi.org/10.1038/nature02553>

Schmidt-Hieber, C., Jonas, P., & Bischofberger, J. (2007). Subthreshold dendritic signal processing and coincidence detection in dentate gyrus granule cells. *Journal of Neuroscience*, *27*(31), 8430–8441. <https://doi.org/10.1523/JNeurosci.1787-07.2007>

Schmidt-Hieber, C., Jonas, P., & Bischofberger, J. (2008). Action potential initiation and propagation in hippocampal mossy fibre axons. *Journal of Physiology*, *586*(7), 1849–1857. <https://doi.org/10.1113/jphysiol.2007.150151>

Schneider, C. J., Cuntz, H., & Soltesz, I. (2014). Linking Macroscopic with Microscopic Neuroanatomy Using Synthetic Neuronal Populations. *PLoS Computational Biology*, *10*(10), e1003921. <https://doi.org/10.1371/journal.pcbi.1003921>

Schröter, K. H., Ruppersberg, J. P., Wunder, F., Rettig, J., Stocker, M., & Pongs, O. (1991). Cloning and functional expression of a TEA-sensitive A-type potassium channel from rat brain. *FEBS Letters*, *278*(2), 211–216. [https://doi.org/10.1016/0014-5793\(91\)80119-N](https://doi.org/10.1016/0014-5793(91)80119-N)

Sharma, A. K., Reams, R. Y., Jordan, W. H., Miller, M. A., Thacker, H. L., & Snyder, P. W. (2007). Mesial temporal lobe epilepsy: pathogenesis, induced rodent models and lesions. *Toxicologic Pathology*, *35*(7), 984–999. <https://doi.org/10.1080/01926230701748305>

- Shin, N., Soh, H., Chang, S., Kim, D. H., & Park, C.-S. (2005). Sodium Permeability of a Cloned Small-Conductance Calcium-Activated Potassium Channel. *Biophysical Journal*, 89(5), 3111–3119. <https://doi.org/10.1529/biophysj.105.069542>
- Shruti, S., Urban-Ciecko, J., Fitzpatrick, J. A., Brenner, R., Bruchez, M. P., & Barth, A. L. (2012). The brain-specific Beta4 subunit downregulates BK channel cell surface expression. *PLoS ONE*, 7(3), e33429. <https://doi.org/10.1371/journal.pone.0033429>
- Šišková, Z., Justus, D., Kaneko, H., Friedrichs, D., Henneberg, N., Beutel, T., ... Remy, S. (2014). Dendritic structural degeneration is functionally linked to cellular hyperexcitability in a mouse model of Alzheimer's disease. *Neuron*, 84(5), 1023–1033. <https://doi.org/10.1016/j.neuron.2014.10.024>
- Smith, J. S., Iannotti, C. A., Dargis, P., Christian, E. P., & Aiyar, J. (2001). Differential expression of kcnq2 splice variants: implications to m current function during neuronal development. *Journal of Neuroscience*, 21(4), 1096–1103.
- Snyder, J. S., Ferrante, S. C., & Cameron, H. a. (2012). Late Maturation of Adult-Born Neurons in the Temporal Dentate Gyrus. *PLoS ONE*, 7(11), e48757. <https://doi.org/10.1371/journal.pone.0048757>
- Softky, W. R., & Koch, C. (1993). The highly irregular firing of cortical cells is inconsistent with temporal integration of random EPSPs. *Journal of Neuroscience*, 13(1), 334–350.
- Solinas, S., Forti, L., Cesana, E., Mapelli, J., De Schutter, E., & D'Angelo, E. (2007). Computational reconstruction of pacemaking and intrinsic electroresponsiveness in cerebellar Golgi cells. *Frontiers in Cellular Neuroscience*, 1, 2. <https://doi.org/10.3389/neuro.03.002.2007>
- Staley, K. J., Otis, T. S., & Mody, I. (1992). Membrane properties of dentate gyrus granule cells: comparison of sharp microelectrode and whole-cell recordings. *Journal of Neurophysiology*, 67(5), 1346–1358.

Stegen, M., Kirchheim, F., Hanuschkin, A., Staszewski, O., Veh, R. W., & Wolfart, J. (2012). Adaptive intrinsic plasticity in human dentate gyrus granule cells during temporal lobe epilepsy. *Cerebral Cortex*, *22*(9), 2087–2101. <https://doi.org/10.1093/cercor/bhr294>

Stocca, G., Schmidt-Hieber, C., & Bischofberger, J. (2008). Differential dendritic Ca²⁺ signalling in young and mature hippocampal granule cells. *Journal of Physiology*, *586*(16), 3795–3811. <https://doi.org/10.1113/jphysiol.2008.155739>

Stonehouse, A. H., Pringle, J. H., Norman, R. I., Stanfield, P. R., Conley, E. C., & Brammar, W. J. (1999). Characterisation of Kir2.0 proteins in the rat cerebellum and hippocampus by polyclonal antibodies. *Histochemistry and Cell Biology*, *112*(6), 457–465. <https://doi.org/10.1007/s004180050429>

Surges, R., Brewster, A. L., Bender, R. A., Beck, H., Feuerstein, T. J., & Baram, T. Z. (2006). Regulated expression of HCN channels and cAMP levels shape the properties of the h current in developing rat hippocampus. *European Journal of Neuroscience*, *24*(1), 94–104. <https://doi.org/10.1111/j.1460-9568.2006.04880.x>

Talley, E. M., Solorzano, G., Lei, Q., Kim, D., & Bayliss, D. A. (2001). Cns distribution of members of the two-pore-domain (KCNK) potassium channel family. *Journal of Neuroscience*, *21*(19), 7491–7505.

Tanner, G. R., Lutas, A., Martínez-François, J. R., & Yellen, G. (2011). Single K ATP channel opening in response to action potential firing in mouse dentate granule neurons. *Journal of Neuroscience*, *31*(23), 8689–8696. <https://doi.org/10.1523/JNeurosci.5951-10.2011>

Tejada, J., Arisi, G. M., García-Cairasco, N., & Roque, A. C. (2012). Morphological alterations in newly born dentate gyrus granule cells that emerge after status epilepticus contribute to make them less excitable. *PLoS ONE*, *7*(7), e40726. <https://doi.org/10.1371/journal.pone.0040726>

Tejada, J., & Roque, A. C. (2014). Computational models of dentate gyrus with epilepsy-induced morphological alterations in granule cells. *Epilepsy & Behavior: E&B*, *38*, 63–70. <https://doi.org/10.1016/j.yebeh.2014.02.007>

- Temprana, S. G., Mongiat, L. A., Yang, S. M., Trincherro, M. F., Alvarez, D. D., Kropff, E., ... Schinder, A. F. (2015). Delayed coupling to feedback inhibition during a critical period for the integration of adult-born granule cells. *Neuron*, *85*(1), 116–130. <https://doi.org/10.1016/j.neuron.2014.11.023>
- Tinel, N., Diochot, S., Lauritzen, I., Barhanin, J., Lazdunski, M., & Borsotto, M. (2000). M-type KCNQ2-KCNQ3 potassium channels are modulated by the KCNE2 subunit. *FEBS Letters*, *480*(2–3), 137–141. [https://doi.org/10.1016/S0014-5793\(00\)01918-9](https://doi.org/10.1016/S0014-5793(00)01918-9)
- Tinel, N., Lauritzen, I., Chouabe, C., Lazdunski, M., & Borsotto, M. (1998). The KCNQ2 potassium channel: splice variants, functional and developmental expression. Brain localization and comparison with KCNQ3. *FEBS Letters*, *438*(3), 171–176. [https://doi.org/10.1016/S0014-5793\(98\)01296-4](https://doi.org/10.1016/S0014-5793(98)01296-4)
- Tippens, A. L., Pare, J.-F., Langwieser, N., Moosmang, S., Milner, T. A., Smith, Y., & Lee, A. (2008). Ultrastructural evidence for pre- and postsynaptic localization of Cav1.2 L-type Ca²⁺ channels in the rat hippocampus. *Journal of Comparative Neurology*, *506*(4), 569–583. <https://doi.org/10.1002/cne.21567>
- Tønnesen, J., Katona, G., Rózsa, B., & Nägerl, U. V. (2014). Spine neck plasticity regulates compartmentalization of synapses. *Nature Neuroscience*, *17*(5), 678–685. <https://doi.org/10.1038/nn.3682>
- Traub, R. D., & Llinás, R. (1977). The spatial distribution of ionic conductances in normal and axotomized motoneurons. *Neuroscience*, *2*(6), 829–849. [https://doi.org/10.1016/0306-4522\(77\)90110-5](https://doi.org/10.1016/0306-4522(77)90110-5)
- Trevelyan, A. J., & Jack, J. (2002). Detailed passive cable models of layer 2 / 3 pyramidal cells in rat visual cortex at different temperatures. *Society*, 623–636. <https://doi.org/10.1013/jphysiol.2001.013291>
- Urbán, N., & Guillemot, F. (2014). Neurogenesis in the embryonic and adult brain: same regulators, different roles. *Frontiers in Cellular Neuroscience*, *8*, 396. <https://doi.org/10.3389/fncel.2014.00396>

- VanDongen, A. M., Frech, G. C., Drewe, J. A., Joho, R. H., & Brown, A. M. (1990). Alteration and restoration of K⁺ channel function by deletions at the N- and C-termini. *Neuron*, 5(4), 433–443. [https://doi.org/10.1016/0896-6273\(90\)90082-Q](https://doi.org/10.1016/0896-6273(90)90082-Q)
- Vega-Saenz de Miera, E., Moreno, H., Fruhling, D., Kentros, C., & Rudy, B. (1992). Cloning of ShIII (Shaw-like) cDNAs encoding a novel high-voltage-activating, TEA-sensitive, type-A K⁺ channel. *Proceedings. Biological Sciences / The Royal Society*, 248(1321), 9–18. <https://doi.org/10.1098/rspb.1992.0036>
- Vemana, S., Pandey, S., & Larsson, H. P. (2008). Intracellular Mg²⁺ is a voltage-dependent pore blocker of HCN channels. *American Journal of Physiology. Cell Physiology*, 295(2), C557–C565. <https://doi.org/10.1152/ajpcell.00154.2008>
- Volgushev, M. (2016). Cortical specializations underlying fast computations. *The Neuroscientist*, 22(2), 145–164. <https://doi.org/10.1177/1073858415571539>
- Wang, B., Bugay, V., Ling, L., Chuang, H.-H., Jaffe, D. B., & Brenner, R. (2016). Knockout of the BK β 4-subunit promotes a functional coupling of BK channels and ryanodine receptors that mediate a fAHP-induced increase in excitability. *Journal of Neurophysiology*, 116(2), 456–465. <https://doi.org/10.1152/jn.00857.2015>
- Wang, B., Jaffe, D. B., & Brenner, R. (2014). Current understanding of iberiotoxin-resistant BK channels in the nervous system. *Frontiers in Physiology*, 5, 382. <https://doi.org/10.3389/fphys.2014.00382>
- Weiser, M., Vega-Saenz de Miera, E., Kentros, C., Moreno, H., Franzen, L., Hillman, D., ... Rudy, B. (1994). Differential expression of Shaw-related K⁺ channels in the rat central nervous system. *Journal of Neuroscience*, 14(3), 949–972.
- Westenbroek, R. E., Merrick, D. K., & Catterall, W. A. (1989). Differential subcellular localization of the RI and RII Na⁺ channel subtypes in central neurons. *Neuron*, 3(6), 695–704. [https://doi.org/10.1016/0896-6273\(89\)90238-9](https://doi.org/10.1016/0896-6273(89)90238-9)

- Wissmann, R., Bildl, W., Oliver, D., Beyermann, M., Kalbitzer, H. R., Bentrop, D., & Fakler, B. (2003). Solution structure and function of the “tandem inactivation domain” of the neuronal A-type potassium channel Kv1.4. *Journal of Biological Chemistry*, 278(18), 16142–16150. <https://doi.org/10.1074/jbc.M210191200>
- Wolf, J. A., Moyer, J. T., Lazarewicz, M. T., Contreras, D., Benoit-Marand, M., O'Donnell, P., & Finkel, L. H. (2005). NMDA/AMPA ratio impacts state transitions and entrainment to oscillations in a computational model of the nucleus accumbens medium spiny projection neuron. *Journal of Neuroscience*, 25(40), 9080–9095. <https://doi.org/10.1523/JNeurosci.2220-05.2005>
- Xia, X. M., Fakler, B., Rivard, A., Wayman, G., Johnson-Pais, T., Keen, J. E., ... Adelman, J. P. (1998). Mechanism of calcium gating in small-conductance calcium-activated potassium channels. *Nature*, 395(6701), 503–507. <https://doi.org/10.1038/26758>
- Xu, J. H., Long, L., Tang, Y. C., Hu, H. T., & Tang, F. R. (2007). Cav1.2, Cav1.3, and Cav2.1 in the mouse hippocampus during and after pilocarpine-induced status epilepticus. *Hippocampus*, 17(3), 235–251. <https://doi.org/10.1002/hipo.20263>
- Xu, J. H., Long, L., Wang, J., Tang, Y. C., Hu, H. T., Soong, T. W., & Tang, F. R. (2010). Nuclear localization of Ca v 2.2 and its distribution in the mouse central nervous system, and changes in the hippocampus during and after pilocarpine-induced status epilepticus. *Neuropathology and Applied Neurobiology*, 36(1), 71–85. <https://doi.org/10.1111/j.1365-2990.2009.01044.x>
- Xu, P., Li, Z., Xuan, Q., & Yang, Z. (2015). Different expressions of large-conductance Ca²⁺-activated K⁺ channels in the mouse renal cortex and hippocampus during postnatal development. *Applied Immunohistochemistry & Molecular Morphology*, 23(2), 146–152. <https://doi.org/10.1097/PAI.0000000000000006>

- Yan, D.-H., & Ishihara, K. (2005). Two Kir2.1 channel populations with different sensitivities to Mg(2+) and polyamine block: a model for the cardiac strong inward rectifier K(+) channel. *Journal of Physiology*, 563(Pt 3), 725–744. <https://doi.org/10.1113/jphysiol.2004.079186>
- Yang, S. M., Alvarez, D. D., & Schinder, A. F. (2015). Reliable genetic labeling of adult-born dentate granule cells using Ascl1CreERT2 and GlastCreERT2 murine lines. *Journal of Neuroscience*, 35(46), 15379–15390. <https://doi.org/10.1523/JNeurosci.2345-15.2015>
- Yarishkin, O., Lee, D. Y., Kim, E., Cho, C., Choi, J. H., Lee, C. J., ... Park, J.-Y. (2014). TWIK-1 contributes to the intrinsic excitability of dentate granule cells in mouse hippocampus. *Molecular Brain*, 7(1), 80. <https://doi.org/10.1186/s13041-014-0080-z>
- Yim, M. Y., Hanuschkin, A., & Wolfart, J. (2015). Intrinsic rescaling of granule cells restores pattern separation ability of a dentate gyrus network model during epileptic hyperexcitability. *Hippocampus*, 25(3), 297–308. <https://doi.org/10.1002/hipo.22373>
- Young, C. C., Stegen, M., Bernard, R., Müller, M., Bischofberger, J., Veh, R. W., ... Wolfart, J. (2009). Upregulation of inward rectifier K+ (Kir2) channels in dentate gyrus granule cells in temporal lobe epilepsy. *Journal of Physiology*, 587, 4213–4233. <https://doi.org/10.1113/jphysiol.2009.170746>
- Yuen, G. L., & Durand, D. (1991). Reconstruction of hippocampal granule cell electrophysiology by computer simulation. *Neuroscience*, 41(2–3), 411–423. [https://doi.org/10.1016/0306-4522\(91\)90337-N](https://doi.org/10.1016/0306-4522(91)90337-N)
- Yunker, A. M. R., Sharp, A. H., Sundarraj, S., Ranganathan, V., Copeland, T. D., & McEnery, M. W. (2003). Immunological characterization of T-type voltage-dependent calcium channel Cav3.1 (alpha1G) and Cav3.3 (alpha1I) isoforms reveal differences in their localization, expression, and neural development. *Neuroscience*, 117(2), 321–335. [https://doi.org/10.1016/S0306-4522\(02\)00936-3](https://doi.org/10.1016/S0306-4522(02)00936-3)

- Zagha, E., Ozaita, A., Chang, S. Y., Nadal, M. S., Lin, U., Saganich, M. J., ... Rudy, B. (2005). DPP10 modulates Kv4-mediated A-type potassium channels. *Journal of Biological Chemistry*, 280(19), 18853–18861. <https://doi.org/10.1074/jbc.M410613200>
- Zahler, R., Zhang, Z. T., Manor, M., & Boron, W. F. (1997). Sodium kinetics of Na,K-ATPase alpha isoforms in intact transfected HeLa cells. *Journal of General Physiology*, 110(2), 201–213. <https://doi.org/10.1085/jgp.110.2.201>
- Zhang, L., Weiner, J. L., Valiante, T. A., Velumian, A. A., Watson, P. L., Jahromi, S. S., ... Carlen, P. L. (1994). Whole-cell recording of the Ca²⁺-dependent slow afterhyperpolarization in hippocampal neurones: effects of internally applied anions. *Pflügers Archiv - European Journal of Physiology*, 426(3–4), 247–253. <https://doi.org/10.1007/BF00374778>
- Zhao, C., Teng, E. M., Summers, R. G., Ming, G.-L., & Gage, F. H. (2006). Distinct morphological stages of dentate granule neuron maturation in the adult mouse hippocampus. *Journal of Neuroscience*, 26(1), 3–11. <https://doi.org/10.1523/JNeurosci.3648-05.2006>
- Zhou, J., Blundell, J., Ogawa, S., Kwon, C.-H., Zhang, W., Sinton, C., ... Parada, L. F. (2009). Pharmacological inhibition of mTORC1 suppresses anatomical, cellular, and behavioral abnormalities in neural-specific Pten knock-out mice. *Journal of Neuroscience*, 29(6), 1773–1783. <https://doi.org/10.1523/JNeurosci.5685-08.2009>
- Zhu, L., McDavid, S., & Currie, K. P. M. (2015). “Slow” voltage-dependent inactivation of CaV2.2 calcium channels is modulated by the PKC activator phorbol 12-myristate 13-Acetate (PMA). *PLoS ONE*, 10(7), e0134117. <https://doi.org/10.1371/journal.pone.0134117>

Figures

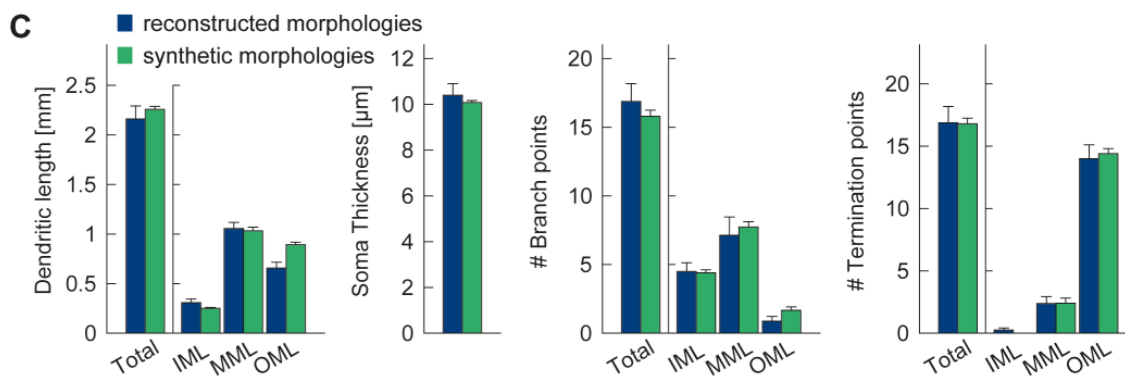
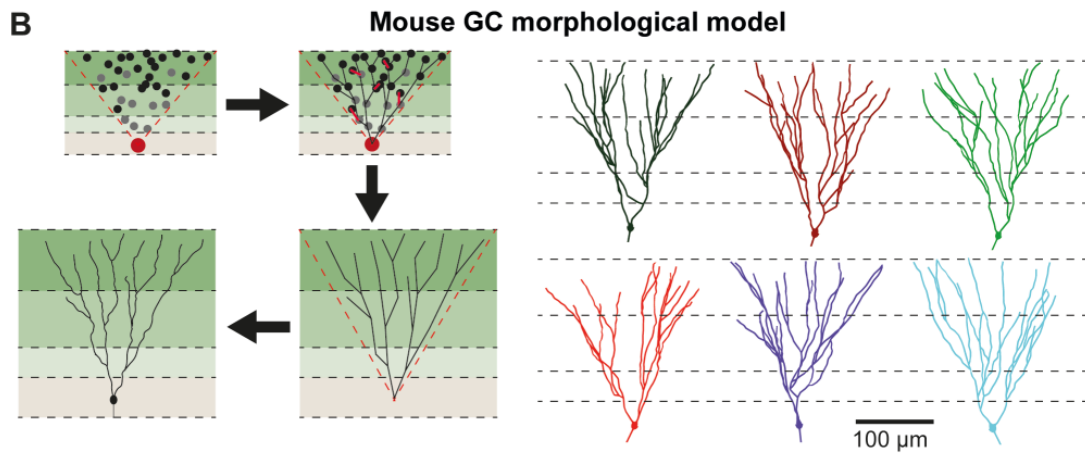
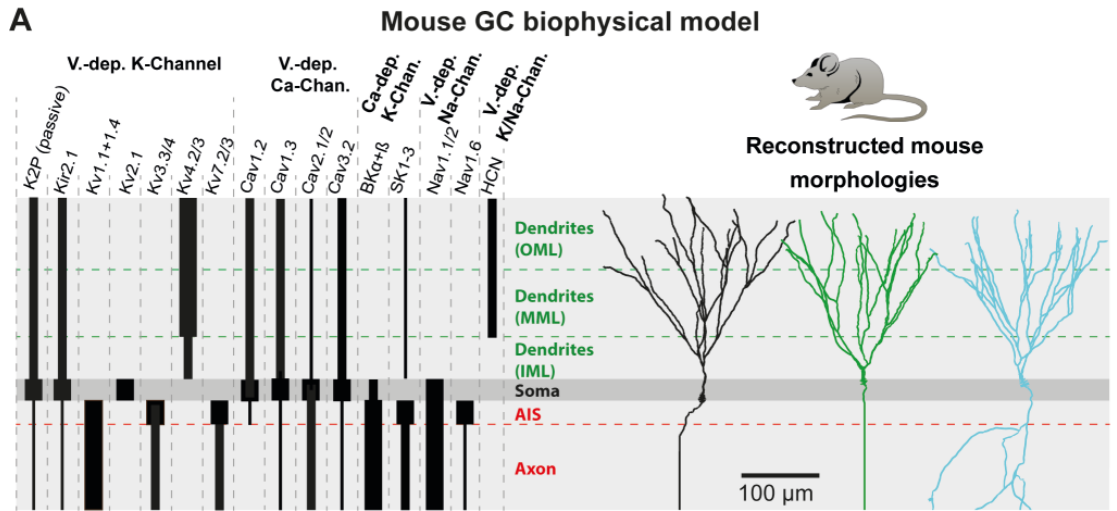


Figure 1. Overview of ion channel composition and morphology of the mouse dentate granule cell (GC) model.

(A) Left: Passive and active ion channels with their specific distribution in six different regions: outer molecular layer (OML), middle molecular layer (MML), inner molecular layer (IML), soma, axon initial segment (AIS) and axon. The relative spatial distribution of voltage-dependent (V.-dep.) and calcium-dependent (Ca^{2+} -dep.) channels is in line with an extensive amount of data from the literature (see Table 1, and Materials and methods for details). Right: Three exemplary morphologies out of eight reconstructed mouse GCs (Schmidt-Hieber et al., 2007) used for compartmental modeling of mouse GCs. (B) Schematic of the morphological model used to generate synthetic mouse morphologies which is analog to the previously reported rat model (Beining et al., 2016; see Material and Methods there for details). Upper left: A synthetic 3D young dentate gyrus (DG) was created comprising different layers (GCL, IML, MML, and OML, from bottom to top). A soma (red dot) was defined and random target points (black dots) were distributed within a 3D cone (red dashed lines). These points were complemented by directed target points (gray dots) that were placed automatically between clusters of target points and the soma. Upper right: The target points were connected by a minimum spanning tree algorithm (Cuntz et al., 2010) and terminal dendritic segments shorter than 20 μm were pruned off (red segments, see Beining et al., 2016). Lower right: The young DG and the dendritic tree have been stretched to their mature size (see Beining et al., 2016 for more information). Lower left: Adding a somatic diameter profile, a synthetic axon, applying jittering and dendritic diameter taper (not shown for visualization purposes) to the dendrites results in realistic synthetic GC morphologies suitable for compartmental modeling. (C) Six out of 15 synthetic morphologies created by the morphological model and used for compartmental modeling with their anatomical borders (gray dashed lines). (D) General and layer-specific structural comparison of the reconstructed (blue, Schmidt-Hieber et al., 2007) and synthetic (green) mouse GC morphologies.

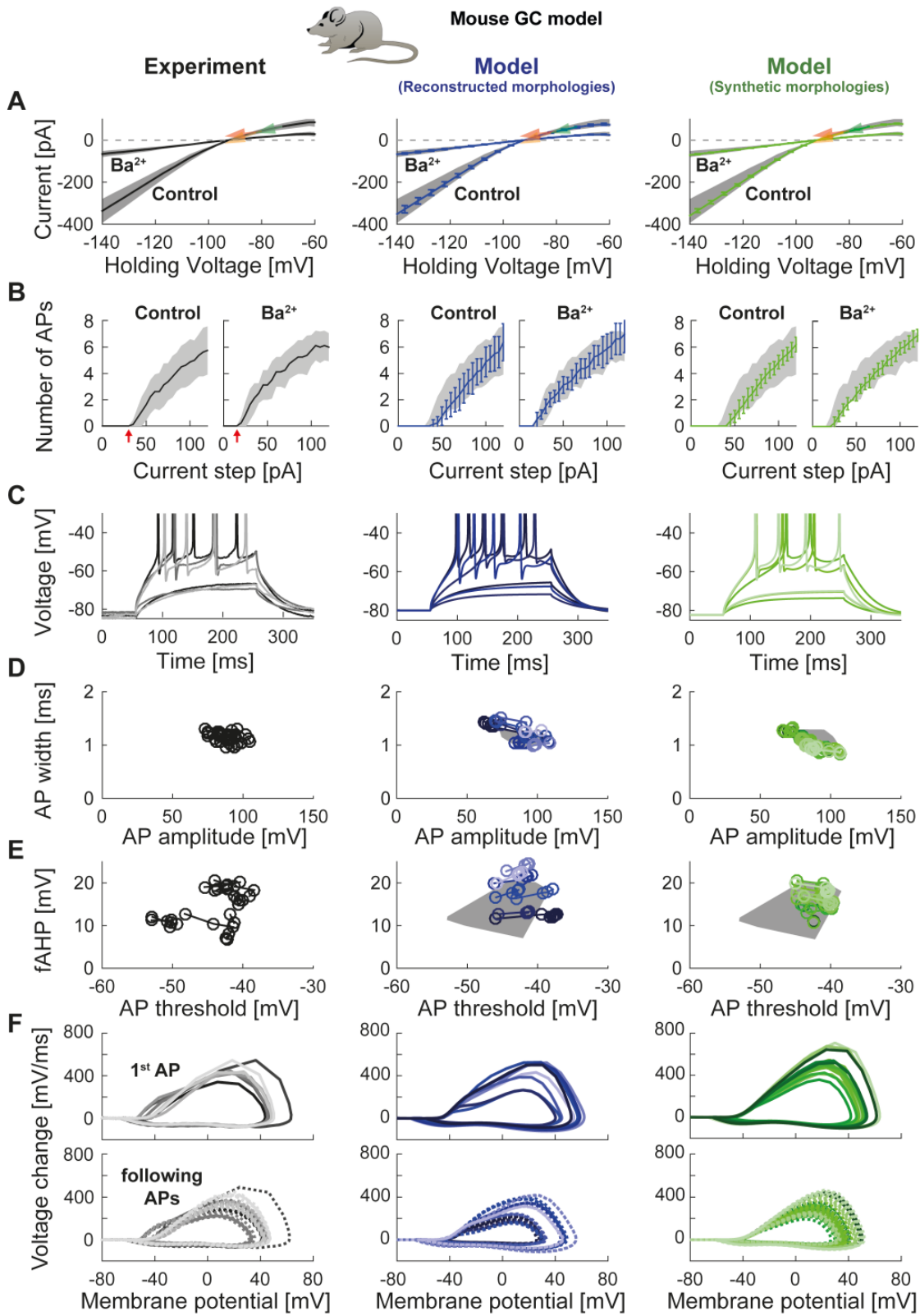


Figure 2. Passive and active properties of the mouse GC model.

Comparison of electrophysiological features between experimental data (left column, grayish colors) (Mongiati et al., 2009), GC model with reconstructed morphologies (middle column, blueish colors) and GC model with synthetic morphologies (right column, greenish colors). **(A)** Current-voltage (I-V) relationships before and after application of 200 μM Ba^{2+} . Simulations (blue and green curves) are compared to experimental data (mean and s.e.m. from raw traces (Mongiati et al., 2009) as black curve and gray patch; arrows are average values reported from further literature: red (Brenner et al., 2005), yellow (Mongiati et al., 2009), green (Schmidt-Hieber et al., 2007)). Ba^{2+} simulations correspond to 99 % Kir2 and 30 % K2P channel blockade. **(B)** Number of spikes elicited by 200 ms current steps (F-I relationship) including Ba^{2+} block as in **A**. Experimental standard deviation is shown as gray patches in all columns. **(C)** Exemplary spiking traces (200 ms, 30 and 75 pA somatic current injections). **(D–E)** Action potential (AP) features (90 pA somatic step current injection, 200 ms). Convex hulls around experimental data are shown in all columns as gray patches. **(D)** AP width vs. AP amplitude. **(E)** Amplitude of fast afterhyperpolarisation (fAHP) vs. AP threshold. **(F)** Phase plots of the first AP (dV/V curve, 90 pA current step, 200 ms).

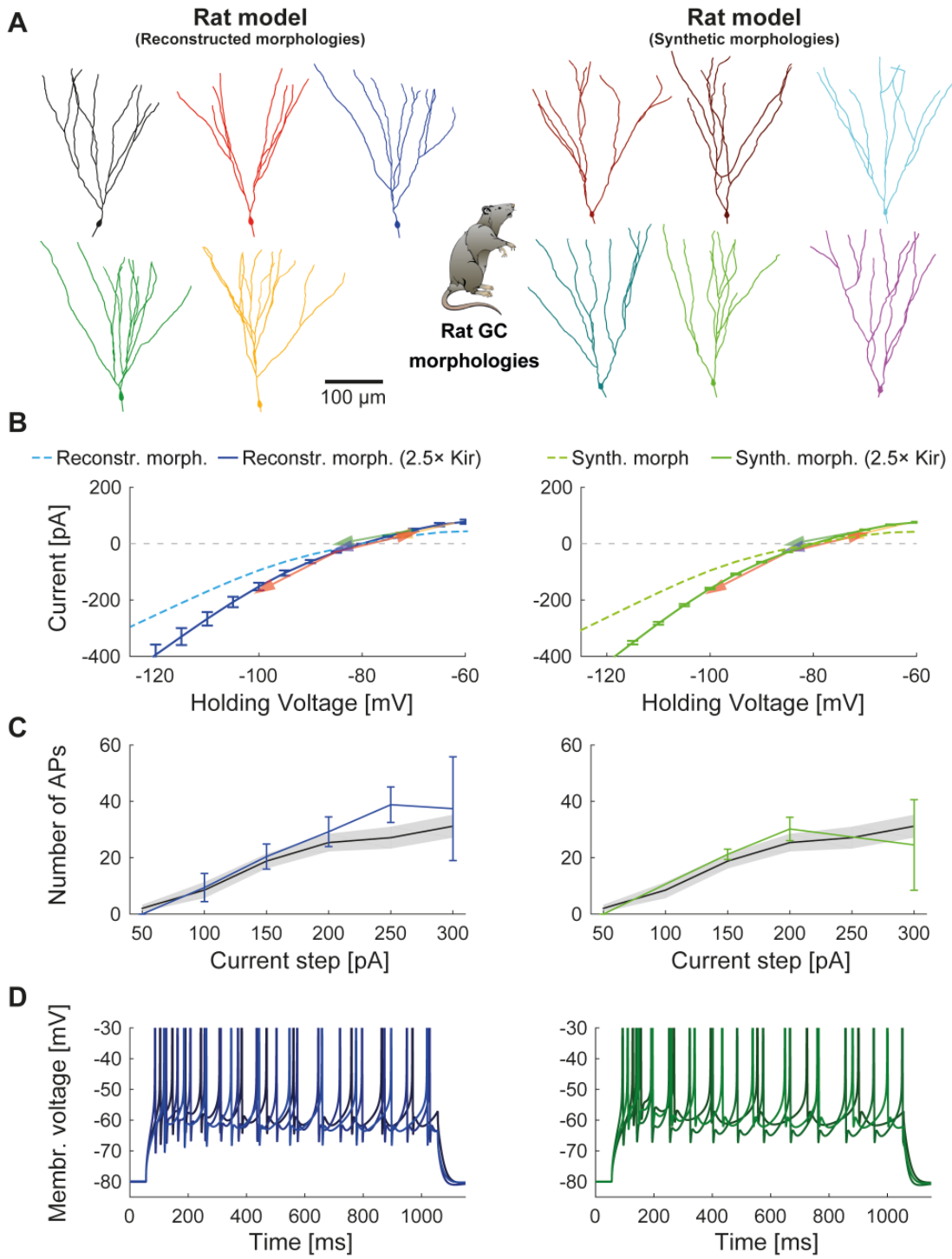


Figure 3. Rat GC model.

Comparison of electrophysiological features between GC model with reconstructed morphologies (middle column, blueish colors) and GC model with synthetic morphologies (right column, greenish colors) as it was adapted for reproducing rat data. **(A)** Illustration of reconstructed (left) and synthetic (right) rat morphologies used for simulations of rat GCs, from (Beining et al., 2016). **(B)** I-V relationship of the model with (dark solid lines) or without (bright dashed lines) adjustment of passive conductances to experimental rat data (indicated by arrows: red (Staley et al., 1992), yellow (Mateos-Aparicio et al., 2014), green (Pourbadie et al., 2015), violet (Schmidt-Hieber et al., 2004)). **(C)** F-I relationship of the model compared to data (black line and standard deviation as gray patch) from (Pourbadie et al., 2015). **(D)** Exemplary spiking traces simulated during a 1 s current injection of 200 pA.

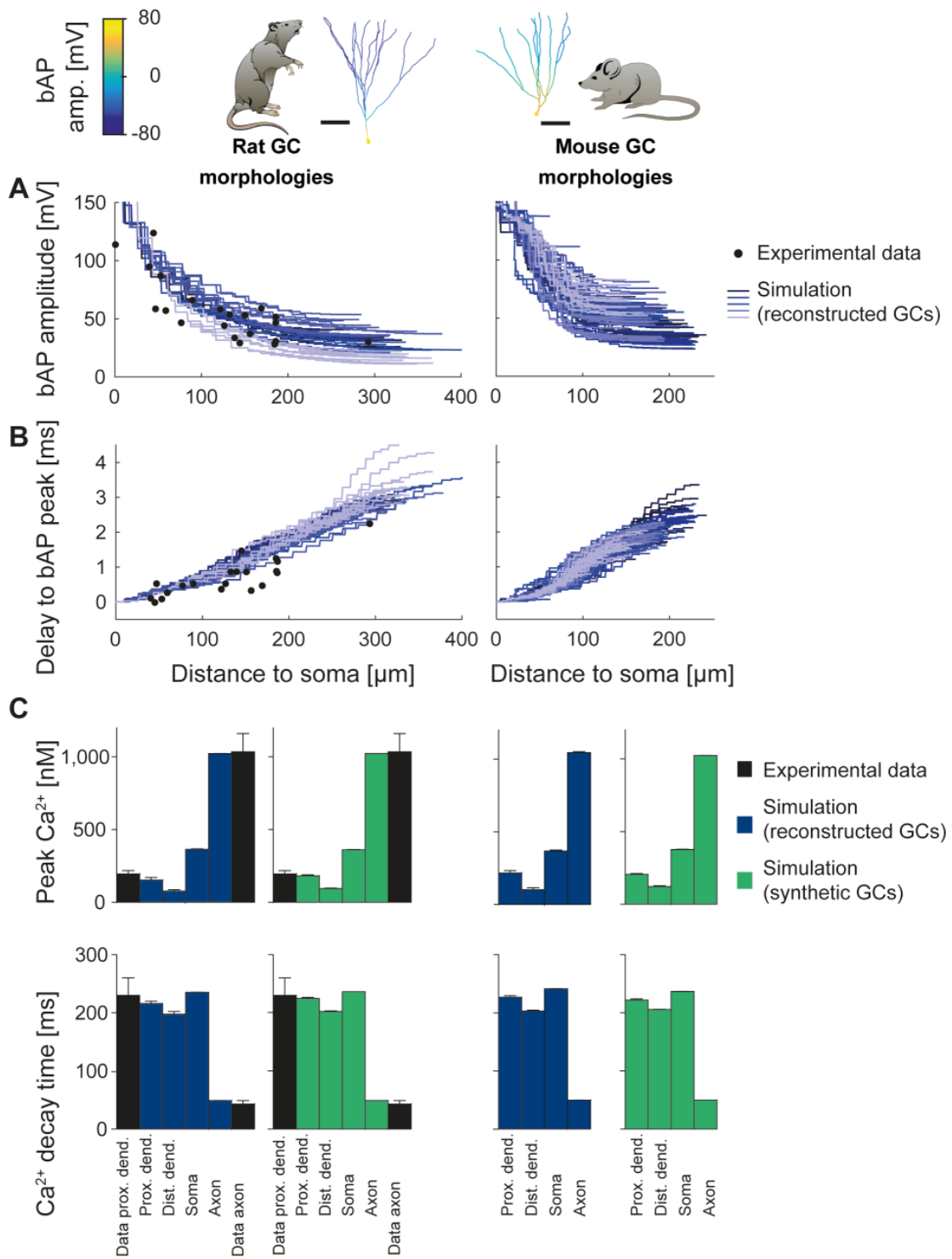
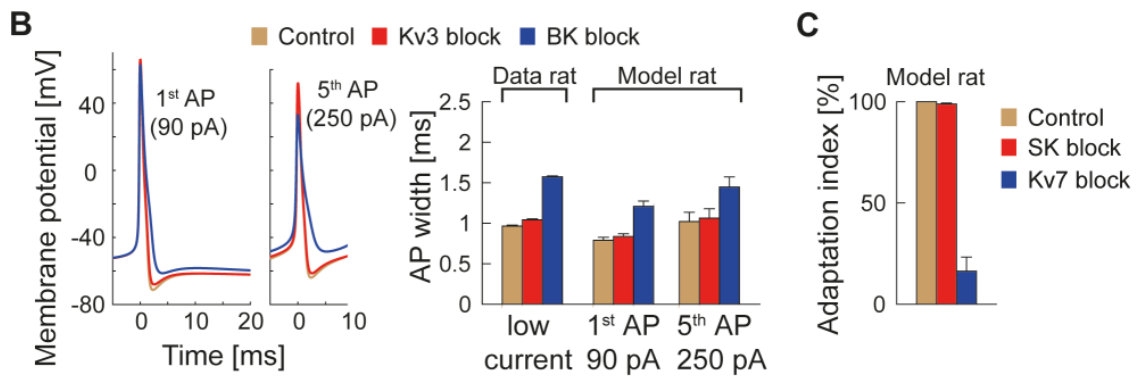


Figure 4. Backpropagating action potentials (bAPs) in mouse and rat GCs.

bAP characteristics at 33 °C (experiment and simulation), elicited in the soma by a brief current injection. Inset: Exemplary rat and mouse GC morphology with local maximum voltage amplitudes. **(A)** Maximal voltage amplitude as a function of Euclidean distance from the soma. Black data points are experimental data from rat (Krueppel et al., 2011). **(B)** Corresponding delay of the maximal bAP amplitude in the model compared to experimental rat data (black dots) (Krueppel et al., 2011). **(C)** Peak Ca^{2+} amplitudes at room temperature following an AP measured at different locations in the rat (left) and mouse (right) GC model using reconstructed (blue) and synthetic (green) morphologies. Experimental rat data measured in proximal dendrites (Stocca et al., 2008) and axonal mossy fiber boutons (MFBs) (Jackson & Redman, 2003) are added as black bars. **(D)** Ca^{2+} decay time constants analog to **C**.

Sensitivity analysis for a 50% reduction in parameter values



Modeling ion channel changes during epilepsy

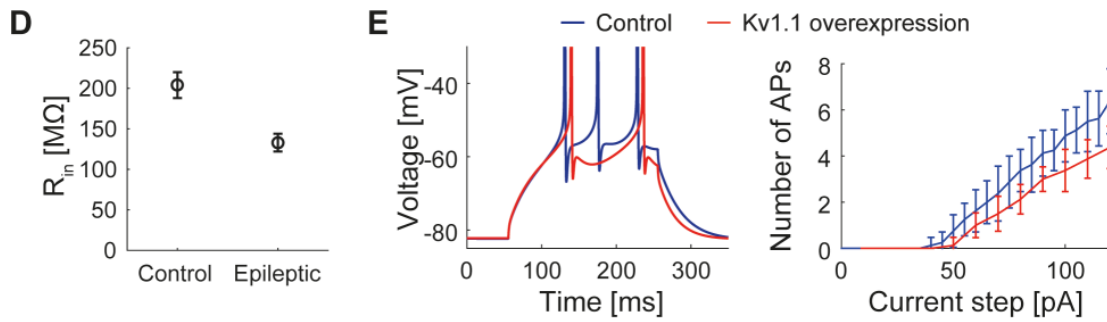


Figure 5. Dependence of the model on specific channels and parameters.

(A) Sensitivity matrix showing the relative change (color-coded) in electrophysiological parameters (y-axis) following a 50 % reduction in ion channel densities or other model parameters (x-axis), except for the cases marked with an asterisk (*): the reversal potential of potassium E_K was raised by +20 mV (to reduce ionic drive) and E_{Na} was lowered by -20 mV. The temperature was raised by +10 °C. cAMP concentration (influencing HCN channels in the model) was raised from 0 to 1 μ M. (B) Left: Exemplary voltage traces during 1 s current injection of 90 pA (left, first AP) or 250 pA (right, fifth AP) under control (black lines), $K_v3.4$ block (red lines) or BK block (blue lines) conditions. Right: Half-amplitude AP widths compared to experimental data that used paxilline to block BK (Brenner et al., 2005; Müller et al., 2007) or BDS-I to block $K_v3.4$ channels (Riazanski et al., 2001). (C) Impact of the blockade of SK and K_v7 channels on spike frequency adaptation. (D) Input resistance measurements in rat GCs in the control case and when post-epileptic conditions are modeled (doubled Kir2 and HCN channel conductance). (E) A reported overexpression of $K_v1.1$ following an *in vivo* approach to elicit temporal lobe epilepsy (Kirchheim et al., 2013) was mimicked *in silico* by a 3-fold increase of $K_v1.1$ channel density. Left graph illustrates increased spiking delay, whereas the right plot shows the reduced excitability.

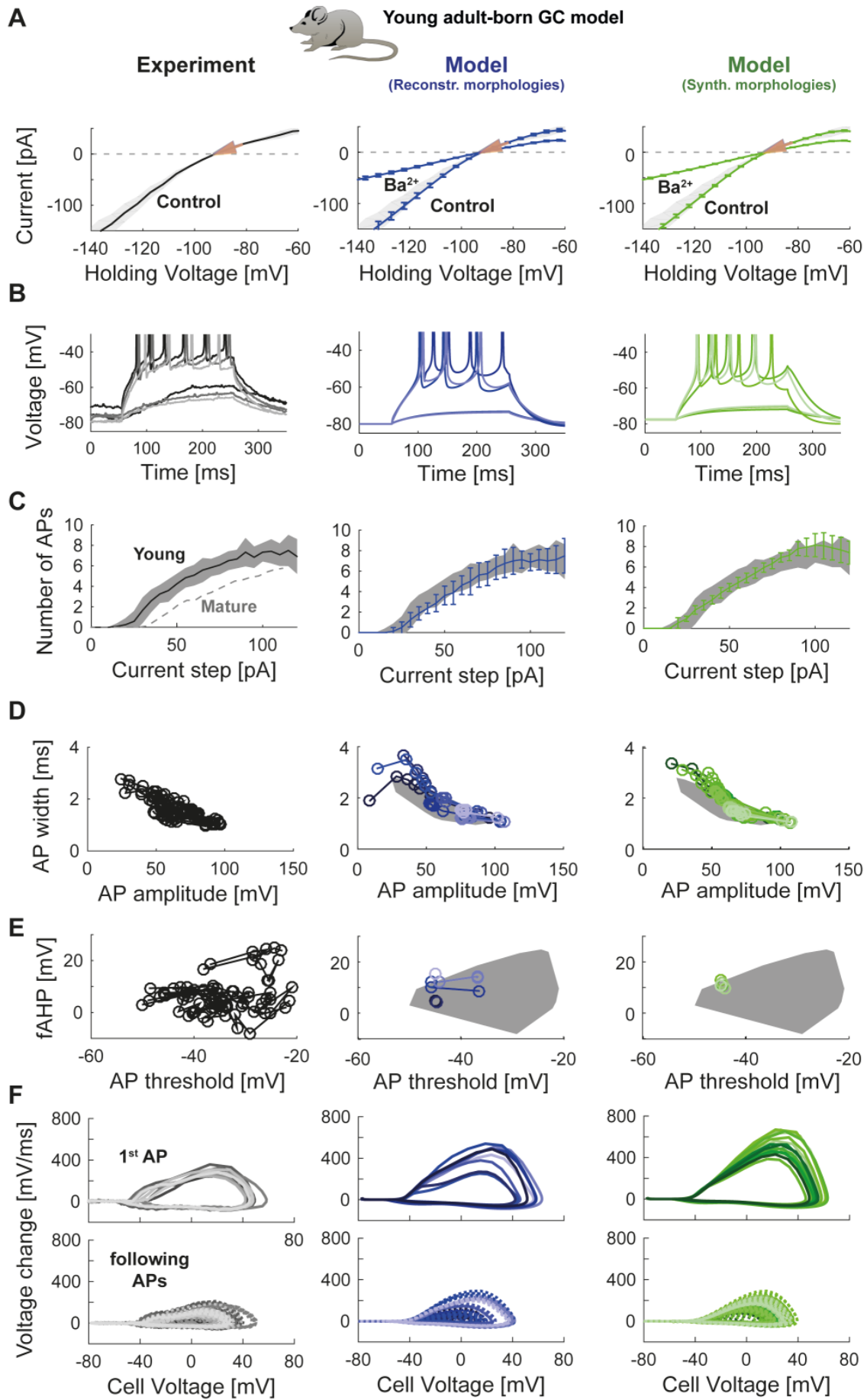


Figure 6. Model of young adult-born granule cells (abGCs).

Panels are analog to Fig. 2, with comparison of electrophysiological features between experimental data (left column, grayish colors), GC model with reconstructed morphologies (middle column, blueish colors) and GC model with synthetic morphologies (right column, greenish colors). The experimental data of young abGCs at a cell age of 28 dpi is from (Mongiati et al., 2009). The model was obtained by a reduction of several ion channels (see Table 3). **(A)** Current-voltage (I-V) relationships before and after application of 200 μM Ba^{2+} ; Ba^{2+} simulations correspond to 99 % Kir2 and 30 % K2P channel blockade. Experimental measurements of R_{in} in 28 dpi old abGCs from further literature are indicated by arrows (red (Mongiati et al., 2009), green (Piatti et al., 2011), pink (Yang et al., 2015)). **(B)** Exemplary spiking traces (200 ms, 10 and 50 pA somatic current injections). **(C)** Number of spikes elicited by 200 ms current steps (F-I relationship). Experimental standard deviation is shown as gray patches in all columns and the F-I curve of mature GCs is plotted in the left column (gray dashed line) for comparison. **(D–E)** Action potential (AP) features (90 pA somatic step current injection, 200 ms). Convex hulls around experimental data are shown in all columns as gray patches. **(D)** AP width vs. AP amplitude. **(E)** Amplitude of fast afterhyperpolarisation (fAHP) vs. AP threshold. **(F)** Phase plots of the first AP (dV/V curve, 90 pA current step, 200 ms).

Figure 7. Synaptic integration in young abGCs vs. mature GCs.

(A) Left: Scheme of the simulation configuration with 15 synapses distributed in the MML and 15 in the OML. Middle: All synapses are activated synchronously at 40 Hz. Note that young abGCs (middle row) followed the input (black vertical lines) better than mature GCs (upper row), but performed similarly (lower row) when the biologically lower synapse number (15 synapses in total, yGC_{15}) was implemented. Right: Summary of the input/output relation at all tested frequencies (5, 10, 20, 40, 75, 100 Hz). Gray dashed line illustrates the theoretically perfect input/output ratio. (B) Upper left: Scheme of the simulation configuration when MML and OML synapses are activated with a delay of Δt to analyze temporal summation of inputs. Upper right: Note that young abGCs perform better than mature GCs at following the 10 Hz input when the MML and OML inputs are delayed (left, -15 ms) compared to synchronous activation (right, 0 ms). Lower row: Summary over all tested frequencies (10, 20, 40, 75 Hz) showing that young abGCs have a broader time window of temporal summation than mature GCs at low frequencies but perform slightly worse than mature GCs at high frequencies.

Supplementary Figures

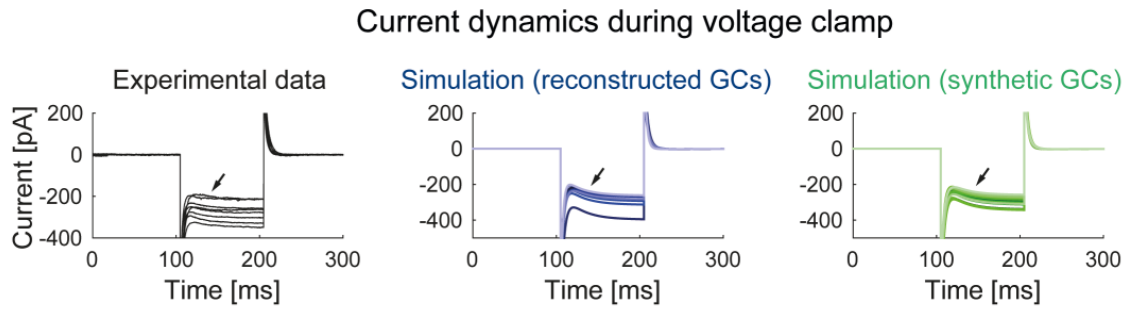


Figure 2—figure supplement 1. Current dynamics during voltage clamp.

Currents measured during a highly hyperpolarized voltage step (-120 mV) in the experiment (left) and the models with reconstructed (middle) and synthetic (right) morphologies. The slowly activating currents (black arrows) originate from Kir currents in the model.

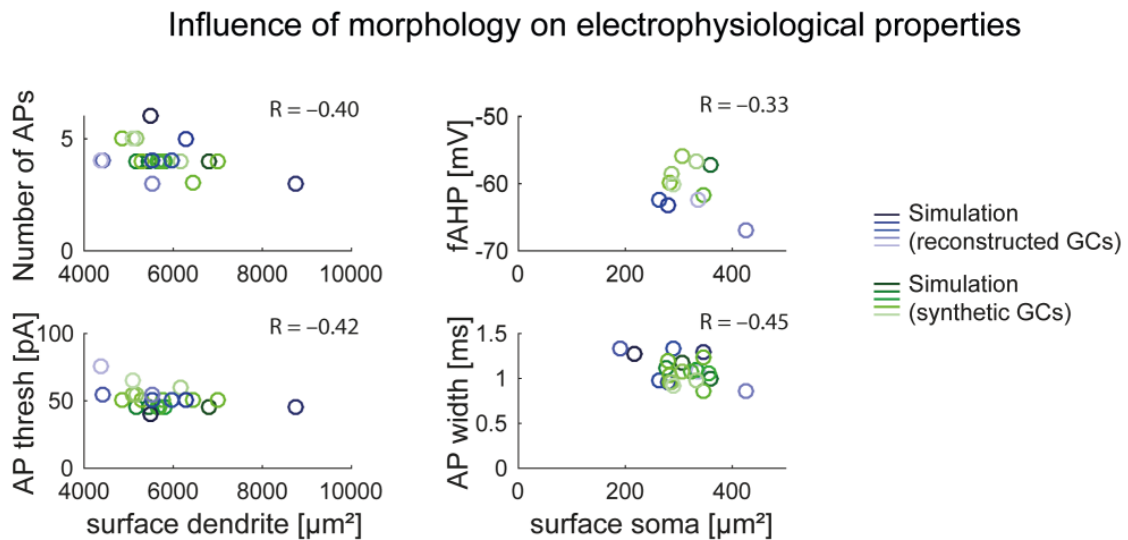


Figure 2—figure supplement 2. Influence of morphology on electrophysiological properties.

Influence of dendritic (left column) and somatic (right column) surface size on electrophysiological parameters (fAHP, AP width, AP threshold and number of APs) in the model with reconstructed (blue circles) and synthetic (green circles) morphologies. Correlation coefficients are given as inset text.

Maximal rate of voltage change during an AP

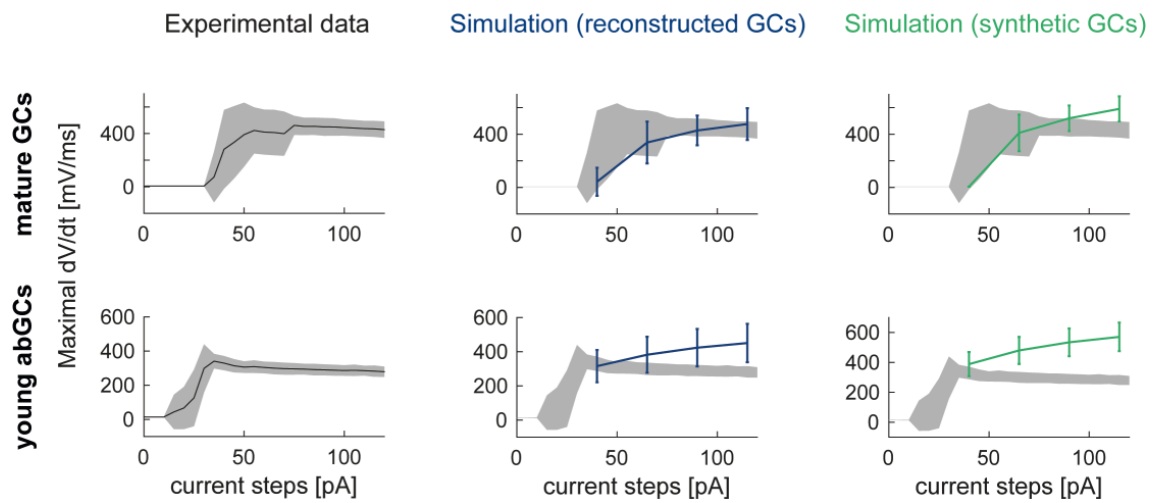


Figure 2—figure supplement 3. Maximal rate of voltage change during an action potential.

The maximal voltage deflection during a spike shows a sudden jump and then slow decay in the experiment when current amplitudes are increased in mature (upper row, left) and young GCs (lower row, left) which is not reproduced in the mature/young GC model with the na8st sodium channel model (from Schmidt-Hieber & Bischofberger, 2010) in reconstructed (middle column) or synthetic (right column) morphologies.

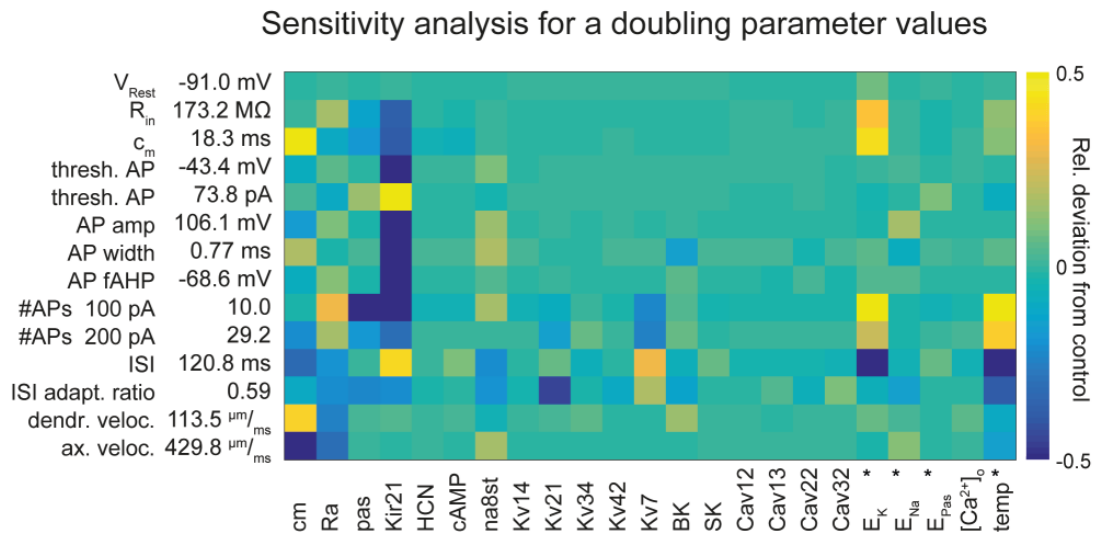


Figure 5—figure supplement 1. Sensitivity analysis for a doubling of parameter values.

Sensitivity matrix analog to Figure 5A but with increased (doubled) instead of reduced channel densities or parameters except for the cases marked with an asterix (*): the reversal potential of potassium E_K was lowered by -20 mV (to increase ionic drive) and E_{Na} was increased by +20 mV. HCN is increased from 0 to 1 μM in both cases. Temperature was reduced from 24 to 14 °C.

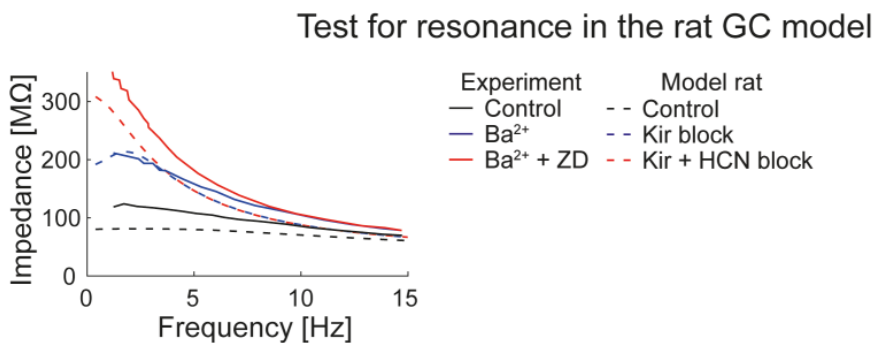


Figure 5—figure supplement 2. Test for resonance in the rat GC model.

GCs were injected with oscillating currents of increasing frequency to calculate their impedance. The graph shows experimental (solid curves, human GCs (Stegen et al., 2012)) and simulation (dashed curves, rat GCs) data under control conditions (black) and when Kir (blue) or Kir and HCN (red) channels are blocked.

Table 1. Summary of all implemented ion channel models with channel density in the mouse mature GC model.

Name	Soma	Axon	AIS	GCL	IML	MML	OML	Ref. on subcellular distribution	Ion channel model and modifications
Na _v 1.1	3	0	0	0	0	0	0	(Schmidt-Hieber & Bischofberger, 2010;	8-state model from (Schmidt-Hieber & Westenbroek, Merrick, & Catterall, 1989)
Na _v 1.2	0	3	3	0	0	0	0	(Kress, Dowling, Eisenman, & Mennerick, 2010; Schmidt-Hieber & Bischofberger, 2010)	Inact. modified according to (Rush et al., 2005; Schmidt-Hieber & Bischofberger, 2010)
Na _v 1.6	0	1	3	0	0	0	0	(Aller & Wisden, 2008; Gabriel et al., 2002; Hervieu et al., 2001; Lesage et al., 1997; Talley et al., 2001; Yarishkin et al., 2014)	(see text)
	88.128	88.128	518.400	-	-	-	-		
K2Ps	3	1	1	2	2	2	2		
	0.014	0.007	0.007	0.014	0.014	0.048	0.014		

Kir 2.x	3	1	1	2	2	2	2	(Karschin et al., 1996; 6-state model, Miyashita & Kubo, 1997; modification see text. Prüss et al., 2003; Stonehouse et al., 1999)
	0.142	0.067	0.067	0.142	0.142	0.142	0.142	
HCN1-3	0	0	0	0	2	2	2	(Notomi & Shigemoto, 2004) model adapted from (Stegen et al., 2012); activation -10 mV, added cAMP-sens. & slow comp. of act.
	-	-	-	-	0.004	0.004	0.004	
K _v 1.1	0	3	3	0	0	0	0	(Grosse et al., 2000; nh model from Monaghan et al., 2001; K (Christie et al., 1989) J Rhodes et al., 1997)
	-	0.250	0.250	-	-	-	-	
K _v 1.4	0	3	3	0	0	0	0	(E C Cooper, Milroy, Jan, n ⁴ h model from Jan, & Lowenstein, 1998; (Wissmann et al., Grosse et al., 2000; 2003) Monaghan et al., 2001; K J Rhodes et al., 1997)
	-	1.000	1.000	-	-	-	-	

261

K _v 2.1	3	0	0	0	0	0	0	(Murakoshi & Trimmer, 1999; K J Rhodes et al., 1997)	mh model, fitted using (Gordon, Roepke, & Abbott, 2006; Kerschensteiner & Stocker, 1999; J. W. Kramer, Post, Brown, & Kirsch, 1998; McCrossan et al., 2003; VanDongen, Frech, Drewe, Joho, & Brown, 1990)
	7.091	-	-	-	-	-	-		
K _v 3.3/4	0	2	3	0	0	0	0	(Chang et al., 2007; Weiser et al., 1994)	mh model, fitted using (Desai et al., 2008; Rettig et al., 1992; Riazanski et al., 2001; Rudy et al., 1991; Schröter et al., 1991; Vega-Saenz de Miera et al., 1992)
	-	7.656	30.781	-	-	-	-		

K _v 4.2/3	0	0	0	1	2	3	3
+KChIP/ DPP6							
	-	-	-	2.175	4.350	4.350	4.350

(Menegola & Trimmer, 2006; Kenneth J Rhodes et al., 2004; Zaghera et al., 2005) & 13-state model from (Barghaan et al., 2008); activation -20 mV according to (Barghaan et al., 2008) Fig. S1A and (An et al., 2000; Bähring, Boland, Varghese, Gebauer, & Pongs, 2001; H H Jerng, Shahidullah, & Covarrubias, 1999; Henry H Jerng, Kunjilwar, & Pfaffinger, 2005; Kaulin, De Santiago-Castillo, Rocha, & Covarrubias, 2008; Kim et al., 2008; Patel, Parai, Parai, & Campbell, 2004; Rüschemschmidt et al., 2006)

K _v 7.2/3 (KCNQ2 &3)	0	2	3	0	0	0	0	(Edward C. Cooper, mh model from Harrington, Jan, & Jan, (Mateos-Aparicio et al., 2001; Klinger, Gould, 2014) ($\eta = 0.5$, see Boehm, & Shapiro, Tab. S1 in (Mateos-2011; Martinello et al., Aparicio et al., 2014)) 2015)
	-	1.3400	6.7000	-	-	-	-	
Ca _v 1.2 (L-type)	3	0	1	1	2	2	2	(Leitch, Szostek, Lin, & mh ₁ h ₂ model Shevtsova, 2009; transferred from Tippens et al., 2008) GENESIS (Evans et al., 2013), added Ca ²⁺ -dep. Inactivation (h2)
	0.0200	-	0.0100	0.0100	0.0400	0.0400	0.0400	
Ca _v 1.3 (L-type)	3	1	2	1	2	2	2	(Leitch et al., 2009; mh ₁ h ₂ model Tippens et al., 2008) transferred from GENESIS (Evans et al., 2013), added Ca ²⁺ -dep. Inactivation (h2)
	0.0160	0.0040	0.0080	0.0040	0.0080	0.0080	0.0080	

Ca _v 2.1/2 (N-/P/Q- type)	3	2	2	1	1	1	1	(Chung et al., 2001; N. C. m ² h model from (Fox Day et al., 1996; Li, et al., 1987); set Bischofberger, & Jonas, inact. time constant to 2007; J H Xu et al., 2010; 100 ms according to Jie Hua Xu, Long, Tang, (Fox et al., 1987; X. Hu, & Tang, 2007) Huang et al., 2010)
	0.3000	0.0500	0.0500	0.0500	0.0500	0.0500	0.0500	
Ca _v 3.2 (T-type)	3	1	1	2	2	2	2	(Craig et al., 1999; 8-state model from Martinello et al., 2015; (Burgess et al., 2002) McKay et al., 2006)
	0.0220	0.0080	0.0080	0.0220	0.0220	0.0220	0.0220	
BK (slo1)	2	3	3	0	0	0	0	(Kaufmann et al., 2010; Model from (Jaffe et Knaus et al., 1996; al., 2011); Misonou et al., 2006; C. modification see text A. Sailer et al., 2006)
αβ / α	3.900 / 15.600	15.600 / 62.400	15.600 / 62.400	-	-	-	-	

SK2	0	2	3	0	1	1	1	(Ballesteros-Merino et al., 2014; Maciaszek, Soh, Walikonis, Tzingounis, & Lykotrafitis, 2012; 1998; Hirschberg, Obermair, Kaufmann, Maylie, Adelman, & Knaus, & Flucher, 2003; Marrion, 1999) C. a. Sailer, Kaufmann, Marksteiner, & Knaus, 2004)
	0.001	0.013	0.083	0.002	0.004	0.004	0.004	

Localization/expression code: 0 = not existent or very weak, 1 = weak, 2 = moderate, 3 = strong.

Table 2. Electrophysiology in mature mouse GCs – experiment vs. model.

Intrinsic properties	Experiment	Model (reconstructed morphologies)	Model (synthetic morphologies)
R_{in} [M Ω] (-70mV)	289.5 \pm 34.9	287.0 \pm 14.7	278.8 \pm 6.9
c_m [pF]	48.9 \pm 5.3	55.7 \pm 2.8	60.4 \pm 1.7
tau [ms]	34.0 \pm 2.0	31.5 \pm 0.2	31.6 \pm 0.1
V_{rest} [mV]	-92.7 \pm 0.5*	-88.7 \pm 0.0	-88.6 \pm 0.0
$I_{threshold}$ [pA]	47.5 \pm 4.5	52.5 \pm 3.7	50.3 \pm 1.6
$V_{threshold}$ [mV]	-46.3 \pm 1.6	-44.9 \pm 0.3	-43.8 \pm 0.2
AP amplitude [mV]	95.6 \pm 2.1	96.3 \pm 2.9	97.7 \pm 1.7
AP width [ms]	1.03 \pm 0.02	1.00 \pm 0.04	0.93 \pm 0.02
fAHP [mV]	15.7 \pm 1.4	17.5 \pm 1.7	15.8 \pm 0.8
Interspike interval [ms]	36.3 \pm 4.9	36.2 \pm 3.2	34.5 \pm 1.1
Max. spike slope [V/s]	450.1 \pm 23.7	428.0 \pm 39.5	519.7 \pm 24.9
g_{Kir} [nS]	5.46 \pm 1.31	5.94 \pm 0.9	5.97 \pm 0.6

* after subtraction of a calculated liquid junction potential of 12.1 mV.

Table 3: Ion channels or currents that were reported to be less expressed in immature GCs and that were partly downregulated in the young GC model

Channel name	Reference	Downreg. [%]
Kir 2.x	(Mongiati et al., 2009)	73
K _v 1.4	(Guan, Horton, Armstrong, & Foehring, 2011; Maletic-Savatic, Lenn, & Trimmer, 1995)	0
K _v 2.1	(Antonucci, Lim, Vassanelli, & Trimmer, 2001; Guan et al., 2011; Maletic-Savatic et al., 1995)	50
K _v 3.4	(Riazanski et al., 2001)	0
K _v 4.2/4.3 +KChIP/DPP6	(Maletic-Savatic et al., 1995; Riazanski et al., 2001)	50
K _v 7.2 & 7.3 (KCNQ2&3)	(Geiger, Weber, Landwehrmeyer, Sommer, & Lerche, 2006; Safiulina, Zacchi, Tagliatela, Yaari, & Cherubini, 2008; Smith, Iannotti, Dargis, Christian, & Aiyar, 2001; Tinel, Lauritzen, Chouabe, Lazdunski, & Borsotto, 1998)	50
Na _v 1.2/6	(Y. B. Liu, Lio, Pasternak, & Trommer, 1996; Pedroni, Minh, Mallamaci, & Cherubini, 2014)	25
Ca _v 1.2	(Jones et al., 1997)	0
Ca _v 1.3 (L-type)	(A. a. Kramer, Ingraham, Sharpe, & Mynlieff, 2012)	50
BK- α / BK- β 4	(MacDonald, Ruth, Knaus, & Shipston, 2006; P. Xu, Li, Xuan, & Yang, 2015)	40 / 100

9. Danksagung / Acknowledgements (German)

Ich möchte mich bei einer Reihe von Personen bedanken, die meine Doktorarbeit erst möglich gemacht, bzw. deutlich farbenfroher gestaltet haben. Ein großer Dank geht an meinen Doktorvater Dr. Stephan Schwarzacher, der mich für dieses vielseitige und spannende Thema begeistert hat, und mir half mich zu fokussieren, wenn ich zu vielen Fragestellungen gleichzeitig hinterhergejagt bin. Die vielen persönlichen Gespräche und das entgegengebrachte Vertrauen und Verständnis waren von großem Wert für mich!

Einen ebenbürtigen Dank gebührt meinen Betreuern Dr. Hermann Cuntz und Dr. Peter Jedlicka, die mich finanziell maßgeblich gestützt und mit viel Begeisterung und Optimismus in die Welt der Computermodelle geführt haben. Ebenso sehr möchte ich mich bei der International Max-Planck Research School (IMPRS) for Neural Circuits für die Aufnahme in ihr Programm und das mehrfache Einspringen bei Finanzierungslücken bedanken. Die spannenden und hilfreichen Seminare und erlebnisreichen Ausflüge werden mir immer in Erinnerung bleiben. Einen besonderen Dank gebührt an dieser Stelle dem Programmkoordinator Arjan Vink, der mir bei meinen vielen Fragen und Bitten hilfreich zur Verfügung stand, der stets bei jeder IMPRS-Party und jedem Retreat dabei ist und mit seiner Freundlichkeit und Empathie bei uns IMPRS-Studenten sehr beliebt ist.

Dank gebührt ebenso Prof. Amparo-Acker Palmer für die offizielle Betreuung im Fachbereich Biowissenschaften, und gemeinsam mit Prof. Manfred Kössl und Prof. Enrico Schleiff für die Einwilligung meine Doktorarbeit zu begutachten und meiner Prüfungskommission beizuwohnen.

Desweiteren bedanke ich mich bei Prof. Dr. med. Thomas Deller, der die häufig nötigen Sachmittel bereitstellte und der mit seiner außerordentlichen Erfahrung und Sachkunde stets sehr wertvolle und präzise Ratschläge für mich hatte.

Desweiteren bedanke ich mich bei Martina Hütten und Ute Fertig, die mir bei der Bewältigung von Papier- und Histoarbeiten oft hilfreich zur Seite standen.

Für die viele gegenseitige Hilfe beim Compartmental Modeling und die wertvollen Diskussionen bedanke ich mich zudem bei meinen ehemaligen

Danksagung

Kollegen Steffen Platschek und Christian Ebner und wünsche ihnen stets bugfreien Code.

Ich bin froh, dass ich sowohl in der IMPRS, als auch am Neuroscience Center und am ESI auf einen lustigen Haufen an Kollegen traf, die mir den Arbeitstag und manchen Feierabend freundlicher und kurzweiliger gestaltet haben. In diesem Zusammenhang bedanke ich mich bei meinen IMPRS Kollegen Andreas Strehl, Eva Harde, Fabio Sartori, Irina Epstein und Isabelle Chang für die gegenseitige persönliche und wissenschaftliche Hilfe und die wunderbare Zeit; bei Aline Blistein, Andreas Vlachos, Christos Galanis, Denise Becker, Matej Vnencak, Michael Rietsche, Namrata Mohapatra und Nadine Zahn und Silvia Rodríguez Rozada vom Neuroscience Center; und bei Marvin Weigand, Alexandra Vormberg, Christian Ebner, Julia Müllerleile, Alexander Prinz, Felix Effenberger und André Castro vom ESI, die mir zudem zum täglichen Training meiner motorischen Fähigkeiten beim Kickerspielen verhalfen. Coconut! Während der letzten Jahre durfte ich einige Module für Masterstudenten betreuen. In diesem Zusammenhang bedanke ich mich bei Saskia Krischok, Norman Seeliger, Jan Koehler und Torsten Felske für ihr Interesse an meinem Thema und die Möglichkeit mit ihnen interessante Nebenprojekte anzugehen. Aus enger Zusammenarbeit geht manchmal auch große Freundschaft hervor! Daher bedanke ich mich ganz besonders bei meinen Mitdoktoranden Tijana Radic und Tassilo Jungenitz für die intensive gegenseitige Hilfe während unserer Studien! Die vielen wundervollen Abende in den Bars, Kinos, Wohnungen, See- und Flussufern rund um Frankfurt sowie die aufregende Zeit in Stockholm werden mir unvergessen bleiben und ich hoffe wir halten den Kontakt, wo auch immer es uns hin verschleppt!

Ein wichtiger Dank geht an meine Freunde Sandra, Dominik, Kai, Jane, Jürgen, Pascal und Anita, die besonders in den schweren Phasen für mich da waren, für jede Schandtät zu haben sind und mir den Blick für das Wesentliche offenhielten. Eure Freundschaft ist unersetzbar!

Ich bedanke mich auch von tiefstem Herzen bei meinen Eltern, Großeltern, Schwiegereltern und Geschwistern, die mir in dieser Zeit eine große finanzielle und persönliche Stütze waren und mit großem Interesse meinen langen Weg zur Dissertation verfolgt haben.

Danksagung

Der wichtigsten Person widme ich den Schluss. Vivien, es gibt keine Worte die meine Dankbarkeit für deine aufbauenden Worte und Gesten, dein großes Interesse, dein Riesenverständnis für die intensiven Arbeitsphasen und deine Liebe auch nur annähernd beschreiben können! Danke, dass es dich gibt!

10. Curriculum vitae

Education

- Since 04/2012 **PhD thesis at the Institute for Clinical Neuroanatomy Frankfurt, Frankfurt Institute for Advanced Studies (FIAS) and Ernst Strüngmann Institute (ESI) for Neuroscience in Coop. with Max-Planck Society**
Supervisors: Stephan Schwarzacher, Peter Jedlicka, Hermann Cuntz
- Since 08/2011 **Enrolled in the International Max-Planck Research School for Neural Circuits Frankfurt**
- 10/2008 – 02/2011 **University of Heidelberg**
Master's degree: Molecular Biotechnology
Master's thesis at DKFZ Heidelberg in the Jörg Langowski lab: BioShuttle, a non-viral, cell-penetrating drug carrier system. Diffusion studies using high-resolution Fluorescence Correlation Spectroscopy and Confocal Laser Scanning Microscopy in living cells
- 10/2005 – 06/2008 **University of Heidelberg**
Bachelor's degree: Molecular Biotechnology

Further Training

- 08/2014 **FIAS Summer School: Advanced Course in Computational Neuroscience**
- 04/2013 **FELASA B course on animal handling**
- 02/2011 **Jülich Spring School: Macromolecular Systems in Soft & Living Matter**

Further (Inter)National Work Experience

08/2007-12/2015 **Student research assistant in the Denk lab (Group Moritz Helmstaedter)**

MPI for Med. Research Heidelberg

08/2009-09/2009 **Internship in the Oliver Wagner lab**

NTHU Hsinchu, Taiwan, Institute of Molecular & Cellular Biology

Publications

1) **Beining M**, Mongiat Lucas A, Schwarzacher SW, Cuntz H⁺, Jedlicka P⁺: A novel comprehensive and consistent electrophysiological model of dentate granule cells (*submitted*)

2) Jungenitz T*, **Beining M***, Radic T, Deller T, Cuntz H, Jedlicka P, Schwarzacher SW: Structural homo- and heterosynaptic plasticity in adult newborn hippocampal granule cells (*submitted*)

3) Radic T, Jungenitz T, Singer M, **Beining M**, Cuntz H, Vlachos A, Deller T, Schwarzacher SW: Time-lapse imaging reveals highly dynamic structural maturation of postnatally born dentate granule cells in organotypic entorhino-hippocampal slice cultures (*submitted*)

4) **Beining M***, Jungenitz T*, Radic T, Deller T, Cuntz H⁺, Jedlicka P⁺, Schwarzacher SW⁺: Adult-born dentate granule cells show a critical period of dendritic reorganization and are distinct from developmentally born cells. *Brain Structure and Function* 2016

5) Radic T, Al-Qaisi O, Jungenitz T, **Beining M**, Schwarzacher SW: Differential Structural Development of Adult-Born Septal Hippocampal Granule Cells in the Thy1-GFP Mouse, Nuclear Size as a New Index of Maturation. *PLoS ONE* 10(8): e0135493.

6) Braun K, **Beining M**, Wiessler M, Lammers T, Pipkorn R, Henrich U, Nokihara K, Semmler W, Debus J, Waldeck W.: *BioShuttle Mobility in Living*

Cells Studied with High-Resolution FCS & CLSM Methodologies. *Int J Med Sci*. 2012; 9(5):339-52.

7) Pipkorn R, Wiessler M, Waldeck W, Hennrich U, Nokihara K, **Beining M**, Braun K: Improved Synthesis Strategy for Peptide Nucleic Acids (PNA) appropriate for Cell-specific Fluorescence Imaging. *Int J Med Sci* 2012; 9(1):1-10.

* Joint-first coauthors + Joint-last coauthors

International Conference Posters

- 05/2014 Jungenitz T, **Beining M**, Radic T, Schwarzacher SW:
Structural prerequisites for functional integration of adult
newborn dentate granule cells in the hippocampus.
Keystone Symposium Adult Neurogenesis, Stockholm,
Sweden
- 10/2015 **Beining M**, Mongiat LA, Schwarzacher SW, Cuntz H,
Jedlicka P: A consistent electrophysiological model of
dentate granule cells based on pharmacology to study
adult-born neurons. SFN 2015, Chicago, USA

Scholarships / Awards

- 06/2016 **1st Poster Award with T. Jungenitz, rmn² meeting
Oberwesel, Germany**
- Since 05/2012 **Member in the Youtrex Career Network Scholar
Program**
- Since 2010 **eFellows Online Scholarship**
- 08/2011-01/2013 **Stipend IMPRS for Neural Circuits Frankfurt**
- 08/2009-09/2009 **DAAD/NSC: Taiwan Summer Institute Program 2009**

Professional Activities

Peer reviewer Development